

TOWARDS AN UNDERSTANDING OF SEISMIC TRIGGERING THROUGH
PRECISE EARTHQUAKE LOCATIONS

A DISSERTATION

SUBMITTED TO THE DEPARTMENT OF GEOPHYSICS

AND THE COMMITTEE ON GRADUATE STUDIES

OF STANFORD UNIVERSITY

IN PARTIAL FULFILLMENT OF THE REQUIREMENTS

FOR THE DEGREE OF

DOCTOR OF PHILOSOPHY

Eva E. Zanterkia

July 2003

UMI Number: 3104183

UMI[®]

UMI Microform 3104183

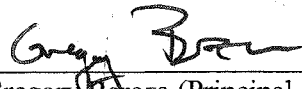
Copyright 2003 by ProQuest Information and Learning Company.

All rights reserved. This microform edition is protected against
unauthorized copying under Title 17, United States Code.

ProQuest Information and Learning Company
300 North Zeeb Road
P.O. Box 1346
Ann Arbor, MI 48106-1346

© Copyright by Eva E. Zanzerkia 2003
All Rights Reserved

I certify that I have read this dissertation and that in my opinion it is fully adequate, in scope and quality, as dissertation for the degree of Doctor of Philosophy.



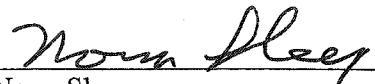
Gregory Beroza (Principal Advisor)

I certify that I have read this dissertation and that in my opinion it is fully adequate, in scope and quality, as dissertation for the degree of Doctor of Philosophy.



Paul Segall

I certify that I have read this dissertation and that in my opinion it is fully adequate, in scope and quality, as dissertation for the degree of Doctor of Philosophy.



Norm Sleep

Approved for the University Committee on Graduate Studies.

ABSTRACT

Spatial and temporal patterns in seismicity contain valuable information about the processes that trigger earthquakes. Large errors, however, in earthquake locations can obscure these patterns making inference of triggering mechanisms difficult, if not impossible. Recent improvements, including double difference relative relocation techniques and cross-correlated waveform data, now make it possible to discern accurately the faults and structures that experience seismic activity, and, therefore, to understand the complex interactions between earthquakes and changes in stress, fault properties, and other earthquakes, as well.

In this dissertation, I use earthquake relocation methods to investigate various triggering phenomena in the Eastern California Shear Zone (ECSZ). One of the largest and most interesting sequence of earthquakes in California over the past 50 years occurred there, the 1992 Joshua Tree – Landers – Big Bear and 1999 Hector Mine earthquake sequences.

Since foreshocks provide the clearest indication of precursory activity prior to large earthquakes, I examine 42 foreshocks of the 1999 M 7.1 Hector Mine earthquake. I am able to obtain useful relative arrival time information and precise relocations even for small events with low signal-to-noise ratios, and for the M 7.1 Hector Mine mainshock. The relationship between the foreshocks and mainshock is interesting in that they occur on different, but subparallel planes, and the mainshock may be in the stress shadow of the events. Coulomb stress calculations from the largest foreshocks on the mainshock initiation point are inconclusive about the stressing effects of the foreshocks.

On the opposite end of the relocation spectrum, I undertake the relocation of over 50,000 earthquakes in the 1992 Joshua Tree – Landers – Big Bear aftershock sequence. 37,939 of the relocated earthquakes occur near the Joshua Tree and Landers mainshock planes. Aftershock locations suggest that strain is more localized on well-developed faults, like the Johnson Valley

and Emerson faults, than in regions where fault segments overlap, or show complexity in the mainshock surface rupture. Changes in the maximum depth of earthquakes over time suggest a temporary increase in the seismogenic zone and may point to velocity weakening behavior initiated by mainshock slip. 11,328 aftershocks fall near the M 6.5 Big Bear mainshock area and define a number of conjugate planes. These planes do not correspond to well-developed faults in the Mojave block, and high values of friction inferred from the calculation of maximum compressive stress suggest that the active faults are immature.

The precise aftershock locations within the Johnson Valley –Homestead Valley fault jog provide compelling evidence of earthquakes triggered by pore fluid changes. The signature of the pore fluid effect is an aftershock sequence that is anomalously protracted in time compared to Omori's law. I find such a sequence within the JV-HV jog following the 1992 M 7.3 Landers earthquake and use earthquake locations to constrain the pore fluid triggering mechanism. Precise aftershock locations define a number of subfaults of varying orientations in the jog. Coulomb stress calculations on these subfaults suggest that the poroelastic effect produces an additional 0.3MPa of Coulomb stress. I may constrain the pore fluid mechanism using the pattern of aftershocks, and find that poroelastic stress transmission is a less likely mechanism than fluid infiltration into the jog or pore space compaction.

Finally, I may use the precise earthquake locations to understand temporal changes in stress using the rate- and state- formulation of *Dieterich* (2000). This approach inverts for Coulomb stress from aftershock rates. A stress increase comparable to that found in the static stress calculations is observed within the JV-HV jog and corresponds to pore fluids triggering earthquakes. I also look more closely at the stress history that leads to the 1999 Hector Mine earthquake. A sequence of earthquakes in 1996, perhaps the result of a creep event, is most like the cause of a stress increase on the future location of the Hector Mine mainshock.

ACKNOWLEDGMENTS

I would like to thank my advisor, Greg Beroza, not only for his indispensable scientific knowledge and academic guidance but also for his patience and kindness. I would also like to thank him for his incredibly speedy reading and editing abilities without which I would still be mired in thesis writing.

Also, I'd like to thank my committee, Paul Segall, Norm Sleep, Amos Nur and David Pollard. Their varying expertise and points of view allowed me to consider the bigger picture and present a far more complete work than I ever thought possible. I am also indebted to Felix Waldhauser and Bill Ellsworth for inviting me to test and use their phenomenal relocation code. Similarly, my work would have been impossible without the cross correlation techniques developed by David Schaff and Gotz Bokelmann.

I had the privilege of working with, but mostly learning from, Jim Dieterich. I appreciated greatly the opportunity to share his office, to use his powermac and crash it on occasion. I'd also like to thank John Vidale for his Hector Mine foreshock data and his enthusiasm for my relocations of those events. I thank Norm Sleep for the mainshock correlation method and Mariagiovanna Guatteri for bootstrap work.

My research was supported by a number of foundations, including the Stanford Graduate Fellowship, in particular the Robert and Marvel Kirby fellowship, and the Southern California Earthquake Center. SCEC is funded by NSF Cooperative Agreement EAR-8920136 and USGS Cooperative Agreements 14-08-0001-A0899 and 1434-HQ-97G01718. Also, support was given by NSF grant EAR-9725238, EAR-0074084 and EAR-0102803, and by the USGS, grants 00HQGR0062, and 02HQGR0039.

Many colleagues were instrumental in all my success. First and foremost are Patti and Xyoli. Their extensive statistics knowledge is only surpassed by their generous friendship. My

Stanford experience would not have been nearly as fun or fruitful without the seismo group: Martin, Hiroe, Anu, Jeff, Satoshi, Dave, Justin and Seok Goo. I'd also like to include two honorary members into that group, Sandra and Jessica. Thank you all for your help.

There are so many friends at Stanford and elsewhere who kept me going, helped me take breaks and always seemed interested in what I was doing no matter how often I talked about it. Thanks to Joern, Teresa, Jocelyn, Christine, Ann, Eugene and Stacy and so many others.

Finally, I'd like to thank my family. Without Elice and Thai, I would have never settled into the Bay Area as easily or been as well fed while I was here. Nothing I ever do could be possible without Elina and Amit to bug or to quote stupid movies with, or Dadi to laugh with. And, of course, I'd like to thank my parents. They always encouraged, and trusted, me to do my best not only while I was at Stanford, but through my whole life.

TABLE OF CONTENTS

| | |
|---|-----|
| List of tables | xi |
| List of figures | xii |
| Chapter 1: Introduction | 1 |
| CHAPTER 2: WAVEFORM ANALYSIS OF THE 1999 HECTOR MINE FORESHOCK SEQUENCE | 13 |
| Introduction..... | 13 |
| Event Identification | 15 |
| Data Analysis..... | 18 |
| Foreshock Analysis..... | 25 |
| Conclusions..... | 30 |
| Chapter 3: Aftershock Analysis of the 1992 Landers and Joshua Tree Earthquakes..... | 31 |
| Introduction..... | 31 |
| Data and Technique | 34 |
| Fault Geometry and Active Features | 37 |
| The April 23 rd , 1992 Joshua Tree Earthquake Sequence | 45 |
| The 1992 Landers Mainshock Faults And Strain localization..... | 50 |
| Fault Discontinuities and Control of Coseismic Slip..... | 55 |
| Off-fault Seismicity | 60 |
| Post-Hector Mine Activity..... | 64 |
| Afterhshock Depth and the Time-Dependence of the Seismic-Aseismic Zone..... | 66 |
| Conclusion | 71 |
| Chapter 4: The 1992 Big Bear Earthquake: Evidence for Faulting on Immature Faults | 74 |
| Introduction..... | 74 |
| Earthquake Relocation..... | 76 |
| Aftershock Geometry..... | 80 |
| time-dependence of earthquake occurrence..... | 90 |
| Conclusions..... | 94 |
| Chapter 5: The Mechanics of Pore Fluid Triggering Following the 1992 M 7.3 Landers | |
| Earthquake | 95 |
| Introduction..... | 95 |
| Evidence of Pore-Fluid Triggering: | 98 |
| Earthquake Relocation..... | 108 |

| | |
|---|-----|
| Fault Orientations | 109 |
| Stress Analysis..... | 114 |
| Constraints on Triggering Mechanism | 118 |
| Conclusion | 125 |
| Chapter 6: Stress Change and Earthquake Triggering in the Landers Earthquake Sequence | 127 |
| Abstract..... | 127 |
| Introduction..... | 127 |
| Calculating Stress Change from seismicity rate | 129 |
| Stress Changes at Landers | 134 |
| Evidence of Stressing from Pore Fluid Effects..... | 139 |
| Stress History Leading up to the Hector Mine Earthquake | 145 |
| Remote Triggering at Big Bear?..... | 152 |
| Conclusions..... | 156 |
| bibliography | 158 |

LIST OF TABLES

| <i>Number</i> | <i>Page</i> |
|--|-------------|
| Table 4.1: Fault orientations for fault planes apparent in the Big Bear earthquake sequence. Dip direction and Dip are determined from earthquake locations, and rake is obtained by nodal plane determined from focal mechanisms..... | 87 |

LIST OF FIGURES

| <i>Number</i> | <i>Page</i> |
|---|-------------|
| <p>Figure 1.1: Map view of California and major faults. Grey area denotes the ECSZ, and box is the study area. Earthquakes in the study area correspond to the 1992 Landers earthquake sequence, and include more than 60,000 events. Thick black lines are the surface ruptures of the 1992 Landers and 1999 Hector Mine earthquakes.</p> | 3 |
| <p>Figure 1.2: Station distribution from the Southern California Seismic Network/ TriNet. Red lines indicate the surface ruptures of the 1992 Landers and 1999 Hector Mine earthquakes. The scarcity of station coverage to the east may affect the resolution of longitude in relocation calculations, particularly near the Camp Rock fault, where the only close station is RMM.</p> | 5 |
| <p>Figure 1.3: Before relocation and after relocation plots for various aftershock sequences. (a) The Yucaipa cluster in the Big Bear earthquake sequence. (b) The Joshua Tree earthquake sequence (c) Aftershocks along the Camp Rock Fault, part of the Landers mainshock rupture (d) The 1992 Pisgah earthquake sequence near the future mainshock of the 1999 Hector Mine earthquake. Circles represent estimated source sizes calculated with a stress drop of 3 MPa. All axes in km.</p> | 7 |
| <p>Figure 2.1: The Hector Mine surface rupture shown in black, aftershocks in gray. Triangles denote the six SCSN stations where all 42 foreshocks were recorded.</p> | 14 |
| <p>Figure 2.2: (a) Seismograms showing 6 sec around the P-arrival time for the 42 foreshocks at CDY. Events are in chronological order; events with bold outlines for previously uncataloged foreshocks. (b) Foreshock magnitude over time in hours before mainshock.</p> | 17 |
| <p>Figure 2.3: Correlations for events 5,15,16 and 21. (a) seismograms for each event at station RMM. (b) Correlation function and re-aligned seismograms for each event pair. Heading lists two events: correlation coefficient: difference time. Useful data can be gleaned through correlation even for events of different magnitudes and very noisy events.</p> | 19 |
| <p>Figure 2.4: (a) Bootstrap realizations for the mainshock location using the original dataset with 352 P-wave observations for the mainshock. Standard deviation in depth : 1 km, latitude: 250 m, and longitude: 250 m. (b) Bootstrap realizations for the mainshock location using the new dataset containing 665 P-wave observations for the mainshock. Standard deviation in depth: 500 m, latitude: 100 m, longitude: 75 m.</p> | 21 |

Figure 2.5: Waveforms, 6 sec around the *P*-wave arrival, for selected foreshocks, with histograms of the *x*, *y*, and depth distributions, in kilometers, of the bootstrapped locations. Events 5, 21 and 38, represented by rows (a), (d) and (e), respectively, are previously uncataloged foreshocks.24

Figure 2.6: (a) Map view of locations with 95% confidence error bars less than 1.5kms. Filled circles are events occurring between 20 and 13 hrs prior to the mainshock, and open circles are foreshocks occurring 8 to 0 hrs before the mainshock. The star represents the relocated mainshock hypocenter, and the focal mechanisms (Hauksson et al., 2002) correspond the mainshock and the six largest foreshocks. (b) A-A' cross-section with 95% confidence error bars. (c) B-B' cross-section with error bars. In the cross-section plots, only events with horizontal errors less than 400m are shown.....26

Figure 2.7: Timing of foreshock occurrence. (a) map view of foreshocks. Color represents time of the foreshock in hours before the mainshock. (b) distance of foreshocks from the foreshocks' centroid in two dimensions. Slight expansion away from the centroid over time. (c) distance of foreshocks from the mainshock in two dimensions. Some later foreshocks occur closer to the mainshock than earlier ones.27

Figure 2.8: Stress change distributions for shear traction change, normal traction, pore pressure change and Coulomb stress. Positive shear, negative normal stress and positive Coulomb stress contribute to failure. The percent of realizations of Coulomb stress that are positive is only 53%.....29

Figure 3.1 Map of catalog locations for earthquakes in the Landers-Joshua Tree earthquake sequence. Gray lines correspond to major faults in the area and the surface rupture of the Landers earthquake. There is no surface rupture associated with the Joshua Tree earthquake. The stars represent the location of the Landers mainshock, the Joshua Tree and Hector Mine earthquakes.33

Figure 3.2a: Map view of relocations for over 37,000 earthquakes. Coordinate system is in km. Black lines are the 1992 Landers earthquake surface rupture. Gray lines correspond to major faults, BCF: Blue Cut Fault, PMF: Pinto Mountain Fault, JVF: Johnson Valley Fault, HVF: Homestead Valley Fault, PF: Pisgah Fault, LF: Lenwood Fault, CR-E: Camp Rock – Emerson Fault, CF: Calico Fault.38

Figure 3.2: Axes in km. (b) Before relocation and after relocation for the aftershocks in the Joshua Tree earthquake sequence. (c) Before and after for Joshua Tree in longitudinal cross section. (d) Before relocation seismicity and after relocation seismicity for the Camp Rock fault aftershocks following the 1992 Landers earthquake. Also included are

off-fault aftershocks trending east to the Calico fault. (e) Before relocation seismicity and after relocation seismicity for the Pisgah earthquake sequence near the future location of the Hector Mine earthquake. Circles represent estimated source size based on a 3 MPa stress drop. In each panel, the same earthquakes are plotted in both the before and after plots.39

Figure 3.3 (a) Reference map of the Landers earthquake sequence rotated into the plane of the strike. The red line represents the surface rupture from the Landers earthquake. (b) Earthquake depth along strike in km. The deepest earthquakes extend to 20kms but these are isolated events. The deepest significant seismicity is ~17kms. (c) Maximum depth of 95% of seismicity along strike. The deepest activity occurs at the southern end of the Johnson Valley fault. Depths are generally greater in the northern end of the rupture and less deep south of the Pinto Mountain fault.....40

Figure 3.4: Precise aftershock locations plotted against the Landers slip distribution calculated by *Wald and Heaton (1995)*. Color represents slip during the 1992 Landers mainshock. Red represents areas of high slip and blue, low slip. Some of the most intense seismic activity occurs at the southern end of the Johnson Valley fault, near the patch of higher slip where the Landers mainshock initiated. Some areas like the northern end of the Johnson Valley fault and the northern end of the Camp Rock fault show activity in areas of very little coseismic slip.....41

Figure 3.5: Map view of aftershocks and cross sections along the strike of the Landers rupture. Each cross section represents 10kms along strike. The width of the fault zone varies dramatically along the length of the rupture. Cross section C crosses the Joshua Tree earthquake aftershocks. Cross section F contains the Landers mainshock, shown as the large circle.....44

Figure 3.6: (a) Map view of the aftershock related to the 1992 Joshua Tree earthquake. Dark gray lines are major faults in the area, and light gray lines are locations of the cross sections. (b) Cross section A, perpendicular to the Joshua Tree strike, shows the variety of fault planes activated following the Joshua Tree earthquake (c) Cross section B traverses the Joshua Tree aftershocks along the mainshock strike.46

Figure 3.8: (a) Aftershocks near the Burnt Mountain and Eureka Peak faults following the Landers earthquake. Blue events are the Joshua Tree aftershocks. Red lines indicate major faults in the area. (b) Close up view of the same aftershocks; circles represent estimated source size based on a circular crack model using 3MPa stress drop. The largest event shown is the M 5.3 Burnt Mountain Fault event.49

- Figure 3.9: Map view and cross sections of aftershocks along the Johnson Valley fault. Red lines indicate the Landers surface rupture and the Gray lines indicate the cross sections. Cross section AA' and BB' traverse a set of en echelon faults that do not correspond the surface rupture in the area. The largest of these faults is 2-4 km depth while the others are shallower. Cross section CC' crosses the end of the Johnson Valley fault which shows a complex surface rupture. Aftershocks also show a complex set of active planes even at depth. Axes in km.53
- Figure 3.10: Map view and cross sections including aftershocks along the Homestead Valley fault, cross sections AA' and BB', the Emerson fault, cross section CC', and the northern section of the Camp Rock -Emerson fault that ruptured, cross sections DD'. Red lines are the Landers' surface rupture and the gray lines indicate the cross sections.54
- Figure 3.11: (a) Map view of aftershocks in the Johnson Valley-Homestead Valley dilatational fault offset. The red lines are the surface rupture of the Landers earthquake; the Johnson Valley fault is to the southwest and the Homestead Valley fault is to the northeast, and the Landers/Kickapoo fault spans the jog between the two faults. Cross sections of various faults within the fault jog. Cross section AA' crosses a left-lateral strike slip fault conjugate to the Johnson Valley fault. Cross section BB' cross cuts two feature to the north of the Johnson Valley fault. Cross section CC' crosses a complexly fractured region in the northern section of the jog near the Homestead Valley fault. (b) Comparison of 1979 Homestead Valley aftershock sequence (red) to the 1992 Landers aftershock sequence.57
- Figure 3.12: Cross sections along two fault offsets along the Landers rupture. Red lines indicate surface rupture and black lines indicate the cross sections. (a) Map view and cross section across the slight compressional jog apparent in the surface rupture along the Camp Rock –Emerson fault. Most of the activity occurs on two northwest trending features of slightly different orientations that correspond the surface rupture. (b) Map view and cross section along the Emerson – Homestead Valley fault jog.58
- Figure 3.13: (a) Map view of aftershocks from the Camp Rock fault to the Calico Fault. Red lines indicate the Landers surface rupture and cross sections are marked by gray lines. (b) Cross section A across the strike of the EW trending fault. The seismicity show a distinct dip to the south of about 80°. (b) Cross section B, along the strike of the EW trending plane, shows discrete segments are active the trend farthest to the east corresponds to a NW trending plane consistent with the Calico fault.62

Figure 3.14 (a) Precise locations for the Pisgah earthquake cluster. Circles represent approximate magnitude and slip experience during those events, using a constant stress drop of 30 bars. (b) Close up of locations show that the Pisgah cluster corresponds very well to the Pisgah fault. (c) Cross section across strike shows the distance between the 1992 Pisgah events and a cluster of events in 1996 that were closer to the future hypocenter of the 1999 Hector Mine earthquake.....63

Figure 3.15 (a) Map view of seismicity along the Landers fault following the 1999 Hector Mine earthquake. Most activity falls within the Johnson Valley Homestead Valley Fault jog. (b) Cumulative number of events over time in the fault jog. There is no sizeable change related to the Hector Mine earthquake, as seen in (c) the close-up of this plot centered around the time of the Hector Mine earthquake.....65

Figure 3.16 (a) depth of events deeper than 10kms over time for various faults along the Landers rupture. (b) Density of events in depth over time for the Joshua Tree earthquake area. There is an increase in the density of events after the Landers earthquake but the maximum depth of events does not reach the same level as after the Joshua Tree mainshock.....67

Figure 3.17 (a) Reference map of the Landers sequence rotated to correspond to the overall strike of the Landers mainshock rupture. (b) Maximum depth of events for 4 times, 1992, 1993, 1995, and 1998, each line represent 4 months of activity. The 1992 line contains events starting at the Landers mainshock, or 1992.5. (c) Minimum depth over the same time periods68

Figure 3.17 cont: (d) Maximum depth over time along the length of the Landers rupture using a finer grid than 3.17(b). Color represents maximum depth. White areas represent no data.....69

Figure 4.1: Map view of the 1992 Landers – Big Bear earthquakes and aftershocks. Major faults are shown in black. Boxed area includes the Big Bear sequence.77

Figure 4.2: Seismograms at stations GRP and LUC of the Big Bear mainshock. The arrival time is difficult to pick because of the M 4.3 event that precedes the mainshock.....79

Figure 4.3: Map view of the Big Bear sequence relocations. Multiple conjugate planes are apparent through the seismicity. Focal mechanisms correspond to large aftershocks immediately after the Big Bear earthquake (*Hauksson et al.*, 1993). Black lines indicate major faults. SJFZ: San Jacinto Fault Zone, SAF: San Andreas Fault, SGF: San Gorgonio Fault, BF: Banning Fault, MCF: Mill Creek Fault, dashed to show inferred orientation,

| | |
|--|----|
| PMF: Pinto Mountain Fault, HF: Helendale Fault, NFFZ: North Frontal Fault Zone, LF: Lenwood Fault..... | 81 |
| Figure 4.4a: (a) map view of aftershocks and cross section locations. The star represents the mainshock location. Major faults marked as in Figure 3. Star is the mainshock location. Axes in km..... | 82 |
| Figure 4.4b: (b) cross sections of various trends across the entire Big Bear sequence. Arrows and fault abbreviations, as in Figure 3, mark locations of major faults. Red star is the mainshock hypocenter..... | 83 |
| Figure 4.5: Earthquake locations in the Big Bear area. Gray lines are major faults in the area. Color represents depth of events in 5 intervals. Red:0-5 km, Yellow: 5-10 km, Green: 10-15kms, Blue: 15-20 km. Black events are >20kms..... | 84 |
| Figure 4.6: Map of conjugate planes with orientations drawn in with black lines. Numbers relate faults to their orientations in Table 4.1. Scale is in kilometers..... | 86 |
| Figure 4.7: (left) PDF of maximum compressive stress direction obtained from bootstrap. Mean value is N5°E. (right) Table listing angle between the maximum compressive stress direction and subfault strike. Subfaults listed as in Figure 4.6..... | 89 |
| Figure 4.8: Depth of 95% of events over time. (a) depth of all events in the Big Bear mainshock sequence over time. Black stars indicate events M>4.0 (b) map view of events in the Big Bear mainshock sequence rotated along strike. Red star is the mainshock. (c) Cross section in depth along the strike of the Big Bear mainshock fault plane. Red star indicated the location of the mainshock..... | 92 |
| Figure 4.9: (a) Maximum depth of 95% of events in the Big Bear mainshock sequence for various time intervals color-coded in the legend. See Figure 6b and 6c for orientation. (b) Minimum depth of events along the strike of the Big Bear mainshock fault plane. The northern segment of the Big Bear rupture shows an increase in the minimum depth of events over time. (c) Minimum depth for the entire Big Bear mainshock sequence from 1992 to 1999. For about three years after the mainshock, minimum depth gradually increases..... | 93 |
| Figure 5.1: Map of the surface rupture and aftershocks of the Landers earthquake. Area in the box is the Johnson Valley – Homestead Valley fault jog. Hector Mine events and rupture are to the northeast..... | 97 |
| Figure 5.2: (a) Frequency magnitude relationship for all earthquakes in the Landers sequence, y-axis is a log scale. (b) Frequency magnitude relationship for earthquakes within the Johnson Valley – Homestead Valley jog. (c) Change in magnitude | |

completeness of the catalog over time within the jog and immediately north and south of it. The magnitude of complete detection is similar for the three regions and approximately constant with time. There is no significant change in completeness level in the time of interest, 1993-1997, and no significant spatial variation in completeness over this region. . 101

Figure 5.3: 5km x 2km boxes used to examine temporal dependence of aftershocks, shown in gray, along the Landers surface rupture..... 102

Figure 5.4: (a) Cumulative number of aftershocks with time for the boxes in Figure 5.3. X-axis is time and Y-axis is cumulative number of events. The protracted aftershocks appear most clearly as a trend of approximately constant slope for boxes 11-16 from 0.5 to 3.5 years after the Landers mainshock. This straight-line behavior represents a constant aftershock rate rather than the decay predicted by Omori's law. The protracted aftershocks are not attributable to variations in the network detection threshold. The detectability threshold for the Landers aftershock sequence changes gradually from south to north because of variations in network coverage; however, a rate change resulting from this would act over larger spatial scales than the variations we observe and would include adjacent straight segments of the fault where the aftershock decay is normal. 103

Figure 5.5: Cumulative number of events over time with the best-fit Modified Omori power law. Residuals from the power law fit. Sequences outside the jog are well fit by the model; those within the jog are not, and have large and systematic residuals..... 105

Figure 5.6: Relative aftershock rate displayed as the percentage of aftershocks in years 1 and 3 following the mainshock that occurred in year 3. Instances of less than 8 total aftershocks within each 0.01 by 0.01 degree box are not plotted. Areas of protracted aftershocks (relatively more aftershocks at later times) show as warm colors (green to red). These are most prominent in the large extensional discontinuity between the Johnson Valley (JV) and Homestead Valley (HV) faults and at the southern end of the rupture. The extensional discontinuity between the Homestead Valley and Camp Rock/Emerson (CR) faults also shows a protracted aftershock sequence, though the effect is subtle. Straight segments of faults plot as cool colors, consistent with decay of the aftershock rate with time. 106

Figure 5.7: Double-difference earthquake locations based on waveform cross correlation derived arrival times for 8390 aftershocks, ~75% of the events in the area. Formal errors are approximately an order of magnitude smaller than for SCSN catalog locations and relocated seismicity align onto distinctly more planar structures..... 110

Figure 5.8: Cross sections of major subfaults. (a) Vertical, left-lateral subfault to the south of the Landers fault, now called subfault a. (b) two subfaults to the north of the Landers fault. The southern subfault, subfault b, dips 30° to the Northeast; the northern subfault, subfault c, dips 60° to the North. (c) Densely fractured area, subfault d, in the northern part of the jog, on the Homestead Valley fault. Aftershocks define many fractures of differing orientations. 111

Figure 5.9: Aftershocks in subfault a plotted with composite mechanisms for similar events (i.e., those that have a high cross correlation coefficient). Color represents timing of the events. Black lines are the Landers mainshock surface rupture. 112

Figure 5.10: As in Figure 5.9, for aftershocks in subfault b. Composite focal mechanisms for highly correlated events. Color represents timing of events..... 113

Figure 5.11: Cross sections of the Homestead Valley fault immediately north of the JV-HV dilatational fault jog..... 114

Figure 5.12: Stress calculations in bars for Subfault a. (a) Coulomb stress calculation in the undrained state, $n = 0.37$, for fault plane and slip direction orientations determined from relocated earthquakes and focal mechanisms of subfault a. (b) Coulomb stress calculation in the drained state, $n=0.27$, for the same plane orientation. (c) the difference between the Coulomb stresses in the undrained and drained states shows a significant additional stress due to poro-elastic effects. 116

Figure 5.13: Stress calculations in bars for Subfault b. (a) Coulomb stress calculation in the undrained state, $n = 0.37$, for orientations described by the structure described by subfault b. (b) Coulomb stress calculation in the drained state, $n=0.27$, for the same plane orientation. (c) the difference between the Coulomb stresses in the undrained and drained states shows a significant additional stress due to poro-elastic effects..... 117

Figure 5.14: Illustration of different mechanisms of pore-fluid induced failure. Left panels are theoretical fluid movements and right panels are ensuing aftershock patterns, where darker stars occur later in time. (a) fluid infiltration, (b) poroelastic stress increase, (c) pore space compaction. Descriptions of each mechanisms in the main text under Pore Fluid Models..... 119

Figure 5.15: (a) Map defining different populations for the aftershock sequence in the jog. (b) Cumulative number of events in the regions described in (a). Both subfaults b and c (red and blue) have a protracted aftershock sequence, while other events in the jog do not. 122

Figure 6.1: Map view of aftershocks of the Landers, Big Bear and Hector Mine earthquakes for 10 years, 1992 -2002. Black lines indicate major faults in the region as well as the surface ruptures of the Landers earthquake and the Hector Mine earthquake..... 133

Figure 6.2: Map of the number of radii needed to meet the minimum earthquake requirement. Areas in red are not as reliable as those blue. Nodes farther from the majority of seismicity are less reliable. Most nodes of interest have radii <4 km..... 135

Figure 6.3: Coulomb stress change following the Joshua Tree earthquake. Color indicates normalized Coulomb stress change. Time interval compares two months prior to the event with two months after the event. Thick solid black lines indicate the rupture planes of the Joshua Tree earthquake. Dashed lines are the trends of secondary features active following the Joshua Tree earthquake. Major faults are marked as follows: SAF: San Andreas Fault, BF: Banning Fault, NFFZ: North Frontal Fault Zone, HF: Helendale Fault, PMF: Pinto Mountain Fault, CF: Calico Fault. Stress increase is mapped primarily in the aftershock sequence of the earthquake. A slight increase is registered near the site where the Hector Mine earthquake eventually initiated. Other areas are not significantly affected. 136

Figure 6.4: Stress change immediately after the 1992 Landers earthquake for the entire region. Color represents stress change; red is increase in stress, blue is a decrease. Thick solid black lines are mainshock rupture planes of the Joshua Tree earthquake. Dashed lines are secondary features. Thin black lines are the surface ruptures of the Landers and Hector Mine events. Major faults are labeled as in Figure 6.3. 139

Figure 6.5: Stress change along the Landers mainshock planes between 1993 and 1997, averaging over 0.5 yr. Red areas show an increase in stress over the time period. The JV-HV fault jog shows an increase in stress over this time period. Black lines are the Landers surface rupture. CR-EF: Camp Rock – Emerson Fault, HVF: Homestead Valley Fault, JVF: Johnson Valley Fault..... 141

Figure 6.6: Map view of the JV-HV fault jog, as well relocated Landers aftershocks. Letters indicate locations of the nodes where stress histories were recovered. Stress vs. time for various nodes corresponding to fractures within the JV-HV fault jog. (a), (b), (c) are fractures within the jog; (d) (e) (f) are outside the jog. P.S. = Protracted aftershock Sequence. Pore pressure, and therefore stress, should gradually increase within the jog, (nodes a, b, and c). 143

Figure 6.7: Coulomb stress change in the Hector Mine area post-Landers. White lines indicate Landers rupture, and black lines are Hector Mine surface ruptures. Squares are Landers aftershocks. Red areas indicate stress increase. Axes are in km..... 146

Figure 6.8: Normalized Coulomb stress changes (blue lines) and normalized cumulative # of events (red lines) vs. time for the Hector Mine area. Time 0 starts as 1992; the Hector Mine earthquake occurred at 7.79. Panel 731: Stress vs. time for the Hector Mine epicenter. Node 176: Stress vs. time on the Lavic Lake fault. Nodes 446 and 372: Stress vs. time within the Pisgah event sequence and Hector Mine sequence. Locations of nodes labeled on Figure 6.9. 147

Figure 6.9: Coulomb stress for various intervals following the 1992 Pisgah earthquake. Time intervals are averaged over 2.5 months. Black lines indicate the 1999 Hector Mine surface Rupture and the black star marks the Hector Mine mainshock location. (a) Stress change in the time interval 1992.4 - 1992.6; this time period encompasses the 1992 Pisgah earthquake. (b) Stress change in the time interval 1992.6 – 1992.9. (c) Stress change between 1992.9 – 1993.1. (d) Stress change between 1993.1 – 1993.3. Numbers represent nodes for which stress histories are plotted in Figure 6.8. Axes are in km. 148

Figure 6.10: Stress evolution following a set of earthquakes in 1996 near the epicenter of the Hector Mine earthquake (black star). Red areas show increase in Coulomb stress. (a) Stress change between 1996.4 to 1996.8. This time interval includes the first of two $M > 4$ events in the sequence. The stress increase occurs to the west of the future location of the Hector Mine mainshock. (b) Stress Change between 1996.6 and 1997.1. This section includes the second $M > 4$ event in the sequence. The stress increase is closer to the Hector Mine mainshock. (c) Stress change in the interval 1996.8-1997.2. There is nearly 0.1MPa of stress decrease in the area of the 1996 earthquake sequence, but the decrease does not equal the previous stress increase. Axes in km..... 150

Figure 6.11: Coulomb Stress change near the Hector Mine mainshock hypocenter (black star). (a) Stress change from the foreshocks of the Hector Mine earthquake. They stress the same area previously stressed by the 1996 earthquake sequence. (b) Stress Change near the Hector Mine mainshock following the Hector Mine earthquake. Axes in km..... 151

Figure 6.12: (a) Earthquakes between 1992-2002 in the Big Bear region. (b) Stress change at Big Bear due to the 1992 Landers earthquake. (c) Stress change 0.5 years after the 1992 Landers earthquake. The time interval represented is 1992.7 – 1993.3. Axes in km. LF: Lenwood Fault, HF: Helendale Fault, NFFZ: North Frontal Fault Zone, PMF: Pinto Mountain Fault, SAF: San Andreas Fault, BF: Banning Fault..... 153

Figure 6.13 Stress change in the Big Bear Region due to the 1999 Hector Mine earthquake.

The time interval spans 1998.5 to 2001. Red Areas indicate a stress increase, and blue areas a stress decrease. A NW trending lineament near the Helendale fault gains stress, while the intersection of the Helendale fault and the NFFZ experiences a stress decrease.

Numbers mark different clusters of earthquakes; 4=Yucaipa Cluster. LF: Lenwood Fault, HF: Helendale Fault, NFFZ: North Frontal Fault Zone, PMF: Pinto Mountain Fault,

SAF:San Andreas Fault, BF: Banning Fault. Axes in km. 155

CHAPTER 1: INTRODUCTION

Seismicity provides a powerful tool for observing the faulting process, and for understanding the mechanisms behind earthquake occurrence. Limitations in the precision of earthquake locations, however, have prevented seismologists from taking full advantage of what may be learned from the spatial and temporal patterns of earthquakes. In this study I use high precision earthquake locations to gain new insight into several aspects of the faulting process.

I am particularly interested in exploring the possibility that patterns in seismicity may help clarify the role of pore fluids in earthquake triggering. In 1923, Terzaghi first developed the concept of effective stress to account for the effects of pore fluids in inducing failure in porous solids. Subsequent studies of triggered seismicity that account for earthquake occurrence through stress changes have often incorporated changes in pore pressure into an apparent coefficient of friction. *Simpson and Reasonberg (1992)* suggested that changes in pore pressure can be related to normal stress through Skempton's coefficient. Studies of Coulomb stress change, such as *Stein et al. (1992)* and *Harris and Simpson, (1992)*, do not explicitly consider the role of pore fluids in the calculation of Coulomb stress change. Instead, fluid effects are represented using an apparent friction, a coefficient that is interpreted as though it is a material property. Thus, the role of pore pressure changes in Coulomb stress changes and triggering earthquakes is not properly represented. In this thesis, I identify a signature of pore fluid earthquake triggering by examining patterns in seismicity and use precisely relocated earthquakes to constrain the mechanism of pore-fluid triggering.

Many studies have documented the interaction between aftershock occurrence and areas of increased Coulomb stress. *Stein and Lisowski (1983)* used a static stress analysis to show that off fault aftershocks from the 1979 Homestead Valley earthquake occurred preferentially in areas of post-seismic increases in Coulomb stress. *Stein et al. (1993)* and *King et al. (1994)* perform

similar calculations to explain the location of aftershocks following the 1992 Landers earthquake. In these instances, Coulomb stress is calculated only for planes optimally oriented in the regional stress field. This approach has the advantage of reducing the tensor stress field to a scalar. The case has been made, however, that non-optimally oriented planes may become active (*Sibson, 1990*). Most static stress studies, like the ones mentioned, do not, however, account for non-optimally oriented planes because the orientations of the actual planes that are active are unknown.

Finally, most studies of earthquake triggering from stress changes consider changes only due to major earthquakes. Stress changes from large events are assumed large enough to overwhelm stress changes from smaller earthquakes. This assumption may be driven by the fact that it is often difficult to determine exact locations and fault planes for small events. Evidence that smaller earthquakes can trigger larger ones does exist for foreshock sequences (*Abercrombie and Mori, 1994*), but also in the effects of other small earthquake sequences (*Kagan and Knopoff, 1981; Felzer et al., 2003*). Understanding the contribution of small earthquakes to earthquake triggering may be possible by tracking stress changes over time.

Precision earthquake locations may be used to clarify these issues in earthquake triggering. Many techniques have been developed to improve hypocenter locations, including the use of station terms to account for near-surface velocity variations (*Pujols, 1988; Shearer, 1997*), inverting for both the earthquake location and the velocity structure jointly (*Crossen, 1976; Ellsworth, 1977; Kissling et al., 1994*), and using relative location techniques that solve for the vector difference between hypocenters (*Poupinet et al., 1984; Got et al., 1996; Waldhauser and Ellsworth, 2000*).

Relative relocation methods may be particularly powerful when paired with arrival time information garnered from cross correlation techniques. Relative arrival times from waveform cross-correlation techniques applied to similar waveforms provide the subsample measurement precision necessary for reducing location errors from kilometers to meters. Cross correlation

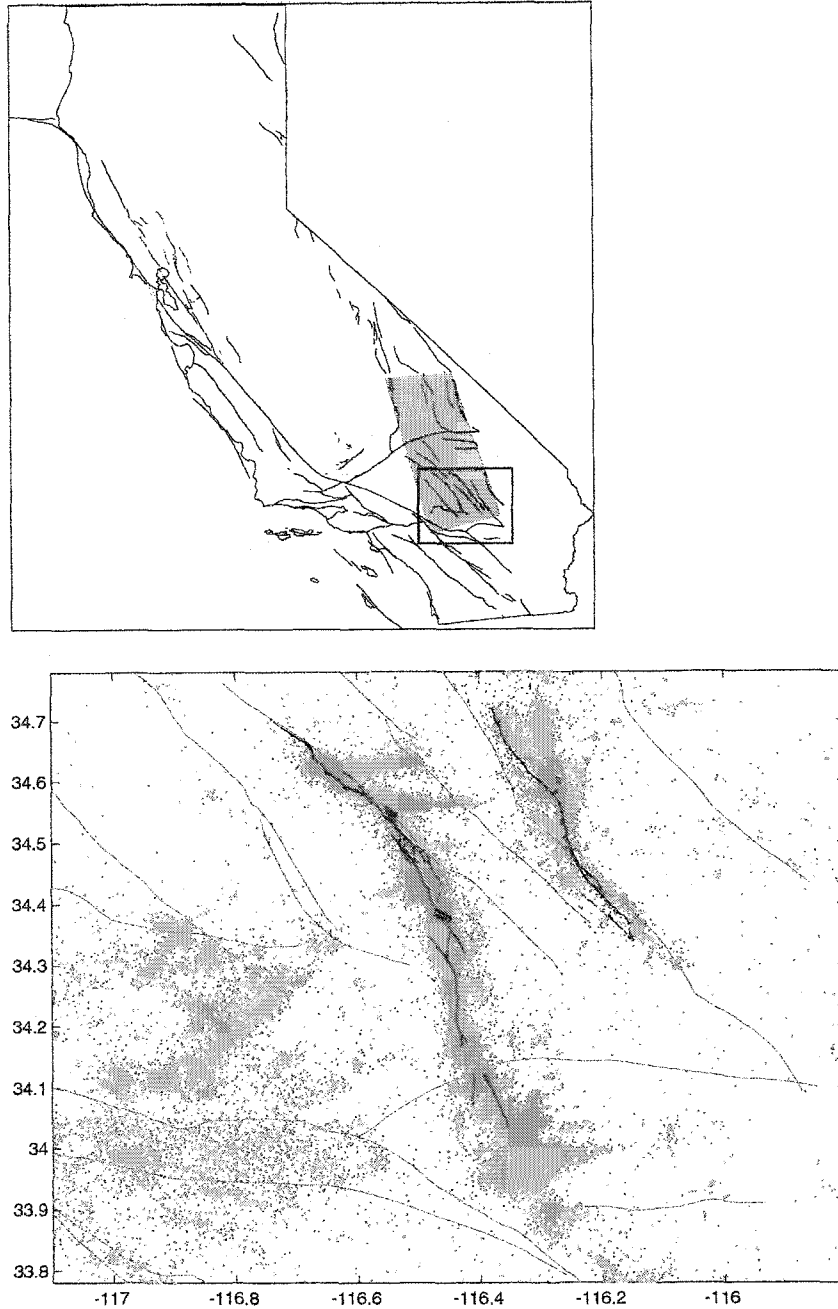


Figure 1.1: Map view of California and major faults. Grey area denotes the ECSZ, and box is the study area. Earthquakes in the study area correspond to the 1992 Landers earthquake sequence, and include more than 60,000 events. Thick black lines are the surface ruptures of the 1992 Landers and 1999 Hector Mine earthquakes.

measurements are also vital for obtaining observations for earthquakes where reliable phase information is not available, such as for small earthquakes, sparse networks, or for S waves. I will use cross-correlation measurement techniques outlined by *Schaff et al.*, (2003), in combination with the double-difference relocation method (*Waldhauser and Ellsworth*, 2000), in order to improve earthquake locations in the Eastern California Shear Zone.

The Eastern California Shear Zone (ECSZ), (Figure 1.1) is a region of abundant seismicity that extends from the San Andreas Fault through the Mojave Desert and up to the Owens Valley and the Eastern Sierra Nevada. The ECSZ is spanned by a number of predominantly northwest trending faults and accommodates 15% -20% of the of the relative plate motion between the North American and Pacific plates (*Sauber et al.*, 1986; *Dokka and Travis*, 1990; *Sieh et al.*, 1993). It is, therefore, not only an interesting tectonic setting, but also an area capable of producing large and damaging earthquakes.

The focus of this thesis is the largest earthquake sequence to have occurred in Southern California during the past 50 years, the 1992 Landers earthquake sequence. The major earthquakes in this sequence are the Apr 23rd, 1992 M 6.1 Joshua Tree, the June 28th, 1992 M 7.3 Landers, the June 28th, 1992 M 6.3 Big Bear, and the 1999 M 7.1 Hector Mine earthquakes. This earthquake sequence is ideal for a study of seismicity and fault mechanics because of the large number of earthquakes and faults that were involved. There are over 63,000 earthquakes $M > 1.5$ that occurred in a 100 x 100 km area over the ten year time period 1992 – 2002, (Figure 1.1).

The Landers earthquake sequence is also an excellent candidate for the application of precision relocation techniques. Standard location errors in the Southern California Seismic Network (SCSN), which was primarily responsible for recording the earthquakes in this sequence, range from 0.5 –1 km horizontally and 1-2 km vertically in this region. In previous studies that utilize these relocation techniques, relative earthquake location errors were reduced from km to the order of tens of meters (*Waldhauser and Ellsworth*, 2000; *Schaff et al.*, 2002). The ECSZ may prove more difficult for improving locations because the station distribution in the

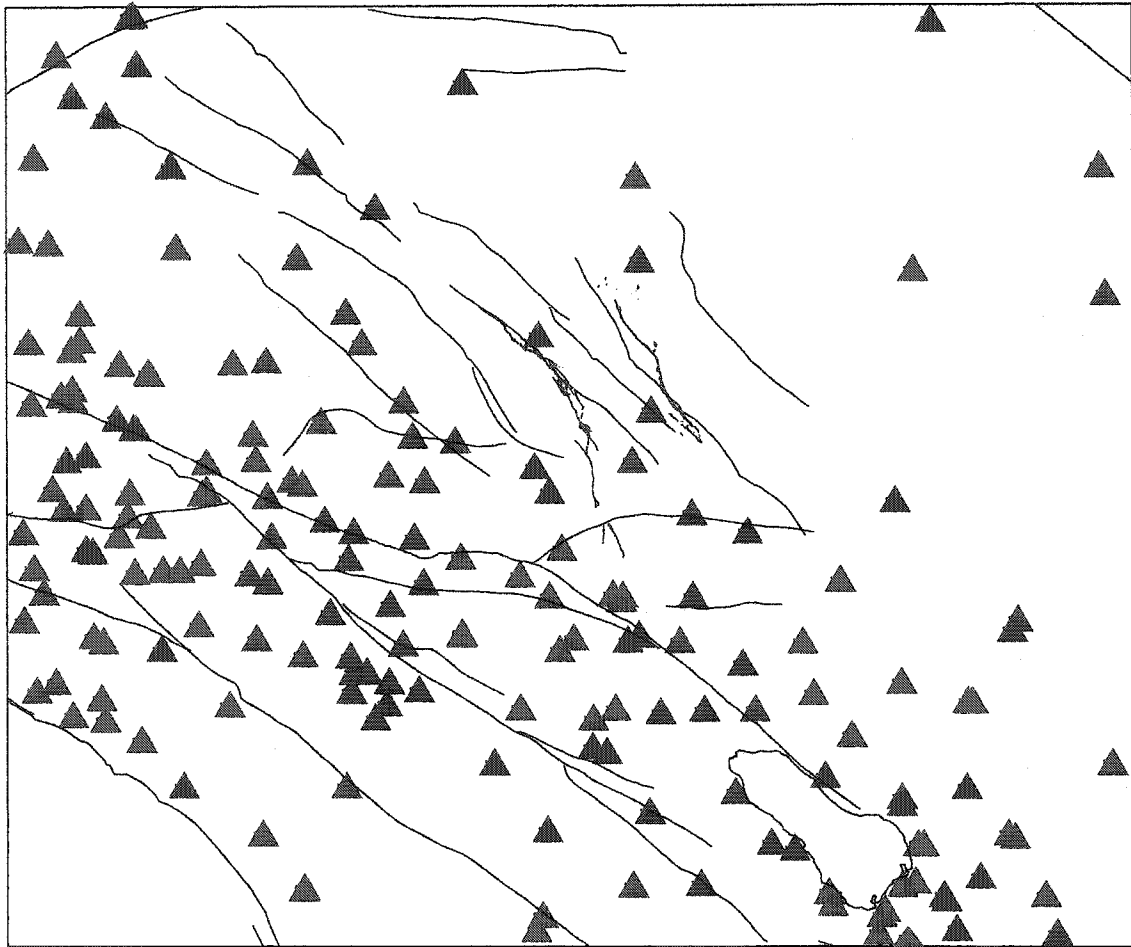


Figure 1.2: Station distribution from the Southern California Seismic Network/ TriNet. Red lines indicate the surface ruptures of the 1992 Landers and 1999 Hector Mine earthquakes. The scarcity of station coverage to the east may affect the resolution of longitude in relocation calculations, particularly near the Camp Rock fault, where the only close station is RMM.

region is not as uniform or complete as the networks near the Calaveras or Hayward faults. Figure 1.2 shows the station distribution in the area of recent major earthquakes. The eastern extent of the network is limited and many stations are not very close to the seismicity. The closest stations to the Landers earthquake sequence are approximately 30 km away from the Landers mainshock. The skewed station coverage degrades earthquake locations, particularly in the east for the Hector Mine earthquake sequence.

Nevertheless, I am able to obtain a marked improvement in relative earthquake locations using cross correlation based arrival time information and the double difference relocation technique. Figure 1.3 contains examples of SCSN catalog locations for small subsets of these earthquake sequences and, for comparison, the precise locations obtained from relocation. In each case the locations are improved and structures that were previously ambiguous come into much clearer focus.

In this thesis, I use earthquake relocation techniques on a variety of scales, from the relocation of tens of earthquakes over 1-2 km scale lengths, to 50,000 earthquakes over 100 km scale lengths. Other studies involving high resolution earthquake locations have compiled precise locations for smaller sets of earthquakes, from 3,200 earthquakes along the San Andreas Fault (*Rubin et al*, 1999) to 8000 earthquakes near the Calaveras Fault (*Schaff et al.*, 2002) on faults that are predominantly simple and planar. The relocation of 50,000 earthquakes required extending the relocation techniques to accommodate large numbers of events and observations.

The following 5 chapters explore several aspects of earthquake mechanics as revealed by precise earthquake locations. In chapter 2, I use relocation techniques to determine the relationship between the 1999 M 7.1 Hector Mine mainshock and its immediate foreshocks. An important aspect of this study is that 24 of the foreshocks that I relocate were not identified in the Southern California Seismic Network earthquake catalog, but rather by visual inspection of continuous waveforms. This suggests that foreshocks are more common and abundant than might be apparent in earthquake catalogs. I am able to cross correlate waveforms from events that have low signal-to-noise ratios and obtain locations for 40 of the 42 identified foreshocks.

Relocating a large earthquake, like the Hector Mine mainshock, using correlation techniques is difficult because the waveforms are strongly clipped resulting in differences in frequency content and waveform shape between large and small events. I resolve this problem by modifying the correlation technique to difference first break times between the mainshock and relatively small aftershocks that can be correlated with other events. This greatly reduces location

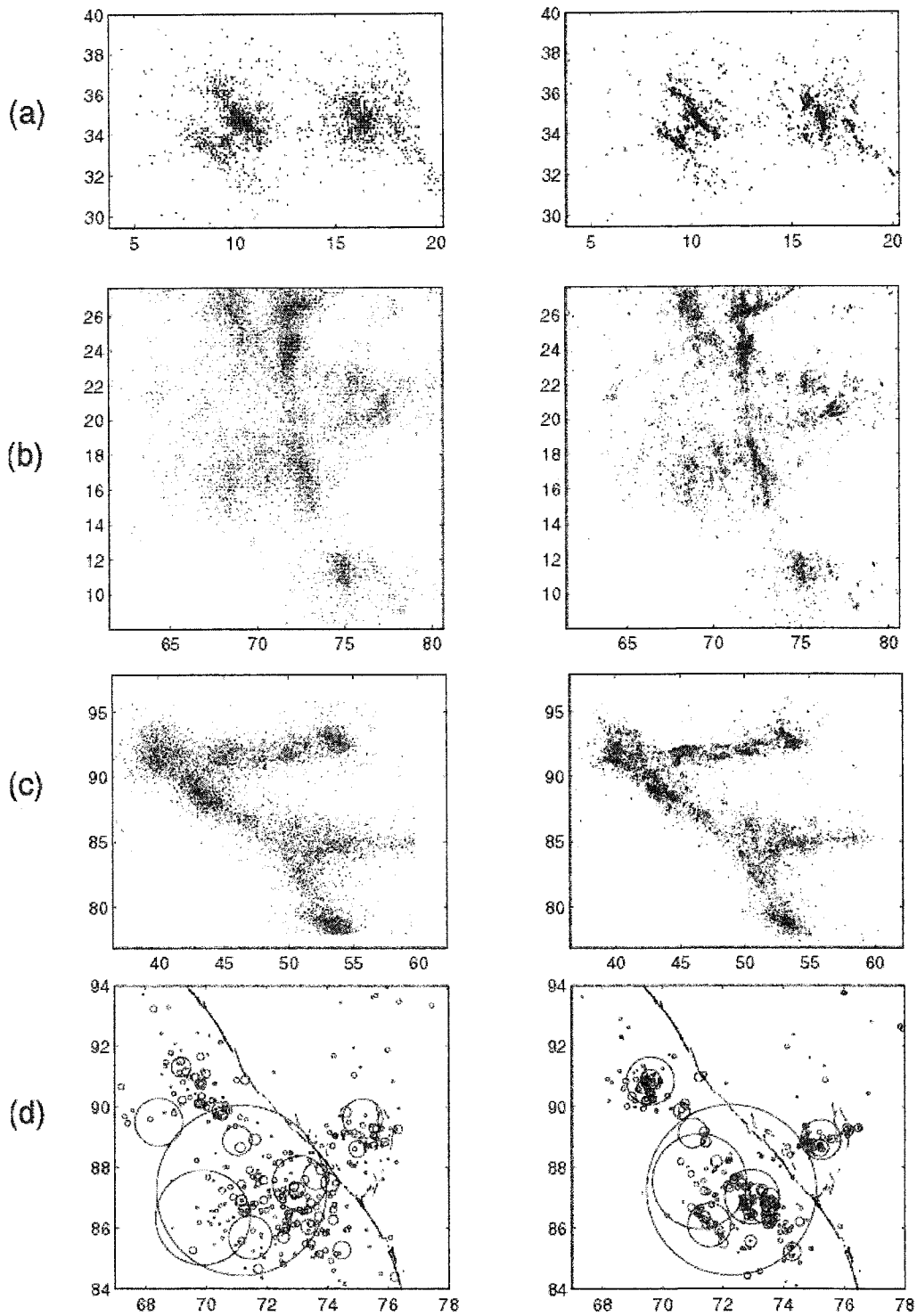


Figure 1.3: Before relocation and after relocation plots for various aftershock sequences. (a) The Yucaipa cluster in the Big Bear earthquake sequence. (b) The Joshua Tree earthquake sequence (c) Aftershocks along the Camp Rock Fault, part of the Landers mainshock rupture (d) The 1992 Pisgah earthquake sequence near the future mainshock of the 1999 Hector Mine earthquake. Circles represent estimated sources sizes calculated with a stress drop of 3 MPa. All axes in km.

error for the mainshock, and allows me to explore the relationship between the mainshock and its foreshocks more accurately.

I find that the foreshocks occur on a plane parallel to, but distinct from, the mainshock initiation plane. I use a probabilistic approach to calculate Coulomb stress change from the six largest foreshocks on the mainshock hypocenter. The precise locations for the foreshocks and mainshock allow me not only to calculate the appropriate spatial relationship of the earthquakes, but also to reduce fault plane ambiguity for the foreshocks.

In chapter 3, I undertake the relocation of over 42,000 earthquakes in the 1992 Joshua Tree-Landers earthquake sequence. The size of the relocation problem requires a means to cull the most important information from cross-correlated arrival time measurements in order to make relocation of this large number of events feasible. After relocating the seismicity, I use patterns of seismicity to understand the complexity of faulting at a small scale, the localization of strain along the Landers earthquake rupture, as well as the extent of mainshock slip, and temporal changes in the depth of the seismic-aseismic transition.

Complex structures apparent in the surface rupture continue at depth, and off fault seismicity suggests wider bands of deformation in certain parts of the sequence. Small fractures of varying orientation occur in the fault jogs that the mainshock ruptured through, including the bifurcation at the southern end of the Johnson Valley fault. Well-developed faults, like the Emerson Fault, show simple planar structures. The Landers slip distribution, fault geometry, and aftershock focal mechanisms (*Hauksson et al.*, 1993), provide insight into the role fault jogs play in promoting or arresting rupture. For instance, I explore the anomalous left-lateral strike-slip events near the northern termination of the Landers earthquake.

The 1992 Landers earthquake also triggered a number of off-fault sequences. The most important of which include the Pisgah earthquake sequence, and the seismicity that trends EW from the Camp Rock fault to the Calico fault. The 1992 Pisgah earthquake is of particular interest

because it occurred close to the later 1999 M 7.1 Hector Mine earthquake. Improvements in the location of these earthquakes provide improved constraints on the potential triggering of the Hector Mine earthquake by smaller earthquakes, rather than by the Landers mainshock.

Improved depths of seismicity from relocation allow us to examine the time-dependence of aftershock depths. I find that the aftershocks occur at shallower depths at later times following the mainshock. This may point to a change in the seismic-aseismic transition as strain rates change following the mainshock, which can be used to constrain fault zone rheology near the base of the seismogenic zone.

In Chapter 4, I use the same relocation techniques outlined in chapter 3 for the sequence of earthquakes in the San Bernardino Mountains following the 1992 Landers earthquake and the 1992 M6.5 Big Bear earthquake, the largest aftershock of the Landers earthquake. Although a large and interesting earthquake in its own right, the Big Bear earthquake has received little study, largely overshadowed by the effects of the Landers earthquake. There is, however, much to be learned about earthquake activity in the San Bernardino Mountain block from studying this earthquake.

I relocate over 11,000 earthquakes in a 55 x 70 km area bounded by the North Frontal Fault Zone, a thrust system, to the north and the San Andreas Fault and the Banning Fault to the south. Following the relocation, I find that a number of well defined planes emerge from the seismicity. Most of these features are small, no more than a few km in any particular direction. Even the earthquakes near the Big Bear mainshock rupture delineate a wide fault zone, suggesting that the fault that ruptured in the mainshock is immature. There is other evidence that the faults in this area are immature (*Dokka and Travis, 1990*). The region is rife with conjugate faults, which are clearly revealed in the relocated seismicity, with NE trending left lateral strike slip faults cross cutting NW trending right lateral faults. I use the orientations of these features, obtained by examining the seismicity as well as focal mechanisms for larger events (*Hauksson et*

al., 1993), to determine stress orientations. I find that the maximum compressive stress direction implies high values of internal friction on these conjugate faults.

I use the improved depth determinations for these aftershocks to discern a deepening of near surface aftershocks over time near the Big Bear mainshock. This may suggest a strain rate dependent rheology of the shallow fault zone, just as has been observed (as a time-dependent shallowing) with the base of the seismogenic zone for the Landers and Morgan Hill mainshocks. The lack of shallow aftershocks for other earthquakes has been attributed to velocity strengthening in thick unconsolidated sediment or fault gouge (*Marone et al.*, 1989). The current geology of San Bernardino Mountains, however, does not indicate whether this is a feasible explanation for the depth of shallow seismicity I observe.

In chapter 5, I find evidence that changes in pore fluids in the earth trigger earthquakes in the Landers aftershock sequence. There is significant evidence of earthquakes triggered by artificially induced pore pressure changes (*Healy et al.*, 1968; *Raleigh et al.*, 1976). Pore fluids have been suggested as a mechanism for aftershock triggering, because temporal changes in pore pressure can explain the time-dependence of aftershock occurrence (*Nur and Booker*, 1972; *Booker*, 1974). To look for naturally occurring tectonic earthquakes triggered by changes in pore fluids, I examine a region where changes in pore fluids should be large enough to affect seismicity in a clearly discernable manner, viz. a fault offset in a fault system that is ruptured in a large earthquake.

An ideal location to observe this effect is the nearly 5 km wide dilatational jog between the Johnson Valley Fault and the Homestead Valley Fault that ruptured during the 1992 M 7.3 Landers earthquake. I find that the aftershock sequence within the fault jog is anomalously extended in time compared to Omori's law. This protracted sequence is a signature of aftershocks triggered due to changes in pore pressure. In addition, the signature of these pore fluid triggered earthquakes is an aftershock rate that remains constant for over three years. This is significantly different from the aftershock rate expected from Omori's law. I study possible mechanisms that

would produce such a protracted aftershock sequence by analyzing the spatial and temporal patterns in 8,390 relocated earthquakes, or ~75% of the jog's seismicity.

Having determined the actual features that aftershocks occurred on within the jog, I perform a static stress analysis in the region. This analysis does not rely on calculating stresses only on optimally oriented planes, an assumption that would be inconsistent with the range of subfaults I observe in the jog. I study the question of whether changes in pore pressure are large enough to produce sufficient stress changes to trigger earthquakes on the subfaults that are actually active.

Also, in this chapter, I attempt to test different models of pore fluid triggering by using the spatial and temporal information in the relocated seismicity. The models I consider are fluid infiltration (*Nur and Booker, 1972*), poroelastic stress transmission (*Booker, 1974*) and pore space compaction (*Sleep and Blanpied, 1992*). Each method may produce different patterns of seismicity, and the precise aftershock locations may provide sufficient resolution to test them.

Finally, in chapter 6, I combine the ~50,000 precisely located earthquake in order to document temporal changes in Coulomb stress using the formulation of *Dieterich (2000)* that relates seismicity rate to Coulomb stress change. *Dieterich (1994)* proposed using a relationship between Coulomb stress increases and increases in seismicity rate developed from a model of earthquake nucleation under rate- and state-dependent friction to map time-dependent fluctuations in Coulomb stress. This method allows me to track changes in Coulomb stress in the Mojave earthquake sequence over time.

In addition to the stress step related to the Landers mainshock, I see evidence of continuing stress increase for approximately 4 years in the Johnson Valley – Homestead Valley fault jog following the mainshock which I attribute to pore fluid pressure changes. I also find that before the Hector Mine earthquake, small clusters of events in 1996 and 1999 stress the nucleation region of the Hector Mine earthquake. In particular, the 1996 sequence may be related to a creep event close to the ultimate location of the Hector Mine mainshock. Finally, I examine

the effects of the Hector Mine earthquake on the Big Bear region, and find that faults on the periphery of the original Big Bear aftershock sequence are active. In particular, areas near the North Frontal Fault Zone, the Helendale Fault, and the Yucaipa cluster show increases in stress. These stress changes, however, may not be related to the Hector Mine earthquake.

CHAPTER 2: WAVEFORM ANALYSIS OF THE 1999 HECTOR MINE FORESHOCK SEQUENCE

A shorter version of this chapter was published in *Geophysical Research Letters*, 30(8), doi: 10.1029/2002GL016383, 2003, with co-authors Gregory C. Beroza and John E. Vidale.

ABSTRACT

Inspection of continuous TriNet waveform data reveals at least 42 foreshocks in the 20-hour period preceding the 1999 Hector Mine earthquake, a substantial increase from the 18 foreshocks in the catalog. We apply waveform cross-correlation and the double-difference earthquake location method to locate these events. Despite low signal-to-noise ratio data for many of the uncataloged foreshocks, there are enough reliable correlation-based arrival time measurements to locate all but three of these events, with location uncertainties ranging from ~100 m to 2 km. We find that the foreshocks fall on a different plane than the initial subevent of the mainshock, and that the foreshocks spread out over the plane with time during the sequence as the time of the mainshock approaches.

INTRODUCTION

Foreshocks provide the clearest indication of precursory activity before at least some earthquakes (*Jones and Molnar, 1979*). For this reason, it is important to understand as much as possible about the mechanics and statistics of foreshock sequences. Nearly half of all well-recorded earthquakes have at least one foreshock (*Jones 1984; Abercrombie and Mori, 1994*).

The M7.1, October 16, 1999 Hector Mine earthquake, shown in Figure 2.1, is documented to have been preceded by a sequence of 18 foreshocks in the 20 hours before the mainshock (*Hauksson, 2002*). These foreshocks were detected and located by the Southern

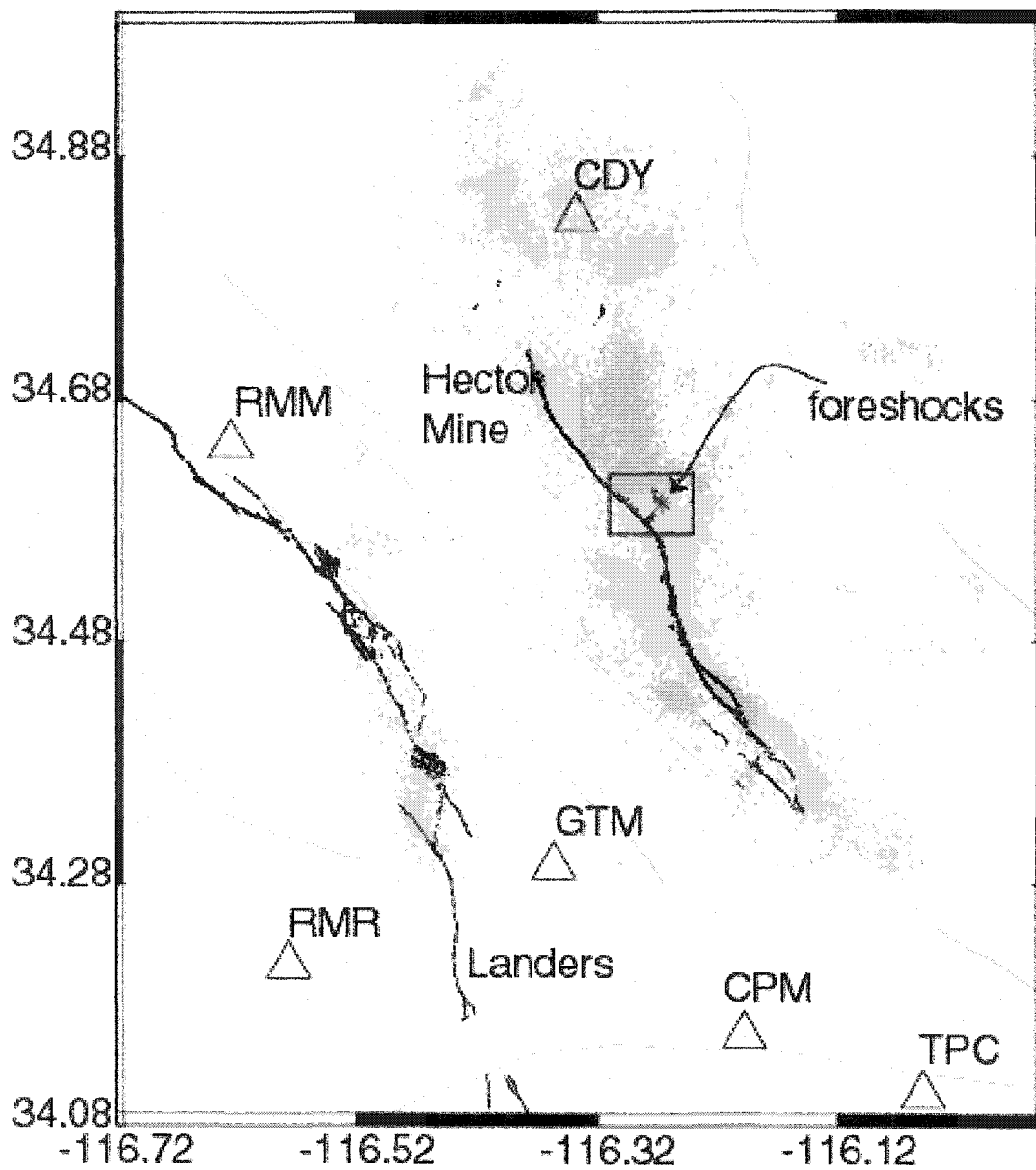


Figure 2.1: The Hector Mine surface rupture shown in black, aftershocks in gray. Triangles denote the six SCSN stations where all 42 foreshocks were recorded.

California Seismic Network (SCSN). The same time-period was examined by eye using continuous waveforms from the stations nearest to the foreshock sequence and at least 42 foreshocks were found in the sequence over this time. Standard event detection algorithms must be conservative, to some extent, in order to avoid many false alarms. However, this difference between the cataloged foreshocks and the additional events found suggests that we may be able to learn a great deal by closely studying continuous data during earthquake sequences of special interest. The fact that so many of the Hector Mine foreshocks went uncataloged suggests that foreshocks may be more common than previously reported.

Although the Hector Mine foreshock sequence occurred in an area of relatively sparse instrumentation, We are able to obtain precise locations for 39 of the 42 foreshocks by making precise arrival time measurements from waveform data even at low signal to noise ratio (*snr*) and double-difference relocation. After relocation, we find that the foreshocks occurred on the mainshock initiation plane and that the extent of the foreshock zone expanded as the time of the mainshock approaches.

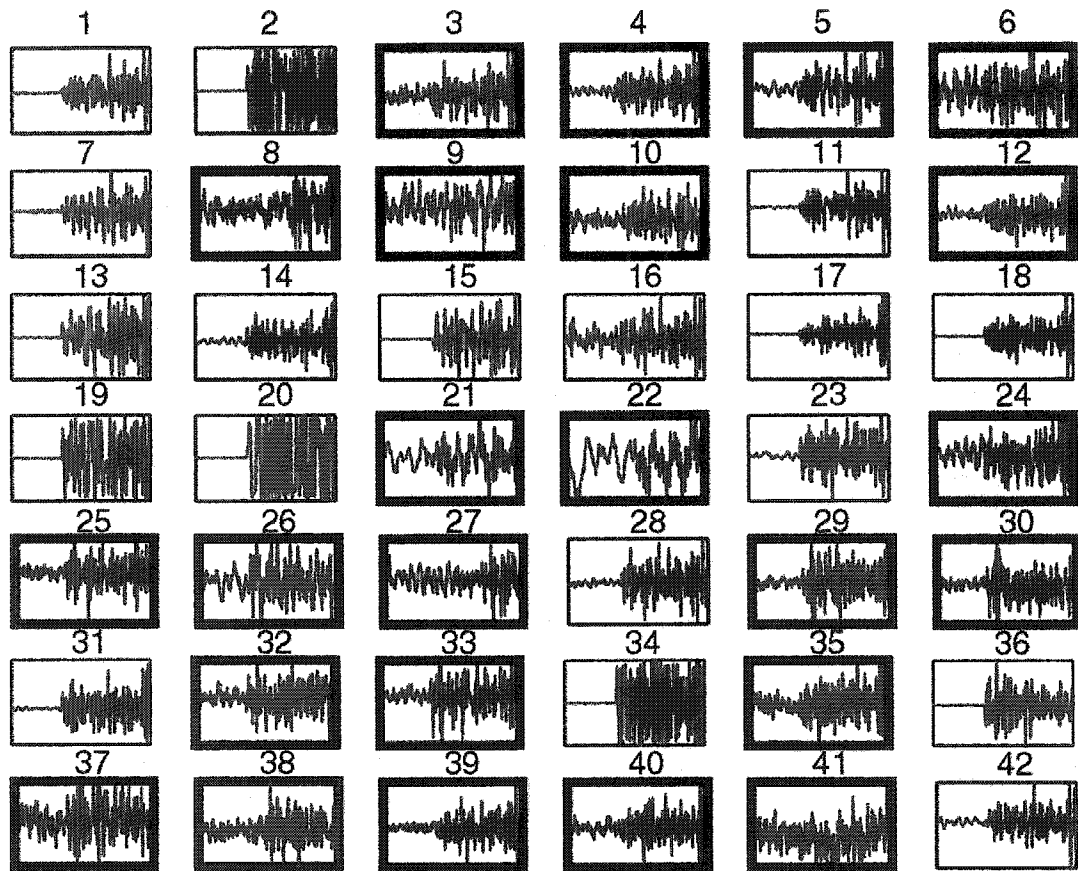
EVENT IDENTIFICATION

Initially, 18 foreshocks were identified by the SCSN in the 20 hours preceding the Hector Mine earthquake. These events were recorded by the TriNet/SCSN network, which is divided into 75 overlapping subnets. The network earthquake detection protocol has several stages. If four or more stations in a subnet detect a signal strength that is greater than the noise, then a trigger is identified for that subnet. An identified event is then reviewed by a seismic analyst for phase picking. The foreshocks to the Hector Mine earthquake range in magnitude from M 1.3 to 3.7, and are grouped in two temporal clusters. Although the network is sparse in this area of California, these events are sufficiently prominent at enough stations to be identified through routine processing and for reasonable locations to be obtained.

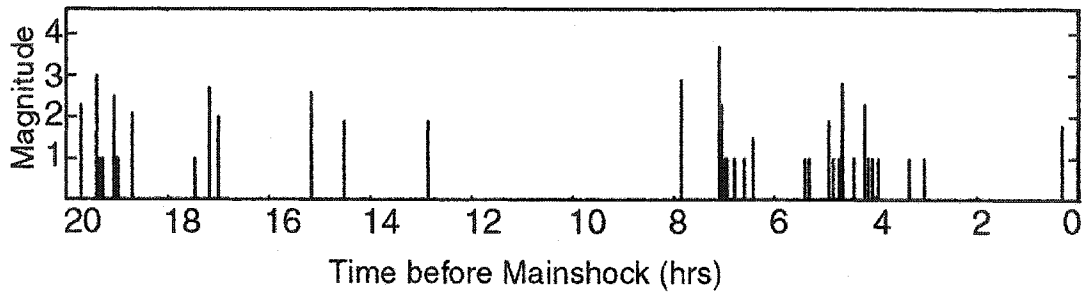
There are, however, other foreshocks in this time period that are neither cataloged nor located. In the continuous records at the six stations closest to the Hector Mine mainshock, an additional 24 foreshocks were found that were not previously cataloged. Moreover, three additional events with similar waveforms can be identified only at CDY, the closest station to the foreshock sequence. This brings the number of foreshocks visible in this sequence to 45, using this method. The first 25 events occur 20-13 hours before the mainshock, and the next 17 begin five hours after that, with the latest occurring just 19 minutes before the mainshock, as shown in Figure 2.2b.

CDY shows the clearest record of the foreshocks (Figure 2.2a). Many of the smaller and uncataloged waveforms have low *snr*. Also, two events with clearly discernable phases show opposite polarity from the other events. This may mean that these events have a different focal mechanism from the other events and suggests the involvement of more than one fault plane at the mainshock initiation point.

The other stations used to relocate the uncataloged events (CPM, GTM, RMM, RMR and TPC) are shown in Figure 2.1. All of the cataloged foreshocks and a few of the uncataloged foreshocks are also detectable at GRP, the sole station nearly due east of the foreshock sequence; however, most of the uncataloged foreshocks are poorly recorded there because the *snr* is too low for such small events. This means that the station coverage is highly non-uniform, with large gaps particularly to the east of the sequence. The network geometry is especially unfavorable for some of the uncataloged events. Although station coverage is not ideal for relocation, there is still enough data to recover good locations for both the cataloged and uncataloged foreshocks, particularly if both *S*-wave arrival times as well as *P*-wave arrival times are measured.



(a)



(b)

Figure 2.2: (a) Seismograms showing 6 sec around the P-arrival time for the 42 foreshocks at CDY. Events are in chronological order; events with bold outlines for previously uncataloged foreshocks. (b) Foreshock magnitude over time in hours before mainshock.

DATA ANALYSIS

CORRELATION

We located the foreshocks using waveform cross-correlation (*Schaff et al.*, 2003) and double-difference relocation (*Waldhauser and Ellsworth*, 2000). We use a time domain correlation method that *Schaff et al.* (2003) have shown to be a robust for obtaining relative arrival times, but use both time and frequency domain correlation techniques to define the quality of the data that we keep (*Schaff et al.*, 2003).

Waveforms at a particular station are correlated in event pairs. We perform the cross correlation over a window centered on a preliminary phase pick, using a 256-sample window and then refine the correlation using a 128-sample window and a 0.01-sec sampling rate. For waveforms at CDY, the preliminary estimate of the arrival times are picked manually, while at the other five stations, the arrivals are estimated relative to the arrival at CDY and visually reviewed. The accuracy of the arrival time difference obtained from the correlation is determined by the correlation coefficient; high coefficients mean that the waveforms are very similar. In datasets of repeating or closely spaced events on the Calaveras fault, *Schaff et al.* (2002) used arrival time measurements with correlation coefficients greater than 70% because these observations were found to provide precise measurements for relocation, based on their low post-fit residuals. In this study, we also use a correlation coefficient of 70% as the cutoff for observations involving uncataloged events. For cataloged events, the number of observations is large enough to allow using only data with a somewhat higher correlation coefficient cutoff of 70%. This higher threshold reduces the possibility of introducing outliers.

After cross correlating the arrivals for the entire populations of cataloged and uncataloged events, we find that we obtain accurate differential arrival times based on correlations at our prescribed cutoffs. This holds true even for events with low *snr*, which correlate not only with events with better signals, but also with themselves (Figure 2.3). Although we cannot ultimately

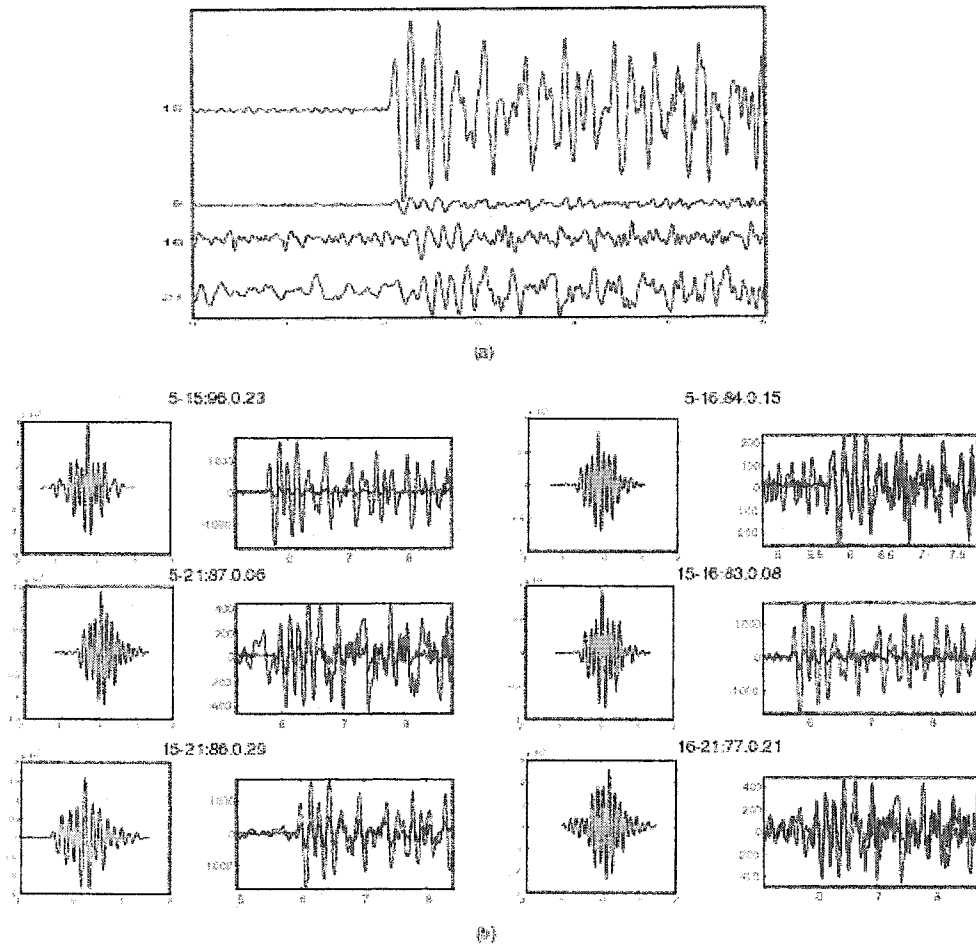


Figure 2.3: Correlations for events 5,15,16 and 21. (a) Seismograms for each event at station RMM. (b) Correlation function and re-aligned seismograms for each event pair. Heading lists two events: correlation coefficient: difference time. Useful data can be gleaned through correlation even for events of different magnitudes and very noisy events.

define at what *snr* noise will be too high to obtain accurate relative arrival time measurements using cross correlation of the underlying signals, our results suggest that waveform correlation may be a viable method for retrieving sufficient arrival time information needed for locating earthquakes in more and varied situations than previously examined.

For cataloged foreshocks, we supplement the data from the six closest stations with relative arrival time measurements from approximately 190 other stations in the southern California network where these events were measured. Unfortunately, this additional information

is not available for the uncataloged events, because these events were too small or noisy to be detected at those stations. This means that during relocation these events may not have enough observations to find a well-constrained solution and may be more strongly influenced by the asymmetric station geometry or outliers, increasing their location error.

MEASUREMENTS FOR LARGE EARTHQUAKES

It is difficult to obtain accurate relative arrival time measurements between a large magnitude event, like the mainshock, and small foreshocks, using cross correlation. While large earthquakes may have many clear, cataloged phase arrivals, small events do not. Waveform cross correlation should eliminate the need for precise phase arrivals (*Schaff et al.*, 2003), but large events and small events do not correlate well, because of waveform clipping and differences in spectral content. In the original correlation process, 352 relative P-wave arrival times were measured. All of these measurements are between the mainshock and the 7 largest foreshocks, and none are between the mainshock and the previously uncataloged foreshocks. Not only does this hamper our ability to locate the small foreshocks with respect to the mainshock, the lack of observations also seriously degrades the solution for the mainshock location.

In order to calculate a more precise location for the mainshock, we make use of a foreshock with a clear first break as a reference event. The reference event is used to assign first break times to foreshocks that correlate well with the reference event. These first break times are then differenced with the mainshock P-wave arrival time to give us relative arrival times between the mainshock and small foreshocks. Using this procedure, we obtain observations between the mainshock and 20 other events including 8 previously uncataloged foreshocks. This nearly doubles the number of relative P-wave arrival time observations for the mainshock, giving us 665 observations. Unfortunately, the S-wave arrival time is not clearly chosen for the reference event, and this procedure cannot be used to gain more relative S-wave arrival times.

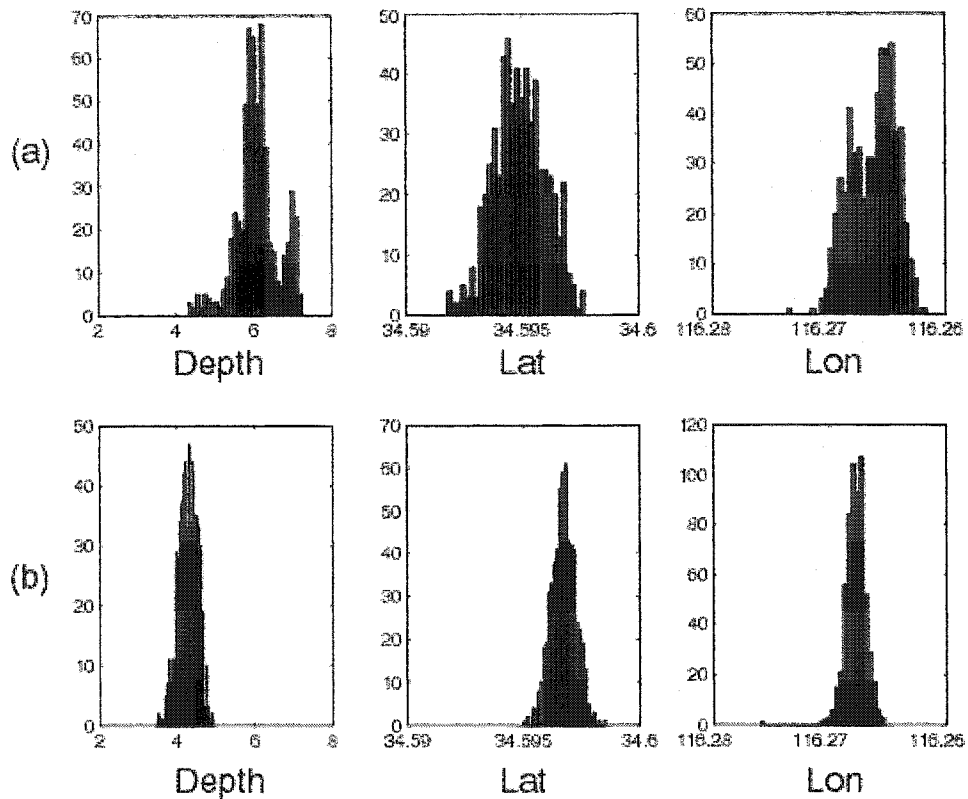


Figure 2.4: (a) Bootstrap realizations for the mainshock location using the original dataset with 352 P-wave observations for the mainshock. Standard deviation in depth: 1 km, latitude: 250 m, and longitude: 250 m. (b) Bootstrap realizations for the mainshock location using the new dataset containing 665 P-wave observations for the mainshock. Standard deviation in depth: 500 m, latitude: 100 m, longitude: 75 m.

Figure 2.4 shows the distribution of possible solutions for the mainshock location in depth, latitude and longitude using the relocation method described in the next section and both the original dataset and the dataset augmented with the additional mainshock observations.

The distribution in depth is improved with the additional observations reducing standard deviation from ~ 1 km to ~ 500 m. Horizontally the location of the mainshock is also constrained better. Location error horizontally is reduced from ~ 200 m to less than 100 m. This is a significant improvement that will help us understand the relationship of the mainshock to its foreshocks far more precisely.

RELOCATIONS

We compiled a dataset of 4111 *P*-wave and 3817 *S*-wave relative arrival times through waveform cross-correlation. The double-difference relocation method allows us to use relative arrival time information and reduces location error due to unmodeled velocity variations (Waldhauser and Ellsworth, 2000). We use the velocity model from Wald *et al.* (1995). This is a standard velocity model for the region. We tested the sensitivity of the locations to the velocity model by testing other models, and changing the velocities and locations of the layers. Since the earthquakes are closely spaced compared to the model layers, the locations depend very little on the chosen velocity model.

We first relocate all the events using all the data, which results in locations for 40 of the 43 events, including the mainshock. Because the uncataloged events do not have initial locations, We assign the uncataloged events a starting location that is the mean location of all the foreshocks. During relocation, data is iteratively culled through residual re-weighting and parameters derived from the relocation, such as the distance between event pairs. This leads to the elimination of approximately 25% of the data and three events. The three events were all uncataloged foreshocks with very low *snr*.

Next, We used a statistical resampling method, the bootstrap, of the post-fit residuals to estimate the relative location error of the events (Efron, 1982; Waldhauser and Ellsworth, 2000). Waldhauser *et al.* used a bootstrap for double-difference locations, as well, to constrain the error in a set of repeating events and found the formal errors to be represented accurately. The situation for the Hector Mine foreshock sequence is quite different. Instead of repeating earthquakes, we have separate events of varying magnitude, location, and with a sparse and uneven station distribution. The data quality in our sequence may stretch the assumption of normally distributed errors, especially for the low *snr* events.

We start the bootstrap by adding randomly re-sampled residuals, with replacement, to the relative arrival times calculated from our locations; this new data is used in the relocation code to

obtain realizations of new locations. This procedure is repeated 600 times, and the locations from all iterations are saved. We may only perform the bootstrap on events that were initially relocated (40 events including the mainshock) since these are the only events for which residuals may be calculated. The final locations are taken as the mean of all locations from all iterations. The bootstrap technique also makes it possible to calculate 95% confidence intervals for each foreshock location. These confidence intervals represent relative location errors only, because the mean location is removed from each iteration.

Our relocations are much more precise than the catalog locations, which for this region have errors on the order of 1 to 2 km. Most events, as shown by the examples in Figure 2.5, have errors on the order of +/- 60-150 m horizontally, and +/- 200-300 m vertically. A few events have errors of 1-2 km. The errors obtained from the bootstrap are anywhere from 5 to 30 times greater than the formal errors calculated during the relocation. Surprisingly, the bootstrap and formal errors in the horizontal are not well correlated; events with large bootstrap errors do not necessarily have large formal errors.

Figures 2.5b and 2.5c show cataloged foreshocks, with event 16 exhibiting an *snr* similar to that of many of the uncataloged events, like event 5 (Figure 2.5a). Despite the greater station coverage for event 16, both events have comparable errors. An event with a clear phase arrival does not necessarily fare significantly better, showing similar levels of location variability to other events. However, foreshocks with very low *snr* show a greater variability in location; event 38 shown in Figure 2.5e, has errors on the order of 500m horizontally and 1-2 km in depth. All events show a greater longitudinal error than latitudinal error, which is attributable to the gap in coverage to the east of the sequence. As expected, the cataloged foreshocks all have small errors, while the uncataloged foreshocks have a wider range of errors, some as small as 100m and others as large 2km.

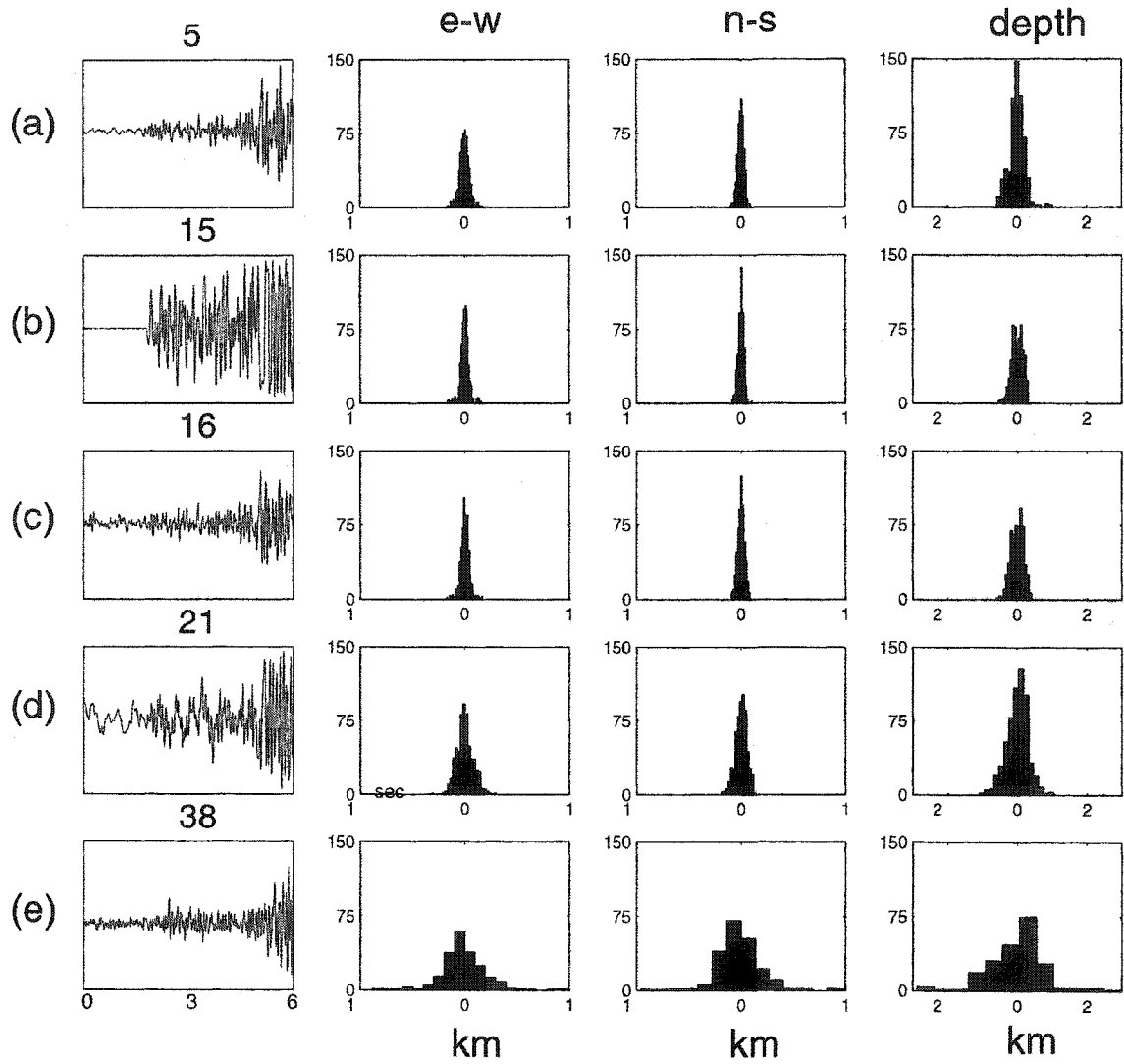


Figure 2.5: Waveforms, 6 sec around the *P*-wave arrival, for selected foreshocks, with histograms of the x, y, and depth distributions, in kilometers, of the bootstrapped locations. Events 5, 21 and 38, represented by rows (a), (d) and (e), respectively, are previously uncataloged foreshocks.

FORESHOCK ANALYSIS

After relocation, most of the 39 foreshocks (Figure 2.6) are compactly clustered in a 1 km by 1 km region and most are near a plane extending ~ 0.75 km in a N12°W direction and vertically in depth. This corresponds with the N-NW trending surface expression of the mainshock rupture near where the mainshock itself initiated (*Hauksson, 2002*). The foreshocks range in depth from 3 to 6 km, with most events clustering at 3.5 to 4.5 km. These events have smaller vertical errors than those at greater depths.

Mechanisms available for six foreshocks are consistent with these locations, as well as the mainshock's first motion mechanism (*Hauksson, 2002*). The relocation of the mainshock, shown by the star in Figure 2.6a, is on a different plane from foreshocks. However, the 95% confidence error bars of the mainshock do overlap with the 95% error bars of a few of the foreshocks in the well-defined plane. By performing a bootstrap test on the best-fitting plane to the foreshocks and comparing the results to the mainshock's position, we can exclude the mainshock from the plane of the foreshocks at a 95% confidence. There are other foreshock sequences that similarly have been displaced from their mainshocks, such as the 1992 Landers earthquake (*Dodge et al, 1996*) or that occurred on distinct planes of different orientation than the mainshock, such as the 1975 Haicheng earthquake (*Jones et al., 1982*).

We also observe that the foreshocks occur in two distinct time periods that exhibit different spatial patterns. 20 to 13 hours before the mainshock, the foreshocks fall almost exclusively on a well-defined plane (black circles in Figure 2.6). There is a five-hour gap between this activity and the cluster occurring from eight to three hours prior to the mainshock (open circles in Figure 2.6).

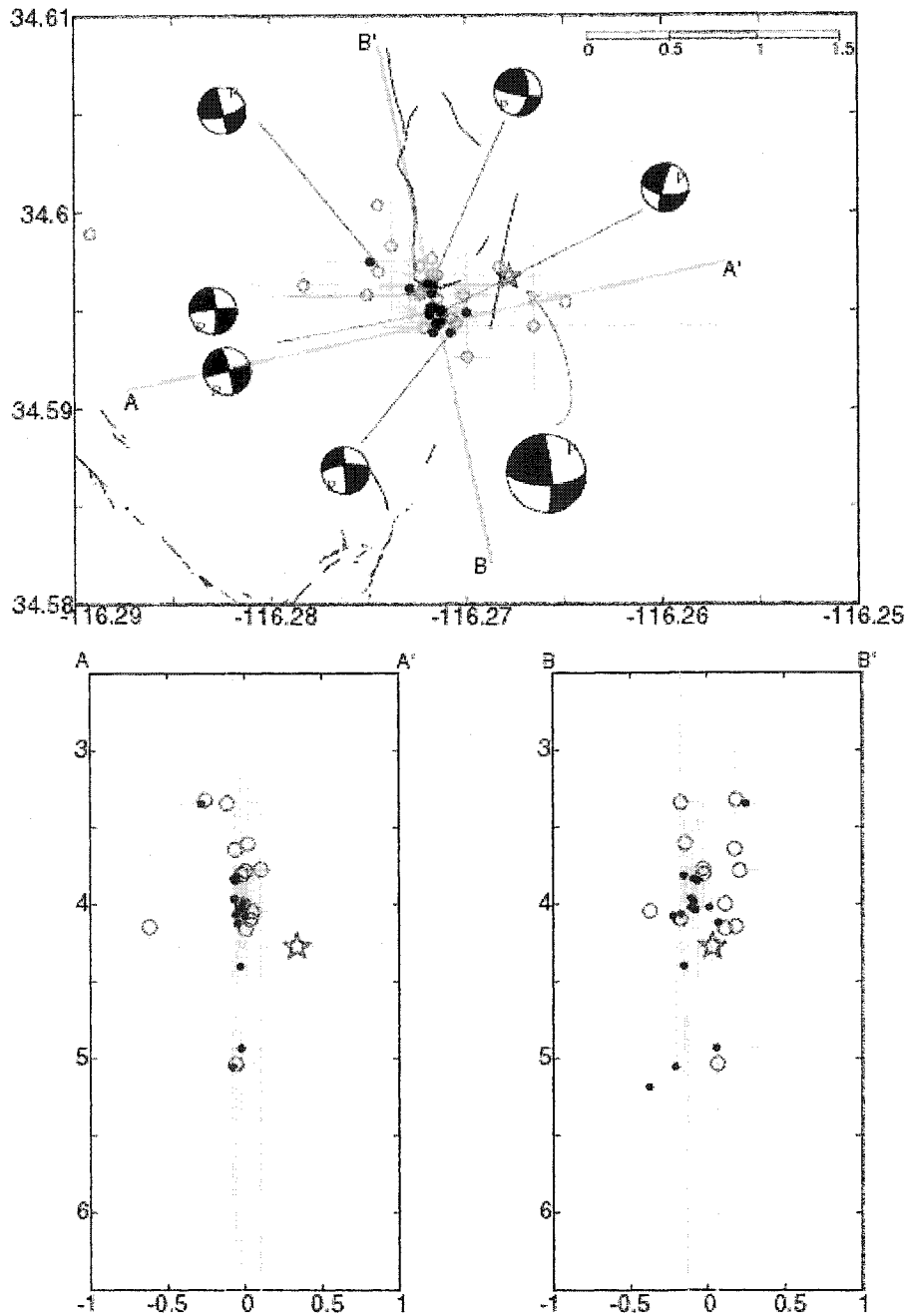


Figure 2.6: (a) Map view of locations with 95% confidence error bars less than 1.5kms. Filled circles are events occurring between 20 and 13 hrs prior to the mainshock, and open circles are foreshocks occurring 8 to 0 hrs before the mainshock. The star represents the relocated mainshock hypocenter, and the focal mechanisms (Hauksson et al., 2002) correspond the mainshock and the six largest foreshocks. (b) A-A' cross-section with 95% confidence error bars. (c) B-B' cross-section with error bars. In the cross-section plots, only events with horizontal errors less than 400m are shown.

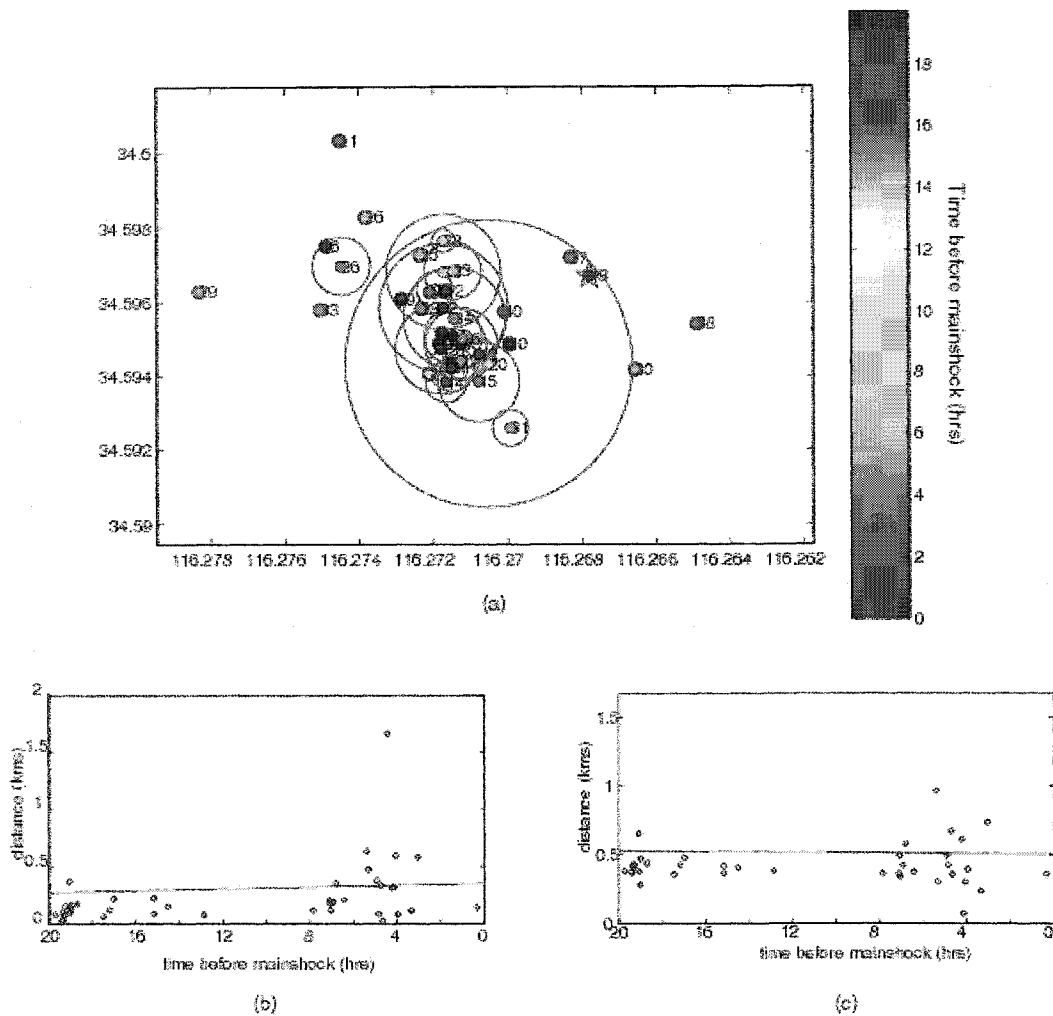


Figure 2.7: Timing of foreshock occurrence. (a) map view of foreshocks. Color represents time of the foreshock in hours before the mainshock. (b) distance of foreshocks from the foreshocks' centroid in two dimensions. Slight expansion away from the centroid over time. (c) distance of foreshocks from the mainshock in two dimensions. Some later foreshocks occur closer to the mainshock than earlier ones.

After a M2.0 and a M3.7 foreshock that occur about eight hours prior to the mainshock, the subsequent foreshocks occur in a more diffuse arrangement. Location error on some of these later events, however, makes it difficult to determine how much of this expansion is real. Also, there is no clear, sequential progression of foreshocks towards the mainshock, or an indication that prior events are directly triggering subsequent events in a sequential manner, as shown in Figure 2.7a.

Other investigators have examined expanding foreshock zones as a potential indication of nucleation zone size (*Ohnaka, 1992; Abercrombie et al, 1995; Dodge et al, 1996*). *Dodge et al.* find that foreshock hypocenters for the six sequences they studied tended towards the mainshock hypocenter over time more than they expand away from their own centroid.

Although there is slightly more spread in location of the later Hector Mine foreshocks than the earlier ones, there is no dramatic expansion away from the foreshock centroid. Unfortunately, this measurement is dominated by the depth variation. Figure 2.7b shows this calculation in only two dimensions; the spreading is not clearly visible in the scatter. If we consider only the distance from the mainshock in two dimensions (Figure 2.7c), we find that some later foreshocks fall closer to the mainshock hypocenter than any of the earlier foreshocks. This might suggest slip localization to a subpatch as described for faults modeled with rate- and state-dependent strength (*Dieterich, 1992*). Also, the size of the Hector Mine nucleation zone is consistent with a possible scaling of foreshock zone extent with earthquake magnitude found by *Dodge et al. (1996)*.

To explore the static stress impact of the foreshocks on the mainshock initiation point, we calculate the cumulative Coulomb failure stress change on the mainshock hypocenter from the largest foreshocks using the method described in *Dodge et al. (1996)*. We use the 6 largest foreshocks, which also have calculated focal mechanisms (*Hauksson et al., 2002*), to perform the stress analysis. As noted by *Dodge et al. (1996)*, since the location error of the foreshocks is on the same scale as the foreshock zone, a probabilistic approach must be used to calculate the stress change tensor on the mainshock hypocenter. For each foreshock we assume normally distributed errors with zero mean for the focal mechanism parameters, strike, dip and rake, a log normal distribution for stress drop and slip, and all 600 realizations of the bootstrapped locations.

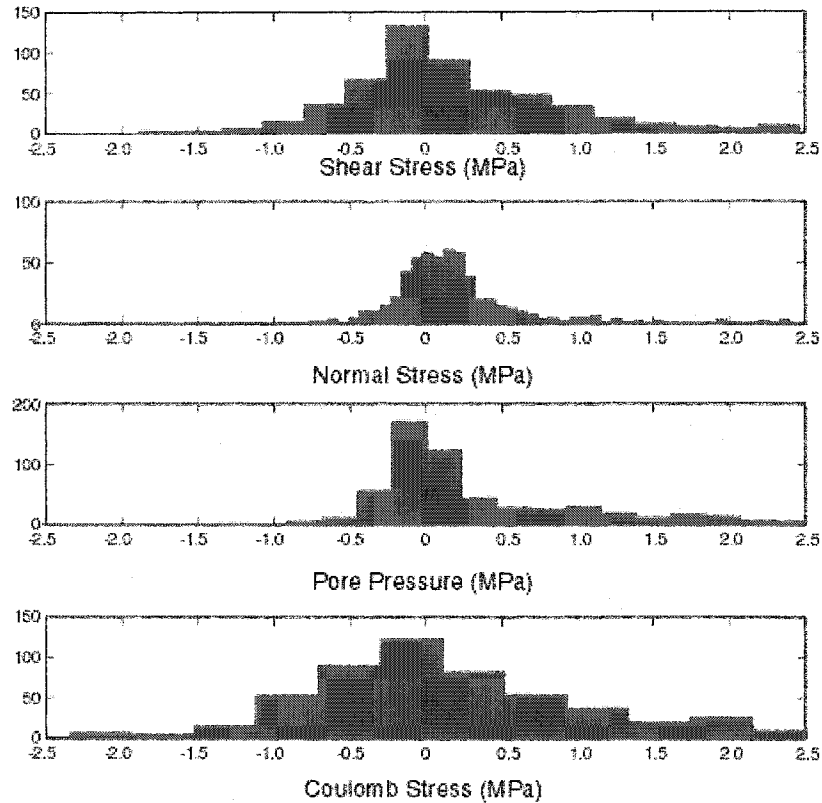


Figure 2.8: Stress change distributions for shear traction change, normal traction, pore pressure change and Coulomb stress. Positive shear, negative normal stress and positive Coulomb stress contribute to failure. The percent of realizations of Coulomb stress that are positive is only 53%.

A Monte Carlo method is used to sample these distributions and calculate shear traction, t , normal traction, σ_n , and mean stress, σ_m , with a method developed by *Okada (1992)*. Coulomb stress, S , may be obtained by

$$S = \tau - \mu(\sigma_n - P) \quad (2.1)$$

where μ is the coefficient of friction, taken at 0.6. Pore pressure, P , is related to mean stress through Skempton's coefficient, B , $P = -B\sigma_m$. B ranges from 0.51 in Tennessee marble to 0.88 for Rhur sandstone (*Rice and Cleary, 1976*). Since mean stress change is relatively small, the exact value of B used is not necessary. We use 0.8, as *Dodge et al., (1996)*.

Figure 2.8 shows the realizations of stress changes on the Hector Mine mainshock hypocenter. The mean Coulomb stress value due to the foreshocks is 0.15 MPa. There are, however, a similar number of Coulomb stress realizations that are negative to those that are positive. Thus, we cannot suggest static stress triggering of the mainshock from the foreshock sequence using this method, but we cannot conclusively exclude it either.

CONCLUSIONS

From a visual examination of the continuous record, we find that the Hector Mine foreshock sequence contains at least 45 events, not just 18 as originally identified from locations in the SCSN. It appears that detectable foreshocks are more common than previously thought. Upon relocation using correlation information to obtain relative arrival time measurements, the foreshock sequence delineated a clear N-NW trending structure, and seems to occur on a different plane from the mainshock initiation; we may definitively eliminate the mainshock from that plane at a 95% confidence level. The foreshock zone expands in a manner consistent with its magnitude, but there is no indication of static stress triggering of the mainshock by the foreshocks. Finally, Low *snr* doesn't necessarily prevent reliable relative arrival time information from cross-correlation, opening up more and diverse regions of seismicity for correlation and relocation.

CHAPTER 3: AFTERSHOCK ANALYSIS OF THE 1992 LANDERS AND JOSHUA TREE EARTHQUAKES

This chapter is being prepared for publication in the Journal of Geophysical Research with co-author Gregory C. Beroza.

ABSTRACT

We examine the seismicity associated with the 1992 Landers earthquake sequence using double difference relocation and waveform-based cross correlation techniques. We improve locations for ~38,000 earthquakes, making it possible to define more precisely the active faults in the sequence. Unlike seismicity on many well-developed faults, seismicity in this sequence shows considerable complexity even at depth. Faults active to the south of the Pinto Mountain fault, including those involved in the Joshua Tree aftershock sequence, show a variety of fault orientations, including two left-lateral strike slip conjugate faults. Along the Landers mainshock faults, aftershocks define complex fractures in three fault jogs as well as along the major fault planes. We are able to discern aftershock activity along the Calico fault and Pisgah fault. In the latter sequence, a series of earthquakes in 1996 gradually propagate towards the future location of the 1999 Hector Mine earthquake. We also note a decrease in the maximum depth of seismicity along the length of the Landers rupture over time. This may suggest a temporary increase in the depth of the seismic-aseismic transition after a large earthquake and reflect a strain-rate dependence to fault zone rheology.

INTRODUCTION

The June 28th, 1992 M 7.3 Landers earthquake, the largest event in 50 years to be recorded in Southern California, was part of a sequence of over 60,000 earthquakes (Figure 3.1). The sequence also included two M>6 events, the 1992 M 6.1 Joshua Tree earthquake occurring

just two months prior to the Landers event, and the M 6.3 Big Bear earthquake, the largest aftershock of the Landers earthquake. Also plotted in Figure 3.1 is the 1999 Hector Mine earthquake that has been closely connected to the Landers sequence. Research suggests that this event may have been triggered by stress changes related to the Landers mainshock either coseismically (*Harris and Simpson, 2002*) or following viscoelastic relaxation of the deep crust (*Freed and Lin, 2002*), or alternatively changes due to smaller events closer to the future hypocenter (*Felzer et al., 2003*).

The Landers sequence ruptured much of the southern end of the Eastern California Shear Zone (ECSZ), which extends from the San Andreas Fault through the Mojave Desert, Death Valley, and along the Owens Valley and the Eastern Sierra Nevada (*Dokka and Travis, 1990*). The ECSZ accommodates approximately 15% of the relative motion between the North American and Pacific plates on numerous north and northwest trending strike-slip faults (*Hart et al., 1990; Wesnousky, 1986*). Although slip rates on these faults are low, many <1 mm/yr, the region has a history of microseismicity and moderate earthquakes like the 1965 Calico earthquake, the 1975 Galway Lake sequence, 1979 Homestead Valley earthquake and the 1947 Manix earthquake (*Ron et al., 2001; Hauksson et al., 1993*).

The abundance of seismicity associated with the Landers sequence gives us a unique opportunity to study features within the ECSZ that may not have been visible in the past. Despite the high-quality data including seismic recordings at over 350 seismic stations operated by the Southern California Seismic Network, SCSN, earthquake location uncertainties are still large enough to obscure structures activated during this aftershock sequence. In this study we present improved earthquake locations for the Landers – Joshua Tree earthquake sequence based on double-difference relocation and relative arrival time generated from waveform cross-correlation. We find that the complexity exhibited in the surface rupture of the Landers earthquake continues to depth. Small fractures of varying orientation occur even in the immediate vicinity of well-developed faults like the Emerson and Johnson Valley faults. First we look at the Joshua Tree

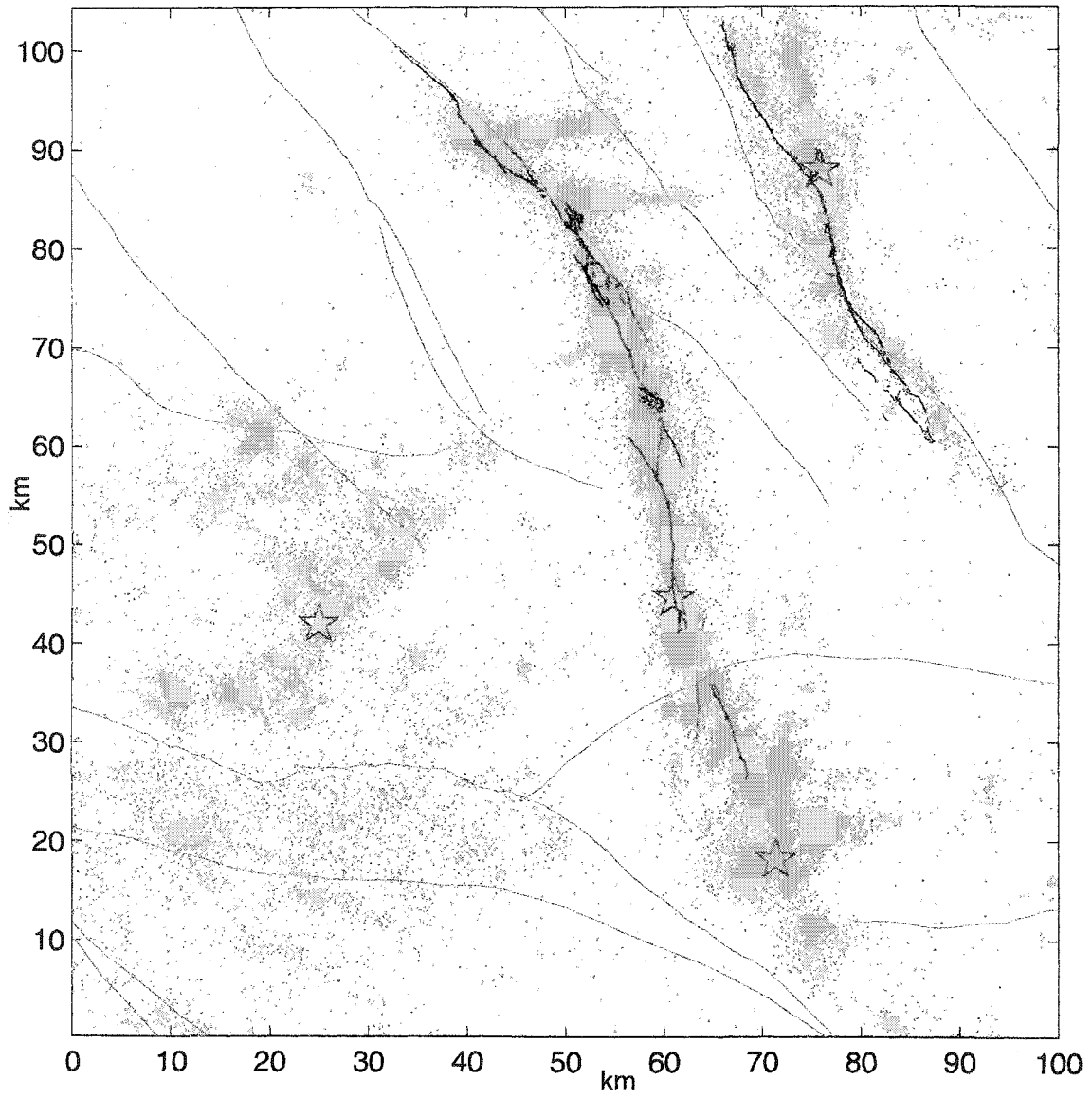


Figure 3.1 Map of catalog locations for earthquakes in the Landers-Joshua Tree earthquake sequence. Gray lines correspond to major faults in the area and the surface rupture of the Landers earthquake. There is no surface rupture associated with the Joshua Tree earthquake. The stars represent the location of the Landers mainshock, the Joshua Tree, the Big Bear and Hector Mine earthquakes.

sequence and the Landers mainshock sequence, to understand changes in strain localization along the mainshock rupture. Second we look at the seismicity that defines the fault offsets along the rupture path and examine how these jogs may have contributed to, or inhibited, mainshock slip. We also examine off-fault seismicity, including the earthquakes occurring on the Calico and Pisgah faults, and determine that the Hector Mine earthquake re-activates structures within the Johnson Valley-Homestead Valley fault offset and the southern end of the Johnson Valley Fault, both areas of protracted aftershock activity following the Landers mainshock. A decrease in the maximum depth of seismicity and an increase in the minimum depth of seismicity are also seen along the entire sequence over time, suggesting that the seismogenic zone may temporarily widen following a large earthquake.

DATA AND TECHNIQUE

Of the ~60,000 $M > 1.5$ earthquakes cataloged at the SCSN and occurring in 10 years in the Landers earthquake sequence, ~42,500 fall within 20km of the faults that ruptured during the 1992 M 7.3 Landers earthquake and the M 6.1 Joshua Tree earthquake. About 22,700 of the events occur within 4 km of the planes that ruptured during the mainshocks; 15,000 events, or about 25%, fall on other features, such as the Calico fault and the Pisgah fault to the east of the Camp Rock fault. These events are related to the Landers mainshock. The close spatial relationship of many of the earthquake allows us to use waveform cross correlation techniques to derive relative arrival time information for the events.

Catalog phase information is often used in the relocation procedure to determine large scale features in the seismicity, whereas relative arrival time data formed from correlation data is more useful for resolving small scale features (*Schaff et al.*, 2003). The quality and abundance of catalog phase arrival information for many of the smaller magnitude events is poor, but since we are interested in the small-scale features not visible in catalog locations, we use waveform correlation data, which does not require exact phase arrival information, to image these features.

We use short period vertical component waveforms from 350 SCSN stations, some as far as 250 km away, totaling over 5 million seismograms. There are over 680 billion possible event pairs, meaning nearly 24 trillion potential relative arrival time measurement. Of course, most of these measurements will provide meaningful relative arrival times or useful information for precise event location. Waveform dissimilarities and differences in path effects for events that are far apart will degrade correlation-based measurements, and relative arrival time information from these events widely separated events will likely be unreliable.

To eliminate these observations we only correlate earthquakes that are within 4 km horizontally. This accounts for errors in catalog location and will give us most of the observations between events that are actually 2km distance from each other, which is the distance determined by *Schaff et al*, (2003), to which correlation measurements are more precise than catalog observations for a similar network in northern California. This limits the number of event pairs we consider to 2,147,385.

We use the mean coherence and normalized cross correlation coefficient of cross-correlated waveforms to determine what observations are reliable. The correlation procedure that we use is described by *Schaff et al.*, (2003). Waveforms are bandpass filtered between 1 and 15 Hz to reduce noise before cross-correlation. Waveforms for two events are first aligned to the nearest sample using 2.56-second windows around a preliminary phase pick. Subsample precision is obtained by correlating the waveforms again using a 1.28-second window. We select only observations with normalized mean coherence and correlation coefficients above 70%. In datasets of repeating or closely spaced events on the Calaveras fault, *Schaff et al.*, (2002) used arrival time measurements with correlation coefficients greater than 70% because, based on their low post-fit residuals, these observations were found to provide precise data for relocation. This should be an appropriate cutoff for this analysis. We obtain 14,928,634 relative arrival time measurements, enough to relocate 38,691 of 43,672 events, using only event pairs with 4 or more observations.

We use the double-difference relocation technique in order to use these relative arrival time measurements directly as data (*Waldhauser and Ellsworth, 2000*). The maximum computational ability at our disposal allowed for relocations with up to 7,000,000 observations in one relocation run. Unfortunately, we have far too many observations to relocate all the events together. The geometry of earthquakes and the inter-event distance cutoff we use, however, allows us to divide the earthquakes and observations in a manner that should not compromise our earthquake locations.

We try to use natural breaks in seismicity along the Landers rupture to separate earthquakes for relocation. The first clear break comes at the Pinto Mountain fault. Events to the south of that fault, which include events related to Joshua Tree earthquake and the Burnt Mountain and Eureka Peak faults, are separated from other events in the Landers sequence by at least 4 km and thus would not be correlated using our cutoff criteria. The second break we make is not as clear. It occurs north of the Johnson Valley –Homestead Valley fault jog. Seismicity is intense on the Homestead Valley fault immediately to the north of the jog, but suddenly diminishes sharply. We use this position more to accommodate the maximum observations we can relocate at one time. In order to account for correlated event pairs that are not in the same sections, we locate these events twice, once in each section. All observations for an event are included in a section, even if those observations are between the target event and events in a different section. Locations for events not initially in the section being relocated, but used for observations, are excluded in the final set of locations. In total, there are only 340 events that are affected by the divisions we make.

We use a 1-d velocity model by (*Wald et al., 1995*). An advantageous aspect of the double-difference relocation method is its ability to diminish the effect of velocity model errors in the earthquake location procedure by eliminating of common mode path effects. It does this by using relative arrival time information, which naturally reduces its dependence on the velocity structure (*Waldhauser and Ellsworth, 2000*). This means that the specific velocity model we

choose should not dramatically change the locations. Using a sequence within the Johnson Valley – Homestead Valley fault jog, we test how much of an influence changes in the velocity model have on our locations. We change velocities and layer location, as well as try the velocity model of *Hauksson et al.*, (1993). Besides shifts in the absolute location of clusters corresponding to significant changes in layer location, the relative locations do not change.

During the relocation procedure, 2,039,193 observations are culled through residual weighting and outlier removal. After correlation, 4981 earthquakes did not have enough observations for relocation, mostly because these earthquakes produced observations at only 1-2 stations. After relocation, an additional 752 earthquakes are removed in from the process, bringing the total number of events that we cannot locate to 5733, or 13% of the total seismicity in the region. The earthquakes are randomly distributed, and the unrelocated earthquakes are proportional in magnitude to the relocated earthquakes, i.e. 97% of unrelocated events are $M < 3.0$. These earthquakes generally are poorly recorded and, therefore, have too few observations to be relocated; while larger earthquakes that are not located are clipped and do not correlate well with smaller earthquakes. This leaves us with 37,939 events, or 87% of the seismicity, relocated.

FAULT GEOMETRY AND ACTIVE FEATURES

Figure 3.2 shows a map view for the nearly 38,000 earthquake relocations. Numerous features previously obscured by location error become visible. A number of sequences along the Landers fault show the improvements that may be gained from the relocations, also shown in Figure 3.2(b-e). In particular, faults active in the Joshua Tree earthquake sequence (Figure 3.2b) become apparent. The station distribution (as plotted in Figure 1.2) is more uniform near the southern end of the Joshua Tree – Landers sequence.

The 1992 Landers earthquake ruptured parts of four well-developed faults, cutting across at least three fault offsets and smaller faults, like the Landers Fault, to do so (*Sieh et al.*, 1993).

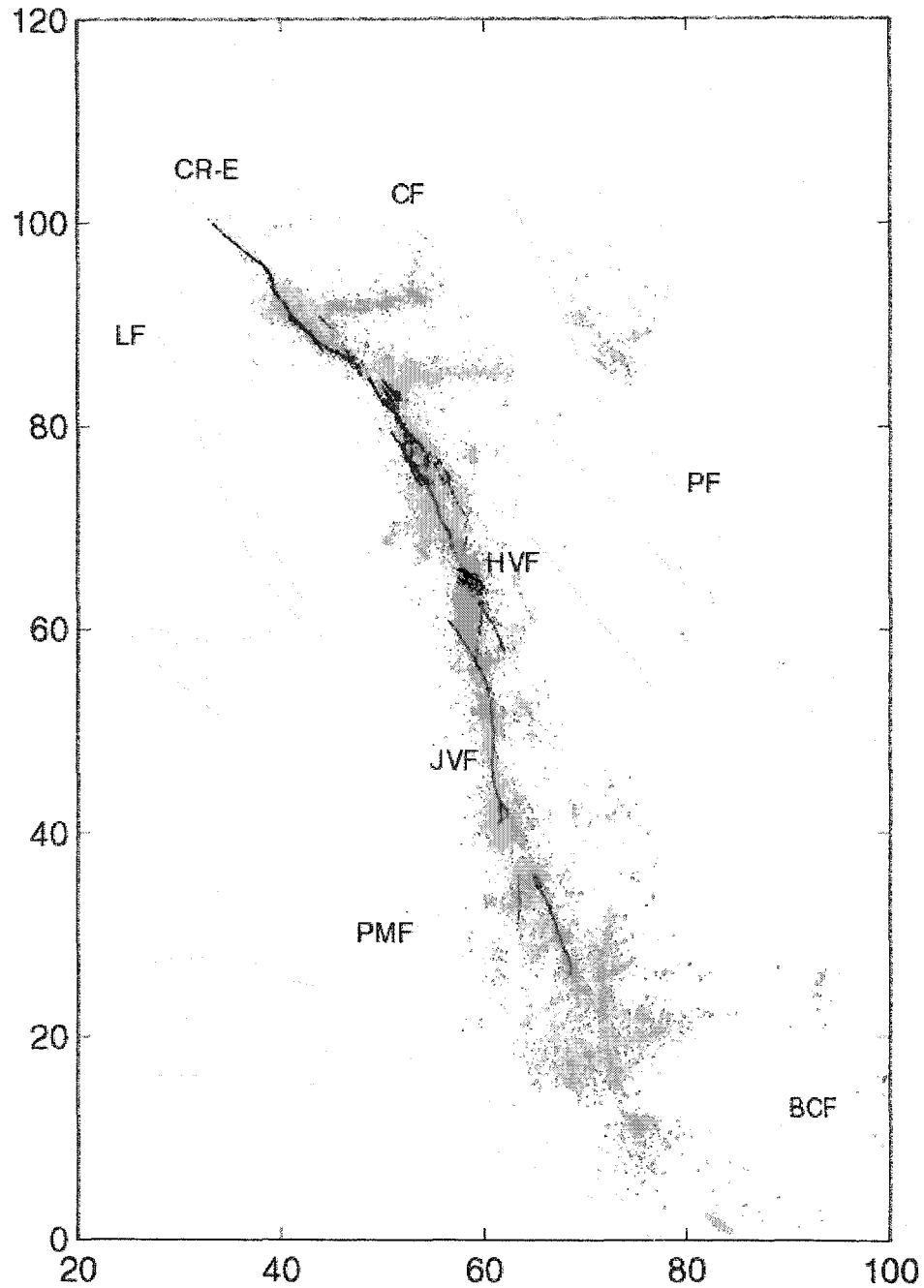


Figure 3.2a: Map view of relocations for over 37,000 earthquakes. Coordinate system is in km. Black lines are the 1992 Landers earthquake surface rupture. Gray lines correspond to major faults, BCF: Blue Cut Fault, PMF: Pinto Mountain Fault, JVF: Johnson Valley Fault, HVF: Homestead Valley Fault, PF: Pisgah Fault, LF: Lenwood Fault, CR-E: Camp Rock – Emerson Fault, CF: Calico Fault.

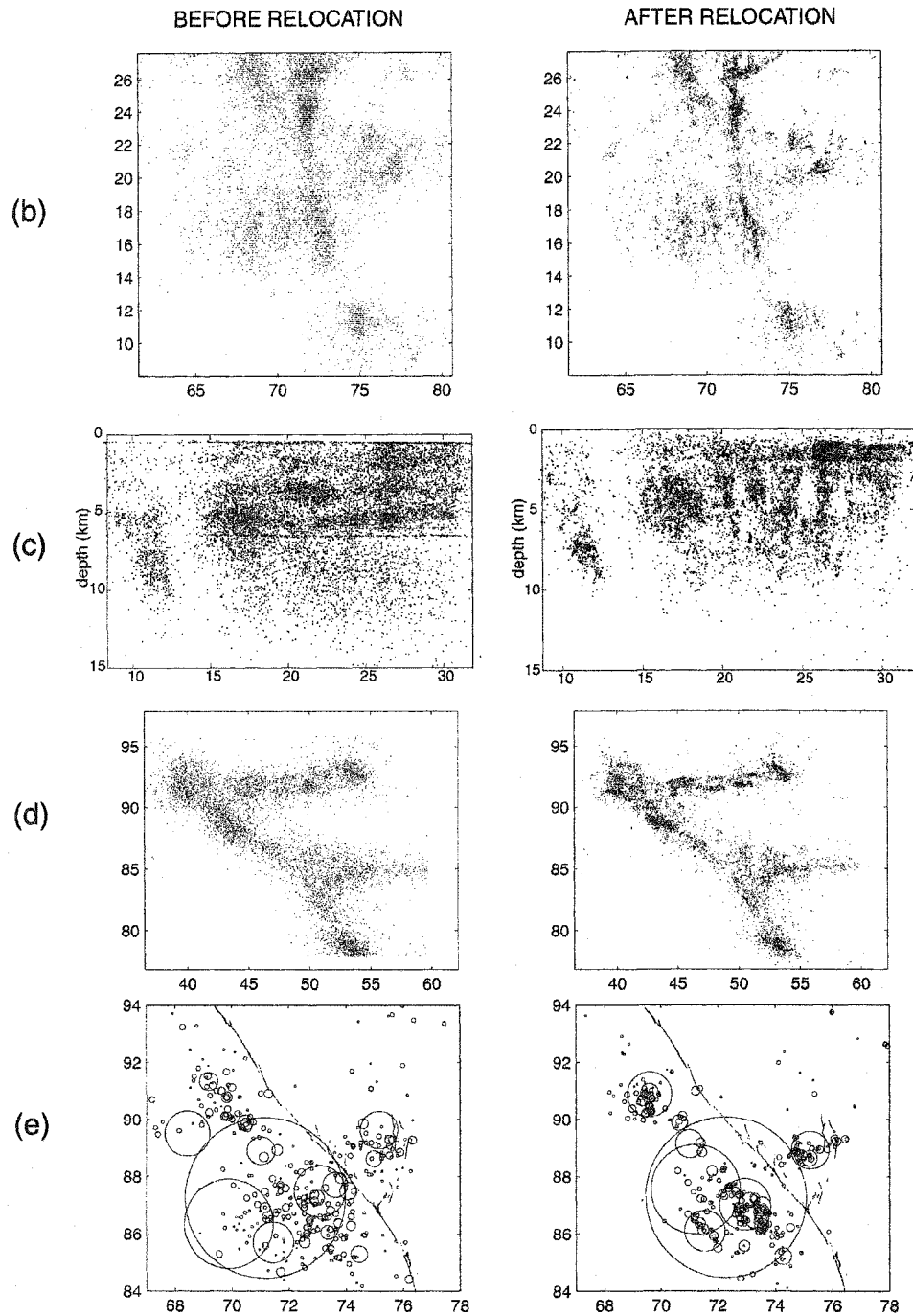


Figure 3.2: Axes in km. (b) Before relocation and after relocation for the aftershocks in the Joshua Tree earthquake sequence. (c) Before and after for Joshua Tree in longitudinal cross section. (d) Before relocation seismicity and after relocation seismicity for the Camp Rock fault aftershocks following the 1992 Landers earthquake. Also included are off-fault aftershocks trending east to the Calico fault. (e) Before relocation seismicity and after relocation seismicity for the Pisgah earthquake sequence near the future location of the Hector Mine earthquake. Circles represent estimated source size based on a 3 MPa stress drop. In each panel, the same earthquakes are plotted in both the before and after plots.

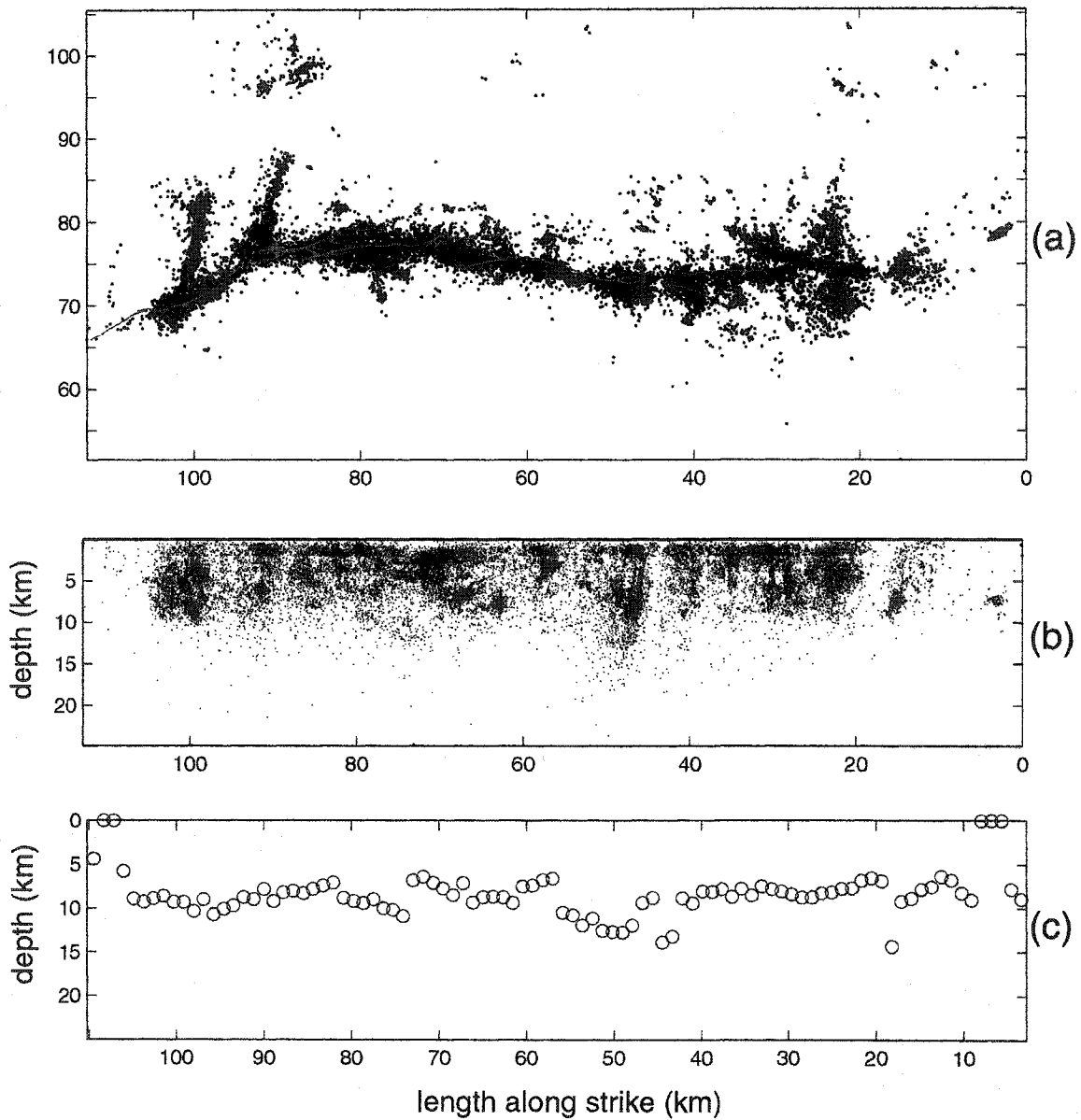


Figure 3.3 (a) Reference map of the Landers earthquake sequence rotated into the plane of the strike. The red line represents the surface rupture from the Landers earthquake. (b) Earthquake depth along strike in km. The deepest earthquakes extend to 20kms but these are isolated events. The deepest significant seismicity is ~17kms. (c) Maximum depth of 95% of seismicity along strike. The deepest activity occurs at the southern end of the Johnson Valley fault. Depths are generally greater in the northern end of the rupture and less deep south of the Pinto Mountain fault.

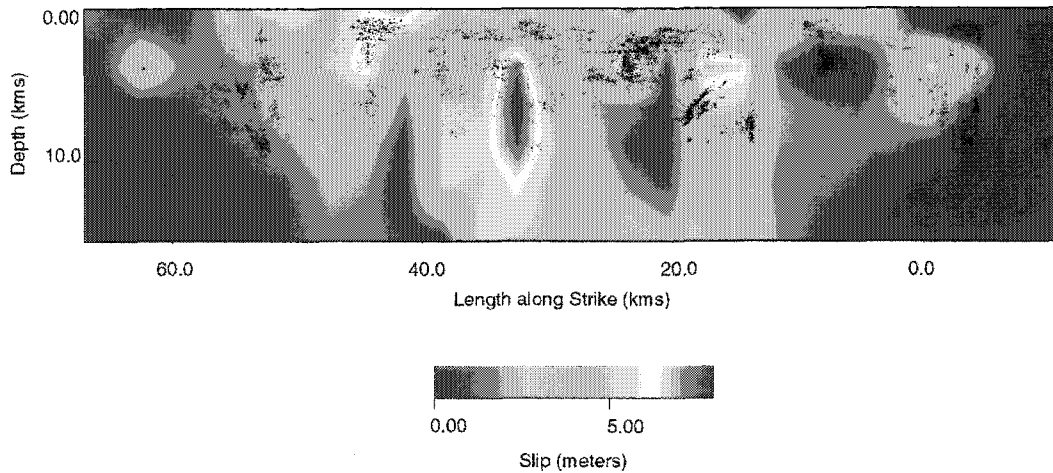


Figure 3.4: Precise aftershock locations plotted against the Landers slip distribution calculated by *Wald and Heaton (1995)*. Color represents slip during the 1992 Landers mainshock. Red represents areas of high slip and blue, low slip. Some of the most intense seismic activity occurs at the southern end of the Johnson Valley fault, near the patch of higher slip where the Landers mainshock initiated. Some areas like the northern end of the Johnson Valley fault and the northern end of the Camp Rock fault show activity in areas of very little coseismic slip.

The major faults are the Johnson Valley Fault to the south, the Homestead Valley Fault, the Emerson Fault, and the Camp Rock Fault. The mainshock initiated on the Johnson Valley Fault, approximately 7 km north of the Pinto Mountain Fault. In addition to these faults, there is triggered seismicity in a number of areas. The Burnt Mountain and Eureka Peaks Faults both slipped either during the mainshock or directly after it (*Hough et al., 1993*). To the south of these faults, the Joshua Tree earthquake, which produced no surface rupture, created its own set of aftershocks on a number of planes of varying orientations.

Our precise locations also help constrain the depth of the seismogenic zone. Figure 3.3 shows a cross section of the seismicity along the fault trace. Certain parts of the sequence have earthquakes occurring at greater depths than other parts. In particular, the southern terminus of the Landers rupture, on the Johnson Valley fault, show seismicity to 17km depth. There are also abrupt changes in the depth of seismicity, such as in the middle of the Johnson Valley fault near the mainshock hypocenter. Despite these variations, the depth of the seismogenic zone for most of the rupture occurs around 10 km.

Figure 3.4 compares the precise earthquake locations with the *Wald and Heaton (1995)* slip model calculated from strong motion and geodetic data. In many places aftershock activity corresponds to areas that slipped in the Landers mainshock, like the Johnson Valley – Homestead Valley fault jog, and along the Emerson fault. Some aftershocks surround areas of high slip, for instance, the southern end of the Johnson Valley Fault, just south of where the mainshock rupture initiated, the deepest seismicity occurs. Aftershocks tend to surround the patch of high slip, approximately 4 m of slip, near the mainshock initiation point. This aftershock behavior has been noted for a number of different earthquakes (*Mendoza and Hartzell, 1988; Beroza and Spudich, 1988; Beroza and Zoback, 1993*). There are also areas of seismicity that occur where there was little slip in the mainshock rupture. These include the *en echelon* faults in the northern part of the Johnson Valley fault, before the fault offset, as well as the aftershocks on the Camp Rock fault. Again, these aftershocks are near but not within areas of higher mainshocks slip. Aftershocks along the length of the Landers mainshock rupture occur at depths similar to the depth of mainshock slip. Only in areas where high slip extends to depths greater than 10 km, does aftershock activity not match those greater depths.

The complexity and variation of the fault zone is evident in the cross sections in Figure 3.5. These cross sections are taken at regular intervals of 10 km along the entire sequence perpendicular to the local strike of the surface rupture in the interval. Near the Joshua Tree earthquake, the width of the aftershock zone is substantial, on the order of 10 km. On other segments the seismicity is confined to a much narrower zone that is related to the surface expression of the fault, like parts of the Johnson Valley fault shown in Figure 3.5f, where the fault zone is approximately 4 km. This may suggest that strain is accommodated in different ways on different parts of the rupture. Well-developed faults accommodate strain in narrower, well-defined zones, while in less developed areas, like the Joshua Tree area require a number of faults to account for strain. In this work, we call faults well-developed if they are the major slip surface in the mainshock rupture and have accommodated significant slip over a long time. The Landers

fault system is composed of a well developed fault zone as defined in structural geology terms because it includes a number of secondary structures such as fracturing associated with fault offsets between older faults. Although the secondary fracturing suggests the well-developed fault zone, we will use the term well-developed only to discuss the older faults and not the secondary features. In Figure 3.5, it's difficult to determine the exact fault width because many subfaults may be included in the same interval.

Thus, in the following sections, we look more closely at the structures illuminated in different parts of the earthquake sequences, and interpret the seismicity in terms of strain localization, the influence of fault complexity on mainshock slip, and the time-dependence of the seismic-aseismic transition. In order to do this we will describe the seismicity from South to North. First we will examine the aftershocks near the Joshua Tree earthquake. Several small faults in varying orientations were active in this sequence, and there was abundant off-fault seismicity. Next we will look at seismicity associated with the major faults of the Landers earthquake, the Johnson Valley Fault, the Homestead Valley Fault and the Camp Rock – Emerson Fault. Then we will look at features activated in the fault offsets ruptured in the Landers earthquake as well off-fault seismicity triggered near the Calico and Pisgah faults.

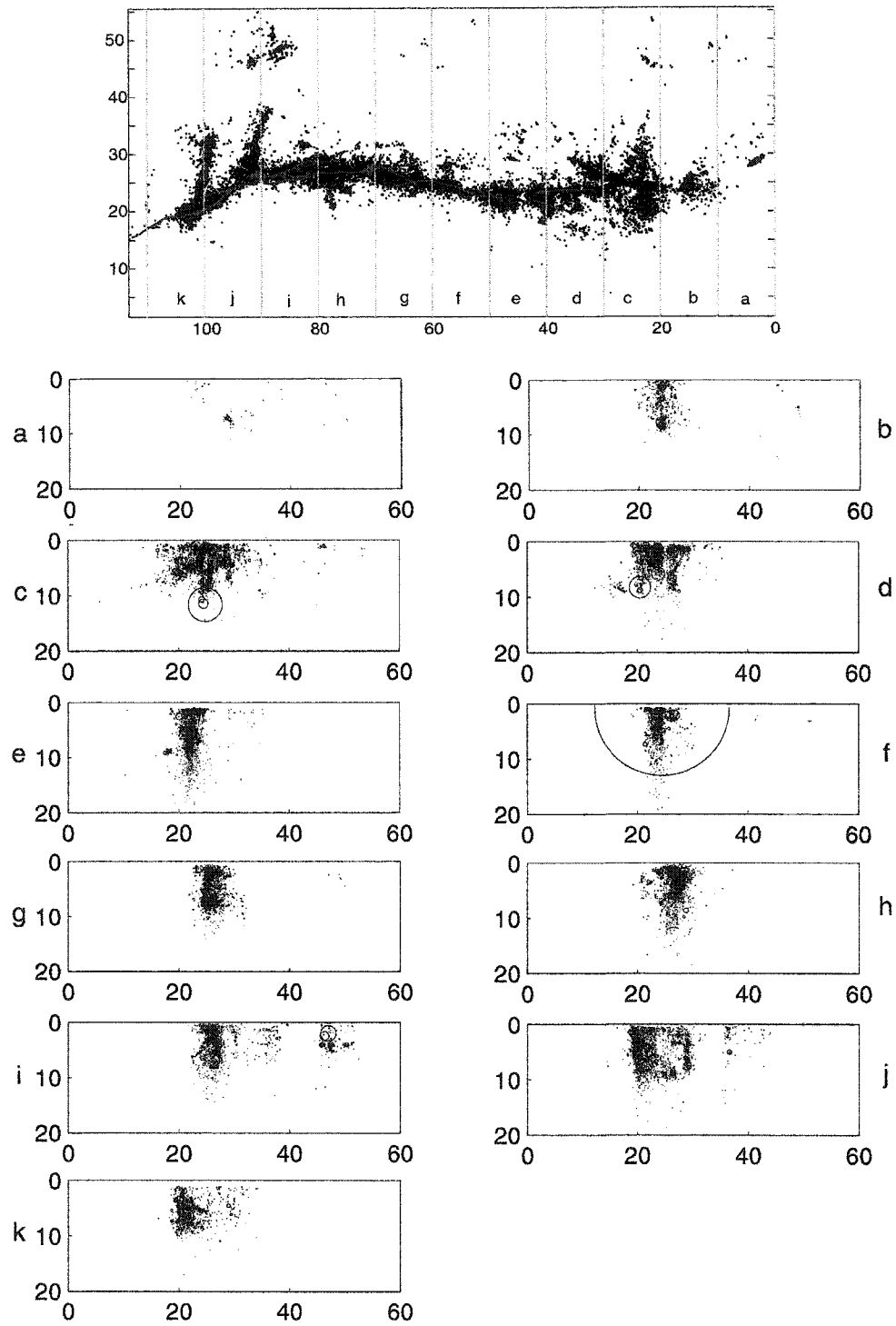


Figure 3.5: Map view of aftershocks and cross sections along the strike of the Landers rupture. Each cross section represents 10km along strike. The width of the fault zone varies dramatically along the length of the rupture. Cross section C crosses the Joshua Tree earthquake aftershocks. Cross section F contains the Landers mainshock, shown as the large circle.

THE APRIL 23RD, 1992 JOSHUA TREE EARTHQUAKE SEQUENCE

The M 6.1 Joshua Tree earthquake of April 23rd, 1992, was the first significant earthquake in the Landers sequence. The event was preceded by a brief foreshock sequence (*Hauksson et al.*, 1993). Despite its magnitude and an abundance of shallow aftershocks, the ~6000 aftershocks we relocate in the sequence range in depth from 0 km to 12 km, the Joshua Tree earthquake produced no surface rupture. After relocation, many features of the aftershock sequence become much clearer, including the mainshock plane and several small off-fault planar subfaults. The planes are rotated slightly from the mainshock plane direction making it difficult to view the subfaults clearly in cross section.

The orientation of the aftershock zone and the mainshock focal mechanism indicates right-lateral faulting with a strike of N20°W and a vertical fault plane (*Hauksson et al.*, 1993). The aftershock location show a complicated pattern of subfaults in which a general structure striking in a N20°W direction is composed of a series of smaller planes. Figure 3.6a shows a plane striking approximately N20°W and one approximately N45°W directly to the south of the mainshock hypocenter, marked by the large circle; to the north and south of this plane, there are two structures that trend north-south. These subfaults occur at 4–6 km depth. The mainshock is displaced to the NE from these aftershocks, but within location error of these events.

To the north of the mainshock, the aftershocks define a NS striking plane, and farther north, as the aftershock zone approaches the Pinto Mountain fault and the southern terminus of aftershocks of the subsequent Landers mainshock, the aftershocks define two planes, one strikes about N15°E, and a well-resolved near vertical conjugate plane striking about N65°E, ranging in depth from 1-9 km. These locations also help us resolve the nodal planes for focal mechanisms calculated by *Hauksson et al.*, (1993), particularly for off-fault planes that were previously not located well enough to determine the strike. The off-fault planes directly to west of the mainshock trend in a similar N20°W direction as the mainshock plane. The dashed lines in Figure 3.7 denote

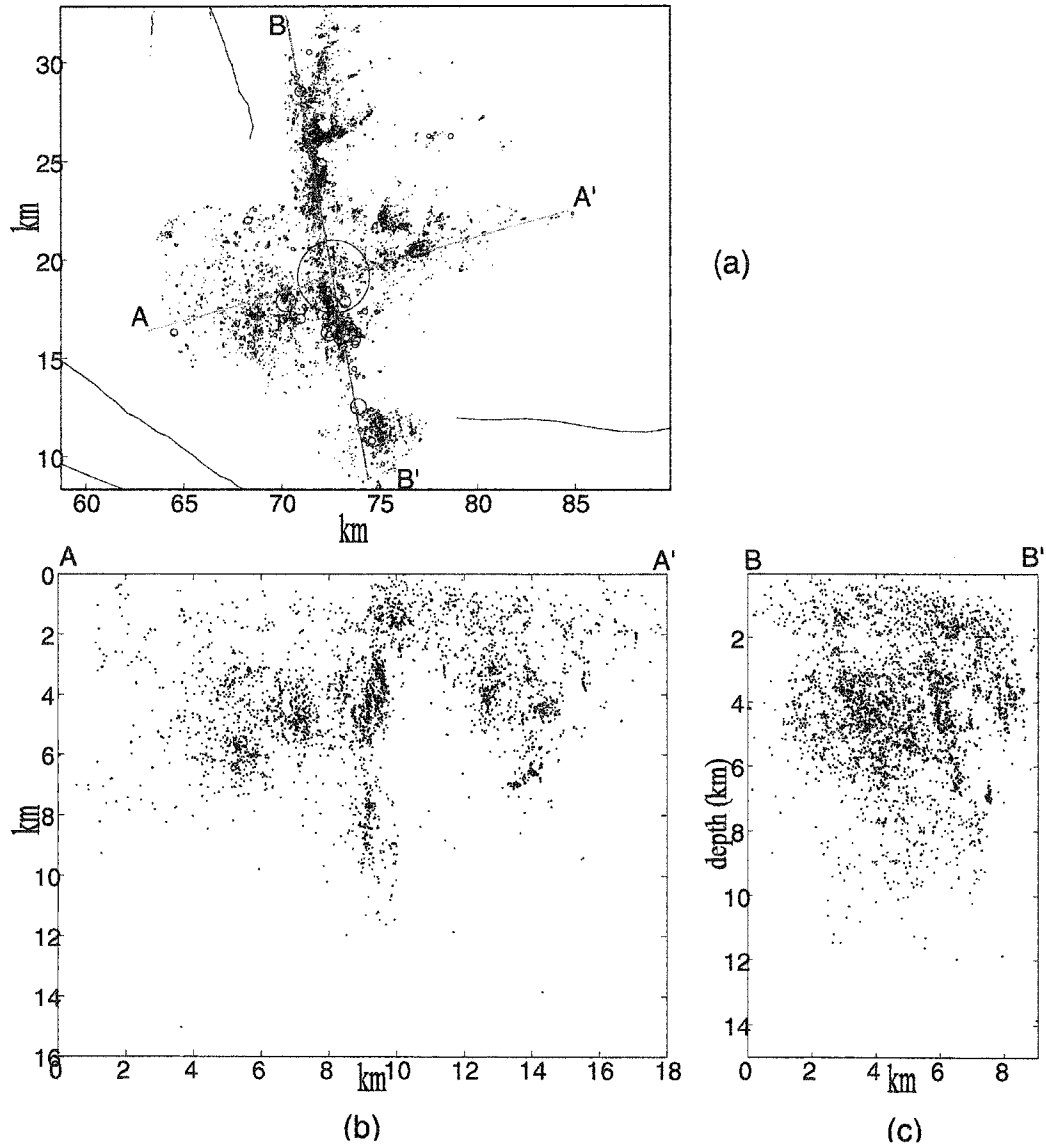


Figure 3.6: (a) Map view of the aftershock related to the 1992 Joshua Tree earthquake. Dark gray lines are major faults in the area, and light gray lines are locations of the cross sections. (b) Cross section A, perpendicular to the Joshua Tree strike, shows the variety of fault planes activated following the Joshua Tree earthquake (c) Cross section B traverses the Joshua Tree aftershocks along the mainshock strike.

the strike of these planes. Off-fault planes to the east, however, define one north-trending plane and at least three planes conjugate to the mainshock fault plane, suggesting left-lateral strike slip on NE-trending planes, from the focal mechanisms.

After the Landers earthquake, some segments in the Joshua Tree sequence remain active while others are abruptly turned off (Figure 3.7). One of the two most prominent changes is a swarm of events to the south of the Blue Cut Fault was activated; the sequence includes two events $M > 4.5$. The other is $N15^\circ E$ striking plane to the east of the Eureka Peak fault that shows no activity after the Landers earthquake even though activity was continuous in that area starting a few weeks after the Joshua Tree earthquake. Coulomb stress modeling for the Landers earthquake places this subfault in narrow area of stress decrease between two areas of stress increase (King *et al.*, 1994). The north trending plane to the southeast of the Eureka Peak Fault shows no change in aftershock rate following the Landers earthquake.

Following Landers a new set of subfaults between the Burnt Mountain and Eureka Peak Faults became active (Figure 3.8). Although these subfaults are physically close the Joshua Tree aftershocks, at some points less than a kilometer away from faults activated by Joshua Tree event, which are shown in Figure 3.8a in blue, these planes show no activity prior to the Landers earthquake. Also, since the Landers earthquake ruptured unilaterally to the north, events south of the Pinto Mountain Fault did not occur on the mainshock plane (Hauksson *et al.*, 1993; Kanamori *et al.*, 1992; Wald *et al.*, 1992); however, aftershock activity immediately after the Landers mainshock and surface afterslip suggest that there was slip on the Eureka peak fault after Landers (Sieh *et al.*, 1993). The aftershocks that point to the afterslip occur to the south of the inferred surface rupture of the Eureka Peak Fault. Hough *et al.*, (1993) also suggest that the surficial offset can be attributed to a $M 5.8$ event and a $M 5.6$ event occurring within minutes following the Landers mainshock.

We are able to relocate the $M 5.6$ event and find that it lies on the Burnt Mountain fault, but were not able to determine a location for the other event. Although these large events correspond to the faults inferred from surface rupture, most of the microseismicity does not. The relocated aftershocks reveal a clear trend, $N58^\circ E$, that experienced a $M 4.5+$ event early in the

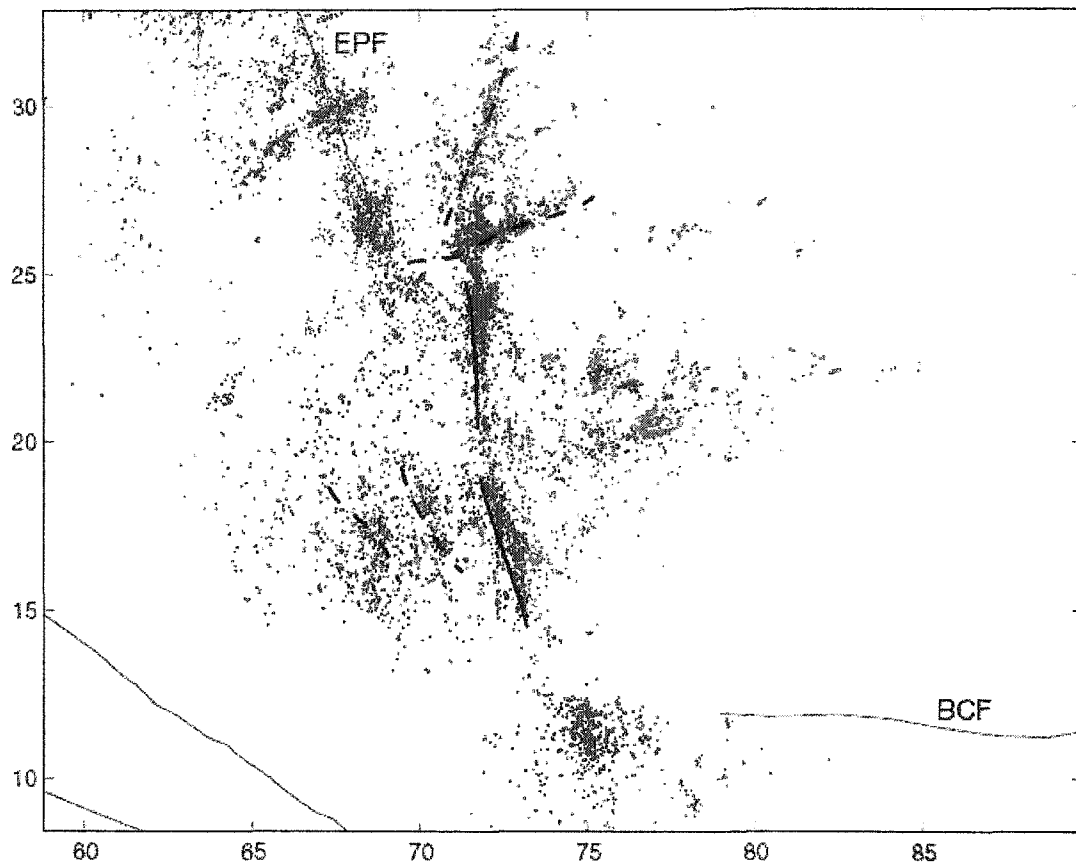
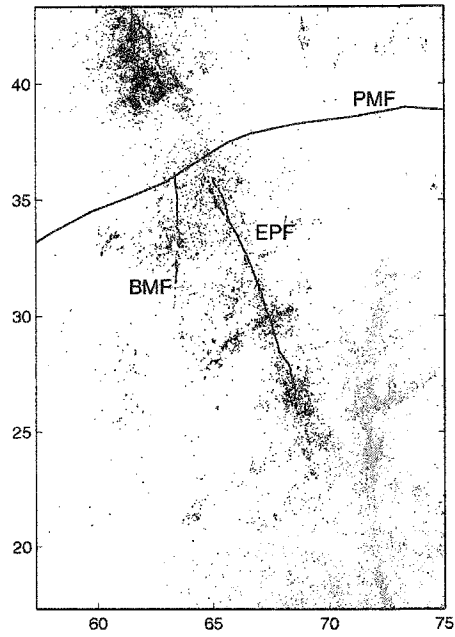
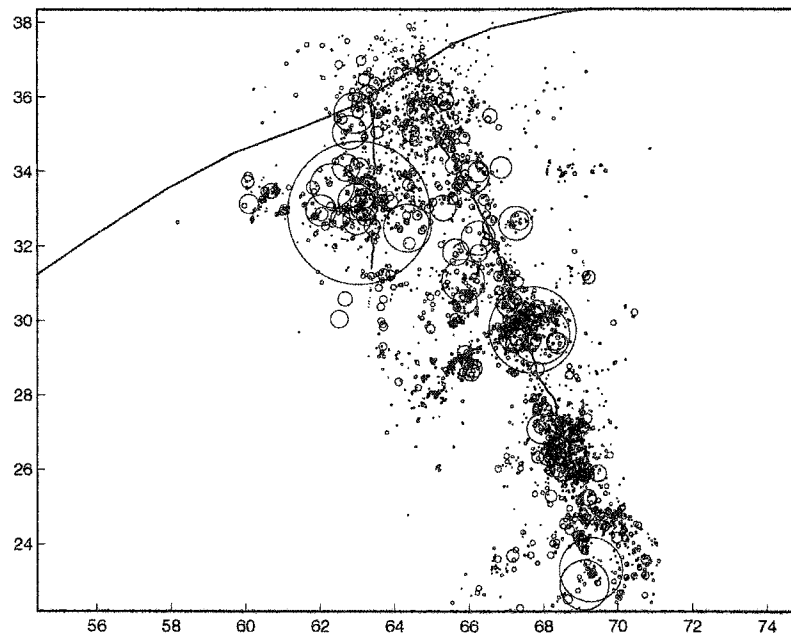


Figure 3.7: Map view of aftershocks following the Joshua Tree earthquake. Events in blue occur after the April 23rd, 1992 Joshua Tree earthquake but before the June 28th, 1992 Landers earthquake. The northeast trending plane to the east of the Eureka Peak Fault (EPF) is not active following Landers. Events in Red are aftershocks following the Landers earthquake. A number of features active following Joshua Tree are not active following Landers. BCF: Blue Cut Fault.



(a)



(b)

Figure 3.8: (a) Aftershocks near the Burnt Mountain and Eureka Peak faults following the Landers earthquake. Blue events are the Joshua Tree aftershocks. Red lines indicate major faults in the area. (b) Close up view of the same aftershocks; circles represent estimated source size based on a circular crack model using 3MPa stress drop. The largest event shown is the M 5.3 Burnt Mountain Fault event.

aftershock sequence. Slip on this fault would be left-lateral based on the focal mechanism for the large aftershock (*Hauksson et al.*, 1993). This feature was also one of the most active after the 1999 Hector Mine earthquake, experiencing another M 4.5+ event. Events closer to the Pinto Mountain Fault are generally diffuse. *Hauksson et al.*, (1993) suggest that faults south of the Pinto Mountain Fault are young and the granitic basement may have many small fractures capable of accommodating slip thus accounting for the diffuse distribution of aftershocks on small structures.

THE 1992 LANDERS MAINSHOCK FAULTS AND STRAIN LOCALIZATION

Aftershocks along the major faults that ruptured during the 1992 Landers earthquake show a great deal of complexity even at depth, despite the maturity (*Sieh et al.*, 1992; *Hauksson et al.*, 1993) of the faults. Unlike other well-developed faults such as the Calaveras and San Andreas Faults, where seismicity defines thin fault zones that correspond to the strike and dip of the fault (e.g., *Schaff et al.*, 2002), the Landers sequence activated multiple structures of varying orientations even along sections of the mature faults. The surface trace of the faults that ruptured during the mainshock also suggests the complexity of faulting in the area, particularly to the north, near the Emerson and Camp Rock Faults. The correspondence between the complexity of surface faulting and the complexity of seismicity at depth in this sequence, however, is highly variable.

We locate 6400, or 80%, of the aftershocks on the Johnson Valley Fault, where the Landers mainshock initiated, south of the fault offset between the Johnson Valley and Homestead Valley faults. Figure 3.9 shows these relocations and cross sections along prominent features. Nearly 25% of these events fall on a set of *en echelon* faults to the north the mainshock hypocenter, cross section AA' and BB'. The strike of these faults does not correspond to the surface trace of the Johnson Valley fault. The largest of the *en echelon* faults strikes N40°W, dips about 85° to the west and occurs at a depth of 3-4 km. The other faults strike in a similar direction

but are very small and very shallow, above 2km depth. North of this section, the mainshock slip on the Johnson Valley Fault decreases significantly (*Wald and Heaton, 1994; Spotilla and Sieh, 1995*) and aftershock activity also drops off. Although the largest of the *en echelon* faults doesn't correspond to the surface rupture trend, it is a narrow well-defined fault, unlike the bifurcation in the southern end of the Johnson Valley Fault.

4200 of the events fall at the bifurcation of the Johnson Valley Fault just south of the mainshock hypocenter and at the end of the mainshock's surface rupture (Figure 3.9, cross section CC'). The densest seismicity in this cluster extends about 2 km past the end of the surface rupture. The deepest events in the Landers sequence occur in this cluster, though the earthquakes near 15 km depth are small events $M < 2.0$. The faulting pattern is very complex at the bifurcation, more so than suggested by the surface fault trace. We identify small subfaults trending East-West as well as at strikes similar to the surface rupture.

The bifurcation is also one of the most active sequences activated following Landers, with the rate of earthquakes remaining high longer than the rest of the Johnson Valley fault. As noted earlier, Figure 3.4, shows that these earthquakes surround the region of high slip that accompanied the mainshock initiation, which is just north of the bifurcation. *Peltzer et al., (1994)* find from InSAR data that an additional 1.5-3.5m of slip may have occurred below 1.5 km between the southern end of the Johnson Valley Fault and north of the Pinto Mountain Fault. This additional deep slip could also contribute to the quantity of seismicity in this region.

Between the *en echelon* faults and the bifurcation, aftershocks correspond very well to the mapped surface expression of the Johnson Valley Fault. Fault width in this section is about 0.3-0.5 km. So, for a large segment of the Johnson Valley Fault, we may say that strain is accommodated in a zone confined to less than 1 km. For approximately 4 km south and 4 km north of the *en echelon* faulting, seismic activity becomes sparse along the Johnson Valley Fault. This entire section of the Johnson Valley Fault experienced very low levels of slip in the mainshock (*Cohee and Beroza, 1994; Wald and Heaton, 1994*). To the north of this section,

aftershocks occur on a left-lateral strike-slip fault denoting the beginning of the 5 km fault offset between the Johnson Valley and Homestead Valley Faults. We will look at this jog more closely in the next section. The part of the HV fault that ruptured past the fault offset between the HV and JV faults, defines a broad shear zone, shown in cross section AA' of Figure 3.10. Geologic evidence suggests the Homestead Valley Fault is comparatively youthful compared to the other faults, like the Emerson Fault (*Zachariassen and Sieh, 1995*), that ruptured in the Landers earthquake. This would be consistent with the larger fault zone width and complex aftershock distribution near the Homestead Valley Fault. Directly to the north of the jog, and the an apparent slip gap in the surface rupture (*Spotilla and Sieh, 1995*), on the Homestead Valley fault, aftershocks define a structure 2 km in length and about 0.5kms width at a depth of 3-4 km. North of this structure, however, the surface rupture indicates that a branch of the Emerson fault overlaps the Homestead Valley fault. The width of the fault zone grows to 5-8 km and discerning the faults that are active becomes more difficult. To the west of the Homestead Valley fault, two off-fault clusters are activated, but it is difficult to determine their precise orientations

The more mature Emerson fault shows a thinner fault zone. Cross section CC', in Figure 3.10, shows this section of the Emerson fault, which has a fault zone width of approximately 1 km, and dip about 70° to the northeast. There is some diffuse seismicity in this cross section both at shallow and depths > 8 km that corresponds to the complexity of the Emerson Fault – Homestead Valley Fault overlap and an E-W trending feature without a surface expression near the Emerson fault. The Landers surface trace also shows that the Camp Rock fault overlaps the Emerson Fault for much of the rupture length. Cross Section DD' shows the northern extent of the aftershock activity. The seismicity is more difficult to interpret because of the complex interaction of the Camp Rock and Emerson fault. It seems, however, that there is no significant change in depth along the major faults, though cross section BB' does show that there is less activity on the Emerson fault than on the Homestead Valley fault. For the most part, events on the major faults fall from 0-10 km depth.

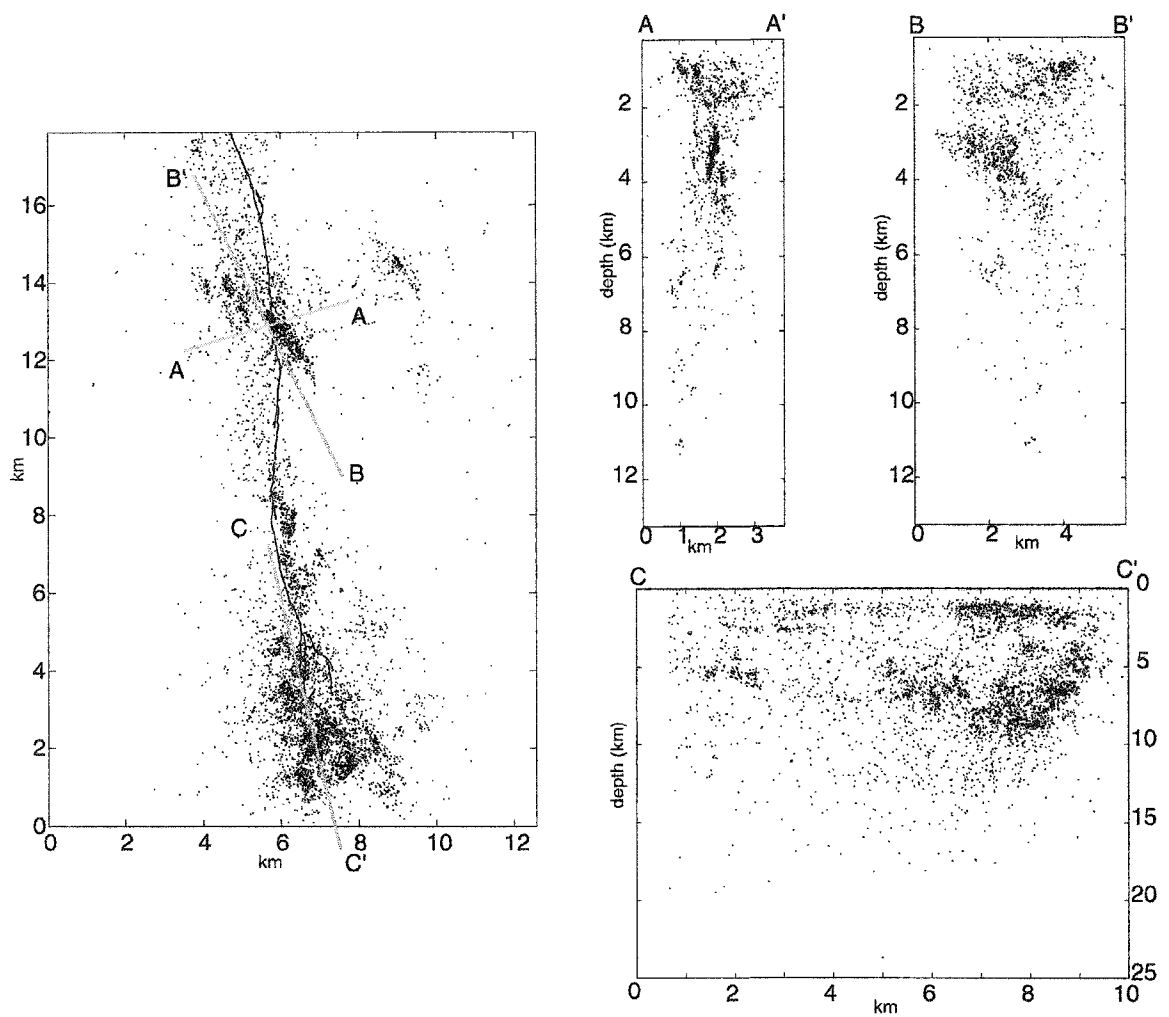


Figure 3.9: Map view and cross sections of aftershocks along the Johnson Valley fault. Red lines indicate the Landers surface rupture and the Gray lines indicate the cross sections. Cross section AA' and BB' traverse a set of en echelon faults that does not correspond the surface rupture in the area. The largest of these faults is 2-4 km depth while the others are shallower. Cross section CC' crosses the end of the Johnson Valley fault which shows a complex surface rupture. Aftershocks also show a complex set of active planes even at depth. Axes in km.

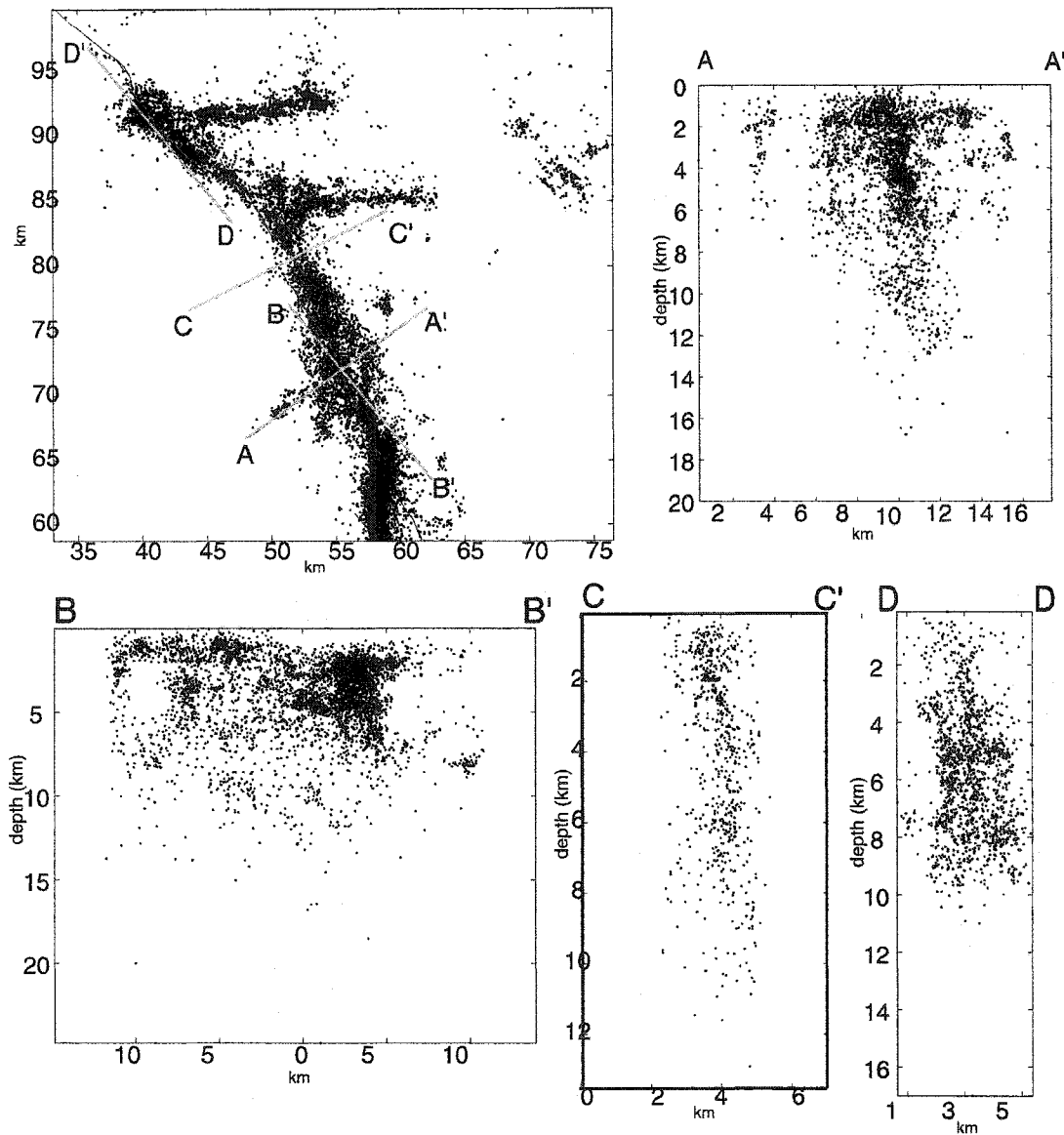


Figure 3.10: Map view and cross sections including aftershocks along the Homestead Valley fault, cross sections AA' and BB', the Emerson fault, cross section CC', and the northern section of the Camp Rock -Emerson fault that ruptured, cross sections DD'. Red lines are the Landers' surface rupture and the gray lines indicate the cross sections.

For the most part well-developed faults, like the Emerson Fault and Johnson Valley have aftershocks tightly clustered in a narrow fault zone, from 0.5 - 1 km wide. The Homestead Valley Fault exhibits this behavior just north of the Johnson Valley – Homestead Valley fault jog, but this fault also exhibits a very wide fault zone, at least 8 km wide, near its overlap with the

Emerson Fault. Areas previously described as youthful, such as the Joshua Tree area (*Hauksson et al.*, 1993), and areas that exhibit extensive surface rupture complexity, such as the bifurcation in the southern terminus of the Johnson Valley fault, show wider fault zones, suggesting that accumulated strain is accommodated more diffusely than on well-developed faults.

FAULT DISCONTINUITIES AND CONTROL OF COSEISMIC SLIP

The Landers earthquake ruptured across three fault discontinuities, the compressional offset, as defined by *Sibson* (1986), between the Emerson and Camp Rock fault, and the dilatational jogs between the Homestead Valley and Emerson Faults, and between the Johnson Valley and Homestead Valley Faults. All three jogs show evidence at depth of complex structure suggested in the surface trace of the Landers rupture; however the features illuminated by the aftershocks do not correspond closely to the fault trace in the surface rupture for the JV-HV Fault offset.

The largest fault discontinuity in the Landers rupture is the dilatational offset between the Johnson Valley and Homestead valley faults, seen in Figure 3.11. The jog is approximately 5 km \times 5 km \times 10km. In numerical models of rupture propagation across discontinuities (*Harris and Day*, 1993), rupture was unable to propagate across discontinuities greater than 5 km. This is corroborated by a survey of field observations of rupture propagation across fault jogs in Turkey (*Barka and Kadinsky-Cade*, 1988) and evidence of earthquakes where rupture has jumped across fault offsets between 1-5 km (*Barka and Kadinsky-Cade*, 1988; *Tchalenko and Ambraseys*, 1970; *Hauksson et al.*, 1993). Numerical models also suggest that faults that span an offset can significantly facilitate the propagation of rupture across fault discontinuities (*Harris and Day*, 1993). This would seem to be the case with the Kickapoo, or Landers fault, which spans the length of the JV-HV fault jog and was only mapped after the Landers earthquake.

In the northern extent of the jog, an apparent “slip gap” was discovered in measurement of surface offset where the Landers fault meets the Homestead Valley fault (*Spotilla and Sieh*,

1995). The slip gap is defined by an area of multiple fractures with minimal surface offset, on the order of 20-50 cm, surrounded to the north and south by high offset on the Homestead Valley and Landers faults respectively. There is also evidence of small amounts of thrust slip in this region. *Spotilla and Sieh* (1995) note that the surface expression may represent slip to up to a depth of 2.5 km. Unlike the other discontinuities, most of the fractures in the JV-HV jog that appear in the seismicity do not correspond to the surface trace of the Landers rupture.

South of the Landers fault abundant seismicity occurs on a left-lateral, strike-slip fault conjugate to the Johnson Valley Fault. To the north of the Landers fault, starting from the Johnson Valley fault, two structures become visible, one dipping approximately 30° to the northwest and the other dipping 60° in a similar direction. These planes do not seem to correspond to the Landers fault, but their location and sense of slip are consistent with secondary fracturing in dilatational fault jogs (*Sibson*, 1986). Mechanisms in the area are diverse including strike slip events as well as thrust events. The Johnson Valley and Homestead Valley faults show few events within the jog. In the area of the slip gap, there is complex fracturing at the surface, though there is little slip recorded. This complexity is reflected in the seismicity in the area, which is abundant and extends to a depth of 4 km, and therefore may be related to deeper slip in the area.

Figure 3.11b shows the location of the 1979 M 5.3 Homestead Valley earthquake and the relationship of the aftershocks in that sequence (red) to the aftershocks of the Landers earthquake. The mainshock and aftershocks of the Homestead Valley earthquake occur to the south of the Landers fault, and the Homestead Valley aftershocks do not overlap with the majority of the Landers aftershocks. In addition there are a number of off-fault aftershocks that do not correspond to the JV or HV faults; again, these events do not activate the same areas that rupture during the Landers aftershock sequence. This may suggest that the Homestead Valley

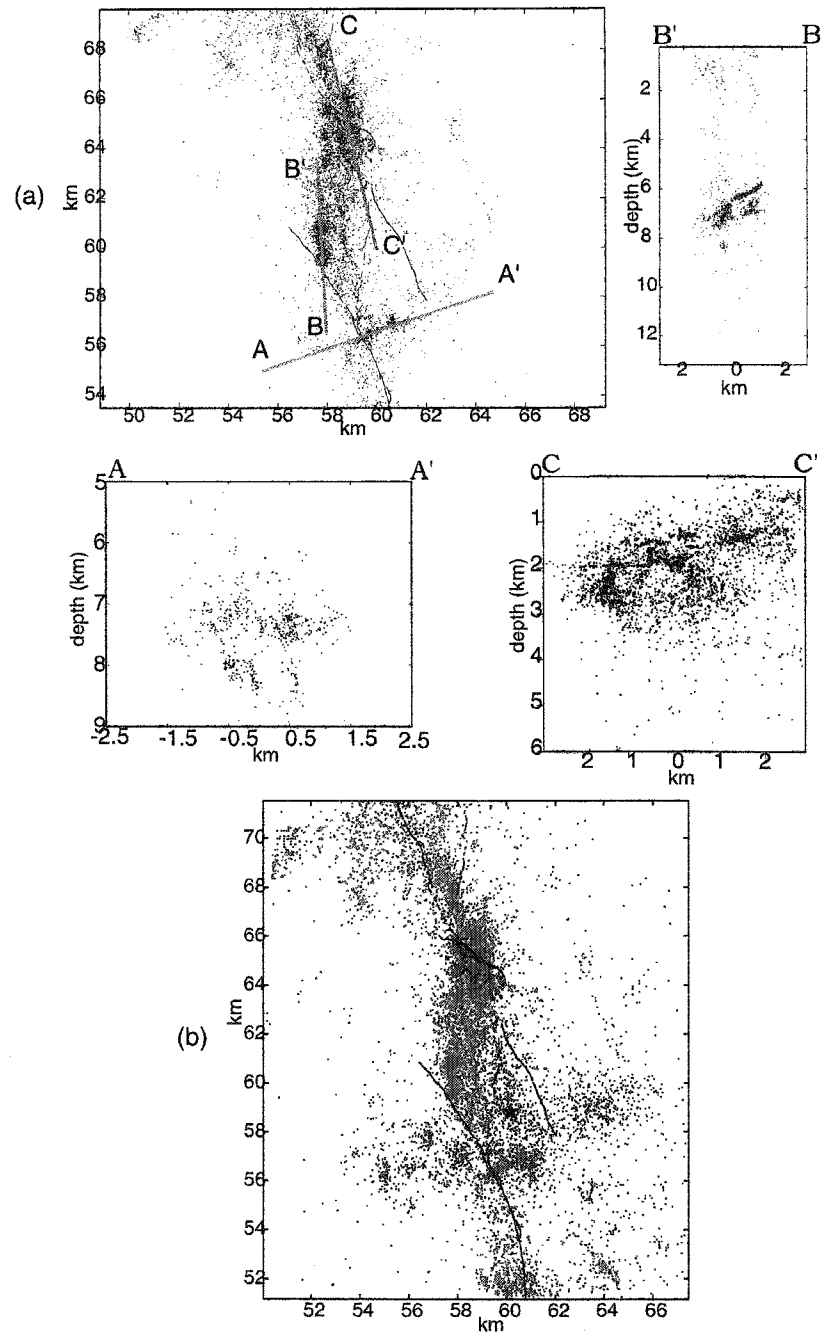


Figure 3.11: (a) Map view of aftershocks in the Johnson Valley-Homestead Valley dilatational fault offset. The red lines are the surface rupture of the Landers earthquake; the Johnson Valley fault is to the southwest and the Homestead Valley fault is to the northeast, and the Landers/Kickapoo fault spans the jog between the two faults. Cross sections of various faults within the fault jog. Cross section AA' crosses a left-lateral strike slip fault conjugate to the Johnson Valley fault. Cross section BB' cross cuts two feature to the north of the Johnson Valley fault. Cross section CC' crosses a complexly fractured region in the northern section of the jog near the Homestead Valley fault. (b) Comparison of 1979 Homestead Valley aftershock sequence (red) to the 1992 Landers aftershock sequence.

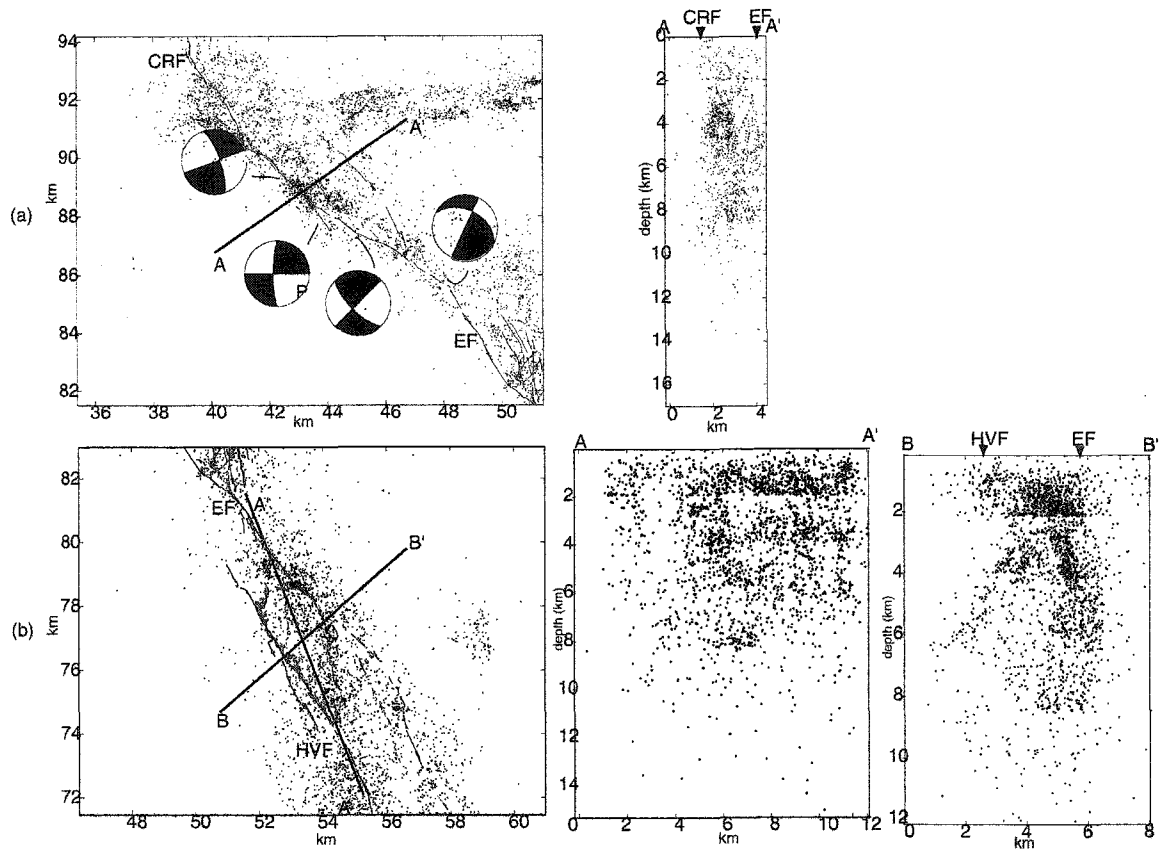


Figure 3.12: Cross sections along two fault offsets along the Landers rupture. Red lines indicate surface rupture and black lines indicate the cross sections. (a) Map view and cross section across the slight compressional jog apparent in the surface rupture along the Camp Rock –Emerson fault. Most of the activity occurs on two northwest trending features of slightly different orientations that correspond the surface rupture. (b) Map view and cross section along the Emerson – Homestead Valley fault jog.

aftershock sequence relieved enough stress along the southern section of the Homestead Valley fault, that it was not reactivated during the Landers earthquake.

The Homestead Valley – Emerson Fault jog is approximately 2 km in width and is cross cut by the Eastern Splay and Northern Cross faults (*Zachariassen and Sieh, 1995*). Our relocations for the jog are shown in Figure 3.11b. We have relocated 2,124 earthquakes in the jog, and find that few earthquakes occur on the northern extent of the Homestead Valley fault. As noted by *Felzer and Beroza (1999)*, there is no evidence that the two faults merge at depths. Both cross

faults show significant activity at depths of 2-8 km. Overall, our depths are shallower than those obtained by *Felzer and Beroza (1999)*. Aftershocks at shallow depths seem to show an artifact of the relocation procedure. In cross section BB' earthquakes at 2 km depth delineate a sharp horizontal line. This is probably not a real feature, nor is it due to the velocity model used, since there is no boundary at 2 km. Instead, it may be explained by degraded waveform correlations for earthquakes in a highly fractured medium, as would be expected in a fault offset. Also, we do not notice a discernable difference in the depth of events in the northern extent of the jog as *Felzer and Beroza (1999)* found in the relocation of 150 events in the area.

Rupture did not stop at either dilatational jogs, even though this behavior has been noted in the past (*Sibson, 1986*). Rupture did cease approximately 5 km to the north of a slight compressional jog between the Emerson and Camp Rock faults, shown in Figure 3.12a. This is also expected behavior from a compressional offset, as seen in the 1968 Borrego Mountain earthquake (*Sibson, 1986*). The southern extent of the Camp Rock fault falls to the east of the Emerson Fault. Most of the seismicity falls on the Emerson fault, defining two planes similar to the surface expression of the fault in the jog. Cross section AA' shows the two structures, the eastern one trends N60°W and is near vertical, the other trends about N45°W.

This is the segment of the Emerson fault for which *Hauksson et al., (1993)* notice the anomalous left-lateral strike-slip focal mechanisms. The mechanisms for the 4 largest earthquakes in that area are plotted in figure 3.12. These mechanisms near the end of the mainshock rupture, and near the restraining bend in the Emerson-Camp Rock Faults, could suggest a dynamic overshoot in mainshock slip. The subsequent reversal in the sense of shear stress on the fault plane would cause left-lateral strike-slip faulting. This behavior is considered very rare, with overshoot effects calculated at ~15% of the difference between dynamic and static friction (*Burridge and Halliday, 1971; Beroza and Zoback, 1993*). The sense of slip exhibited by approximately 76 aftershocks, only within this northern compressional jog and on the mainshock fault planes as expressed by surface rupture, is interesting. They suggest that the Camp Rock fault

may have slipped under low friction since during the mainshock the fault experienced more than complete stress drop, and reversal of slip was possible. The total stress accommodated by these aftershocks should be equal to the excess stress accommodated by the mainshock; determining this amount of stress from the aftershocks is not possible.

Only 4 km to the north of this junction, aftershock activity terminates on the Camp Rock Fault, though surface offset is recorded for another 5 km, and aftershock activity continues on a east trending feature. *Hauksson et al.*, (1993) suggest that the change in fault direction at the Camp Rock –Emerson Fault jog causes a change in off-fault strains here, and this may be responsible for the lack of aftershock activity.

OFF-FAULT SEISMICITY

A distinctive characteristic of this earthquake sequence is that a multitude of aftershocks were triggered on faults that did not slip during the Landers or Joshua Tree earthquakes. These include subfaults close to the Joshua Tree – Landers mainshock ruptures as well as more remote structures.

The two most prominent offshoots extend east to northeast from the Emerson – Camp Rock fault to the Calico fault ~10 km away. Small surface offsets on faults trending slightly northeast were recorded here following Landers (*Hart et al.*, 1993). *Hauksson et al.*, (1993) suggest that left lateral slip might be triggered on these faults by either the unsuccessful attempts of the rupture to jump to the Calico fault, or fracturing from strain due to the change in fault strike from N10°W to N45°W on the Camp Rock fault. The southern feature is composed of a diffuse set of ~1100 events close to the Emerson fault that tapers into a shallow, 0-4 km, eastward trending fault towards the Calico fault. The northern structure, Figure 3.13, has far more earthquakes, ~1800 events, and clearly defines specific fractures, including, apparently, the NW trend of the Calico fault, as seen in cross sections BB' and CC'. An approximately 3 km section

of the Calico fault is activated at a depth of 4-8 km dipping 80° to the northeast and trending $N40^\circ W$. Three other fractures are apparent in the eastward feature connecting the Camp Rock fault to the Calico fault.

To the east of the Calico fault events, another sequence of earthquakes was triggered after Landers. The largest of these events was a M 5.3 earthquake occurring on July 5th, 1992, just a week after the Landers mainshock. This event was termed the Pisgah earthquake because its proximity to the fault of that name. It had a focal mechanism consistent with NW oriented right-lateral strike slip. In Figure 3.14 we map the earthquakes in this cluster. A clear NW trend is associated with the Pisgah event. A cluster of events occurs to the northwest of the Pisgah mainshock, and a small parallel strand of earthquakes occurs a kilometer to the southwest, but the main set of earthquakes in this cluster occurs on a $N45^\circ W$ plane dipping 50° to the southwest. The depth of the events generally ranges from 3-8 km in the main cluster. The events to the north are shallower at 0-3km depth.

In addition to the events that occurred in the 1992 Pisgah cluster immediately following the Landers mainshock, we also relocate a set of earthquakes that occurred in August-October 1996. This sequence included two $M > 4$ events and has been suggested more likely to trigger the 1999 Hector Mine earthquake than the Landers earthquake itself (*Felzer et al.*, 2003). Unlike the trend of the 1992 Pisgah cluster, these earthquakes trend to the northeast about 40° and occur at a depth of ~ 5 km. The earthquakes that occur in October of 1996 are slightly farther east, and closer to the initiation point of the Hector Mine earthquake, than those that occurred in August. The 1992 sequence also produced a few small events near the initiation point of the Hector Mine earthquake. The 1996 cluster fills in the area between the previous set of events and the rest of the Pisgah cluster.

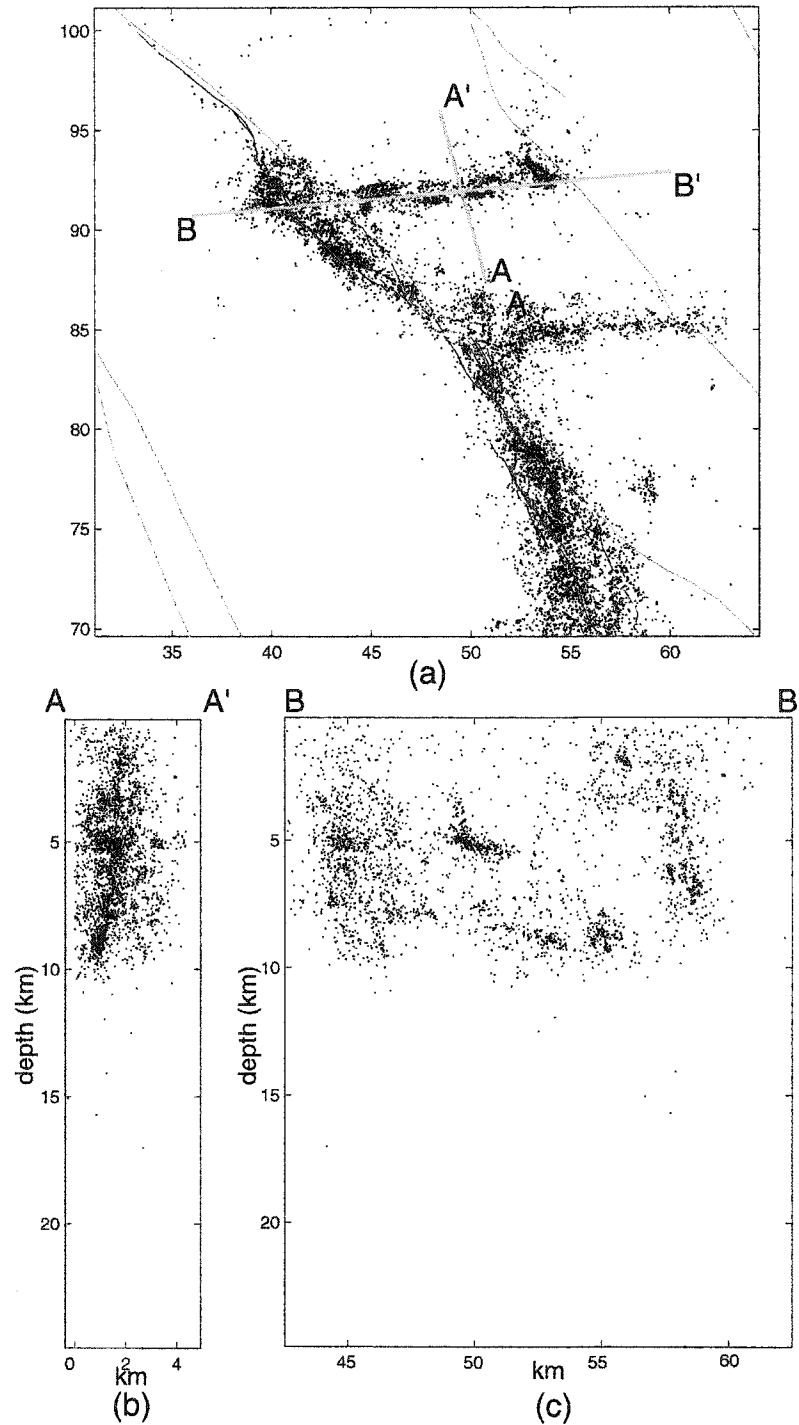


Figure 3.13: (a) Map view of aftershocks from the Camp Rock fault to the Calico Fault. Red lines indicate the Landers surface rupture, and gray lines mark cross sections. (b) Cross section A across the strike of the EW trending fault. The seismicity shows a distinct dip to the south of about 80° . (c) Cross section B, along the strike of the EW trending plane, shows discrete segments are active the trend farthest to the east corresponds to a NW trending plane consistent with the Calico fault.

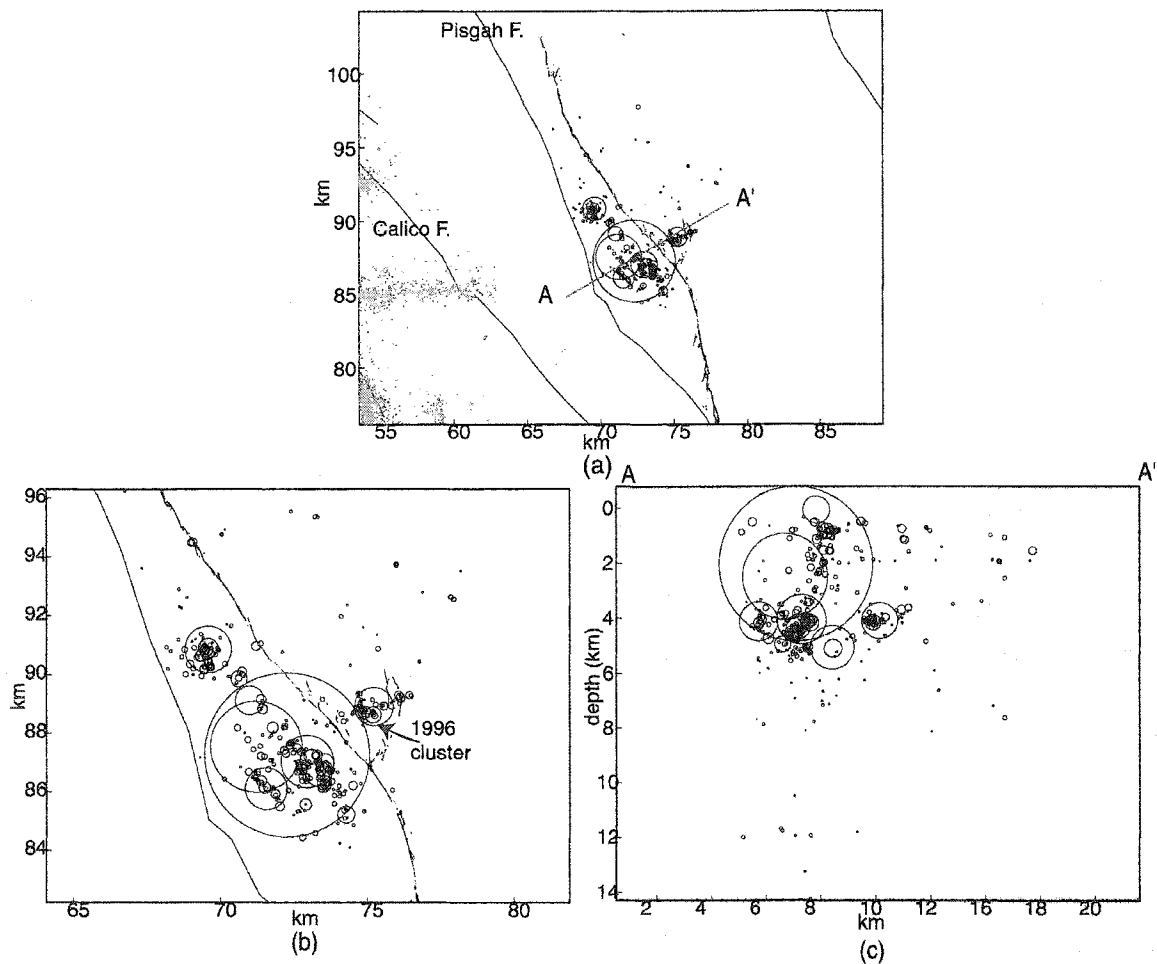


Figure 3.14: (a) Precise locations for the Pisgah earthquake cluster. Circles represent approximate magnitude and slip experience during those events, using a constant stress drop of 30 bars. (b) Close up of locations show that the Pisgah cluster corresponds very well to the Pisgah fault. (c) Cross section across strike shows the distance between the 1992 Pisgah events and a cluster of events in 1996 that were closer to the future hypocenter of the 1999 Hector Mine earthquake.

Prior to the Pisgah earthquake sequence, there was a single M 2.4 event triggered in the vicinity by the Joshua Tree earthquake. Before that, relocations of the 21 earthquakes from 1980-1992 in the Pisgah/Hector Mine area show a number of isolated earthquake clusters. The two most active ones occurred in 1988 and 1986. There are no earthquakes in the Pisgah area or the Hector Mine mainshock area before 1992.

POST-HECTOR MINE ACTIVITY

The most recent large earthquake in the Landers sequence was the October 16, 1999 Hector Mine earthquake. This M7.1 event occurred approximately 30 km northeast of the Landers rupture. In addition to triggering ~6000 earthquakes in the vicinity of the Hector Mine rupture, this event also triggered earthquakes in the Landers area. We plot the 1060 triggered post Hector Mine activity on Landers rupture in Figure 3.15. Most of the events occur on features that showed the most activity during the Landers aftershock sequence. Of these earthquakes, 539 occur in the Johnson Valley –Homestead Valley fault jog. Although Figure 3.15b shows that most of the aftershocks occur in a cluster a few months after the Hector Mine mainshock, the Hector Mine earthquake did not trigger any new features in the jog. Instead, the two planes north of the Landers fault remained active.

Other areas that show activity following the Hector Mine earthquake is the bifurcation at the end of the Johnson Valley fault. There are approximately 100 events in this area, and they form a diffuse swarm of activity. The other sequence that shows activity in this time period is along the Eureka Peak fault. Most of this seismicity is more likely related to a M 4.9 and M 4.1 earthquakes that occurred here in April 1999. The sequence of events on the north-trending feature previously activated in the Joshua Tree earthquake and turned off by the Landers earthquake is reactivated in 2001 with a swarm of events occurring late in the year.

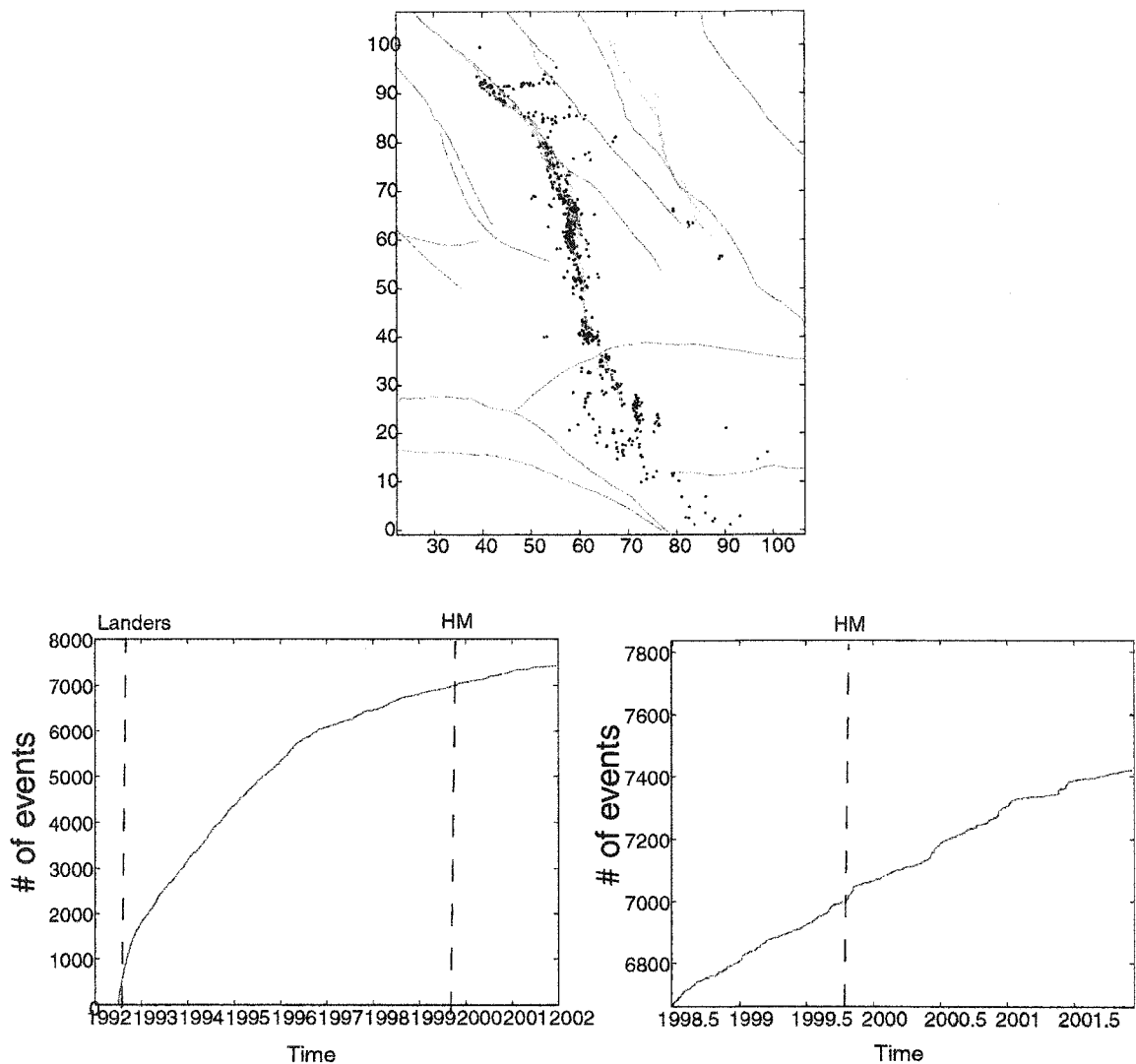


Figure 3.15: (a) Map view of seismicity along the Landers fault following the 1999 Hector Mine earthquake. Most activity falls within the Johnson Valley Homestead Valley Fault jog. (b) Cumulative number of events over time in the fault jog. There is no sizeable change related to the Hector Mine earthquake, as seen in (c) the close-up of this plot centered around the time of the Hector Mine earthquake.

AFTERSHOCK DEPTH AND THE TIME-DEPENDENCE OF THE SEISMIC-ASEISMIC ZONE

Changes in the maximum depth of earthquakes attest to the complexity of the crust in the Eastern California Seismic Zone. Looking at the spatial variation of depth in Southern California, *Nazareth and Hauksson (1998)* find that maximum depth of seismicity can significantly vary within a fault zone. Figure 3.2c shows that in the Landers sequence depth also varies strongly along the length of the fault, with a 10 km depth of the base of the seismogenic zone being a reasonable average.

Not only can the depth of the seismic zone change spatially, but it can also change over time. *Schaff et al., (2002)* note a change in maximum earthquake depth over time following the 1984 Morgan Hill earthquake sequence. They associate a 500 m increase in maximum depth immediately after the Morgan Hill mainshock to a temporary deepening of the seismic-aseismic transition due to increased strain rates from the mainshock. As in their study, our relocations also allow us to track changes in depth more precisely. In Figure 3.16, we plot earthquake depths over time for the entire Landers-Joshua Tree sequence and for various faults separately. It appears that immediately after a large event like the two mainshocks, aftershocks extend to greater depths than they do later in the sequence.

In Figure 3.16b, the depth change in the Joshua Tree area is plotted as density (number of earthquakes in each depth bin) over time for 3 years, encompassing the times of both large earthquakes. There is an increase in maximum depth in the area following the Joshua Tree earthquake, and the density of events at a depth of 8 km also increases after the Landers earthquake. These later deep earthquakes all occur in a single cluster in the southern end of the Joshua Tree earthquake, near the San Andreas Fault. Although the density quickly diminished at greater depths following Joshua and in some cases, there are events later in the sequence that are deeper, density of events at depth over time show that there are far more events at greater depth

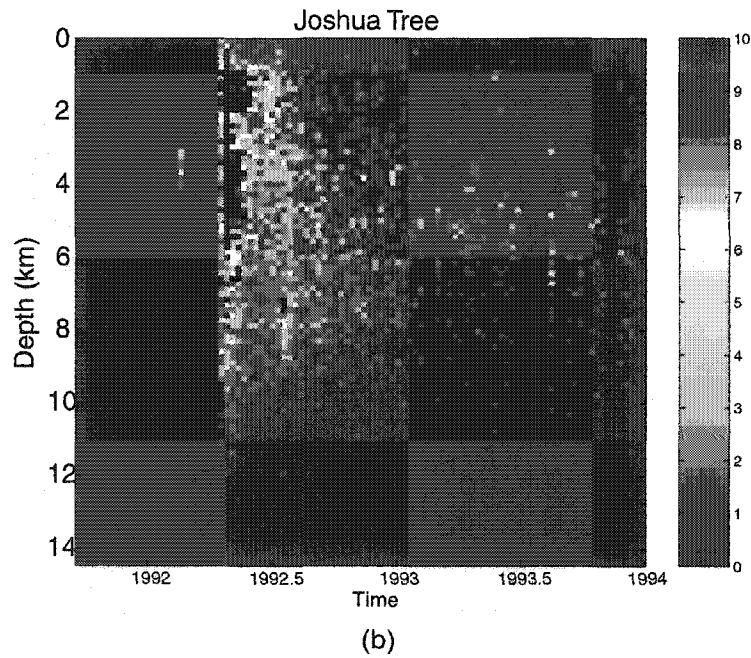
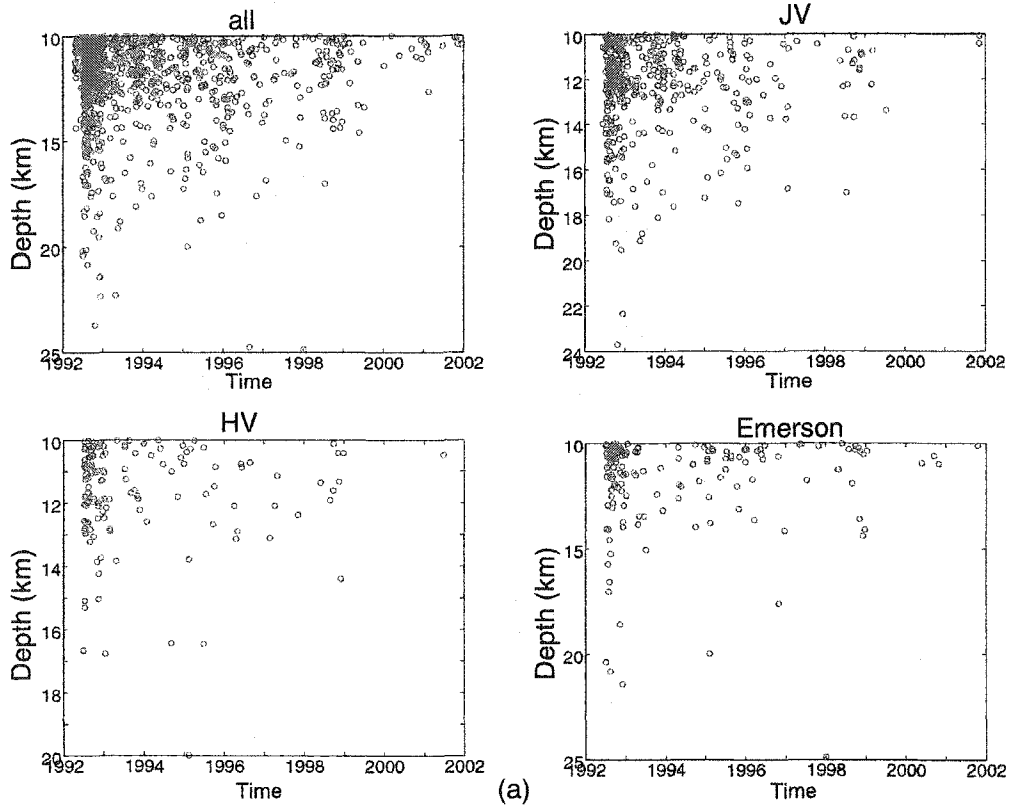


Figure 3.16 (a) depth of events deeper than 10kms over time for various faults along the Landers rupture. (b) Density of events in depth over time for the Joshua Tree earthquake area. There is an increase in the density of events after the Landers earthquake but the maximum depth of events does not reach the same level as after the Joshua Tree mainshock

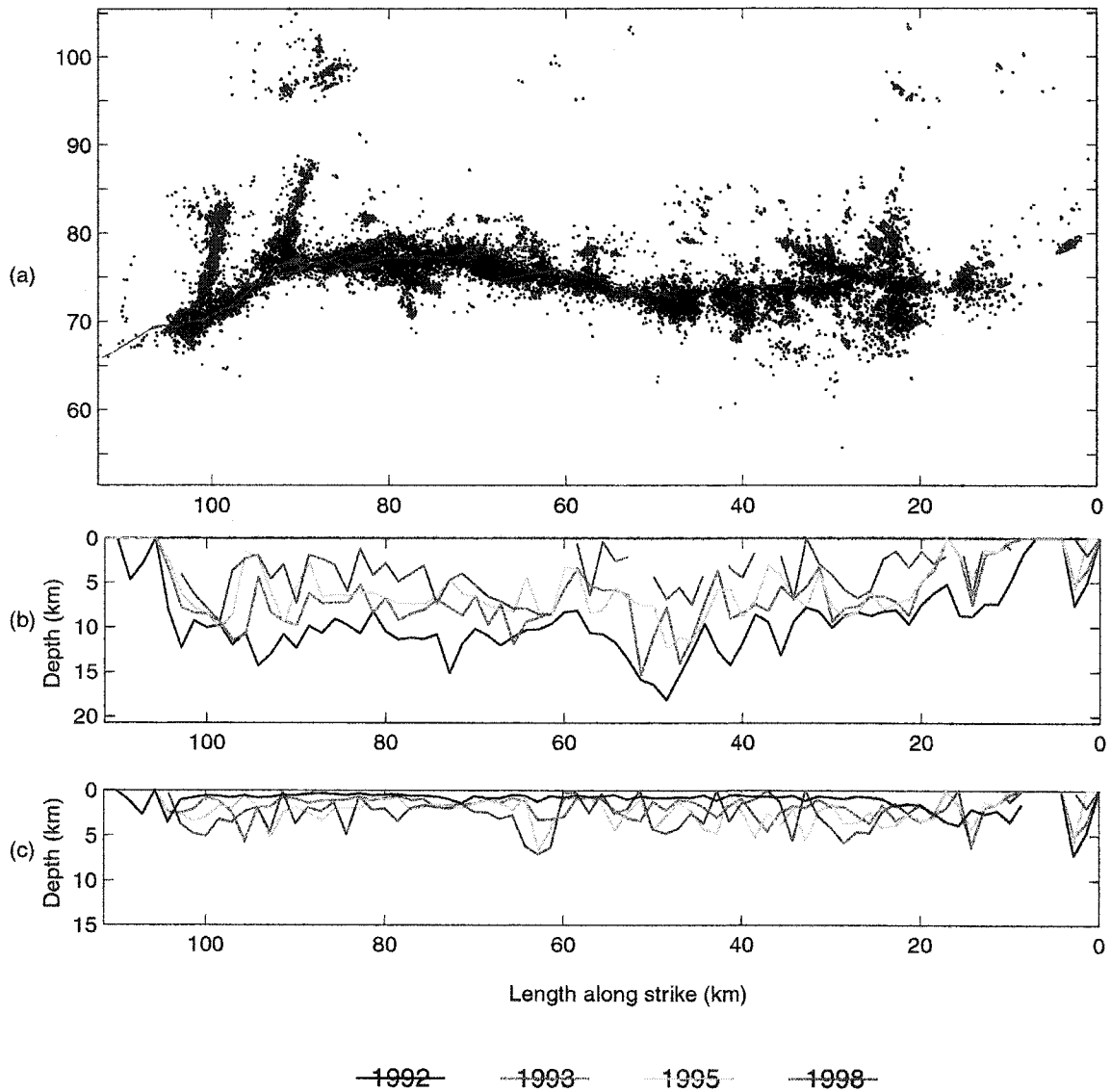


Figure 3.17 (a) Reference map of the Landers sequence rotated to correspond to the overall strike of the Landers mainshock rupture. (b) Maximum depth of events for 4 times, 1992, 1993, 1995, and 1998, each line represents 4 months of activity. The 1992 line contains events starting at the Landers mainshock, or 1992.5. (c) Minimum depth over the same time periods

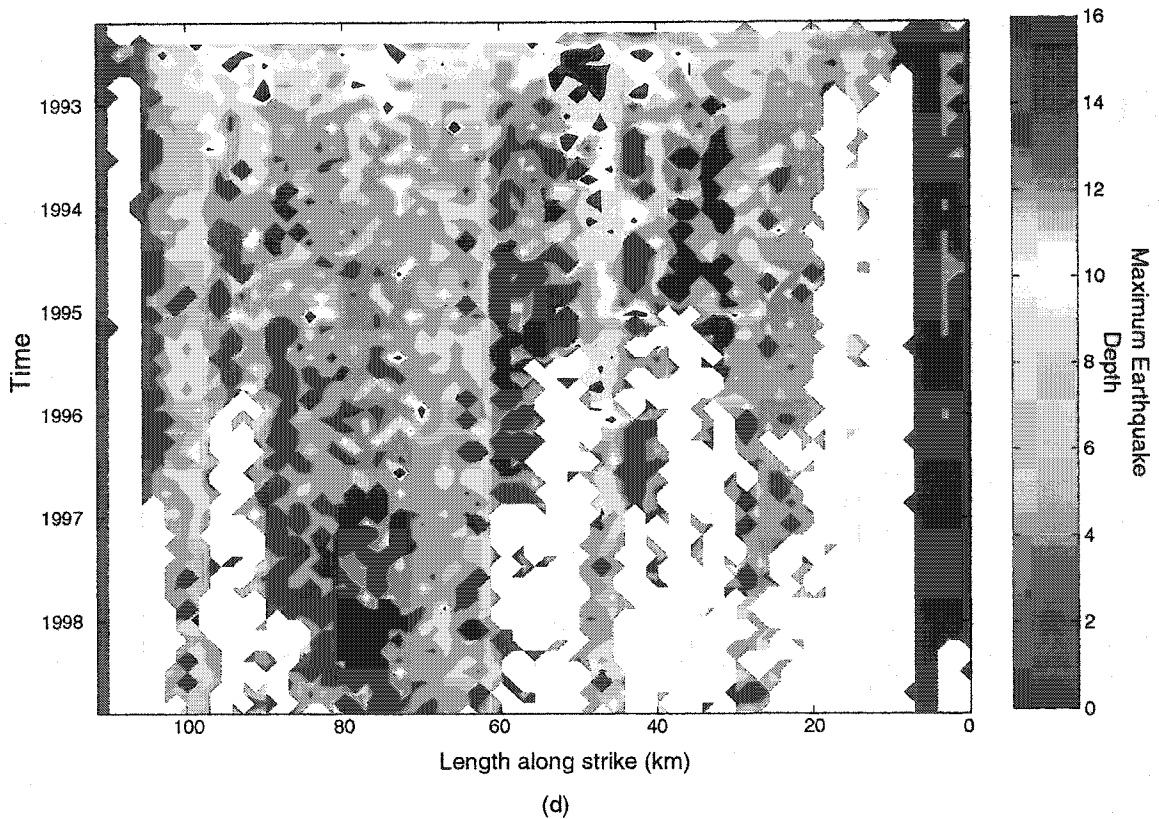


Figure 3.17 cont: (d) Maximum depth over time along the length of the Landers rupture using a finer grid than 3.17(b). Color represents maximum depth. White areas represent no data.

early in the sequence and only isolated events at later time. This suggests that there is increase in the seismic zone immediately following the Joshua Tree earthquake, and a reactivation of a deep, 8-km, structure following the Landers earthquake.

The depth dependence of the Landers aftershocks is much clearer. We define the maximum depth of earthquakes as the depth as which 95% of seismicity is represented in the bin. To determine this depth, we divide the earthquakes in a selected area into 100 bins by depth. The value of the shallowest bin that is deeper than 95% of the seismicity is taken as the maximum depth for that area. In this approach, the actual percentage of the events accounted for in the maximum depth may vary from 95% to 100% of the seismicity. We use a 20 earthquake minimum before calculating maximum depth in a bin. This prevents deep outliers from affecting

the maximum depth measurement. It is still possible to see a clear change in maximum depth of seismicity over time for many segments of the Landers sequence.

In Figure 3.17b, we have divided the length of the sequence into 2km sections and calculated maximum depth in each section for 4-month time intervals. Immediately after the Landers mainshock, the maximum depth ranges from 5 km to 17 km, with an average of 11 km. The deepest events occur at the end of the Johnson Valley fault; this is an area of complex faulting and a dense concentration of earthquakes. By 1993 the maximum depth of earthquakes had shallowed to an average of 7 km, and by 1998 the maximum depth is reduced to 5 km. We note that the scale of the changes is much larger in extent and in the range of depth variation than found by *Schaff et al.*, (2002). The effect they observe was limited to several km of the total mainshock rupture in the Morgan Hill earthquake. In contrast, we find it extends over nearly the entire length of the Landers rupture. *Schaff et al.*, (2002) found a change in depth of perhaps 1 km; whereas, we find a change of closer to 5 km. The difference may be attributable to the combination of much greater mainshock slip in the Landers earthquake and much lower background slip rate on the faults that ruptured in them relative to the Morgan Hill earthquake and the Calaveras fault.

We are also able to track changes in minimum depth over time. Similar to the changes in maximum depth, the minimum depth changes slightly, as shown in Figure 3.17c. In 1992 the average minimum depth is 1 km. In 1993 and 1995 this depth has increased to 2 km and by 1998, the average minimum depth is near 4 km. The deepest minimum depth in later times occurs in the northern end of the Johnson Valley fault near a left-lateral strike slip feature at the end of the fault offset. By 1995 the minimum depth is near 8 km, the depth of the strike slip feature. Over time, the seismogenic zone narrows to a few kilometers between 4 and 8 km depth.

Schaff et al., (2002) associated this change in earthquake depth over time as a change in the Brittle-Ductile transition due to strain rate changes from the mainshock. Studies of the velocity dependent behavior of serpentine (*Reinen et al.*, 1992) suggest that high slip rates

coming from a mainshock could induce velocity weakening behavior and hence unstable slip in the material. As the additional velocity from the mainshock slip dies away the more characteristic velocity strengthening behavior, which would invoke fault creep, would ensue. Serpentine, however, has been found mostly in weak faults like the San Andreas and in oceanic transform faults. Subsequent studies have shown that the same behavior is possible in bare granite in laboratory experiments when normal stress remains high (*Kilgore et al.*, 1993; *Beeler et al.*, 1996, *Blanpied et al.*, 1998). The velocity-weakening behavior gradually reduces over time. Granite gouge, however, has been shown to display velocity-strengthening behavior with increased slip rate (*Marone et al.*, 1990). This velocity weakening behavior could account for the temporary increase in seismic activity at depth following the Landers mainshock, even though aftershocks do not occur in areas of the greatest mainshock slip (Figure 3.4), most aftershocks occur in areas of some mainshock slip.

Also, as shown in Figure 3.17c, we plot the minimum depth of earthquakes over the same time periods as the maximum depth. We see scant evidence for an immediate post-seismic deepening of shallow earthquakes. The same mechanism, however, could be used to explain this behavior. *Blanpied et al.*, (1998) note that lower levels of normal stress can reduce the magnitude of the velocity-weakening behavior. Thus, producing a less noticeable change in depths.

CONCLUSION

Using waveform cross-correlation techniques on earthquakes in a sparsely instrumented region like the ECSZ provides valuable information for obtaining precise earthquake locations in the area. We use relative arrival time information and the double difference relocation method to determine locations for nearly 38,000 earthquakes in the 1992 Landers-Joshua Tree earthquake sequence. From these relocations we are able to discern a number of features previously obscured by location error.

For instance, we are able to clarify nodal plane ambiguity in certain focal mechanisms in the Joshua Tree earthquake. We find a number of planes conjugate to the strike of the Joshua Tree mainshock plane. In the Landers sequence, we find that there is considerable fault complexity even at depth along the mainshock fault planes where the surface faulting is relatively simple. Many of the features at depth are represented in the surface trace of the rupture, but there are features that are only expressed at depth, such as the structures active in the Johnson Valley-Homestead Valley Fault jog, and a set of *en echelon* faults at depth along the Landers mainshock rupture on the Johnson Valley Fault.

There is significant off fault seismicity near the Calico Fault and the Pisgah Fault to the north and east of the Landers mainshock. Small, EW trending, left-lateral strike slip fractures lead up to a NW-trending feature on the Calico Fault. *Hauksson et al.* (1993) suggests that this may be due to the rupture front trying to jump to the Calico Fault, or the result of strains related to the change in fault angle on the Camp Rock –Emerson Faults.

We find that aftershock activity on well-developed faults, like the Emerson Fault, defines a 0.5-1km fault, suggesting that strain is accommodated in a narrow zone. Other areas, like the Joshua Tree faults, have a wide fault zone, on the order of a 5-10 km. The faults south of the Pinto Mountain Fault may be immature faults cutting through granite, accounting for the variety of fault orientations and the need for strain to be accommodated in a broad zone.

Finally, the precise locations allow us to map the change in earthquake depth over time for the sequence. As *Schaff et al.*, (2002) note for the Morgan Hill earthquake, we notice a decrease in the maximum earthquake depth along the sequence over time. This would suggest that the seismic-aseismic transition temporarily increases in depth following a large earthquake. This may be due to temporary velocity weakening in the fault zone, similar to the behavior found in samples of granite and serpentine in the laboratory. Such velocity weakening at depth may be related to high slip rates caused by the mainshock. Although there is an increase in the depth of the seismic zone in the Joshua Tree area following the 1992 Joshua Tree earthquake, the Landers

earthquake does not produce a significant change in the seismogenic zone in the Joshua Tree area, except for activating a one deep structure in the southern end of the Joshua Tree sequence. The Landers earthquake, however, did not affect aftershock rates in most of the Joshua Tree sequence, thus the lack of deep events following the Landers earthquake may be expected.

CHAPTER 4: THE 1992 BIG BEAR EARTHQUAKE: EVIDENCE FOR FAULTING ON IMMATURE FAULTS

This chapter is being prepared for publication in Geophysical Research Letters with co-author Gregory C. Beroza.

ABSTRACT

We examine the aftershock sequence of the 1992 M 6.5 Big Bear Earthquake, the largest aftershock of the 1992 M 7.3 Landers earthquake. We use waveform cross correlation to obtain precise relative arrival time information, and the double difference earthquake location method to reduce location errors. This allows us to discern more clearly the complicated network of fault planes active in the Big Bear sequence. We find that several northeast and northwest trending planes, as well as sets conjugate fault planes, are active during the Big Bear sequence. The limited length of these active faults and the apparent coefficient of friction of 0.6 in the region both suggest that these faults are not well developed, and that if the fault structure of the Mojave block extends into the San Bernardino block, these mature faults are not active during the sequence. Aftershocks in the Big Bear sequence extend to depths of 15 km, and their depths appear to shallow with time; however, this trend may not be significant given the error in earthquake depths.

INTRODUCTION

The June 28, 1992, M 6.5 Big Bear earthquake was the largest aftershock of the June 28, 1992 Landers earthquake. Although interesting in its own right, the event has received remarkably little attention. The Big Bear earthquake occurred in the San Bernardino Mountain region, bounded to the north by the North Frontal Fault Zone (NFFZ) and to the south by the strike-slip San Andreas, and the San Gorgonio and Banning thrust faults. There was no surface

rupture observed in the earthquake and there is no surface expression of a fault with the orientation and location of the primary mainshock rupture. The Big Bear earthquake was followed by over 13,000 aftershocks from 1992 to 2002. While the mainshock did not rupture the surface, many of the aftershocks, as well as focal mechanism determinations of the mainshock location suggest left-lateral strike slip on a NE trending plane during the mainshock (*Hauksson et al.*, 1993). Aftershock activity is widespread, however, and involves planes with various orientations and mechanisms.

Errors in earthquake locations obscure many of the small-scale features of the Big Bear sequence. We use a combination of double difference location and cross correlation derived relative arrival time measurements to improve locations and examine the detailed structure of faults that were active during both the Landers and Big Bear earthquakes. We are able to locate 11,328 of the aftershocks. The mainshock, however, cannot be precisely located due to the combination of a foreshock immediately preceding it and the rapid clipping of the mainshock waveform.

We find planes defined by the relocated seismicity that correspond to the mainshock's rupture planes. Although preliminary investigations of the mainshock fault planes suggest a single NE trending plane (*Hauksson et al.*, 1993; *Kanamori et al.*, 1992), subsequent studies suggest two conjugate nodal planes may also have ruptured during the mainshock (*Jones and Hough*, 1995; *Jones et al.*, 1993). Our relocations of aftershocks show activity near the mainshock occurs on both a NE trending plane and a conjugate NW trending plane consistent with these mainshock planes.

Earthquakes in the Big Bear aftershock sequence occur predominantly on a variety of small NW or NE trending planes. With the combination of focal mechanisms and precise locations that allow us to resolve the fault plane/nodal plane ambiguity, we can constrain the stress direction and coefficient of friction consistent with the observed pattern of active faulting.

EARTHQUAKE RELOCATION

The 1992 M 6.1 Big Bear earthquake occurred at 15:05 GMT on June 28, 1992, three hours after the M 7.3 Landers mainshock. Because it occurred within a fault length of and immediately after the Landers earthquake, the Big Bear earthquake is considered an aftershock of Landers (*Sieh et al*, 1993). In this paper, however, we will treat the Big Bear earthquake as a mainshock with its own set of foreshocks and aftershocks. Figure 4.1 shows the relationship of the Big Bear event and its aftershocks to the Landers rupture, as well as major faults in the area. The event occurred 30-40 km away from the Landers rupture and had approximately 13,000 aftershocks $M > 1.5$ from 1992-2002. Most of the events fall on a Northeast trending structure defined as part of the mainshock rupture (*Hauksson et al.*, 1993). Other events seem to trend Northwest in a conjugate plane that may also have slipped in the mainshock (*Jones and Hough*, 1995). Catalog locations errors, on the order of 1km horizontally and 2 km in depth, make it difficult to clearly discern the fine structure of faults activated by the Landers and Big Bear events. For that reason we use waveform cross correlation and double difference relocation to improve the aftershock locations.

We examine seismograms recorded at 350 stations from the TriNet/SCSN network. The station distribution for the Big Bear events is more favorable than for other events in the Joshua Tree-Landers-Hector Mine sequence, with good azimuthal coverage, due to the proximity of Big Bear to the closely monitored San Andreas fault and the vulnerable conurbation of Los Angeles. While Hector Mine and the northern area of the Landers rupture have only a few stations to the east, there are more than 20 stations to the east of the Big Bear sequence. This makes it possible to obtain better longitudinal control on event locations here than for other events in other Landers sequence.

If all 13,000 events were correlated with each other, there would be over 84 billion correlations at each station. We limit the event pairs by considering only correlating only events

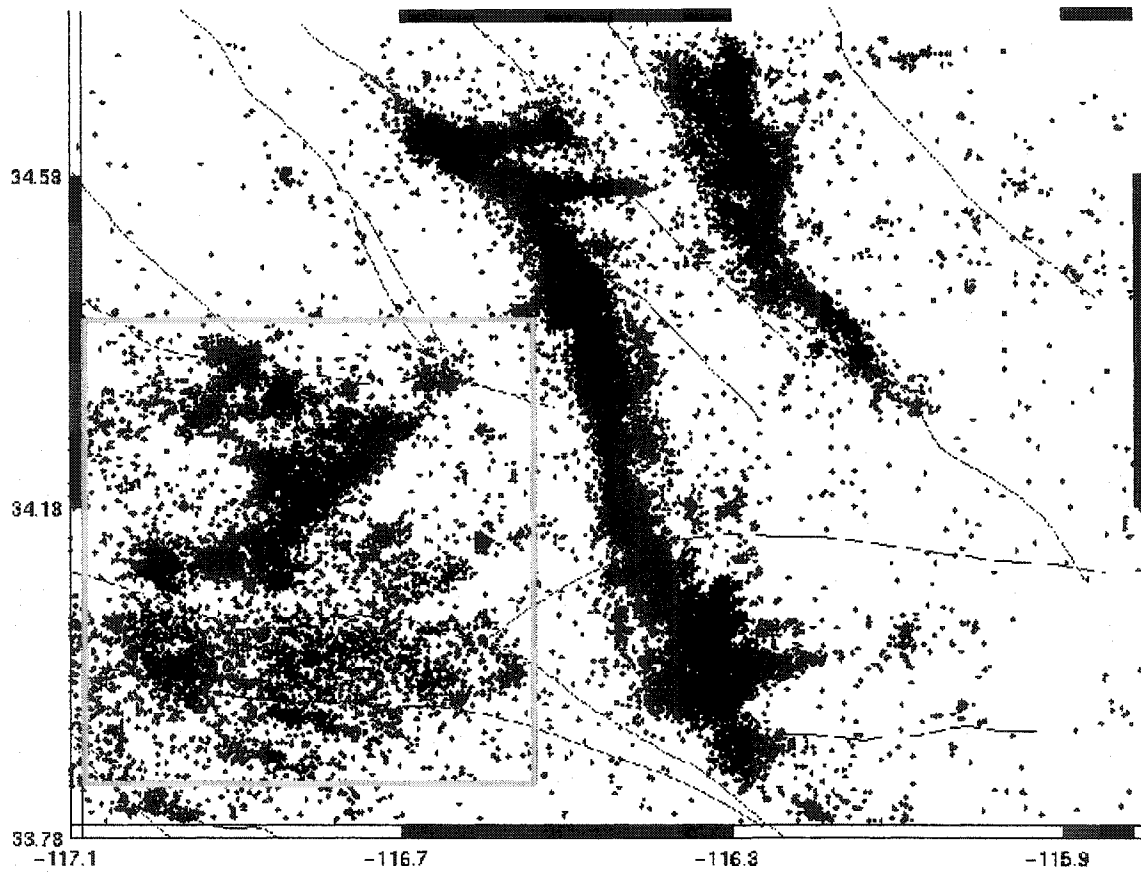


Figure 4.1: Map view of the 1992 Landers – Big Bear earthquakes and aftershocks. Major faults are shown in black. Boxed area includes the Big Bear sequence.

within 4 km. from each other horizontally. This limits the number of correlation measurements to $\sim 4,500,000$ event pairs for both P and S waves. We use a time domain correlation method that *Schaff et al.*, (2003) have shown to be a robust method for obtaining relative arrival times, but use both time and frequency domain correlation techniques to define two different measures of the quality of the arrival time measurements that we make. Each seismogram is bandpass filtered using a 2nd order zero-phase Butterworth filter between 1 and 15 Hz. before correlation to eliminate noise while retaining most of the frequency content of the waveforms. All waveforms at a particular station are cross-correlated twice over a window centered on a preliminary phase

pick, first using a 256-sample window and then using a 128-sample window with the original 0.01-sec sampling rate.

In datasets of repeating or closely spaced events on the Calaveras fault, *Schaff et al.*, (2002) used arrival time measurements with correlation coefficients greater than 70% because these observations were found to provide data for relocation that were more precise than observations in the catalog, based on an analysis of post-fit residuals. In this study, we use a the same correlation coefficient cutoff of 70%.; this threshold reduces the possibility of introducing outliers, while still retaining enough data to perform the relocation.

The mainshock was preceded by a M4.3 event, occurring just 40 seconds before the mainshock. This foreshock clipped nearby stations and obscured the first arrival of the mainshock (Figure 4.2). Coupled with the difficulty of correlating large magnitude events with smaller events, this made relocating the mainshock difficult. We are able to correlate the mainshock with only one other event, which is not enough to obtain a reliable location. Even using a reference event technique described in the Hector Mine chapter will not help because the events correlate above the cutoff value at only two stations, while at least 4 are needed for accurate relocation. But we may find a location for the mainshock using catalog phase arrival time information. We obtain 2,330 relative P-wave arrival times between the mainshock and aftershocks $M > 4$. We choose only arrival times at stations that are recorded with high precision, 0 or 1 on the quality scale. Using phase data means the location of the mainshock will not be as precise as those relocated using correlation information.

Our cross correlation analysis produces 3,110,267 P-wave and 1,127,231 S-wave relative arrival time measurements for 461,834 event pairs. We have enough event pairs to attempt to relocate 11,478 from a total of 13,363 events from 1992 to 2002 in the Big Bear area between the San Andreas Fault and the North Frontal Fault Zone.

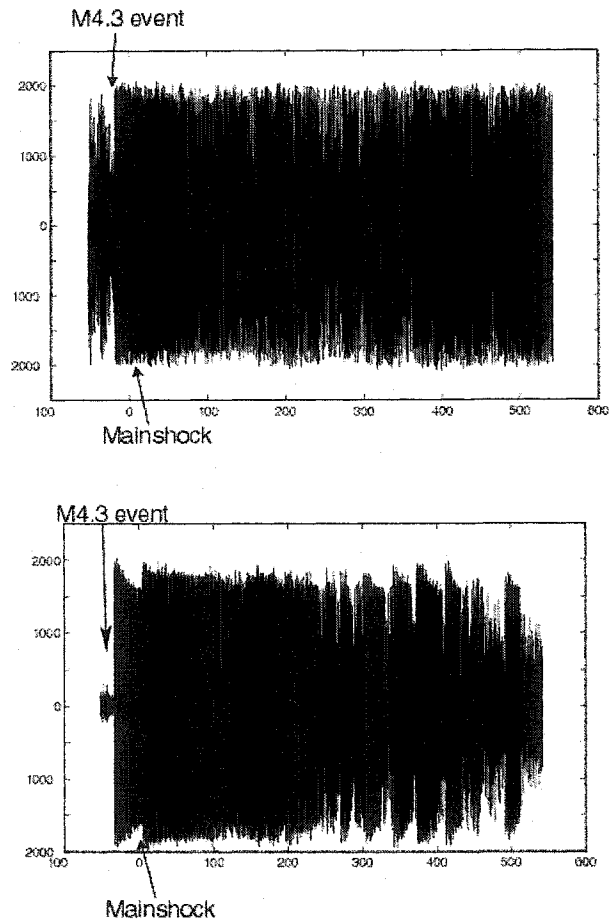


Figure 4.2: Seismograms at stations GRP and LUC of the Big Bear mainshock. The arrival time is difficult to pick because of the M 4.3 event that precedes the mainshock.

The double-difference relocation method that we use in this study allows us to use relative arrival time information and so reduce location error due to unmodeled velocity variations (*Waldhauser and Ellsworth, 2000*). We use a basic 1-d velocity model for the region from *Wald et al., (1995)*. During relocation 12% of the data is culled through residual reweighting and outlier detection. This processing renders 150 of the selected events un-located. Thus, after relocation we have improved locations for 11,328 events, ~ 85% of the events in the area. Not surprisingly, after relocation many aftershocks are more tightly clustered onto distinct planes. Location errors estimated from the relocation procedure suggest that the locations are

accurate to within a tens of meters horizontally and 50 to 100 m vertically. In our study of the Hector Mine foreshock sequence, we found that these error estimates understated the true error, but those events were low *snr* events recorded by a sparse network. We expect that the estimated errors for the Big Bear region should be more representative of the true errors, as found for the Hayward fault by *Waldhauser and Ellsworth (2000)*.

AFTERSHOCK GEOMETRY

Our relocation of earthquakes in the Big Bear sequence limns many structures and planes that were previously obscured by location errors. The relocations, with focal mechanisms for the largest events, are shown in map view in Figure 4.3. A large fraction, ~4500 of the Big Bear aftershocks fall on an approximately 30 km long structure trending 50° NE with an average width of ~3 km. This plane is consistent with the mainshock focal mechanism of the initial rupture plane indicating left-lateral faulting (*Hauksson et al., 1993*). To the south of this structure, between the Mill Creek and San Andreas faults, there is an apparent gap in the seismicity. Activity resumes between the San Andreas and the San Geronio Pass thrust fault, but events are deeper and lack the sets of NW and NE trending structures seen in the San Bernardino block. To the north the seismicity is bounded by the North Frontal Fault Zone (NFFZ), the thrust fault that marks the northern border of the San Bernardino Mountains.

Figure 4.4 shows cross sections along different sections of the seismicity, similar to the cross sections illustrated in *Hauksson et al., (1993)*. Cross sections AA' and BB' show longitudinal cross sections of aftershocks that occur on or near the mainshock fault planes; EE' crosses the mainshock fault. Cross section AA' trends northeast along the strike of the main Big Bear rupture. Earthquake depths range consistently from 0 to 12 km along the entire length of this structure. The sequence is not confined to a single well-defined plane, rather it is composed of many complex structures of varying orientations. Aftershocks clearly define a conjugate plane

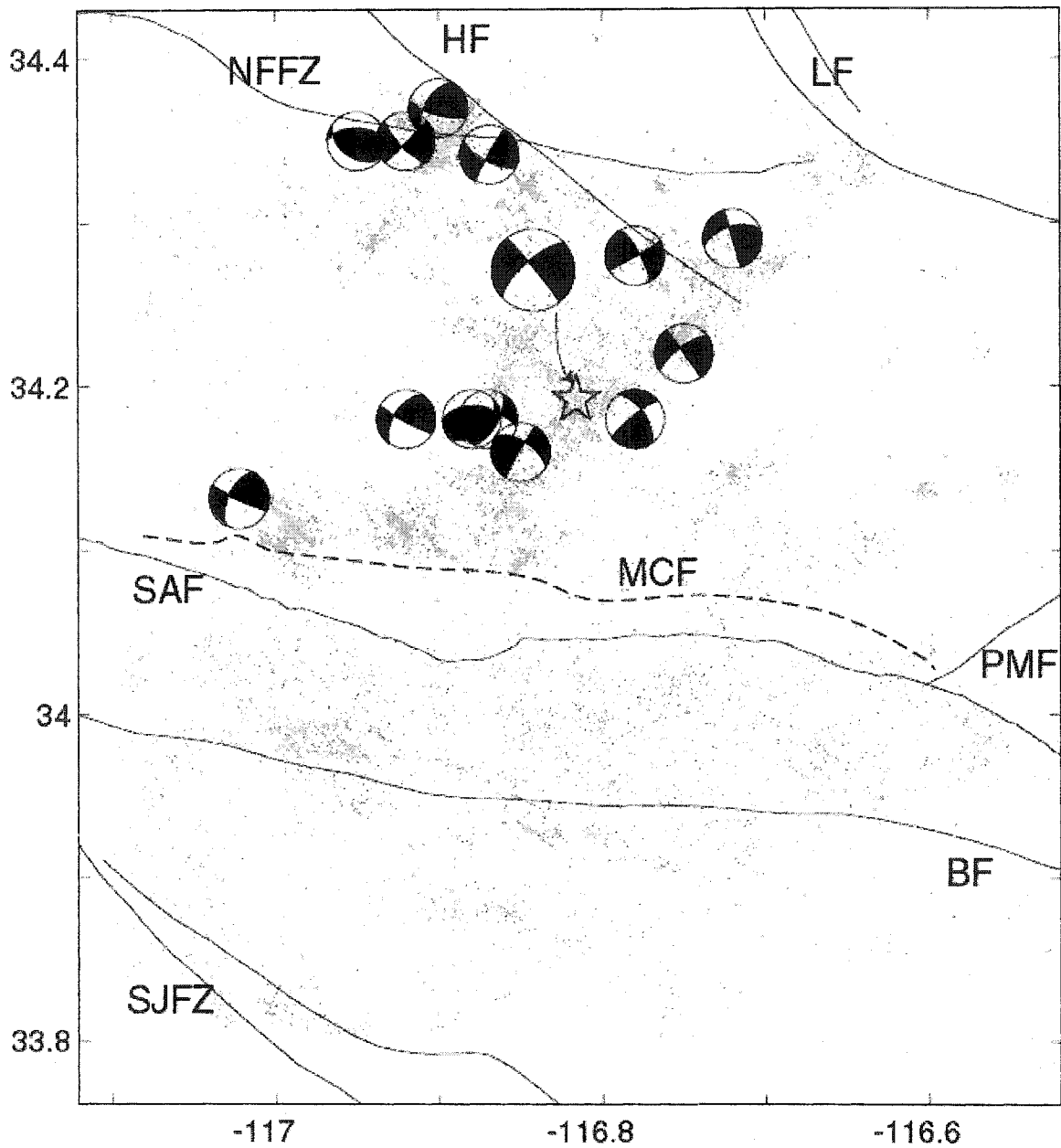


Figure 4.3: Map view of the Big Bear sequence relocations. Multiple conjugate planes are apparent through the seismicity. Focal mechanisms correspond to large aftershocks immediately after the Big Bear earthquake (*Hauksson et al., 1993*). Black lines indicate major faults. SJFZ: San Jacinto Fault Zone, SAF: San Andreas Fault, SGF: San Geronio Fault, BF: Banning Fault, MCF: Mill Creek Fault, dashed to show inferred orientation, PMF: Pinto Mountain Fault, HF: Helendale Fault, NFFZ: North Frontal Fault Zone, LF: Lenwood Fault.

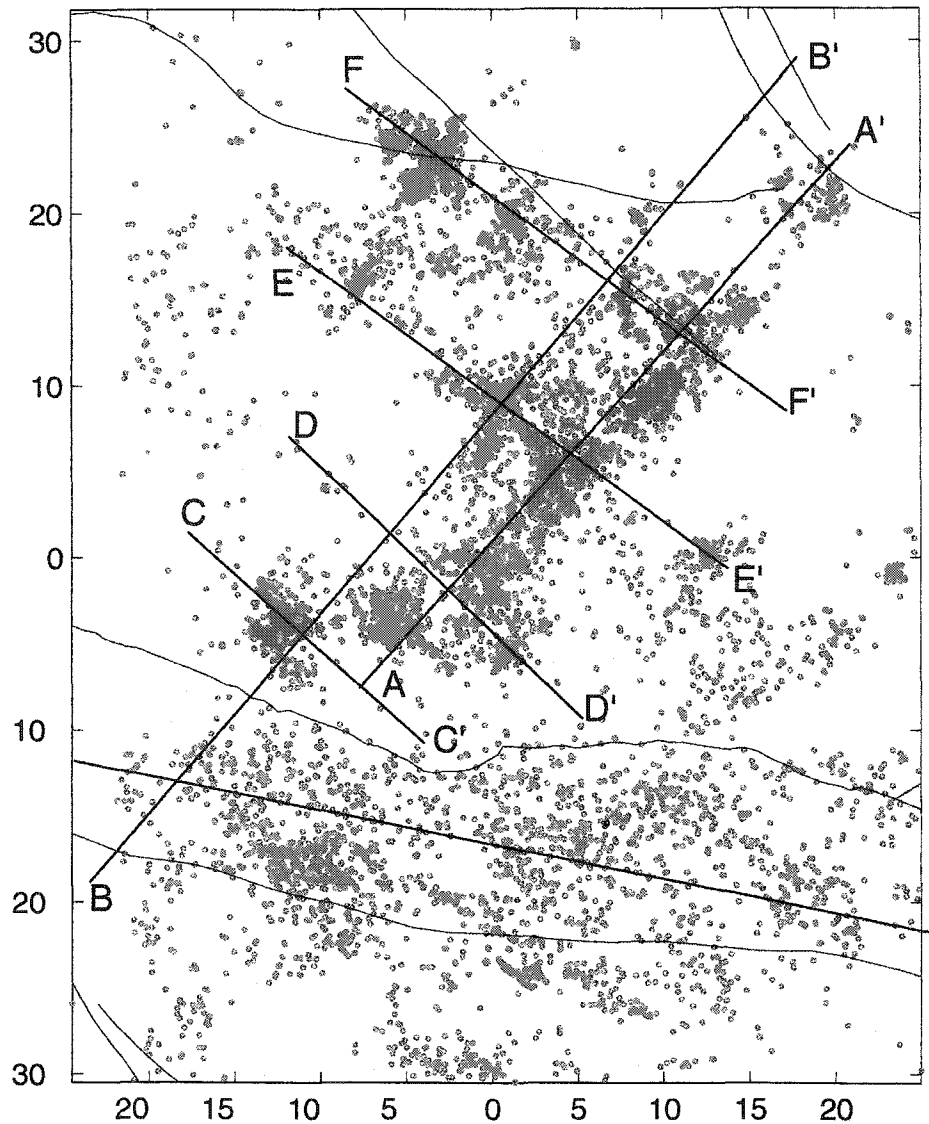


Figure 4.4a: (a) map view of aftershocks and cross section locations. The star represents the mainshock location. Major faults marked as in Figure 3. Star is the mainshock location. Axes in km.

matching the direction of the NW trending rupture plane *Jones and Hough (1995)* suggest was active during the mainshock and may have accommodated most of the mainshock moment release. Another plane, approximately 4 km to the NW of the major mainshock rupture, crosscuts the NW trending plane; this plane, seen in cross-section BB' and EE' is shallower than the mainshock fault planes.

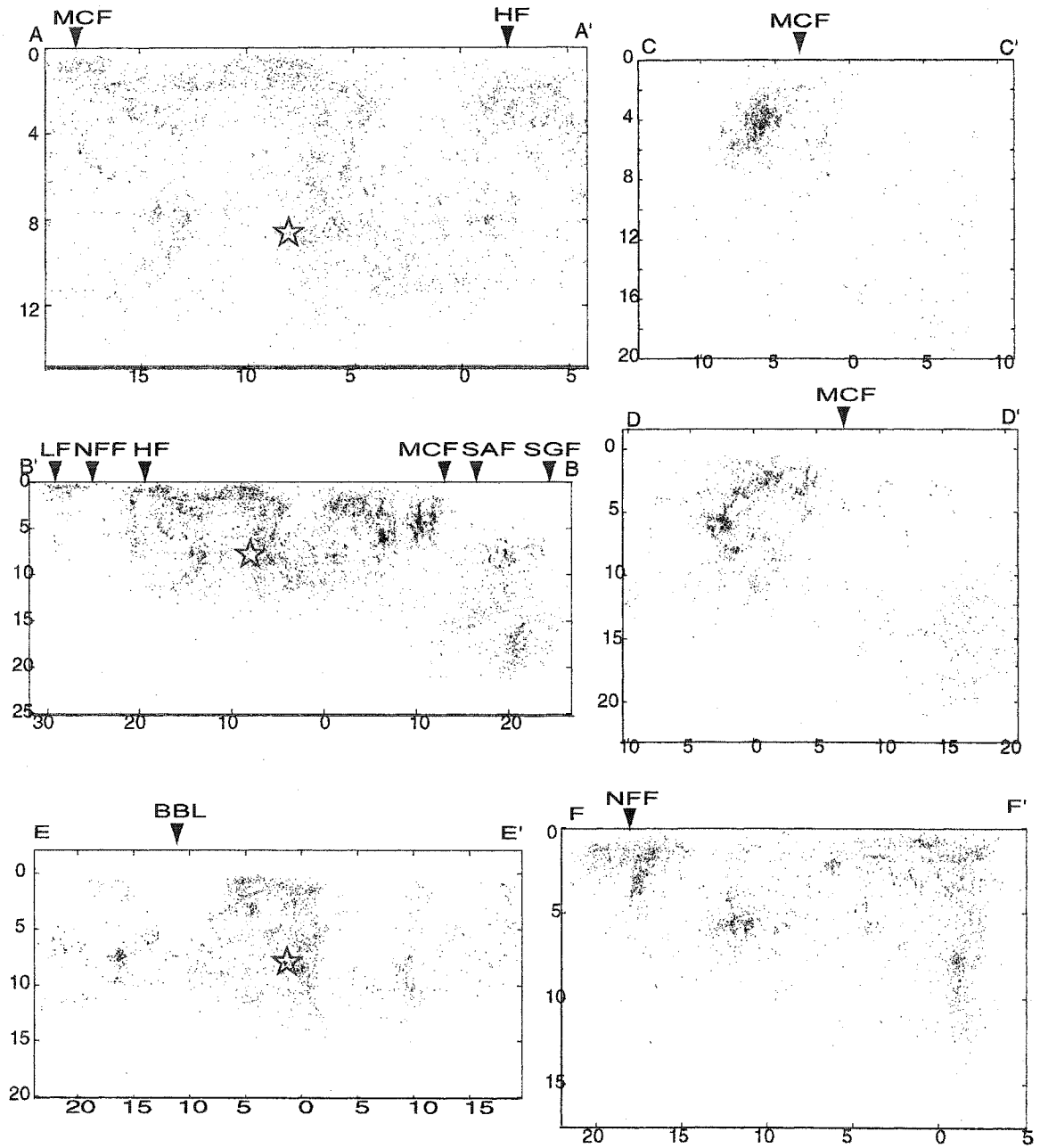


Figure 4.4b: (b) cross sections of various trends across the entire Big Bear sequence. Arrows and fault abbreviations, as in Figure 3, mark locations of major faults. Red star is the mainshock hypocenter.

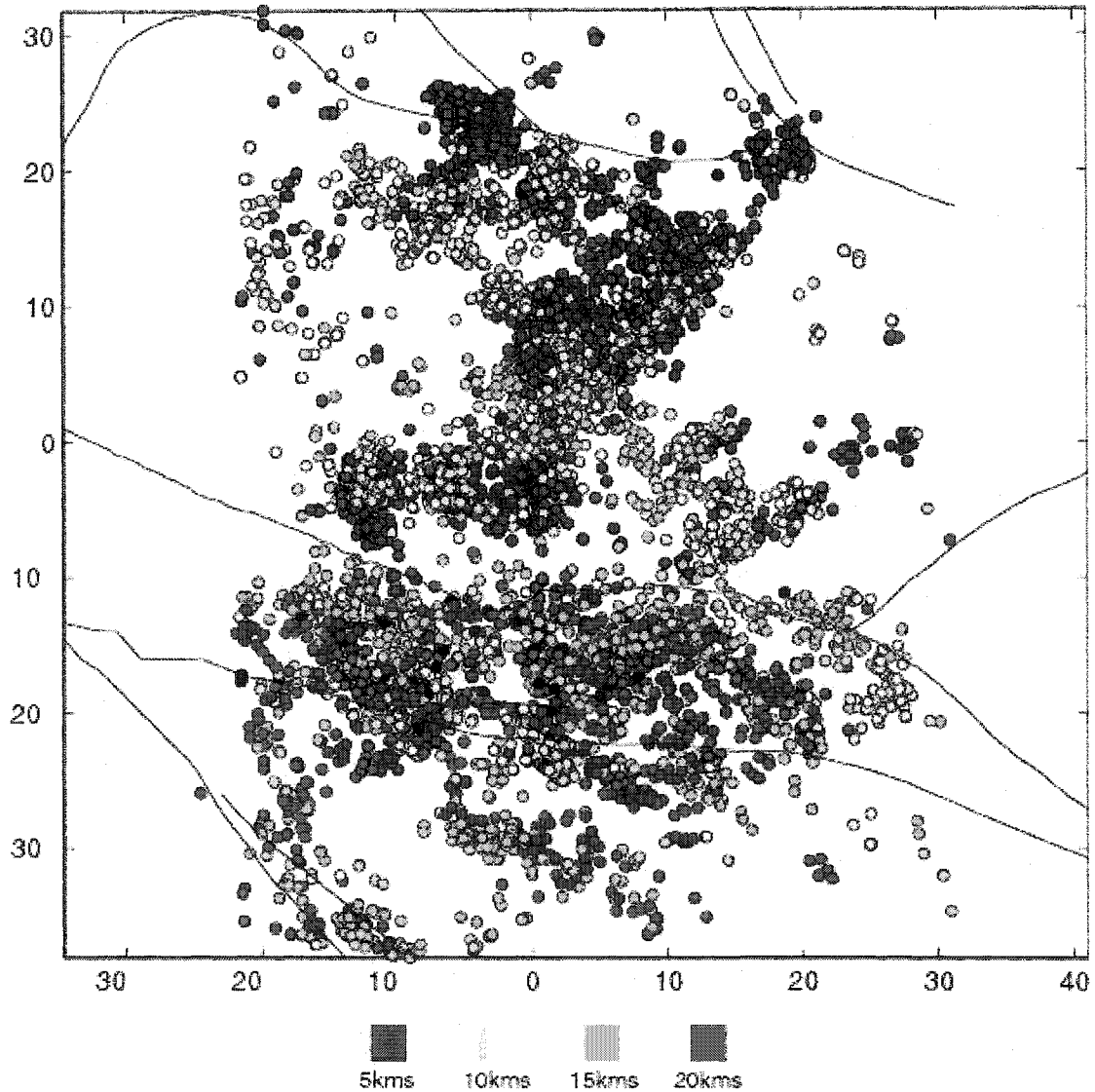


Figure 4.5: Earthquake locations in the Big Bear area. Gray lines are major faults in the area. Color represents depth of events in 5 intervals. Red:0-5 km, Yellow: 5-10 km, Green: 10-15kms, Blue: 15-20 km. Black events are >20kms.

Also evident in the cross sections, and in Figure 4.5 which plots earthquakes according to depth, is the shallower depth of events near the boundaries of the San Bernardino block, with the deepest events occurring near the Big Bear rupture. This decrease in earthquake depth is seen both near the NFFZ and the Mill Creek fault to the south. *Hauksson et al.*, (1993) suggest a step in the crustal structure at depth evidenced by deep activity to the south in cross section FF', which

corresponds to the mainshock rupture, and shallow activity near the NFFZ. Since 1993, another cluster of events falls within that cross section between the previous two clusters both horizontally and in depth, suggesting a less clear step in structure but still some structural control on deeper earthquakes near the middle of the San Bernardino Mountains.

The earthquakes we relocated also include a number of events between the San Andreas and the San Geronimo and Banning faults. Cross section BB' shows the sharp contrast between the depths of events in the Big Bear sequence and those near the San Andreas. Earthquakes south of the San Andreas Fault have depths between 5 and 30 km, and though their northern boundary is very clearly defined by the San Andreas Fault, the events do not delineate any specific planes that correspond to the major faults in the region. This is unlike the events north of the San Andreas, which predominantly cluster into small well-defined planes.

CONJUGATE PLANES

Although not common, conjugate faulting has been identified for a number of earthquakes, including the Chalfant sequence (*Smith and Priestley, 1988*) and Superstition Hills (*Hudnut et al., 1989*), as well as the Big Bear event (*Jones et al., 1993; Jones and Hough, 1995*). In addition to the conjugate NW and NE trending planes of the Big Bear mainshock, there are a variety of conjugate and nodal planes in other parts of the Big Bear sequence. Figure 4.6a shows a number of well-defined faults delineated by the aftershock activity. These planes trend either to the NW 35-60°, or to the NE 40-50°. Fault orientations that are readily measured are listed in Table 4.1. The planes, however, excluding those involved in the mainshock rupture, are small, no longer than 5 km, and many do not correspond to mapped faults.

Particularly well defined are two sets of NW trending planes, the Yucaipa cluster (*Hauksson et al., 1993*), to the south of the Big Bear rupture. Not only do these structures mark the terminus of the Big Bear rupture and the Big Bear aftershock sequence, there is virtually no activity between the Yucaipa cluster and the San Andreas Fault. Although it is roughly parallel to

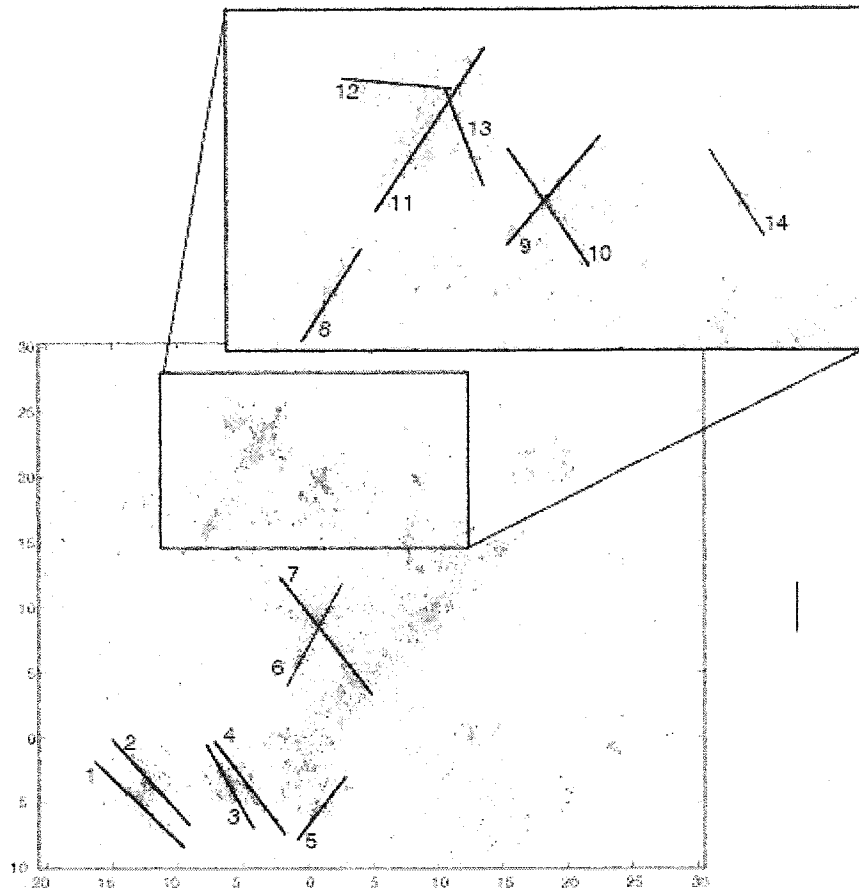


Figure 4.6: Map of conjugate planes with orientations drawn in with black lines. Numbers relate faults to their orientations in Table 4.1. Scale is in kilometers.

the San Andreas Fault, the NW trend does not lie on that fault (*Hauksson et al., 1993; Matti et al., 1992*). To the east of the Yucaipa structure is a NE trending sequence, striking N48°E; although the planes are very close and in conjugate directions, they do not abut.

Several NW and NE trending structures do crosscut each other, as shown in Figure 4.6. The most prominent feature is a cluster near the NFFZ activated in late 1992 with two large events, a NE trending M5.3 event and a M 5.1 thrust event that appears to occur on the NFFZ. The angle between the two planes is approximately 80°. There is also a NE trending structure, activated after the 1999 Hector Mine event, which seems to be an extension of the NFFZ cluster.

| | Dip Direction | Dip | Rake |
|----|---------------|-----|------|
| 1 | 46 | 80 | 180 |
| 2 | 47 | 80 | 180 |
| 3 | 53 | 80 | 180 |
| 4 | 35 | 60 | 180 |
| 5 | 142 | 90 | -180 |
| 6 | 137 | 90 | -180 |
| 7 | 51 | 90 | 180 |
| 8 | 132 | 90 | -180 |
| 9 | 144 | 55 | -180 |
| 10 | 52 | 55 | 180 |
| 11 | 140 | 70 | -180 |
| 12 | 190 | 30 | 70 |
| 13 | 61 | 70 | 180 |

Table 4.1: Fault orientations for fault planes apparent in the Big Bear earthquake sequence. Dip direction and Dip are determined from earthquake locations, and rake is obtained by nodal plane determined from focal mechanisms.

NE trending faults are not prominent in this region (*Dokka and Travis, 1990*), and these two clusters do not lie on any known fault.

Another interesting set conjugate nodal planes occur just to the SE of the NFFZ cluster. This set of NW trending and NE trending planes are 90° to each other. The NW trending plane follows the trace of the Helendale Fault, a prominent NW trending fault defining the boundary between the Mojave Block and the San Bernardino Block. If this sequence does correspond to the Helendale fault, then only a small segment of that fault was active, which again demonstrates that known major faults in the San Bernardino block were not notably involved in the Big Bear sequence.

The prevalence of NW and NE trending planes and conjugate strike-slip faults in the Big Bear sequence corroborates the suggestion that the Mojave block may persist beneath the San Bernardino Mountains (*Jones and Hough, 1995; Dokka, 1990*). As we have noted, however, the earthquake activity is not occurring on previously mapped faults. This is also confirmed by the relatively large coefficient of friction we obtain from the direction of maximum compressive stress.

Using a method similar to *Angelier (1979)* to estimate the stress tensor that relies on slip vector and fault plane orientation, we may use the geometry of the active faults uncovered through our relocation to determine stress orientation in the region and the coefficients of friction for each plane. We use only planes for which we have constraints on the strike, dip, and slip direction; this includes the NFFZ cluster, the NW trending portion of the Big Bear mainshock sequence, the Yucaipa cluster and the conjugate planes near it. These are listed in Table 4.1, and numbered in Figure 4.6. Bootstrap analysis over the errors in the fault plane orientations provides an estimate of the standard deviation of the calculated stress orientation.

The direction of the maximum compressive stress is approximately $N5^{\circ} \pm 10^{\circ}E.$, orienting the maximum compressive stress from $35-85^{\circ}$ from the strike of the faults. Figure 4.7 shows the probability distribution of solutions for maximum compressive stress obtained by bootstrapping over the parameters, as well as a table listing the angles between fault strikes and stress direction. The distribution has long tails with small probabilities that are not shown in the figure. The directions in Figure 4.7b are substantially different orientations of the maximum compressive stress than found for mature faults, like the San Andreas and Calaveras Faults, for which the maximum compressive stress is oriented at high angles to the fault (*Zoback et al., 1987; Townend and Zoback, 2001; Schaff et al., 2002*). These high angles suggest that either pore pressure is high along the fault, or coefficient of friction is very low, around 0.1, allowing the fault to slip at low levels of resolved shear stress (*Schaff et al., 2002*). In contrast, the inferred coefficient of friction for the active planes in the Big Bear sequence ranges from 0.35 to 0.75. The combination of higher friction for faults in the Big Bear region, together with the activity on multiple, short faults, suggest that many of these faults are not mature.

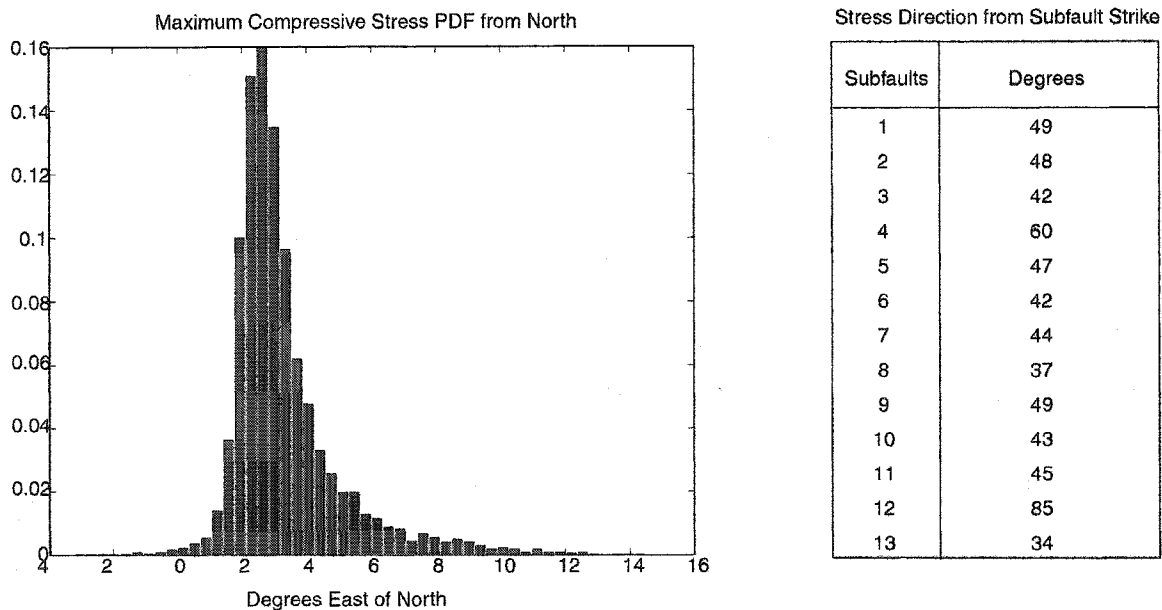


Figure 4.7: (left) PDF of maximum compressive stress direction obtained from bootstrap. Mean value is N5°E. (right) Table listing angle between the maximum compressive stress direction and subfault strike. Subfaults listed as in Figure 4.6.

The immaturity of these active faults is supported by the structure of the Mojave block and the San Bernardino Mountains. Well-developed NW trending strike slip faults have existed in the Mojave for over 10 Ma. as part of the Eastern California Shear Zone, there is evidence that in the last 1 Ma. and the active zone of faulting has been moving westward from Granite Mountain and Bristol Mountain faults to the Camp Rock, Lenwood and Helendale faults. Although this faulting trend is visible in the Big Bear region, well-developed NW trending strike-slip faults have not been mapped in the San Bernardino block, suggesting that the NW trending faults in the San Bernardino block are not as mature as ones in the Eastern Mojave (*Dokka and Travis, 1990*). Although the faulting structure of the Mojave block may extend into the San Bernardino block, the active faults in the Big Bear sequence do not correspond to these faults, or the active structures may be immature branches of the major NW trending faults, like the Helendale fault, in the Mojave.

In addition, the angles between NW trending right-lateral faults and NE trending left-lateral faults are generally less than 90° . This is far less than the 120° between other active planes in the Landers sequence to the east of the Big Bear sequence (*Ron et al.*, 2001). The large angle between the Emerson-Camp Rock fault and faults that trend east from that fault to the Calico fault suggests that the Camp Rock fault is an older feature that has rotated out of an optimal direction for slip. Block rotation of the northern Mojave, north of the Helendale fault, and the southeastern Mojave, to the east of the Pinto Mountain fault the orientation of the conjugate planes, and the lack of rotation in the Big Bear block has been well documented (*Carter et al.*, 1987; *Humphreys and Weldon*, 1994; *Ron et al.*, 2001).

TIME-DEPENDENCE OF EARTHQUAKE OCCURRENCE

Improved depth determination for the Big Bear sequence makes it possible to note changes in earthquake depth over time. The cross sections in Figure 4.4b show that depths varies for the different structures in the area, with the deepest events occurring on the Big Bear rupture planes. *Schaff et al.*, (2002) find that for part of the 1984 Morgan Hill aftershock sequence, deep events occur only in the immediate postseismic period. They suggest the base of the seismogenic zone temporarily deepens due to the increased strain rates from the mainshock and a strain-rate dependent rheology at the base of the seismogenic zone.

In Figure 4.8a, earthquake depths are plotted against time for events on the Big Bear mainshock plane sequence. Although the plot show more dense populations of earthquakes at all depths, there are deep events even at later times. Figures 4.8b shows the evolution of maximum depth that includes 95% of events over a period of 5 years following the Big Bear mainshock. The depth of the seismogenic zone is deeper immediately after the mainshock. The depth decreases quickly after this immediate post-seismic period. Merely 6 months after the mainshock the seismogenic zone settles to approximately 10kms along the entire length of the Big Bear rupture for the next 4 years. To verify that other large events ($M > 4.0$) are not causing strain rates

to increase at later times we examine the timing of large events, and find that there is a large event that occurs at a depth of 10 km in the Big Bear mainshock sequence; this may account for a brief increase in the depth extent of events in that area.

We perform a similar analysis on the evolution of the minimum depth of events over time for both structures. Figure 4.9b shows minimum depth over time for the Big Bear mainshock sequence. This shows a much clearer trend over time away from the surface. Immediately after Big Bear earthquakes are as shallow as 1 km in most areas; the northern section of the sequence is also shallower than the southern section.. By 1995 the shallowest depth of events has increased to 2 km, and by 1996 the shallowest depth is 2.5 km, but the area that had previously shown the shallowest depths (near the 15km mark on the x-axis of Figure 4.8b), now has a minimum depth of events at 5 km. This deepening of shallow events over time would suggest a strain rate dependence in shallow depths as well as at greater depths near the boundary of the seismogenic zone.

While the lack of shallow events has been explained as the effect of velocity-strengthening in unconsolidated sediment or severe fault gouge in well-developed fault zones for aftershock sequences on mature faults, this mechanism may not explain the aftershock pattern we see in the Big Bear sequence (*Marone et al.*, 1989). Earthquakes in the Big Bear sequence do occur near the surface immediately following the mainshock; it is only later that this activity diminishes. Also, the velocity-strengthening behavior may not be in effect here since there is no thick layer of unconsolidated sediment or fault gouge near the faults within the San Bernardino Mountains. Increased velocity-weakening behavior in bare granite due to high slip that gradually dies away has been observed in the laboratory at high normal stress (*Beeler et al.*, 1996; *Blanpied et al.*, 1998). If normal stress were high enough at shallow depths, then an immediately postseismic velocity-weakening would enable unstable slip at those depths. As the velocity-weakening decays, the shallowest aftershocks would stop occurring.

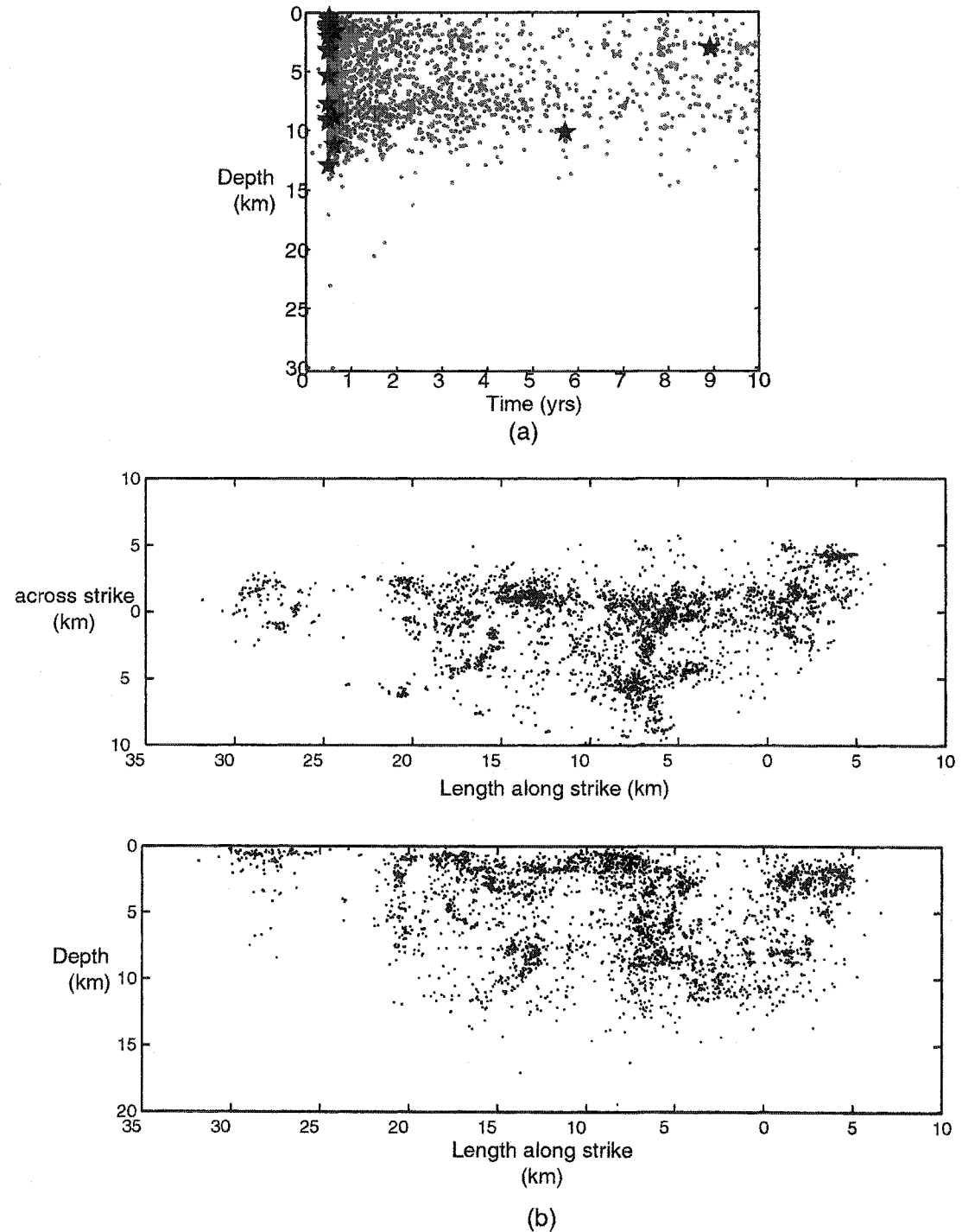


Figure 4.8: Depth of 95% of events over time. (a) Depth of all events in the Big Bear mainshock sequence over time. Black stars indicate events $M > 4.0$ (b) map view of events in the Big Bear mainshock sequence rotated along strike. Red star is the mainshock. (c) Cross section in depth along the strike of the Big Bear mainshock fault plane. Red star indicated the location of the mainshock.

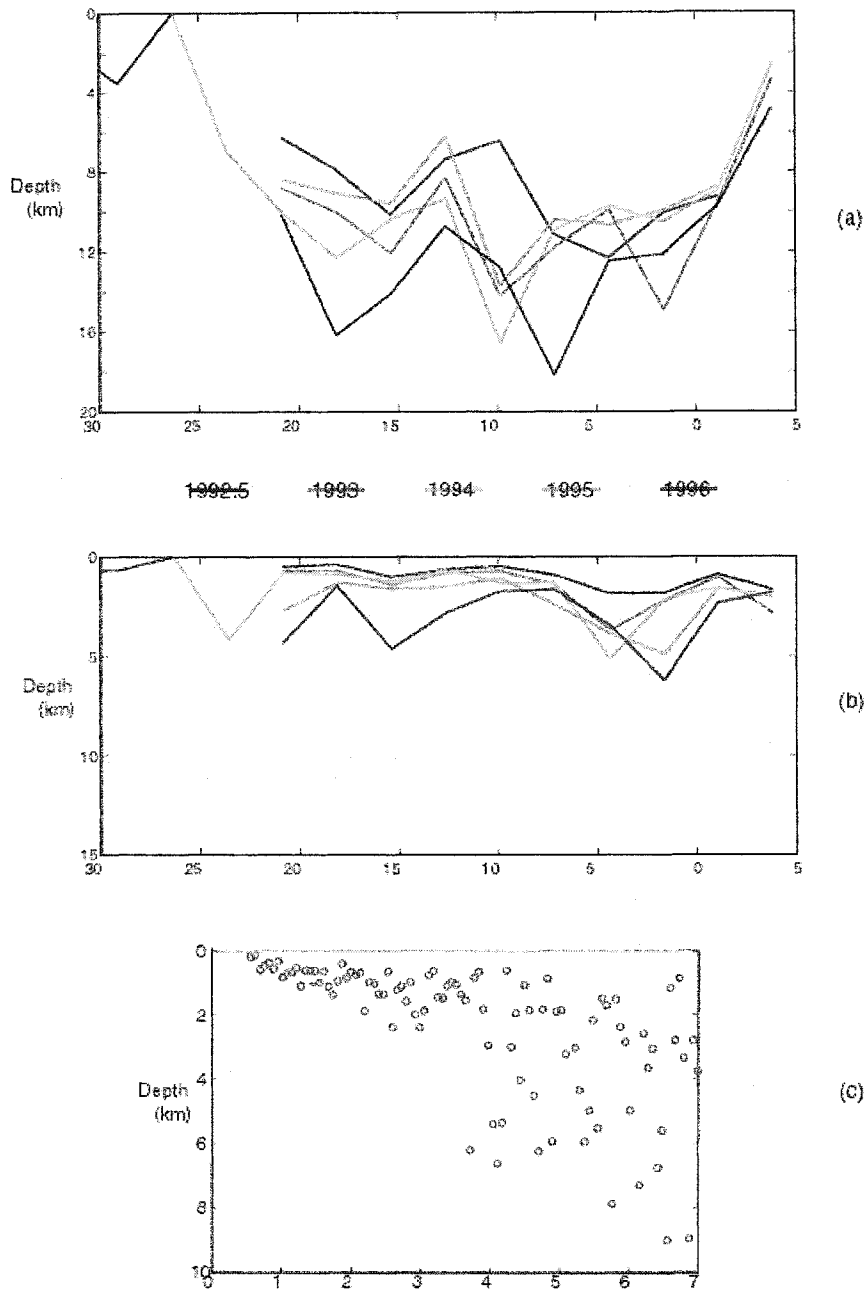


Figure 4.9: (a) Maximum depth of 95% of events in the Big Bear mainshock sequence for various time intervals color-coded in the legend. See Figure 6b and 6c for orientation. (b) Minimum depth of events along the strike of the Big Bear mainshock fault plane. The northern segment of the Big Bear rupture shows an increase in the minimum depth of events over time. (c) Minimum depth for the entire Big Bear mainshock sequence from 1992 to 1999. For about three years after the mainshock, minimum depth gradually increases.

CONCLUSIONS

Relocation of over 11,300 events occurring for ten years after the 1992 M 6.1 Big Bear earthquake reveal many aspects of the active faulting in the San Bernardino Mountain fault block. Evidence that the mainshock ruptured two conjugate planes is corroborated by the relocated aftershocks that illuminate both a NW and a NE trending plane. In addition to the conjugate planes involved in the mainshock rupture there are a number of other conjugate planes, including a set near the NFFZ and another near the segment of the Helendale fault that extends into the San Bernardino Mountains. Although the NW trending structures may trend similar to the major Mojave block faults that may traverse the San Bernardino block, the direction of maximum compressional stress and high values of friction suggest that the faults activate in the Big Bear sequence are immature.

We find only weak evidence for a time-dependence to the base of the seismogenic zone resulting from a strain-rate dependent rheology as found by *Schaff et al.*, (2002). We do, however, find strong evidence that the depth of the shallowest earthquakes in the sequence increases with time. This may result from a similar mechanism in which shallow seismic-aseismic transition is also strain-rate dependent, and may be due to a similar velocity weakening behavior seen in bare granite due to mainshock slip.

CHAPTER 5: THE MECHANICS OF PORE FLUID TRIGGERING FOLLOWING THE 1992 M 7.3 LANDERS EARTHQUAKE

Parts of this chapter are in revision for Nature, with co-authors Gregory C. Beroza and Karen R. Felzer (“Evidence of Pore Fluid Triggering”), and prepared for Science, with co-author Gregory C. Beroza.

ABSTRACT

We have compiled evidence that suggests that pore fluids play an important role in triggering earthquakes in the 1992 Landers aftershock sequence. In this chapter, I use precise earthquake locations to examine the aftershocks in the Johnston Valley – Homestead Valley fault jog in order to test possible mechanisms of pore fluid triggering. I find that if present, poroelastic stress transmission appears to have only a secondary effect, with fluid flow and/or pore space compaction likely to be the dominant mechanisms for increasing pore pressure, and in turn triggering aftershocks in this region. While these mechanisms are only directly implicated in the protracted earthquake sequence within the fault jog, they are also likely to operate more generally in earthquake triggering and faulting.

INTRODUCTION

Pore fluids have long been identified as a possible important factor in many aspects of the faulting process, including slip on misaligned faults (*Sibson, 1990; Rice, 1992*), the heat flow paradox on the San Andreas (*Lachenbruch, 1986*) and the time-dependence of aftershock occurrence, known as Omori’s law, (*Nur and Booker, 1972; Booker 1974*). Pore fluid changes can account for this time-dependence through induced, time-varying, post-seismic pore pressure changes. Pore fluid effects have also been shown to be capable of triggering earthquakes

artificially by elevating pore pressure (*Healy et al., 1968; Raleigh et al., 1976*). Induced seismicity near reservoirs has also been closely linked to either pressure or stress changes from reservoir loading (*Bell and Nur, 1978; Talwani and Acree, 1985; Simpson et al., 1988*).

While these instances of artificially induced seismicity indicate that pore fluid effects can be important in triggering earthquakes in particular situations, evidence of the possible pore fluid triggering for naturally occurring tectonic earthquakes at seismogenic depths is tenuous. In this chapter, I examine a naturally occurring earthquake sequence where we expect to find evidence of pore fluid triggering if it is important.

Pore fluid effects should be most noticeable where changes in pore pressure are both large and predictable. A fault offset in the midst of a large earthquake rupture is an obvious example, as fault discontinuities have been previously identified as areas where significant mean stress change would induce a change in pore pressure after a large earthquake (*Segall and Pollard, 1980; Sibson, 1986*). The large change in pore pressure may then be linked to additional aftershock production, as we describe in the next section.

We examine the 1992 M 7.3 Landers aftershock sequence to determine whether or not the aftershock sequence is protracted within its most prominent fault jog. The Landers earthquake is ideal for this analysis, since the rupture was strongly segmented, including two dilatational jogs created by right steps in the right-lateral fault system (Figure 5.1). The most prominent of these is the 5-km dilatational fault jog between the Johnson Valley (JV) and Homestead Valley (HV) faults, which should be subject to a large decrease in mean stress due the Landers mainshock and thus an ideal location to search for pore fluid effects. We find that aftershocks within the JV-HV fault jog are anomalously extended through time with respect to Omori's law. The protracted duration of these aftershocks suggests that pore pressure effects induced by the mainshock rupture acted to trigger events within the jog.

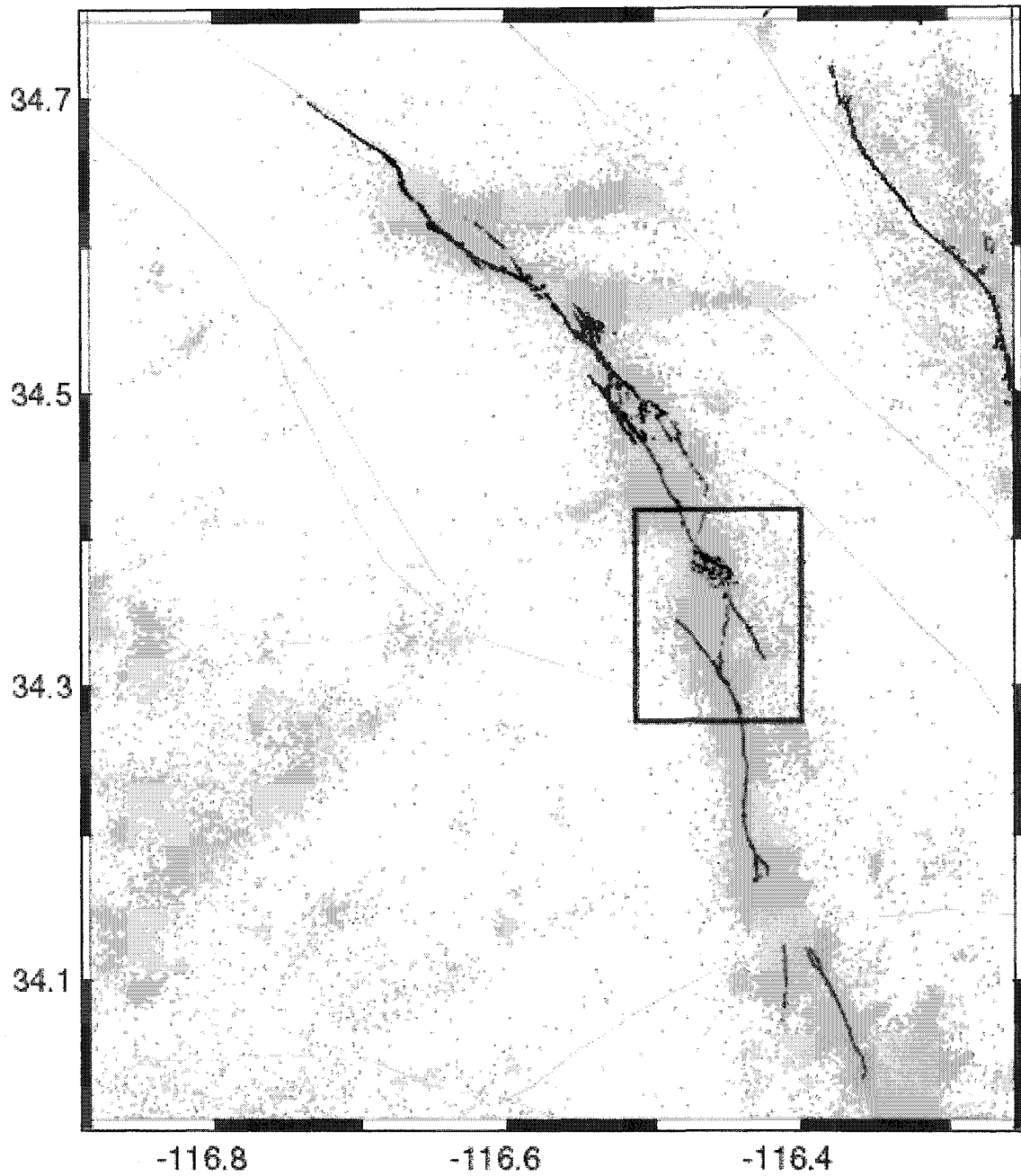


Figure 5.1: Map of the surface rupture and aftershocks of the Landers earthquake. Area in the box is the Johnson Valley – Homestead Valley fault jog. Hector Mine events and rupture are to the northeast.

The small extent of the jog and the relatively large standard errors in earthquake locations obtained from the Southern California Seismic Network makes it difficult to understand the protracted sequence in terms of active faulting within the jog. We use high-resolution earthquake location, a combination of waveform cross correlation and the double difference location method, on approximately 11,000 aftershocks occurring within the jog from 1992 to 2000 to uncover the active features within the jog. After relocation, the protracted seismicity defines near planar features that exhibit a complex three-dimensional geometry within the jog.

Knowing the geometry of faulting in the jog allows us to explore more thoroughly the nature of stress and triggering in the area. We can calculate Coulomb stress change using the fault planes that are triggered following the mainshock and also test the three candidate triggering mechanisms by examining the spatial and temporal behavior of the aftershocks in the protracted sequence. We consider three models by which pore fluids may trigger earthquakes: fluid infiltration, poroelastic consolidation, and pore space compaction. We observe that each fracture, or subfault, by itself, exhibits a protracted sequence and find that the location of the relocated aftershocks does not support poroelastic consolidation as the primary mechanism for triggering the protracted aftershocks, but that either pore fluid diffusion or pore-space reduction following the mainshock remain viable triggering mechanisms.

EVIDENCE OF PORE-FLUID TRIGGERING:

Researchers have long pursued evidence that stress changes induced by pore fluids can cause earthquakes. *Terzaghi* (1923) first formulated the concept of effective stress, which was used to explain the low apparent strength of faults in fluid-saturated rocks by *Hubbert and Rubey* (1959). Since then, other mechanisms involving pore fluids have also been suggested to accompany and facilitate faulting in the Earth (*Nur, 1972; Scholz et al., 1972; Sibson, 1994*). There is clear evidence that pore fluid effects can trigger earthquakes by artificially elevated pore

pressures (*Healy et al, 1968; Raleigh et al, 1976*). In this study, however, we are looking for a seismic signature of pore fluid triggering in ordinary tectonic events.

In order to find this seismic signature, we must understand how elevated pore pressures may trigger earthquakes. Immediately after a large earthquake, the regional stress field is altered and pore pressure, P , is changed by an amount proportional to the mean stress, σ , induced by the earthquake,

$$(5.1) \quad P = -B\sigma$$

where the constant of proportionality, B is known as Skempton's coefficient. Skempton's coefficient is a constant related to constituent compressibilities and defines the portion of the mean stress transferred to pore fluid in a porous rock. It is usually assumed to equal one for fluid saturated soils and is empirically determined to range between 0.5 and 0.9 for a range of rock types (*Nur and Booker, 1972*).

This induced pore pressure change can initiate shear failure through a change in poroelastic stress, or by reducing the effective normal stress acting across a fault until it is exceeded by the shear stress. The latter method is described by the Coulomb failure criterion, where pore pressure reduces the effective normal stress, i.e. the difference between normal stress, σ_n , and pore pressure, P ,

$$(5.2) \quad \tau = C - \mu_s(\sigma_n - P)$$

where τ is shear stress, C is cohesive strength, and μ_s is the coefficient of static friction. Failure occurs when the right-hand side of equation 2 is greater than the left-hand side.

We consider a case where changes in pore pressure are likely to be large and clearly discernable, a dilatational fault offset in the midst of a large earthquake rupture.

FAULT OFFSETS

Fault offsets have been previously identified as areas where a significant mean stress change would induce a change in pore pressure in an earthquake (*Sibson, 1987*), and are a natural location to search for pore-fluid effects on earthquake behavior. A dilatational fault discontinuity, such as right step in a right-lateral strike slip fault system, would produce a large coseismic pore pressure decrease.

The 1992 M 7.3 Landers, California earthquake ruptured over 85 km with several prominent extensional fault discontinuities (*Sieh et al., 1993*) as shown in Figure 5.1. Two dilatational jogs are apparent in the surface rupture, a small offset between the Homestead Valley and Emerson faults, and an almost 5km fault offset between the Johnson Valley and Homestead Valley faults (boxed area in Figure 5.1). The Landers, or Kickapoo fault, which was not mapped before the mainshock, spans the length of the jog, and may have been instrumental in the transfer of slip from the JV fault to the HV fault (*Harris and Day, 1999*).

Figure 5.2a shows that the Landers sequence follows a typical frequency magnitude relationship, with b-value near 1. The overall temporal behavior of the Landers aftershock sequence is well described by Omori's law (*Wiemer and Katsumata, 1999*) so that we can characterize the temporal behavior of aftershocks using t^{-1} decay as a standard. Others have also suggested that pore fluids may have played a role in the postseismic deformation of the Landers earthquake (*Peltzer et al., 1996*) or even that it may have played a role in triggering Landers aftershocks (*Bosl and Nur, 2002*), and the Landers sequence is not the only one in which pore fluid triggering has been hypothesized (*Hudnut et al., 1989*).

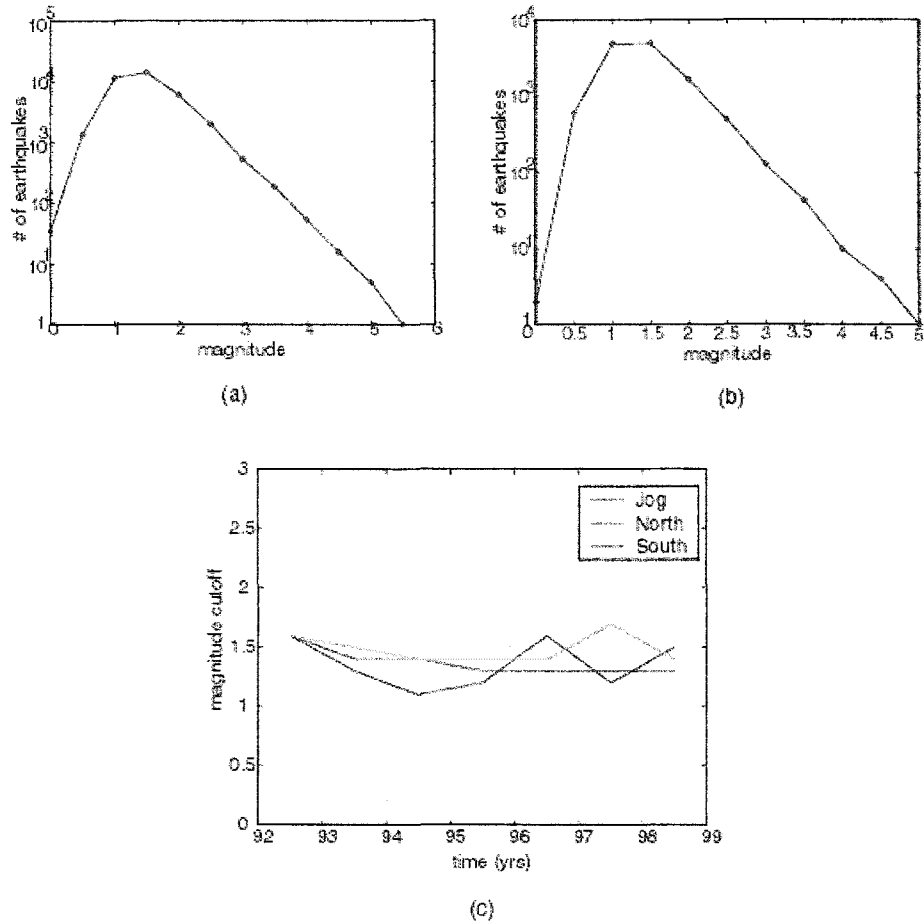


Figure 5.2: (a) Frequency magnitude relationship for all earthquakes in the Landers sequence, y-axis is a log scale. (b) Frequency magnitude relationship for earthquakes within the Johnson Valley – Homestead Valley jog. (c) Change in magnitude completeness of the catalog over time within the jog and immediately north and south of it. The magnitude of complete detection is similar for the three regions and approximately constant with time. There is no significant change in completeness level in the time of interest, 1993-1997, and no significant spatial variation in completeness over this region.

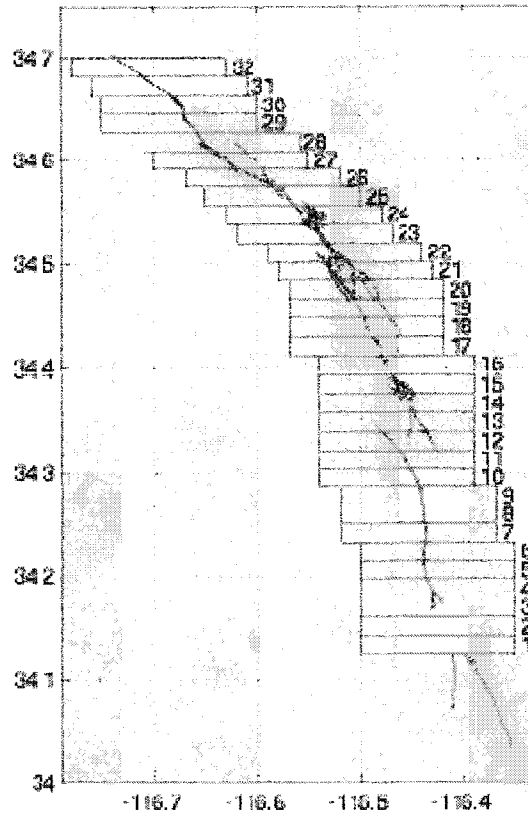


Figure 5.3: 5km x 2km boxes used to examine temporal dependence of aftershocks, shown in gray, along the Landers surface rupture.

PROTRACTED AFTERSHOCK SEQUENCE

Following a large earthquake across a dilatational fault discontinuity, the time-dependence of aftershock decay should demonstrate the effects of a large change in pore pressure if pore fluids are present and play a role in triggering earthquakes at seismogenic depths. Pore pressure in the jog will re-equilibrate as the system evolves from an undrained to a drained state. During this transition, the area within the jog should experience a steady increase in pore pressure and thus a decrease in effective normal stress. This should manifest itself in the aftershock sequence as a period of extended aftershock activity since the effect of the transition from undrained to drained conditions is to “buffer” the long-term effective stress change. Thus, we

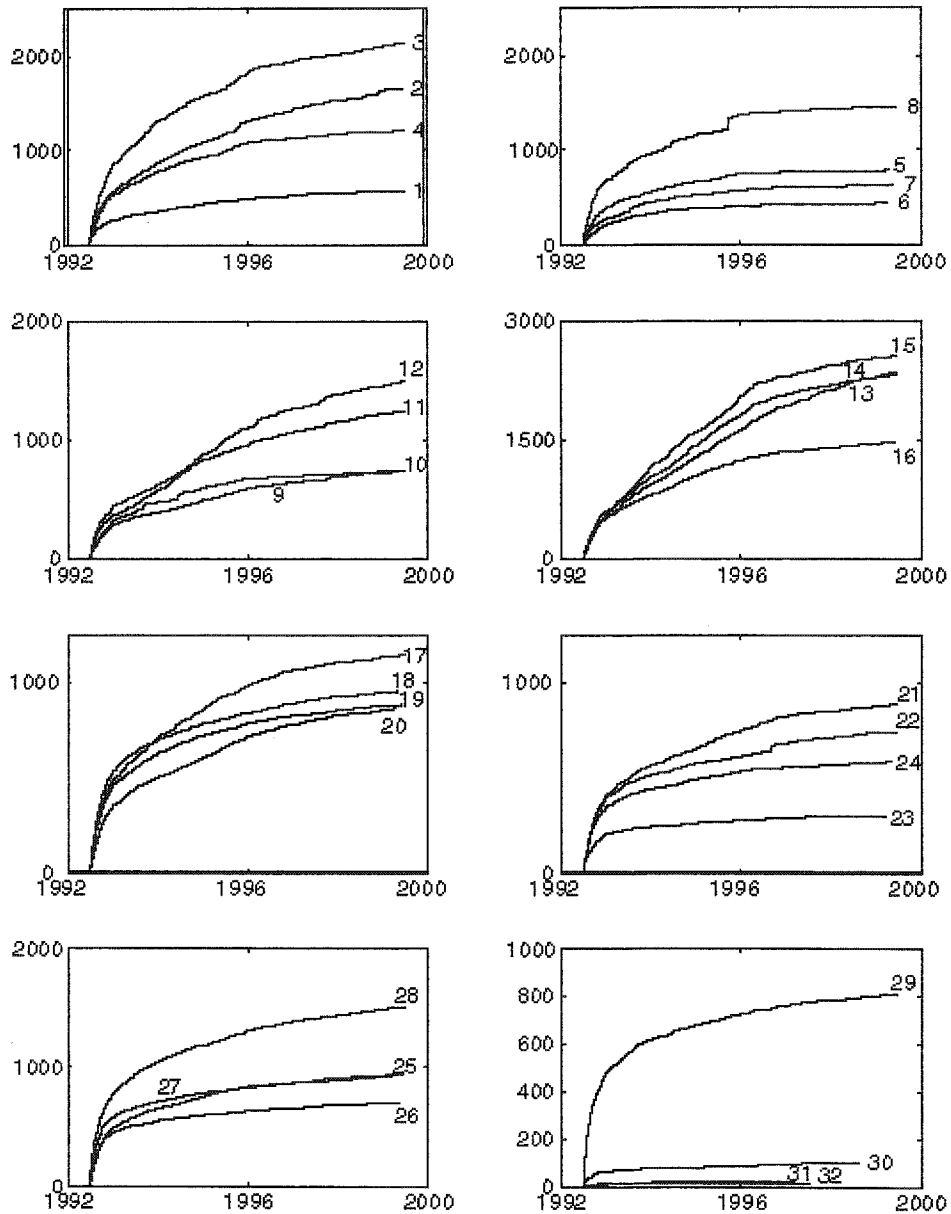


Figure 5.4: (a) Cumulative number of aftershocks with time for the boxes in Figure 5.3. X-axis is time and Y-axis is cumulative number of events. The protracted aftershocks appear most clearly as a trend of approximately constant slope for boxes 11-16 from 0.5 to 3.5 years after the Landers mainshock. This straight-line behavior represents a constant aftershock rate rather than the decay predicted by Omori's law. The protracted aftershocks are not attributable to variations in the network detection threshold. The detectability threshold for the Landers aftershock sequence changes gradually from south to north because of variations in network coverage; however, a rate change resulting from this would act over larger spatial scales than the variations we observe and would include adjacent straight segments of the fault where the aftershock decay is normal.

would expect that the earthquake sequence in the fault jog would be protracted relative to what it would be in the absence of pore fluids, i.e. relative to Omori's Law. Pore fluids may still be responsible for triggering earthquakes outside the jog, but these sequences would not deviate from Omori's law. The magnitude of the pore pressure change and possible differences in material properties within the jog create the protracted earthquake sequence.

To search for evidence of this hypothesized protracted aftershock sequence within the Landers sequence, we divide the aftershock zone into sub-areas that extend 5 km to either side of the fault trace (Figure 5.3). Within each of these we plot the cumulative number of aftershocks against time after the mainshock. The curves in Figure 5.4 show that for most of the fault the aftershocks accumulate rapidly shortly after the mainshock, with the rate gradually decreasing, as Omori's law predicts. Areas 11-16 behave in a similar fashion to the other areas for the first 6 months following the mainshock; however, after that they show a distinctly different behavior. For about 3 years, each of these areas shows an approximately constant aftershock rate. This constant aftershock rate is the manifestation of the protracted aftershock sequence and is situated, as expected, directly within the most prominent extensional offset in the fault trace. This suggests that pore fluid effects do play an important role in triggering aftershocks.

The protracted aftershocks can not be explained by spatial variations in the detectability threshold of the seismic network because they are limited to a very small area, with normal aftershock decay on either side, and the detectability threshold should not change appreciably over such small distances. Figure 5.2c confirms this by showing that the minimum catalog completeness magnitude does not dramatically change over the time of interest either within the jog or to the north or south. Moreover, the deviation of the aftershock rate we observe in the fault discontinuity from Omori's law is statistically significant (Figure 5.5).

We can get a clearer view of the spatial extent of protracted aftershocks by considering smaller areas and using a simple measure of aftershock decay. Figure 5.6 shows how closely the protracted aftershocks correspond to the confines of the fault discontinuity between the Johnson

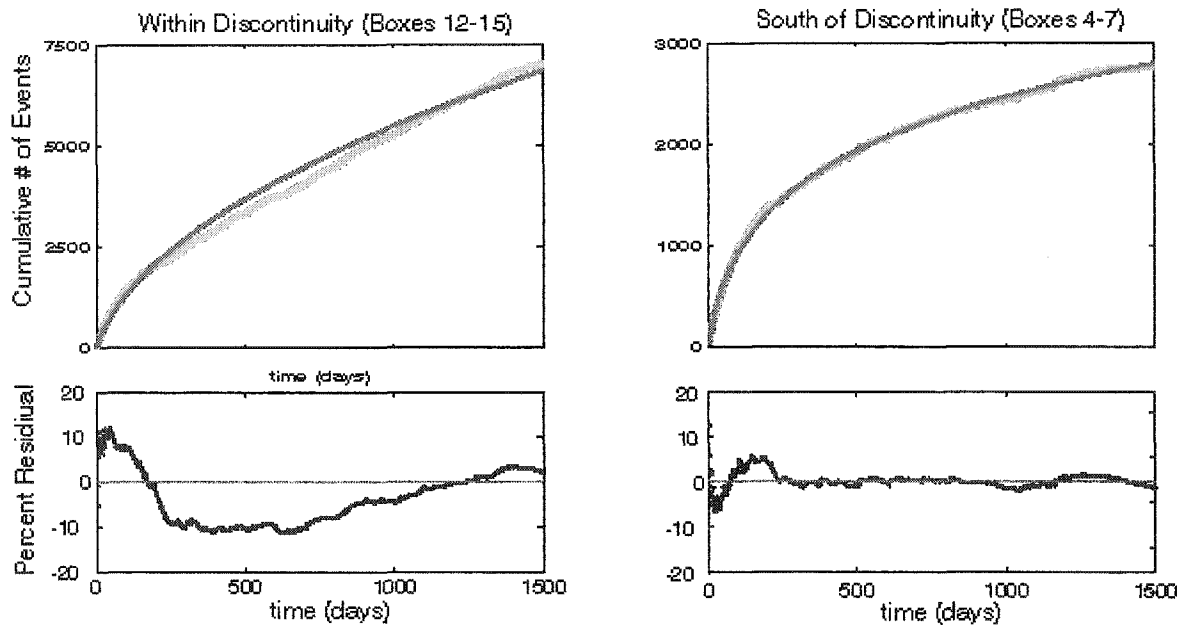


Figure 5.5: Cumulative number of events over time with the best-fit Modified Omori power law. Residuals from the power law fit. Sequences outside the jog are well fit by the model; those within the jog are not, and have large and systematic residuals

Valley and Homestead Valley faults. Within the offset, the rate of aftershocks does not decay with time for about 3.5 years after the mainshock. The short scale length of this effect precludes visco-elasticity of the lower crust, because it would operate over much larger spatial scales.

Other areas also appear to show a protracted aftershock sequence. Near the southern end of the surface rupture there is another prominent area of protracted aftershocks. The surface rupture bifurcates and terminates in this region, so it is difficult to assess whether this activity might also be attributed to pore-fluid effects. There is, however, some evidence of afterslip in this region. Although *Hough et al.*, (1993) identify significant slip immediately after Landers on the Burnt Mountain and Eureka Peak faults, attributed to two large aftershocks, the bifurcation is not included in this region. *Peltzer et al.*, (1994) note from InSAR information that about 1.5-3 m of afterslip is conceivable in the region north of the Pinto Mountain Fault and south of the Johnson Valley Fault.

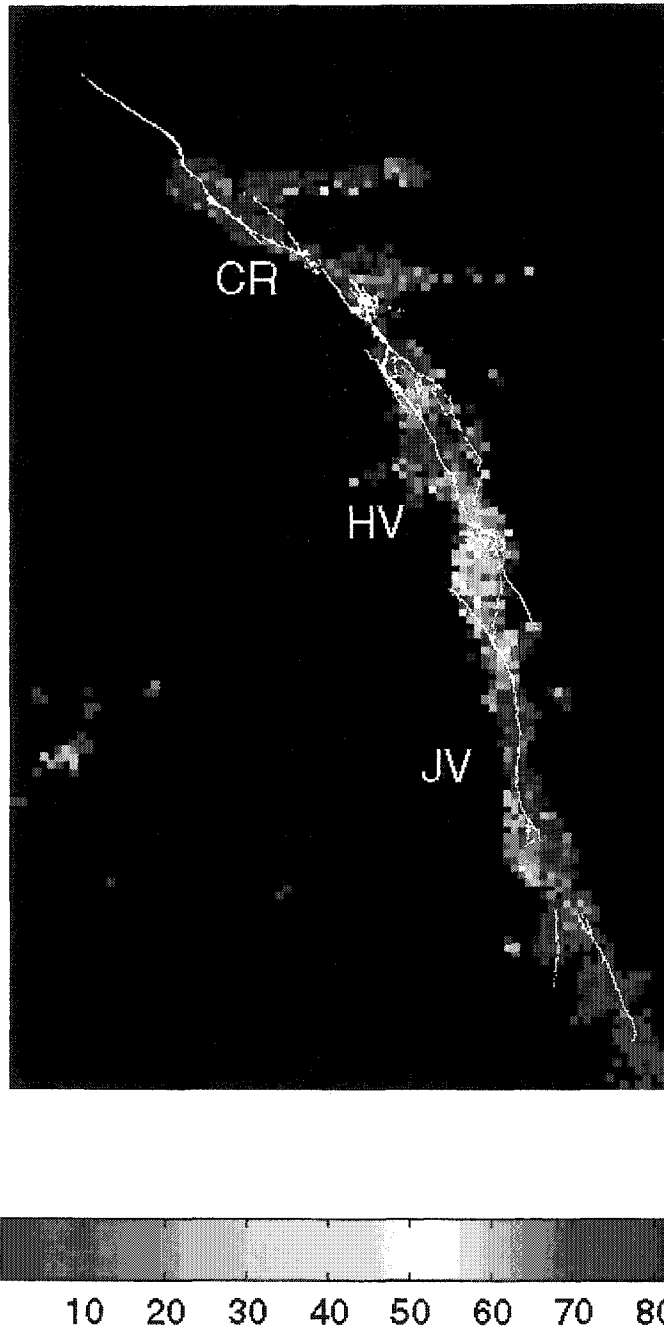


Figure 5.6: Relative aftershock rate displayed as the percentage of aftershocks in years 1 and 3 following the mainshock that occurred in year 3. Instances of less than 8 total aftershocks within each 0.01° by 0.01° box are not plotted. Areas of protracted aftershocks (relatively more aftershocks at later times) show as warm colors (green to red). These are most prominent in the large extensional discontinuity between the Johnson Valley (JV) and Homestead Valley (HV) faults and at the southern end of the rupture. The extensional discontinuity between the Homestead Valley and Camp Rock/Emerson (CR) faults also shows a protracted aftershock sequence, though the effect is subtle. Straight segments of faults plot as cool colors, consistent with decay of the aftershock rate with time.

We also observe protracted aftershock activity in the smaller offset between the Homestead Valley and Camp Rock-Emerson faults (Figure 5.4), but the effect is subtle. *Peltzer et al.*, (1996) found evidence for poroelastic deformation in the post-seismic InSAR data for this fault discontinuity, as well. There is a small compressional offset in the Camp Rock-Emerson fault, but we find only equivocal evidence for an abbreviated aftershock sequence at this location. Aftershocks on the straight fault segments consistently show a rapid decay.

OTHER MECHANISMS VS. PORE FLUID EFFECTS

Other mechanisms of earthquake triggering, such as viscoelastic relaxation (*Freed and Lin, 2000*) or rate and state variable friction laws without pore pressure considerations (*Dieterich, 1994*), no doubt influence the temporal behavior of the aftershock sequence. They, however, cannot explain the protracted sequence because these mechanisms should not affect a fault offset differently from the rest of the ruptured faults. The length-scale of the viscoelastic effect observed by *Freed and Lin (2000)* is on the order of 20km, too large to influence exclusively the jog area. Rate and state variable friction laws predict an Omori's law decay, even if changes in normal stress are considered (*Linker and Dieterich, 1992*)

Fluid effects have been independently implicated from post-seismic deformation measurements for this earthquake (*Peltzer et al., 1996*). The effect was seen most prominently in the Johnson Valley-Homestead Valley fault jog. The surface deformation was centered on the fault trace, whereas the protracted aftershocks were located to the west of the fault trace. The difference may be attributable to changes in the fault geometry and slip distribution with depth. The decay time for poroelastic effects in the surface deformation was 270 days (*Peltzer, 1996*), rather than ~3 years as we have found, and the depth of the source of the deformation anomaly was modeled as 0-4 km (*Peltzer et al., 1998*).

In this case, the protracted aftershock sequence, indicative of pore fluid triggering, was recognizable because of the large and predictable change in mean stress. The mean stress is nodal along the fault plane for a uniform planar fault, which will make it more difficult to evaluate its possible role in triggering for most aftershocks; however, there are other situations in which the signature of pore fluids may be recognizable. For example, earthquakes that have prominent off-fault aftershock sequences ought to show asymmetry in their temporal decay. Evidence for this behavior has not been widely sought after, but it has been documented for the 1968 Borrego Mountain earthquake sequence (*Li et al.*, 1987).

EARTHQUAKE RELOCATION

Standard earthquake locations from the SCSN catalog in the Landers region have, on average, horizontal errors of 0.5-1.0 km, and vertical errors of 1.0-2.0 km. Earthquakes in and near the fault jog that we are interested in span an area of approximately 5 km x 5 km horizontally, and perhaps 10 km in depth. The large errors in the SCSN catalog locations will interfere with our attempts to discriminate between different mechanisms for pore-fluid triggering. Thus, we aim to improve the aftershock locations.

RELOCATION TECHNIQUE

To improve earthquake locations we use a precise relative relocation technique known as the double-difference method (*Waldhauser and Ellsworth*, 2000) and combine it with waveform-based arrival time differences (*Schaff et al.*, 2002). We apply these techniques to the approximately 11,000 events occurring within the Johnson Valley – Homestead Valley fault jog over a period of seven years following the 1992 Landers mainshock.

We perform time- and frequency-domain cross-correlations on over 1,000,000 seismograms at 250 stations in the SCSN network, recovering 565,994 event pairs with 4 or more observations and more than 6,000,000 differential arrival time measurements. Of these, 4,922,457 are P-wave relative arrival times and 1,286,773 are S-wave arrival times. We select only

observations with correlation coefficient and mean coherence above 70%. In datasets of repeating or closely spaced events on the Calaveras fault, *Schaff et al.*, (2003) used arrival time measurements with correlation coefficients greater than 70% because these observations, based on their low post-fit residuals, were found to provide relative arrival time measurements that were more precise than could be obtained from differencing the highest quality catalog observations. We used this cutoff in order to minimize outliers, while still retaining enough measurements to locate the aftershocks.

We use a one dimensional velocity model taken from *Wald et al.*, (1995). This is a standard velocity model for the region, similar to the one used by *Hauksson et al.*, (1993) for relocations based on station corrections. We tested the sensitivity of the locations to the velocity model by testing other models, and changing the velocities and locations of the layers. Since the earthquakes are closely spaced compared to the model layers, the locations depend only weakly on the chosen velocity model. We are able to relocate approximately 75%, or 8390, of the aftershocks, and we reduce location error by about an order of magnitude relative to that in the catalog. Typical errors after relocation are ~50 m in the horizontal position and ~100 m in the vertical. Because of the uneven station distribution we find that the longitudinal error is slightly larger than the latitudinal error.

FAULT ORIENTATIONS

Figure 5.7 shows the improved aftershock locations obtained from relocation. Instead of the diffuse pattern of events in the catalog locations, the relocations reveal a complex and truly three-dimensional geometry in the dilatational jog. There is a set of distinct planes in and near the fault jog that are illuminated by the aftershocks. These planes are consistent with the secondary fracturing expected within a dilatational jog (*Sibson*, 1986). Depths of aftershocks range from 0 km to 10 km, with the greatest concentrations of events at 2-3km and 6-8 km.

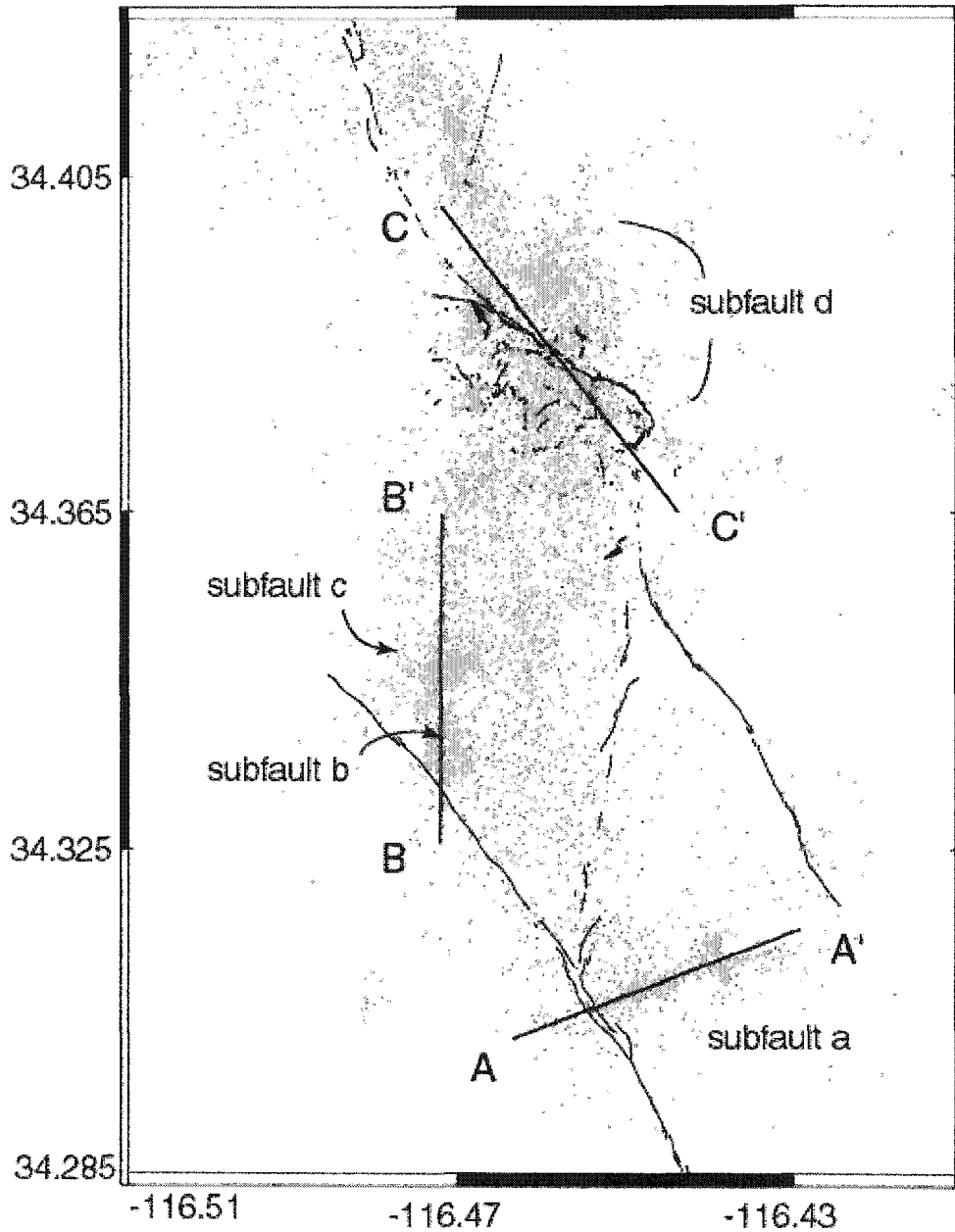


Figure 5.7: Double-difference earthquake locations based on waveform cross correlation derived arrival times for 8390 aftershocks, ~75% of the events in the area. Formal errors are approximately an order of magnitude smaller than for SCSN catalog locations and relocated seismicity align onto distinctly more planar structures.

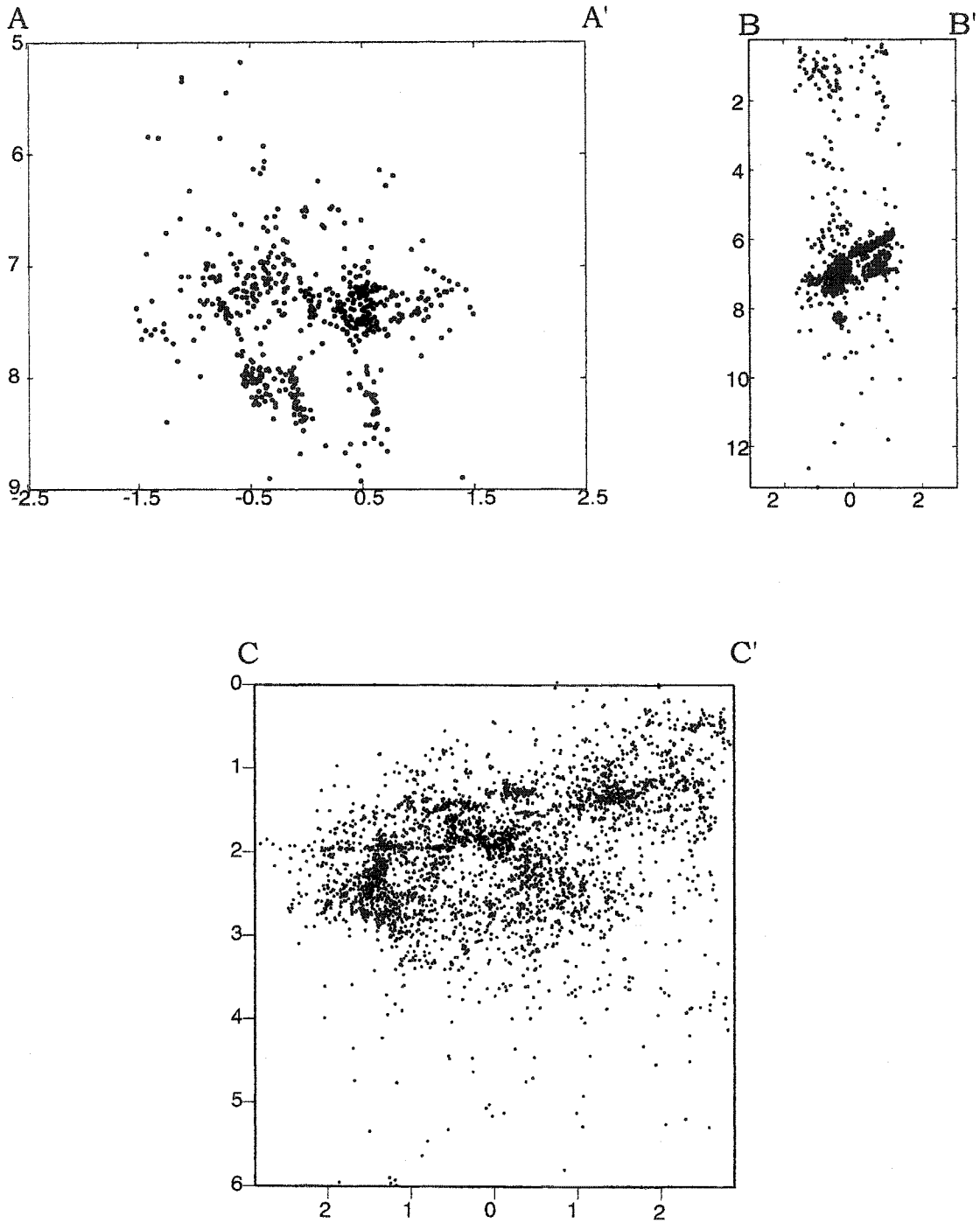


Figure 5.8: Vertical cross sections of major subfaults. (a) Vertical, left-lateral subfault to the south of the Landers fault, now called subfault a. (b) two subfaults to the north of the Landers fault. The southern subfault, subfault b, dips 30° to the Northeast; the northern subfault, subfault c, dips 60° to the North. (c) Densely fractured area, subfault d, in the northern part of the jog, on the Homestead Valley fault. Aftershocks define many fractures of differing orientations.

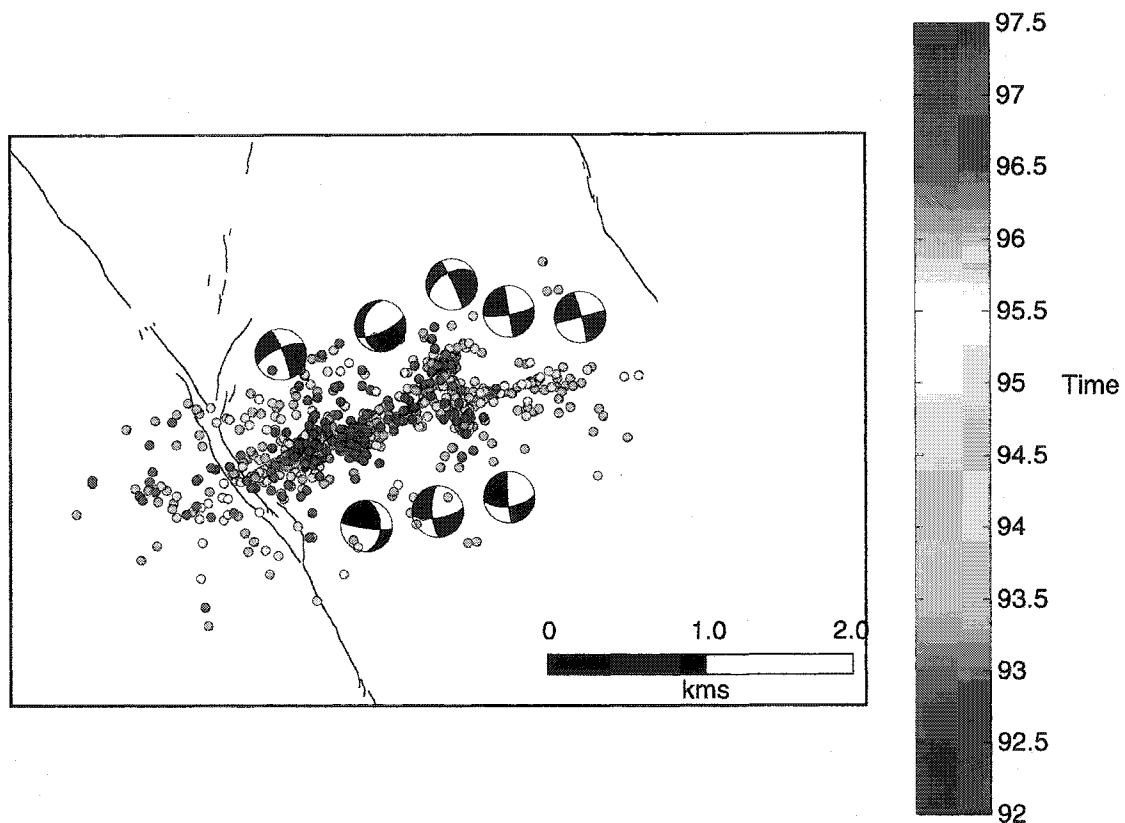


Figure 5.9: Aftershocks in subfault a plotted with composite mechanisms for similar events (i.e., those that have a high cross correlation coefficient). Color represents timing of the events. Black lines are the Landers mainshock surface rupture.

The aftershocks exhibit a variety of orientations and faulting mechanisms on these secondary fractures (Figure 5.8). In the southern end of the jog, aftershocks delineate a left-lateral, vertical strike-slip fault perpendicular to the JV fault from 7-9km depth, subfault a, as shown in Figure 5.9. We have plotted composite fault plane solutions, determined using very similar sets of closely spaced aftershocks, and the time history of aftershocks on subfault a. To the north of the Landers fault and the JV fault are two sets of planes, subfaults b and c, from 6-8km depth. Subfault b dips at approximately 30° to the northeast and Subfault c dips at 60° to the north. Neither nodal planes for focal mechanisms calculated for subfault b do not correspond exactly to

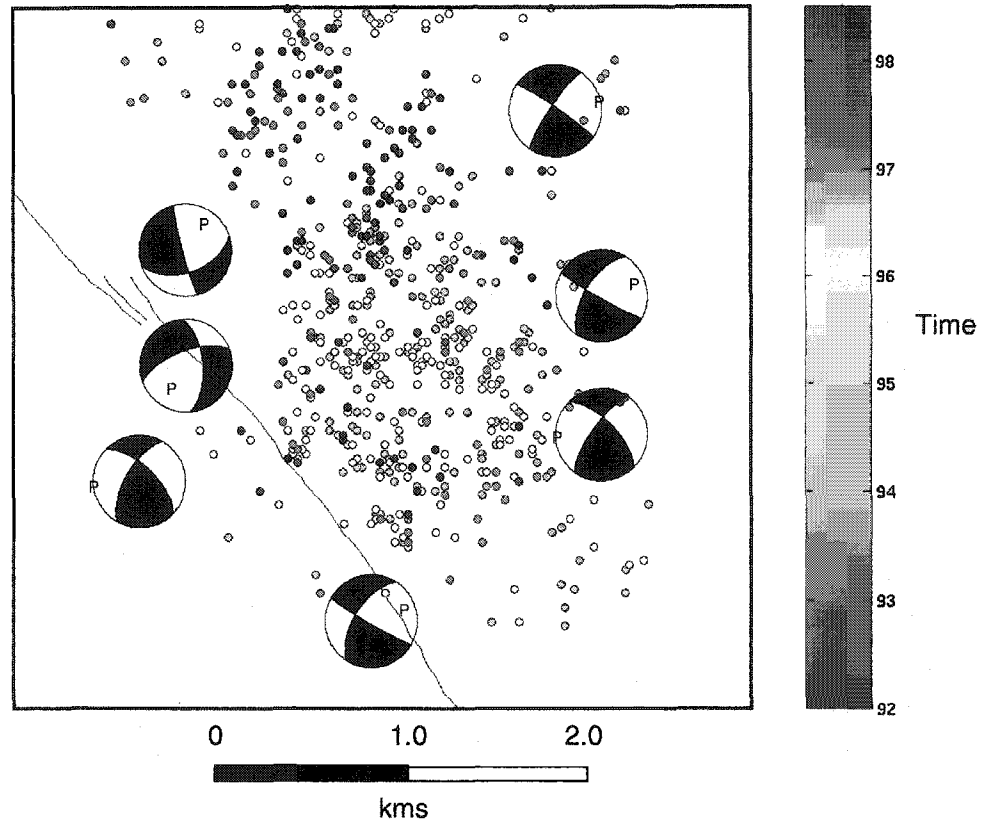


Figure 5.10: As in Figure 5.9, for aftershocks in subfault b. Composite focal mechanisms for highly correlated events. Color represents timing of events.

the orientation of the fault, but the right-lateral nodal planes are closer (Figure 5.10). Neither subfault corresponds to the orientation of the Landers fault if projected in depth.

In the northern section of the jog, approximately half of all the jog's aftershocks occur in what appears to be a complexly fractured area near the HV fault. Although not a single subfault, we call this entire area subfault d. Surface faulting in this area is also very complex, including small faults in varying orientations with strike-slip and thrust displacements (*Spotilla and Sieh, 1996*), suggesting that the new aftershock locations are illuminating the actual structure of the area. Even in this area, most of the aftershocks fall on small, defined faults. The aftershock activity becomes two-dimensional again directly outside the jog, north of the complexly fractured area on the HV fault (Figure 5.11). Both the aftershock locations on this part of the fault and focal mechanisms (*Hauksson et al., 1993*) suggest a near vertical fault with right-lateral strike slip.

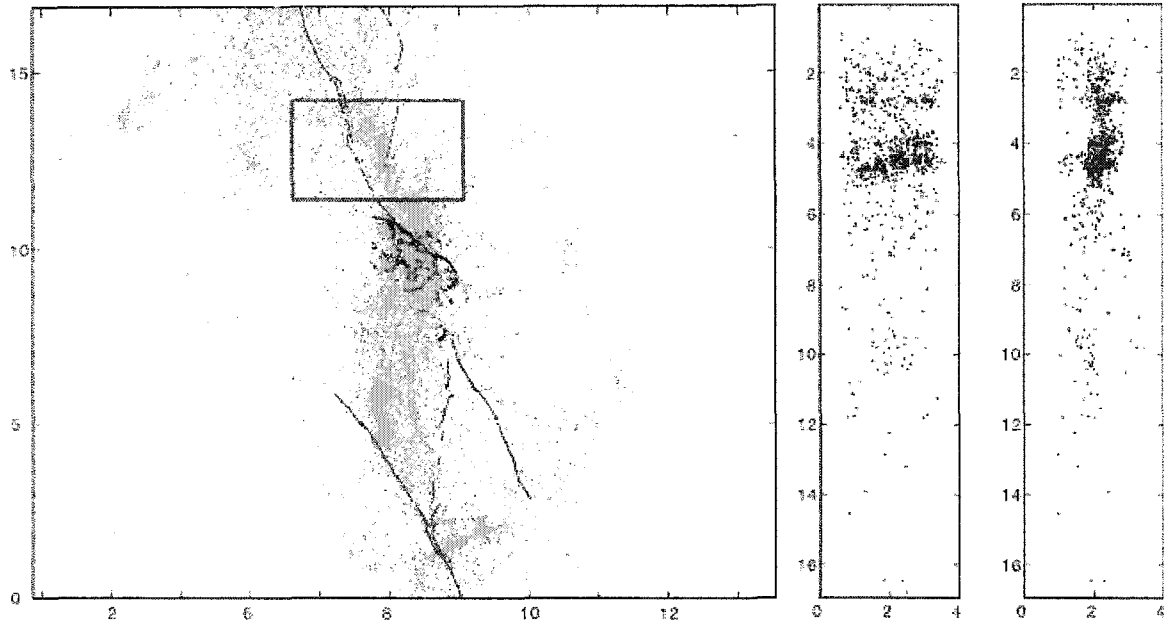


Figure 5.11: Cross sections of the Homestead Valley fault immediately north of the JV-HV dilatational fault jog.

Similarly, directly to the south of the jog on the JV fault aftershock activity shows a simpler geometry, but there is not enough activity to discern a clear plane.

STRESS ANALYSIS

By reducing location errors of the aftershocks and determining composite focal mechanisms we may discern the position, orientation, and sense of slip of several active fault structures within the jog. Most Coulomb stress studies rely on the assumption that activated faults are optimally oriented in the stress field (*Stein et al., 1992; King et al., 1995; Kilb, 2002*). This may not take into account the triggering of a large number of earthquakes that occur on planes of differing orientations. The precise relocations allow us to compute Coulomb failure stresses for these specific fault planes, which is important, as they may not be optimally oriented.

We follow a method similar to the one used by *Peltzer et al.*, (1998) to model uplift observed in the jog using InSAR measurements. We calculate Coulomb stress in both drained and undrained conditions by using Poisson's ratios of 0.27 and 0.35 respectively (*Peltzer et al.*, 1998). While this does not resolve the time dependence of the transition from undrained to drained conditions, we can use it to examine the cumulative long-term poroelastic effect. We model Coulomb stress changes due to poroelastic effects by calculating shear and normal stress for two elastic dislocation models each with different Poisson's ratios described above (*Okada*, 1985). In each case we use the fault planes and slip directions we have determined and equation (2) to obtain Coulomb stress change.

To perform this analysis at the small-scale length we are interested in, we form a composite slip model for the Johnson Valley Fault, Landers fault and Homestead Valley fault. Slip at depth is taken from the mainshock slip model of *Wald and Heaton*, (1994). This model, however, does not consider the complex geometry of the fault offset, which is critical to understanding the protracted aftershock sequence we observe. We use the surface fault trace (*Sieh et al.*, 1993) to define the geometry of the jog and surface co-seismic slip measurements (*Sowers et al.*, 1994; *Spotilla and Sieh*, 1996) to define the jog at shallow depths. This and the deeper slip model (*Wald and Heaton*, 1994) characterize variable slip from the surface to 10-15 km depth. In our model, slip tapers off in the northern end of the JV fault and the southern end of the HV fault.

Spotilla and Sieh, (1996) note a "slip gap" just north of where the HV fault and Landers fault meet; this is the same region that exhibits complex geometry in the aftershock locations. While minimal surface slip was noticed there following the Landers mainshock, it occurred on small fractures of varying orientations. Slip at greater depth, however, is not clearly discounted. *Peltzer et al.*, (1998) are concerned primarily with the southern part of the jog, to the south of the Landers fault. Therefore, they do not constrain deeper slip in the apparent slip gap.

In Figure 5.12, Coulomb stress calculations are shown for subfault a, a left-lateral vertical fault corresponding with the area that is activated by the aftershocks on that structure. The

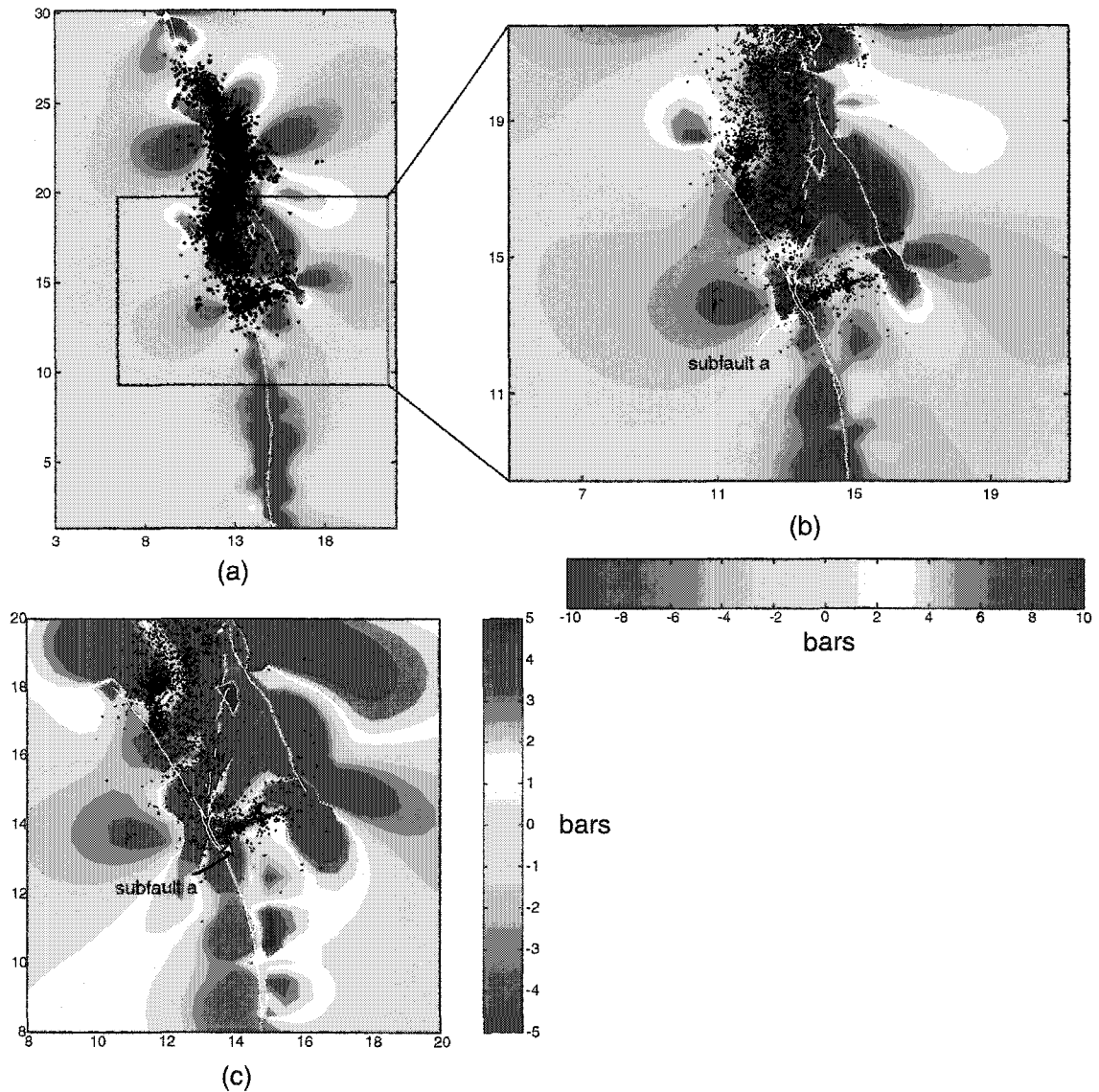


Figure 5.12: Stress calculations in bars for Subfault a. (a) Coulomb stress calculation in the undrained state, $n = 0.37$, for fault plane and slip direction orientations determined from relocated earthquakes and focal mechanisms of subfault a. (b) Coulomb stress calculation in the drained state, $n=0.27$, for the same plane orientation. (c) the difference between the Coulomb stresses in the undrained and drained states shows a significant additional stress due to poroelastic effects.

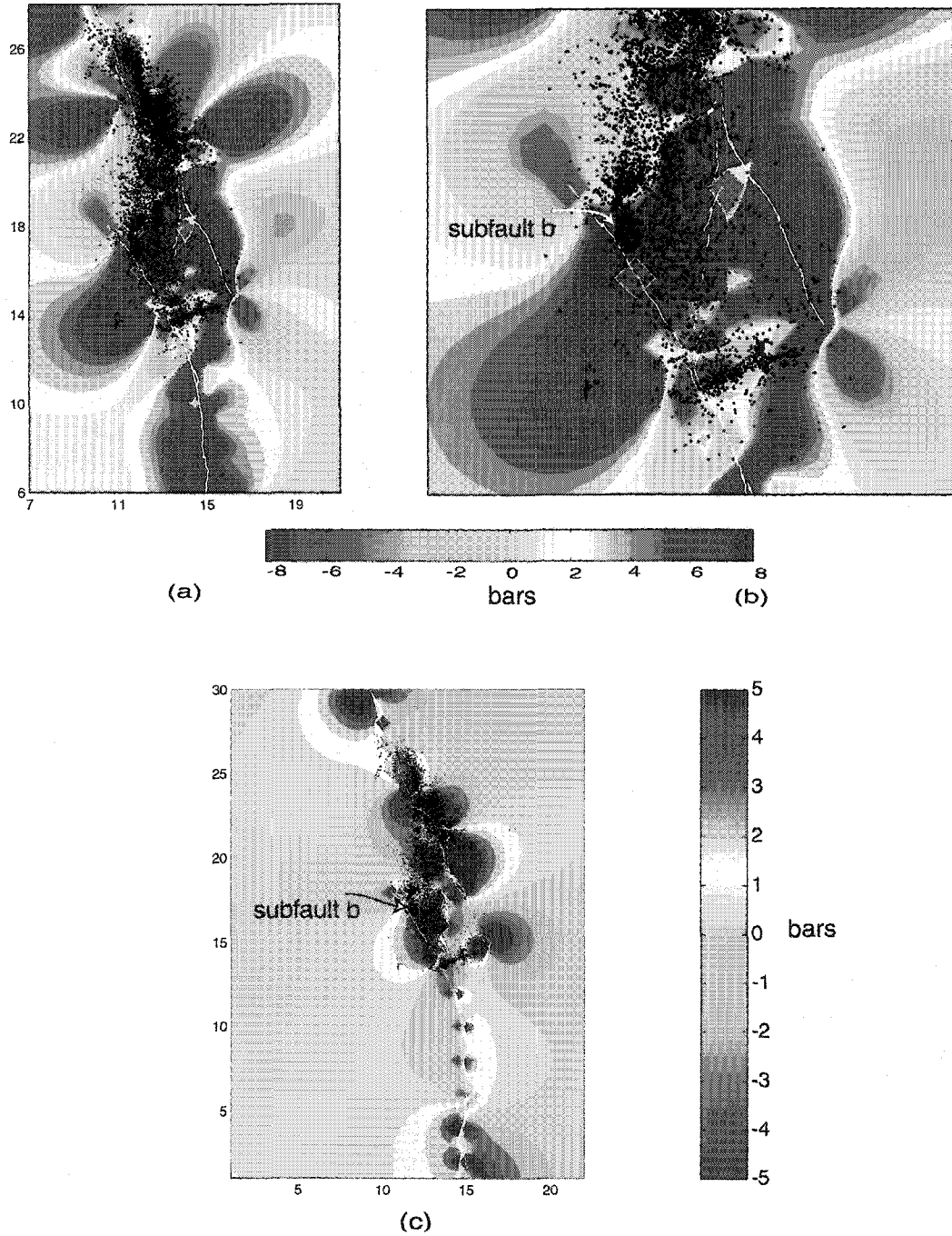


Figure 5.13: Stress calculations in bars for Subfault b. (a) Coulomb stress calculation in the undrained state, $n = 0.37$, for orientations described by the structure described by subfault b. (b) Coulomb stress calculation in the drained state, $n = 0.27$, for the same plane orientation. (c) The difference between the Coulomb stresses in the undrained and drained states shows a significant additional stress due to poroelastic effects.

difference between the stress calculated in the drained case and that in the undrained case will give us the magnitude of the poroelastic effect of Coulomb stress. Figure 5.12c shows this difference; the warm colors along the length of subfault a suggest that the stress from the undrained case is greater than that in the drained case for this fault plane. The poroelastic effect adds approximately 0.2-0.4 MPa of stress to the fault plane. In contrast, the difference in normal and shear stress between the drained and undrained cases is on the order of 0.0001 MPa.

We see a similar effect for one of the structures directly north of the JV fault, subfault b, plotted in Figure 5.13. In this case, the area of high Coulomb stress is located near the northern part of the JV fault, clearly encompassing subfault b. The stress difference between the drained and the undrained states again shows a net increase Coulomb stress due to poroelastic effects of 0.2-0.3 MPa. In both these cases, the areas of large Coulomb stress increase correspond very well with the seismicity. Other planes, subfaults c and d, are not as easily defined, and thus it is problematic to perform our analysis on them. Where we can perform similar analysis, we find that poroelastic effects contribute a substantial stress change that is of the right orientation to trigger the protracted aftershock activity we observe within the jog.

CONSTRAINTS ON TRIGGERING MECHANISM

Our precise relocations allow us to examine more than the magnitude of the potential poroelastic effect within the jog. The spatial and temporal patterns apparent in the protracted aftershock sequences are indicative of the underlying pore fluid mechanism. We try to illuminate the characteristics of this mechanism by comparing the results of the relocation with three potential mechanisms by which pore fluids may trigger earthquakes. Pore fluids have often been invoked to explain the occurrence of earthquakes, and different mechanisms that describe the interaction of pore fluids and faulting have been posited, such as poroelastic stressing (*Booker, 1974*), pore fluid infiltration (*Nur and Booker, 1973*), and pore pressure increase due to the

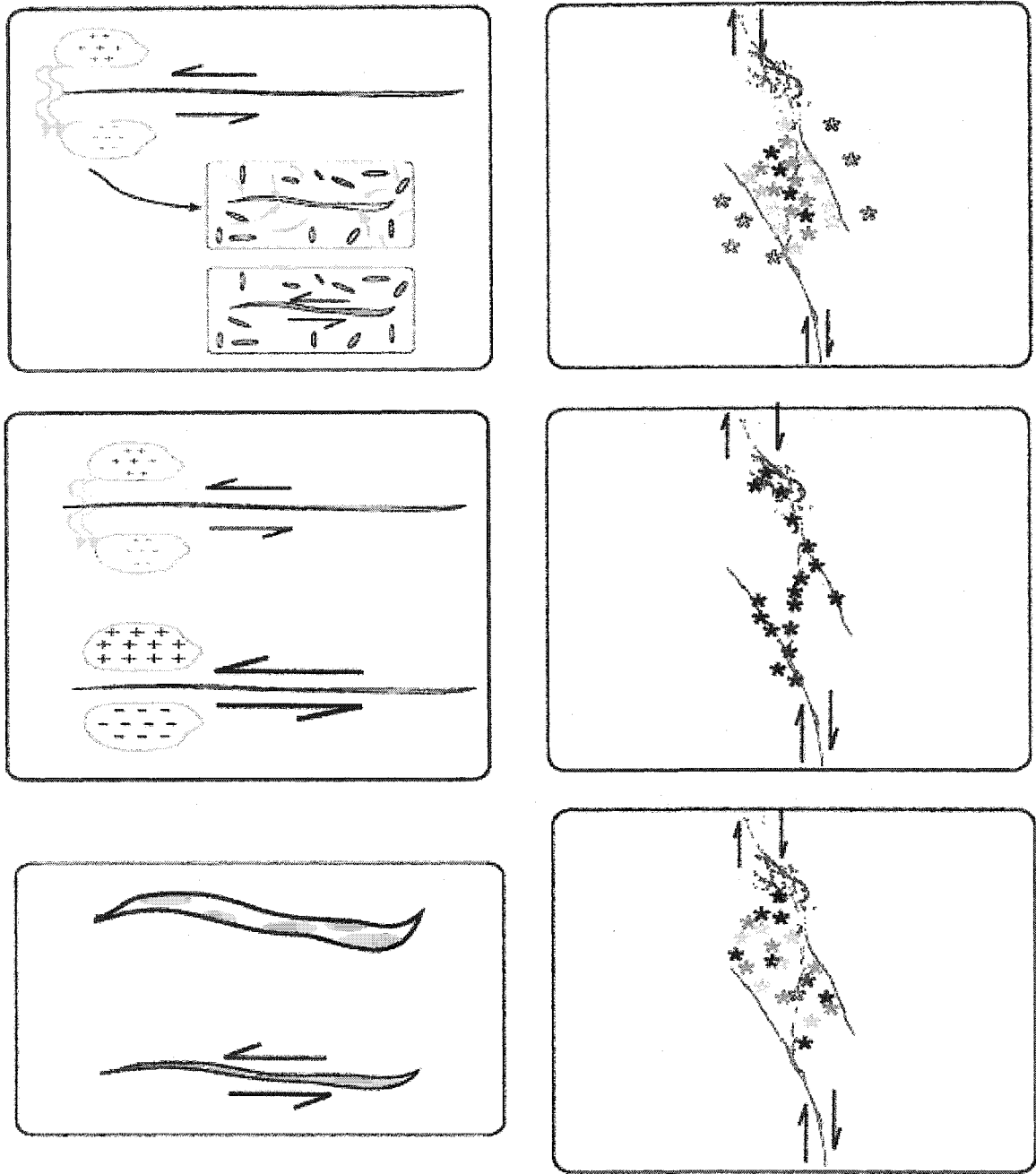


Figure 5.14: Illustration of different mechanisms of pore-fluid induced failure. Left panels are theoretical fluid movements and right panels are the ensuing aftershock patterns, where darker stars occur later in time. (a) fluid infiltration, (b) poroelastic stress increase, (c) pore space compaction. Descriptions of each mechanisms in the main text under Pore Fluid Models.

evolution of porosity (*Sleep and Blanpied, 1992*). Figure 5.14 is a cartoon illustrating the three mechanisms that we consider in our interpretation of the relocated seismicity.

PORE FLUID MODELS

Mechanism I: Pore Pressure Increase Due to Fluid Flow.

In this model, pore fluid migration decreases effective normal stress as fluid infiltrates areas of co-seismically reduced mean stress. In these areas, pore pressure will increase as pore-fluid flow re-equilibrates to the pressure gradient induced by the mainshock. This increase in pore pressure can trigger shear failure as it reduces the effective normal stress, i.e. the difference between normal stress, σ_n , and pore pressure, P , in accordance with the Coulomb failure criterion expressed in equation 2. As pore pressure rises in areas of dilatation, aftershocks will occur with a temporal signature related to the time it takes for fluid to migrate (*Rice and Cleary, 1975; Nur and Booker, 1972*).

Mechanism II: Poroelastic Stress Transmission.

In this model, additional shear failure is induced along a mainshock rupture plane when pore-fluid flows across the fault plane in response to pore pressure gradients induced by the mainshock. In areas of dilatation, pore pressure increases post-seismically, causing more expansion in that region. And as pore pressure decreases in areas of compression, contraction increases. This intensification of the induced pressure field causes additional strain on the fault, which stresses the fault in the direction of the original shear offset along the fracture (*Booker, 1974*). This model is coupled with Mechanism I since the movement of fluids creates the additional poroelastic stresses. Patterns in the seismicity, however, may allow us to determine which of the mechanisms is predominantly responsible for the aftershocks that occurred.

Mechanism III: Pore Pressure Increase Due to Compaction.

As with the fluid infiltration, this model depends upon the reduction of effective normal stress for slip along fractures within an area of post seismically induced dilatation. In this scenario, however, flow of pore fluids does not cause the increase in pore pressure. Post-seismically, the pore space induced by dilatancy by shear failure in the mainshock gradually heals, or is closed by creep (*Sleep and Blanpied, 1992*). As the pore spaces close, pore pressure increases, reducing effective normal stress and triggering earthquakes. Continuous aseismic creep may cause pore space compaction (*Sleep, 1994; Sleep and Blanpied, 1992*). There is no signature of this creep occurring over this duration in the aftershock sequence; however, since it would be happening at depth, and at the scale of the dilatant volume, it may not have a detectable deformation signature at the surface.

Any of these mechanisms may contribute to the protracted aftershock sequence we observe in the jog. To discriminate between these models we examine more closely the spatial and temporal evolution of the aftershocks. Our expectation is that each model may trigger earthquakes in different patterns. Mechanism I, fluid infiltration, should show a time dependent signature related to the rate at which fluid moves into the jog; it may also show a migration of aftershocks from the outside of the jog towards its interior. For Mechanism II, poroelastic stress increase, aftershocks should occur on the same fault planes that slipped during the mainshock. Also, this mechanism should affect the entire volume within the jog equally. Mechanism III, pore space compaction, is more difficult to test. We would not necessarily expect migration of aftershocks over time as with Mechanism I, and aftershocks may be triggered anywhere dilatant pore volumes are compacting post seismically.

EVIDENCE AGAINST POROELASTIC STRESS TRANSMISSION

80% of the aftershock activity within the jog falls on well-defined subfaults. Examining the spatial and temporal evolution of the aftershocks on these subfaults may help us understand if,

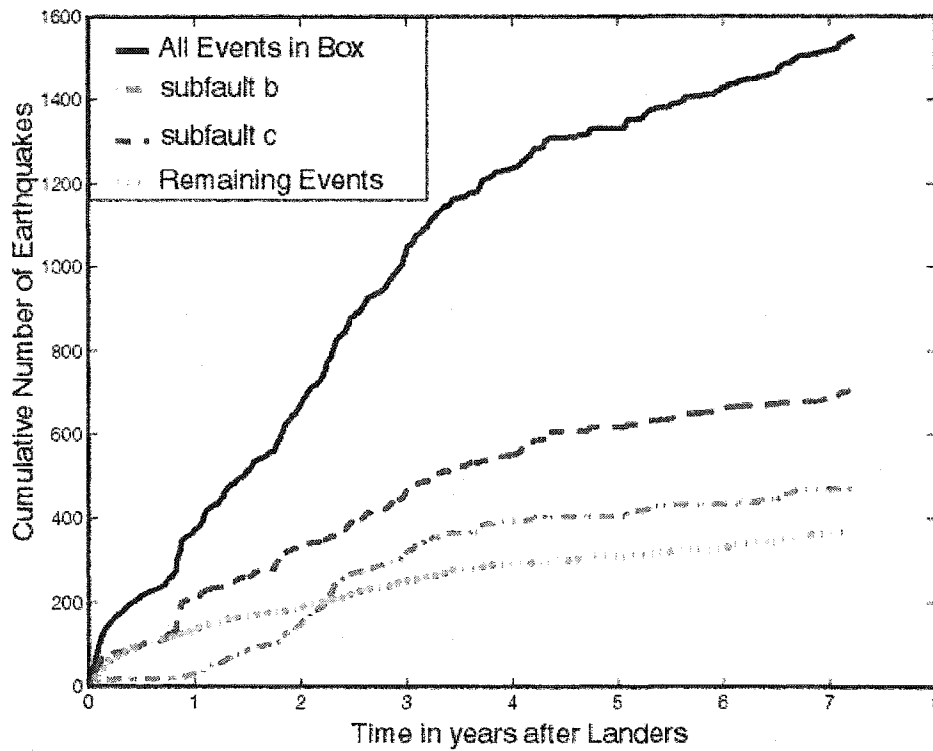
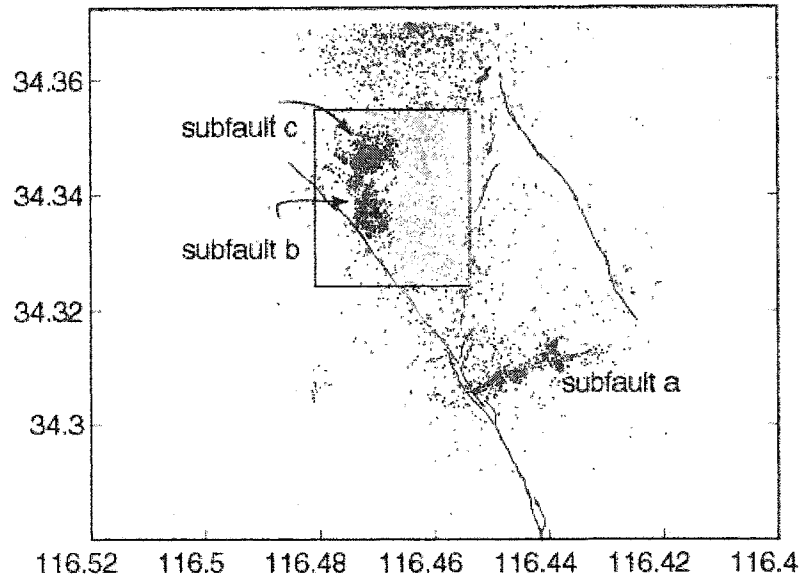


Figure 5.15: (a) Map defining different populations for the aftershock sequence in the jog. (b) Cumulative number of events in the regions described in (a). Both subfaults b and c (red and blue) have a protracted aftershock sequence, while other events in the jog do not.

and how, fluids may be triggering earthquakes in the jog. In Figure 5.15, the aftershock sequences on these subfaults are expressed as the cumulative number of events over time. The protracted sequence is clearly visible on the subfaults b and c, but is not apparent in the aftershocks diffusely distributed within the jog. Since these distributed aftershocks are not protracted relative to Omori's law, the pore fluid mechanism appears only to operate on the well-defined subfaults.

The approximately constant rate of aftershocks is different for each subfault. For instance, subfault b shows little activity until nearly a year after the mainshock, at which point the rate of aftershock occurrence increases to approximately 140 events per year. After 2.5 years the protracted sequence decays. For approximately three years, activity does not diminish on either subfault b or subfault c. This is true of the sequences for subfault a and d (Figure 5.4, trend 11 and trends 14 –15, respectively), as well.

Mechanism II, poroelastic stress transmission, does not appear to explain our observations. Were this mechanism triggering earthquakes it would stress both the subfaults as well as more distributed seismicity within the jog equally. Moreover, we do not observe protracted aftershocks on fault segments immediately outside the jog. There do not appear to be protracted aftershocks on nearly all of the continuous and planar segments of the Landers rupture, except perhaps in the northern part of the jog, on the very southernmost reaches of the Homestead Valley fault. Thus, mechanism II does not appear to play an important role in triggering aftershocks.

Mechanisms I and III, fluid infiltration and pore space compaction, both appear capable of explaining our observations. For mechanism I, fluid infiltration may occur along the large subfaults, which may act as conduits for fluid infiltration into the jog due to shear induced permeability. An estimate of diffusivity, using the overall time of the protracted sequence as a measure of saturation and the length of the jog, yields $c \approx 100$ cm/s. This is very high compared with laboratory measurements (*Li et al.*, 1984); however, well developed fracturing, as suggested by the subfaults within the jog, suggest that pore fluid migration may be fracture controlled and

thus conduct fluid more readily than would occur in a homogeneous medium. Mechanism I also provides a suitable explanation for the abrupt onset of the protracted sequence on subfault c. This sudden increase in aftershock activity would be related to the fluids infiltrating into the jog reaching the subfault.

The expected migration of aftershocks over time, however, is not clearly seen in the aftershock locations. If aftershocks occur along a fluid infiltration front, then they should migrate farther into the jog with time. None of the subfaults show a clear progression of earthquakes into the jog with time. In Figure 5.9, subfault a is conjugate to the JV fault, and aftershock focal mechanisms indicate left-lateral slip. Although there seems to be an apparent movement of events towards the JV fault over time, closer inspection reveals that the easternmost section of the subfault is active for a few months in 1993 and then shuts off completely. The rest of subfault a shows, at best, a subtle progression of events into the jog over time.

Figure 5.10 shows the timing of events and focal mechanisms, calculated in the same way, in subfault b. The aftershocks show a variety of mechanisms. The planes defined by the structures that emerge from the relocations are more consistent with right-lateral strike slip. There is, however, no clear progression of events into the jog over time. While it appears that there are more later events (colored red) occurring farther away from the JV fault, the result is not definitive.

Compaction, Mechanism III, does not necessarily predict a progression of events along the fractures, but it would cause aftershocks exclusively on fractures where porosity was created and then healed over time. Since we see aftershocks that exhibit a protracted sequence on specific fractures, we may expect porosity to be created exclusively along these secondary fractures within the jog. This would account for both the spatial and temporal patterns we see in the aftershocks. It is not possible, however, to rule out infiltration, Mechanism I, since fluid flow into the jog may be complex, making direct correlation to earthquake progression difficult to ascertain.

CONCLUSION

We find compelling evidence of aftershocks triggered by pore fluids in the 1992 Landers aftershock sequence. The signature of the pore fluid effect is a protracted aftershock sequence in a region of high postseismic mean stress decrease. The protracted sequence we find in the JV-HV fault jog lasts for nearly four years between 1993 and 1997, and is expressed as a constant rate of aftershock activity in that time interval. Omori's law, on the other hand, suggests that aftershocks rate should decay like a power law over time.

By studying the aftershock patterns determined by precise earthquake relocation, we may further characterize both the stress field in the fault jog and the pore fluid triggering mechanism. Using correlation techniques to obtain relative arrival time information, we relocate 8390 aftershocks within the jog with the double difference relocation method. The relocated aftershocks indicate a number of well-defined subfaults within the jog that correspond to secondary features expected in such a dilatational offset (*Sibson, 1986*).

Calculating the exact orientations of these secondary features allows us to perform a Coulomb stress analysis that would be otherwise impossible. Instead of calculating stresses on optimally oriented planes we can determine the Coulomb stress along the fractures that are actually active. We take advantage of this ability to determine the extent of the poroelastic effect on two fractures within the jog. We find an additional 0.2-0.4 MPa of stress acting on these planes due to pore fluid effects. This is substantial enough to trigger the earthquakes in the protracted aftershock sequences.

The precise fault plane orientations allow us to constrain the pore fluid mechanism further by using the spatial and temporal evolution of the sequences to eliminate certain models. We find that poroelastic stressing may play a secondary role to pore space compaction and fluid infiltration, since the protracted aftershock sequences occur exclusively on well-defined planes within the jog, not on the mainshock fault planes or in the diffuse swarms of seismicity also in the

jog. Fluid infiltration is also the most consistent with the abrupt onset of the protracted sequence on subfault c, and thus provides the most complete solution.

CHAPTER 6: STRESS CHANGE AND EARTHQUAKE TRIGGERING IN THE LANDERS EARTHQUAKE SEQUENCE

This chapter is being prepared for publication in G-cubed with co-authors J.H. Dieterich and G.C. Beroza.

ABSTRACT

We follow *Dieterich et al.* (2000) in using seismicity rate change as an indicator of Coulomb stress change and apply his method to examine stress interactions between the April 24, 1992 M 6.2 Joshua Tree earthquake, June 28, 1992 M 7.3 Landers, the June 28, 1992 M 6.5 Big Bear and the October 16, 1999 M 7.1 Hector Mine earthquakes. *Dieterich's* (1994) formulation allows us to resolve stress steps associated with these large earthquakes despite the lack of significant background activity in many of the areas. In addition to the stress step related to the Landers mainshock, we see evidence of continuing stress increase for approximately 4 years following, which we attribute to a post-seismic pore fluid pressure increase in the Johnson Valley – Homestead Valley fault jog. We also track the evolution of stress before the Hector Mine earthquake and find that small clusters of events in 1996 and 1999 stress the nucleation region of the Hector Mine earthquake. Finally, we observe stress changes in the Big Bear region and examine the potential far-field effects from the Hector Mine earthquake.

INTRODUCTION

The 1992 Landers earthquake sequence included four large events, the Apr 24th, 1992 M 6.1 Joshua Tree event, the June 28th M 7.3 Landers and M 6.5 Big Bear events and the October 16th, 1999 M 7.1 Hector Mine event, as well as over 60,000 aftershocks from 1992-2002 (*Sieh et al.*; 1993; *Hauksson et al.*, 1993; *Hauksson et al.*, 2002). These events occur on faults with

earthquake reoccurrence times measured in thousands of years (*Wesnowsky, 1986; Jennings, 1994*) so that their close temporal proximity indicates that they are closely related to each other. An important question for earthquake physics and in particular for earthquake forecasting, is how are they related?

The correlation between Coulomb stress changes and the locations of foreshocks, large earthquakes and aftershocks in the sequence has been well documented (*Stein et al., 1992; King et al., 1994; Harris and Simpson, 2002*). Most studies consider stress changes only from slip in the mainshock or large events and compare ensuing seismicity to these changes. This does not take into account possible stress changes from smaller events or the evolution of stress over time, which can be important, or even dominant, factors in earthquake triggering (*Kagan and Knopoff, 1981; Simpson and Reasenber, 1994; Abercrombie and Mori, 1996; Felzer et al., 2003*).

Dieterich (1994) proposed mapping fluctuations in Coulomb stress using a relationship between Coulomb stress increases and increases in seismicity rate developed from a model of earthquake nucleation under rate- and state-dependent friction. This approach successfully explains the time dependence of aftershocks following large earthquakes known as Omori's law, and has since been used to track the stress driving the rift system at Kilauea volcano, Hawaii.

In this study we apply the approach in different environment, the earthquake sequences involved in the Landers-Big Bear-Hector Mine earthquakes. In particular we are interested in documenting stress changes driving seismicity in the Johnson Valley – Homestead Valley fault jog, which ruptured in the 1992 Landers mainshock. Our interest stems from the observation that these earthquakes are protracted relative to earthquakes on the surrounding fault segments. Their temporal decay cannot be described by Omori's law with a lower p value. Rather, the aftershocks in the fault jog show a more or less constant rate of occurrence for years following the Landers mainshock. We have taken this as evidence that pore pressure changes due to the re-equilibration of pore fluids in the post Landers stress field are responsible. Pore fluid effects have been suggested independently as a mechanism for surface deformation in this jog (*Pelzer et al., 1996*)

and for aftershocks in the Landers sequence in aggregate (*Bosl and Nur, 2002*). By using Dieterich's method to determine the stress history in the jog implied by the protracted aftershock sequence, we hope to constrain models of the pore pressure changes responsible for the triggering.

We also examine the evolution of stress prior to the onset of the Hector Mine earthquake. Previous stress triggering studies have suggested that the Hector Mine earthquake may have fallen in the stress shadow of the Landers earthquake (*Harris and Simpson, 2002*), that the mainshock may have ultimately have been triggered by the dynamic field of the Landers mainshock (*Kilb, 2002*), that the loading due to visco-elastic relaxation of the lower crust following the Landers earthquake may have been responsible (*Freed and Lin, 2000*), or that the 1992 M5.4 Pisgah event, which occurred about a week after the Landers mainshock, may have been part of a cascade of failure that ultimately triggered the Hector Mine earthquake (*Felzer et al., 2003*). Our findings support this last notion that smaller events including several that occurred in 1996, due to their closer proximity to the future Hector Mine mainshock initiation point, were crucial in triggering that earthquake.

We examine the effects of the Hector Mine earthquake on earthquake triggering in the Big Bear area. Although it is somewhat distant from the Hector Mine earthquake, we find that two areas in the region appear to be stressed following the Hector Mine earthquake. The seismicity in the Big Bear area had significantly decreased by 1999, until the Hector Mine earthquake. The San Bernardino segment of the San Andreas Fault, and the Banning Fault, also show evidence of Coulomb stress increase following the Hector Mine earthquake. Finally, we examine whether the stress changes in the area are truly due to the Hector Mine earthquake.

CALCULATING STRESS CHANGE FROM SEISMICITY RATE

Triggering of earthquake activity is often attributed to changes in the Coulomb stress (*Das and Scholz, 1982; Stein and Lisowski, 1983*), which suggests it should be possible to resolve

stress change using earthquake rates. Due to the non-linear nature of the interaction of stress and earthquake rate, it is important to properly model the relationship between stress and earthquake occurrence. To this end, *Dieterich* (1994) developed a theory for earthquake triggering based on nucleation under rate- and state-dependent friction for an earthquake population that without a stress perturbation would have experienced a constant rate of seismicity. Rate- and state-variable friction is observed in laboratory experiments on a wide range of materials (*Dieterich*, 1994) and has been used to explain both the t^{-1} time-dependence of aftershock rates and the duration of aftershock sequences as a function of the long-term stressing rate. In this formulation, the rate of earthquake activity R can be expressed as

$$R = \frac{r}{\gamma \dot{S}_r} \quad (6.1)$$

where γ is a state variable, r is the steady-state earthquake rate at the reference stressing rate, \dot{S}_r . State evolves with time, t , as:

$$d\gamma = \frac{1}{A\sigma} [dt - \gamma dS] \quad (6.2)$$

where A is a dimensionless fault constitutive parameter with values ranging from 0.005- 0.015 in laboratory measurements (*Dieterich*, 1994; *Dieterich and Kilgore*, 1996; *Scholz*, 1998), and S is the modified Coulomb stress function defined as

$$S = \tau - \mu\sigma \quad (6.3)$$

where τ is shear stress acting across a fault plane, μ is the coefficient of friction, and σ is the effective normal stress, i.e., the normal stress less the pore pressure. If a stress step is introduced, equations 6.1 and 6.2 indicate that the R will develop in time according to an Omori t^{-1} aftershock decay law. The ensuing aftershock duration is defined as,

$$t_a = \frac{A\sigma}{\dot{S}} \quad (6.4)$$

where \dot{S} is the stressing rate. This is an important step, because the aftershock duration is more readily determined from an aftershock sequence than is the stressing rate. Stress change can be estimated from these relationships following *Dieterich (2000)*. Stress over time is determined by calculating γ over time from equation (1). Change in stress is then calculated for a stress step in the middle of the time step Δt ,

$$\Delta S = A\sigma \ln \left[\frac{\gamma_i + \frac{\Delta t}{2A\sigma}}{\gamma_{i+1} - \frac{\Delta t}{2A\sigma}} \right] \quad (6.5)$$

where γ_i and γ_{i+1} are estimates of γ at the beginning and end of the time step. Since changes in σ are considered small compared to σ , $A\sigma$ is effectively constant and the stress solution may be normalized by it. Stress histories can be obtained for specific volumes of seismicity by solving equation 5 for successive time intervals.

The spatial distribution of stress in a specific time interval is similarly calculated by assuming constant \dot{S} before and after a stress step. Maps of Coulomb stress for a time period may be obtained in this way for a gridded area defined by the seismicity. Figure 6.1 shows the 120×110 km region we investigate, including the Joshua Tree, Landers, Big Bear and Hector

Mine earthquakes and aftershocks. Our data consists of earthquakes for a 10 year period, between 1992 and 2002, of magnitude 1.5 and greater, giving us a total of over 63,000 events in the sequence. A magnitude minimum of 1.5 is appropriate for this region because the completeness level of the Southern California Seismic Network, SCSN catalog is at least M 1.5 in general. This level is only degraded following large earthquakes like the Landers event, after which the completeness magnitude increased to M.3 for weeks after the mainshock (*Weimer and Katsumata, 1999*). We obtain times and locations from the SCSN catalog. Where available we replace event locations with those obtained by double-difference relocation; however, at the scale of our grid, the improved locations do not substantially influence our results.

Seismicity rates are obtained by taking a cylindrical volume of seismicity, defined about the center points of a grid. The grid points, or nodes, are evenly spaced horizontally, and the depth extent, which defines the height of the cylinder, we take from 0 to 15 km. Solutions are only obtained for grid points, or nodes, that meet a minimum average earthquake frequency per year. If the initial volume does not include enough events to meet this criteria, the search radius is increased incrementally until the criteria is met, or the maximum search radius is reached. *Dieterich (2000)* use a minimum of 8 earthquakes per year and a maximum search radius of 2.83 km. We increase the minimum earthquake rate to 16 earthquakes per year to improve the robustness of our results. In order to best describe the stress histories for different earthquake sequences, we perform multiple inversions, varying the grid spacing from a minimum of 0.5km, and a maximum search radius of 6 km, to a grid spacing of 2 km, and maximum search radius of 2km, depending on the area or earthquake sequence we are observing.

A key parameter in this approach is the aftershock duration, t_a , which ranges from 1.5 to 4 years. This value is determined by examining the rate of aftershock activity within a specified area and is modified using a trial and error approach to produce a seismicity response that corresponds to an initial step in the immediate aftermath of the mainshock. On average, $t_a = 2.5$ yr and this value is used by default when there is not sufficient seismicity to determine it.

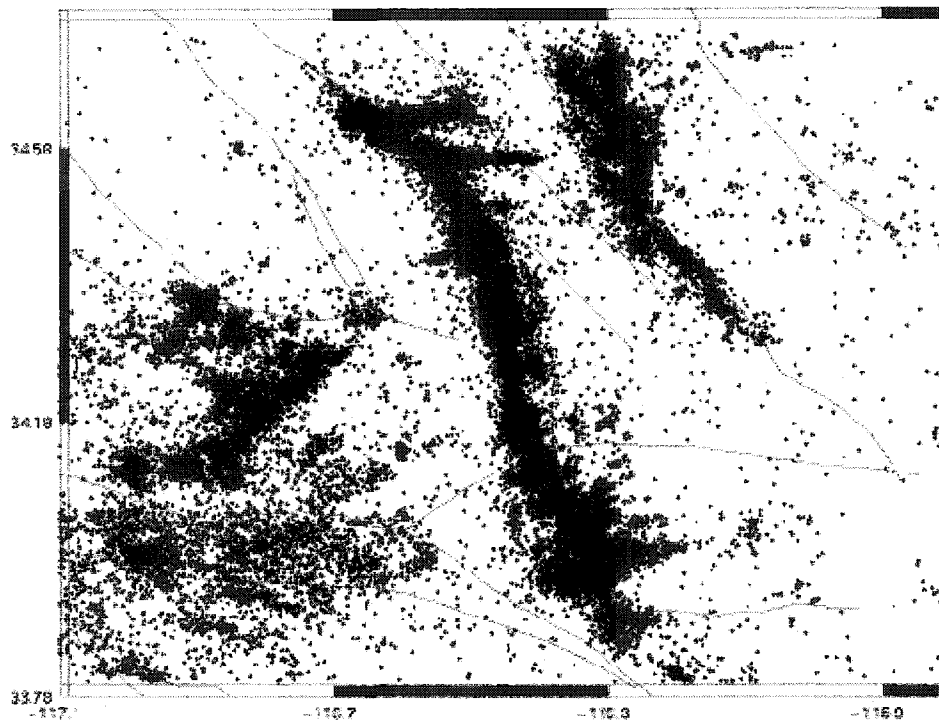


Figure 6.1: Map view of aftershocks of the Landers, Big Bear and Hector Mine earthquakes for 10 years, 1992 -2002. Black lines indicate major faults in the region as well as the surface ruptures of the Landers earthquake and the Hector Mine earthquake.

This value is similar to values obtained independently by *Gross and Kisslinger (1997)* for the Mojave region. The Hector Mine event, in particular, has a short aftershock duration, ~ 1.5 yr. This is convenient for our purposes because it allows us to perform some analysis of stress change in the area even with only slightly more than two years of data.

$A\sigma$ appears only as a product in *Dieterich's* formulation so it is not necessary to estimate A and σ independently; however, the product is still difficult to measure. A can range over an order of magnitude and σ depends not only on the normal stress but also on the pore pressure. *Gross and Kisslinger (1997)* find values of A for the Mojave region that range from 0.0003, assuming a pore pressure of zero, to 0.01 assuming the pore pressure approaches lithostatic

pressure. Using $\rho=2600 \text{ kg/m}^3$ and a representative depth of 3 km, $A\sigma$ can range from 0.75 to 0.02 MPa, we assume hydrostatic pore pressure and a value of A that is consistent with both laboratory values and values inferred for the Mojave region. This leads to a value of $A\sigma$ of 0.35 MPa. Below we examine how well this value fits data from other measurements of Coulomb stress.

Using this procedure, we are able to map Coulomb stress changes for the regions of active seismicity in the Mojave and San Bernardino Mountain blocks. Since the method relies upon seismicity rates, we cannot interpret stress changes when and where there is no seismicity. Notwithstanding this limitation, we are able to get a comprehensive picture of Coulomb stress history in the Landers earthquake sequence.

STRESS CHANGES AT LANDERS

The 1992 M 7.3 Landers earthquake significantly increased seismic activity throughout Southern California, triggering earthquakes at Big Bear, Hector Mine, and as far away as the Long Valley Caldera and Yellowstone, Wyoming (*Hill, 1994; Hauksson et al., 1993*). The majority of Landers aftershock sequence died away within 1.5 years. Without considering the occurrence of the 1999 M 7.1 Hector Mine event, the Landers earthquake was expected to influence seismicity in the region until ~2007 (*Gross and Kisslinger, 1997*).

In this study we use seismicity rate changes to estimate time-dependent stress changes due to the Landers sequence. This is complicated somewhat by the generally low background seismicity in much of the region prior to the April 24th, 1992 Joshua Tree earthquake. We first examine the Coulomb stress change associated with the 1992 Joshua Tree earthquake. The entire 120×110 km area is used in this analysis, with a grid spacing of 1 km in both directions and a maximum search radius of 5km. Figure 6.2 shows the radii used in the analysis as a function of position.

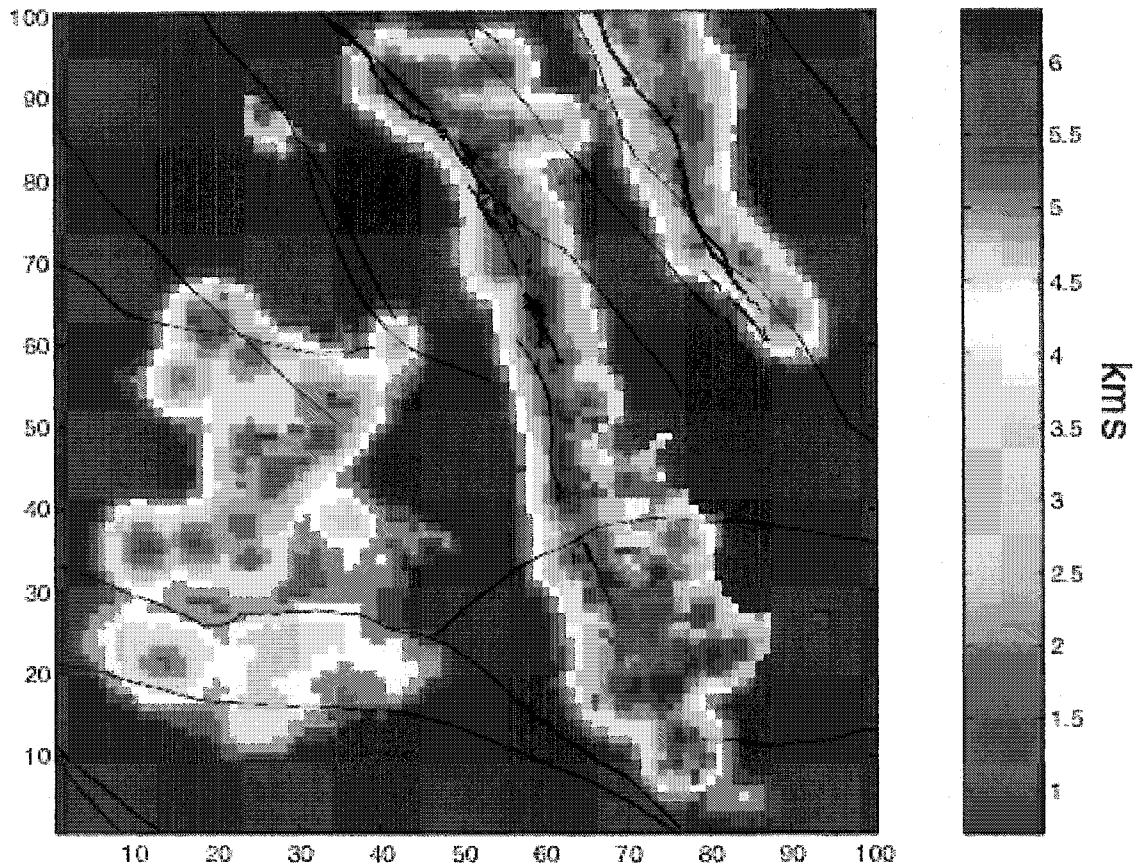


Figure 6.2: Map of the number of radii needed to meet the minimum earthquake requirement. Areas in red are not as reliable as those in blue. Nodes farther from the majority of seismicity are less reliable. Most nodes of interest have radii <4 km.

In our analysis we consider events immediately after the April 24th, 1992 Joshua Tree event up to the initiation of the June 28th, 1992 Landers earthquake. Areas in green represent nodes where a solution is calculated at some time step, but which undergo no stress change in the current time step, areas in red represent an increase in Coulomb stress, and areas in blue denote decreases in Coulomb stress in the time step. White areas have no solution calculated at any time. Stress is increased, as expected, near the area of the Joshua Tree rupture. For the most part, this

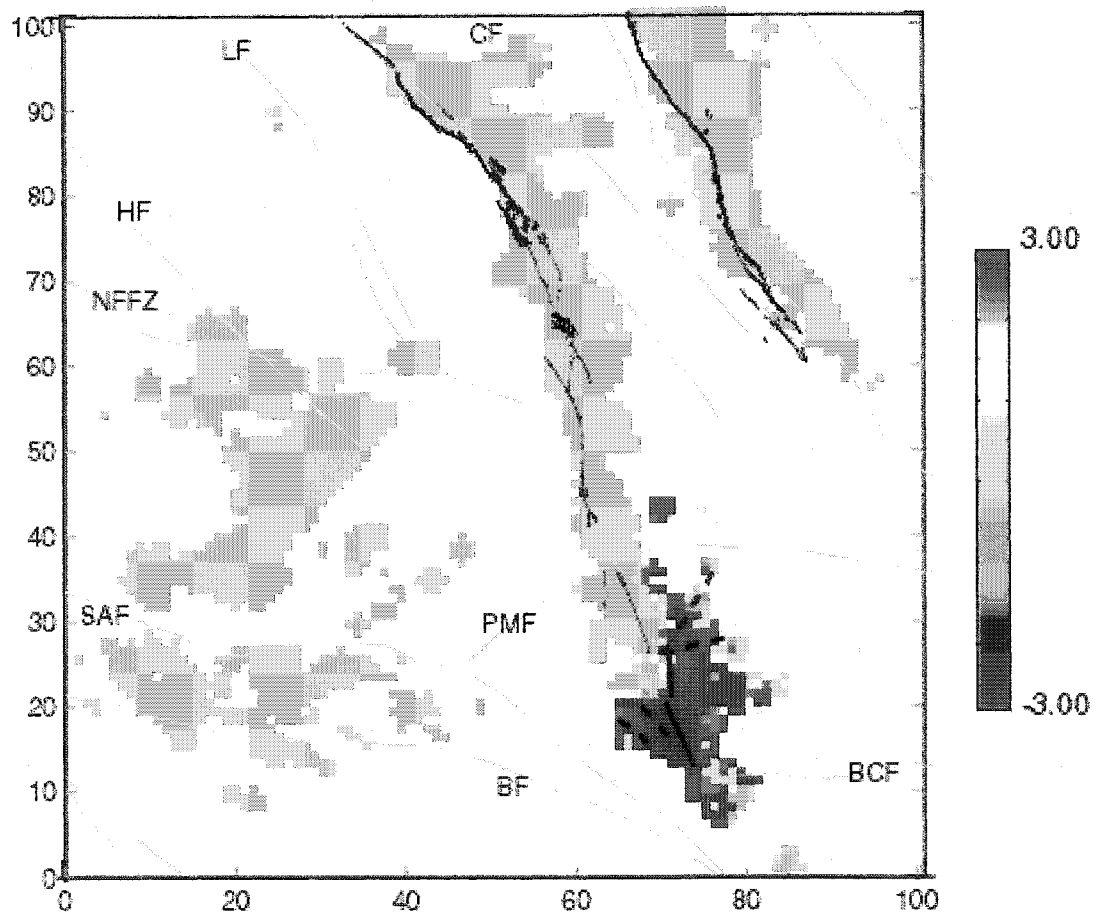


Figure 6.3: Coulomb stress change following the Joshua Tree earthquake. Color indicates normalized Coulomb stress change. Time interval compares two months prior to the event with two months after the event. Thick solid black lines indicate the rupture planes of the Joshua Tree earthquake. Dashed lines are the trends of secondary features active following the Joshua Tree earthquake. Major faults are marked as follows: SAF: San Andreas Fault, BF: Banning Fault, NFFZ: North Frontal Fault Zone, HF: Helendale Fault, PMF: Pinto Mountain Fault, CF: Calico Fault. Stress increase is mapped primarily in the aftershock sequence of the earthquake. A slight increase is registered near the site where the Hector Mine earthquake eventually initiated. Other areas are not significantly affected.

earthquake did not strongly affect seismicity in the region outside of the immediate aftershock zone. It is clear, however, that there were an abundance of off-fault aftershocks within a source length of the Joshua Tree mainshock. It is difficult to see an evolution of stress on the Landers fault planes due to this earthquake because a suitable time step that provides an accurate stress average while excluding the effects of the Landers mainshock, which occurs 2 months later, is not possible. The number of aftershocks for an earthquake of such modest magnitude, however, approximately 6000 over a two-month time period, is exceptional.

Three clusters of earthquake of earthquakes occur to the north of the Joshua Tree earthquake, near the future location of the Landers earthquake. One of these clusters is the foreshock sequence of the Landers earthquake, and it is visible as a small stress increase in Figure 6.3. The other two clusters occur to the east of the foreshock sequence. They are also apparent in Figure 6.3 as a single red area to the right of the bifurcation in the Johnson Valley fault. These two clusters are not active after the Landers earthquake. The slight stress increase near the future location of the Hector Mine earthquake is the result of a single M 2.4 earthquake. Although there are a few, small, isolated clusters of earthquakes near the Bullion Fault prior to this event, this is the only event within a 4 km radius in the 30 years prior to the Hector Mine earthquake.

The M 7.3 Landers mainshock occurred approximately two months after the M 6.1 Joshua Tree event. Figure 6.4 shows the post seismic stress change associated with this event. Coulomb stress increases dramatically in most of the region. From our estimated value of $A\sigma = 0.35$ MPa, stress changes are as large as 1.2 MPa, much higher than the approximately 0.5 MPa predicted by *Stein et al.*, (1992). This may suggest that we have overestimated $A\sigma$, or perhaps that stress changes due to aftershocks play an important role in the evolution of the stress field (*Felzer et al.*, 2002).

The Big Bear region, as well as part of the San Andreas Fault also experience stress changes from this earthquake. Most of the area around Joshua Tree event, however, shows either

no increase in Coulomb stress, or a noticeable decrease. The off-fault aftershocks to the northeast and to the east of the southern end of the Landers rupture zone which were active leading up to the Landers earthquake shows a large decrease in stress. These aftershocks, delineating northeast trending and east-west trending planes, fall in the compressional quadrant of the Landers rupture, and as such are expected to experience a decrease in stress. The off-fault structures that trend in a NW direction to the west of the Joshua Tree mainshock, and a set of events between the Blue Cut and San Andreas faults are restressed by the Landers earthquake. The sequence of earthquakes near the San Andreas Fault is composed of two discrete clusters, one following the Joshua Tree earthquake and the other after Landers. Aftershock activity and stress die away soon after the Landers earthquake.

The Joshua Tree mainshock planes are interesting in that there is no increase or decrease in stress there following the Landers earthquake. This apparent lack of a stress change could mean that stress produced from the Landers event on the Joshua Tree rupture zone are relaxed by creep and this leads to stress increase only at the ends of the rupture zone. Afterslip was recorded near the Eureka Peak fault to the north (*Hough et al.*, 1993; *Massonnet et al.*, 1994), as well between the Pinto Mountain and Johnson Valley Fault (*Peltzer et al.*, 1994). There is, however, no clear geodetic information for creep near the Joshua Tree mainshock. InSAR data is not available prior to Landers, and is poor in the region following the event.

The area near the 1992 M 5.4 Pisgah event, to the northeast of the Landers rupture, and the future location of the 1999 Hector Mine earthquake, shows a clear increase in Coulomb stress, despite the fact that in static stress triggering studies this area is within the stress shadow of the Landers earthquake (*Harris*, 2000; *Harris and Simpson*, 2002). We will look more closely at that sequence of events in the Hector Mine section below.

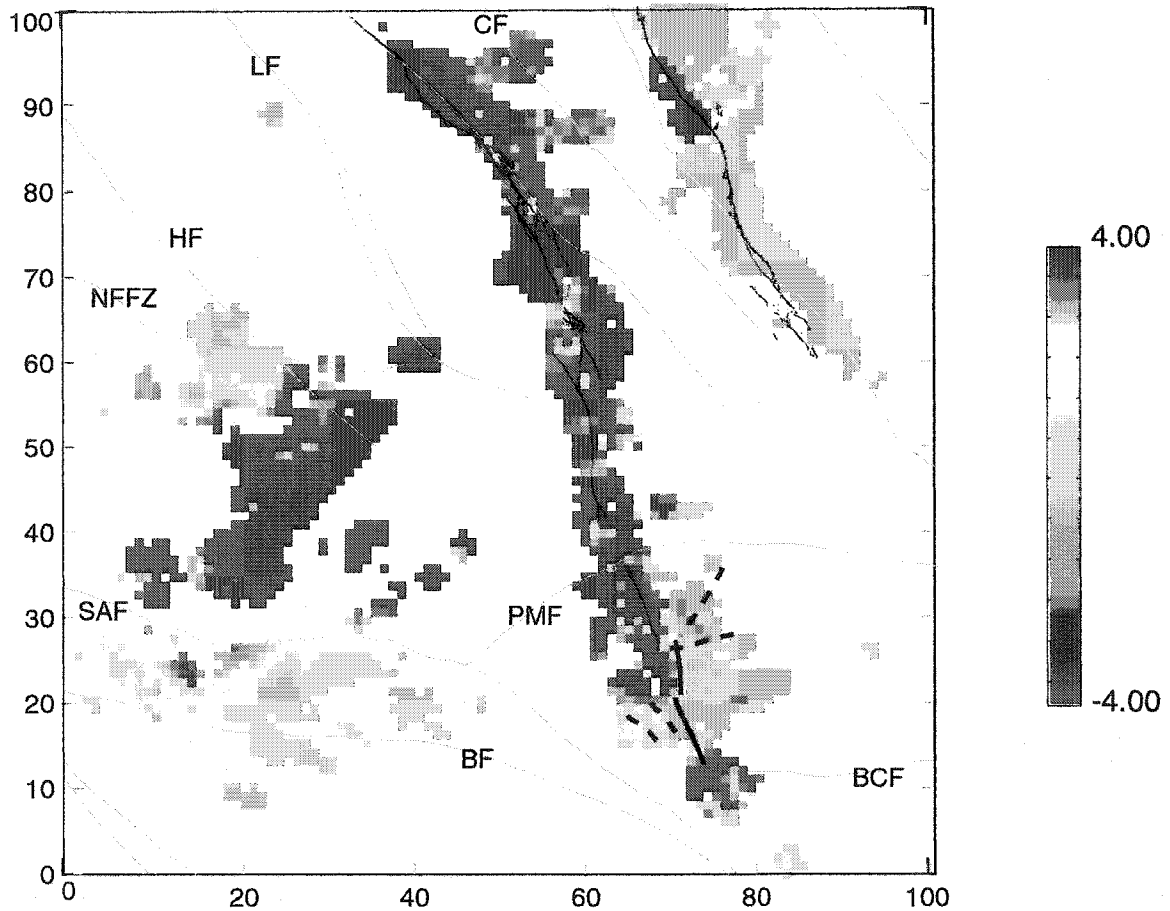


Figure 6.4: Stress change immediately after the 1992 Landers earthquake for the entire region. Color represents stress change; red is increase in stress, blue is a decrease. Thick solid black lines are mainshock rupture planes of the Joshua Tree earthquake. Dashed lines are secondary features. Thin black lines are the surface ruptures of the Landers and Hector Mine events. Major faults are labeled as in Figure 6.3.

EVIDENCE OF STRESSING FROM PORE FLUID EFFECTS

Evidence of pore fluid effects in the Landers sequence has been invoked not only to explain InSAR measurements of surface deformation (*Peltzer et al.*, 1996; 1998), but also to account for unusual aftershock behavior during the aftershock sequence (*Beroza et al.*, 2003), and for triggering of the aftershock sequence as a whole (*Bosl and Nur*, 2002).

In our analysis we focus on the signature and extent of the stress increase in the JV-HV jog. The signature of pore fluid in the aftershock sequence is noted by *Beroza et al.* (2003) as a deviation from the typical t^{-1} decay described by Omori's law for aftershock decay. In particular, the aftershock sequence in the fault jog is protracted with a rate of aftershock occurrence that remains elevated for approximately 4 years, between 1993 and 1997, as pore fluids gradually re-equilibrate to the stress field generated by the Landers mainshock. Since a single stress step leads to the t^{-1} decay of a typical aftershock sequence (*Dieterich, 1994*), we expect the stress signature of the protracted aftershock sequence to be an increase in stress with time.

First, we consider the total change in Coulomb stress expected from pore pressure changes within the jog. As shown in Chapter 5, Coulomb stress calculations that simulate the transition from the undrained to the drained state, suggest that on the faults activated in the jog a stress change of up to 0.3 MPa could be due to pore pressure changes (*Zanzerkia and Beroza, 2003*). In this model slip during the mainshock is used to calculate stresses based on the method of *Okada* (1985). The incremental stress change due to the poroelastic effect is determined by taking the difference in Coulomb stress in the drained and the undrained state. The difference between the undrained and drained state may be emulated by changing Poisson's ratio from 0.27 for the drained and 0.31 for the undrained (*Rice and Cleary, 1976*). We use a larger value for the undrained value, 0.35, obtained by *Peltzer et al.* (1998) for this region.

To compare our result with the stress modeling from the aftershock rate, we plot the difference in Coulomb stress between 1993 and 1997, averaging over 0.5 yr in order to eliminate noise and short-term stress changes. Figure 6.5 shows, in map view, that in this time period most of the area is either experiencing a decrease in stress or showing no change in stress. The JV-HV fault jog, however, shows a clear increase in stress over those 4 years. The increase is significant; using values of $A\sigma$ determined from *Gross and Kisslinger* (1997), the stress change is inferred to be 0.7-1.2 MPa.

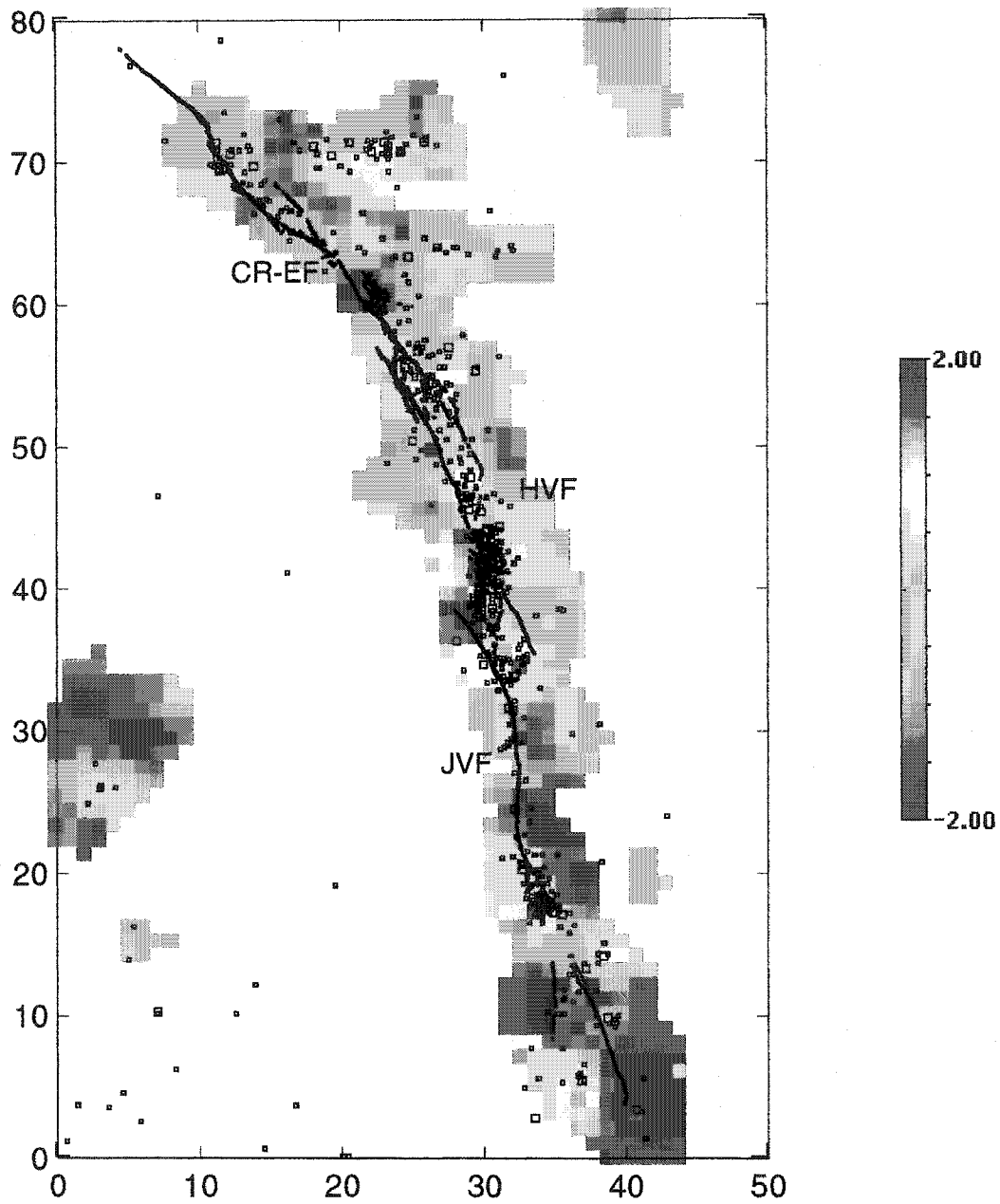


Figure 6.5: Stress change along the Landers mainshock planes between 1993 and 1997, averaging over 0.5 yr. Red areas show an increase in stress over the time period. The JV-HV fault jog shows an increase in stress over this time period. Black lines are the Landers surface rupture. CR-EF: Camp Rock – Emerson Fault, HVF: Homestead Valley Fault, JVF: Johnson Valley Fault.

We find the results that fit best with our Coulomb stress modeling and with the stress change equivalent to the protracted sequence in the jog suggests a value of $A\sigma$ of 0.15 – 0.2 MPa. We find this value by calculating the factor that will equate the maximum value in the stress change from aftershock rate with the maximum stress change from the Coulomb stress modeling. This value is somewhat low compared to values between 0.25 - 0.45 MPa found by *Dieterich* (2000) for Kilauea volcano, Hawaii, from comparisons of normalized Coulomb stress and deformation modeling.

Our value may be appropriate for an area of relatively high pore pressure. This is consistent with other evidence of the existence of high fluid pressure in the crust and its importance in the faulting process. The presence of super-hydrostatic pore pressure within the crust has been widely acknowledged as present in such regimes as sedimentary basins at depth (*Fertl et al.*, 1976), as potentially important in crustal deformation (*Fyfe et al.*, 1978), as well as seismic rupture (*Davis et al.*, 1983; *Sibson*, 1990). The presence of high fluid pressures within the fault jog would be consistent with evidence of active faulting associated with stress dependent dilatancy (*Parry et al.*, 1991; *Coombs* 1993; *Sibson* 1994).

Since the inversion produces a stressing history, we relate changes in stress within the jog during the transition to the drained state with time-dependent changes in pore pressure. We find stress as a function of time for specific fractures that are defined by relocated seismicity within the jog. To incorporate our knowledge of the active features in the jog, we use a grid spacing of 2.5 km, with a maximum radius fixed at 2.5kms, and position the nodes to include only one or part of one feature determined by earthquake locations. We plot stress vs. time in Figure 6.6 for various nodes inside and outside the jog. Also plotted is a loess fit to the curves; the loess fit gives the overall trend beneath short-term fluctuations in stress (*Cleveland*, 1979). Some of the short-term stress changes may be artifacts due to random variations in seismicity or due to catalog fluctuations (*Dieterich*, 2000); however, they also may represent real changes in the stressing rate.

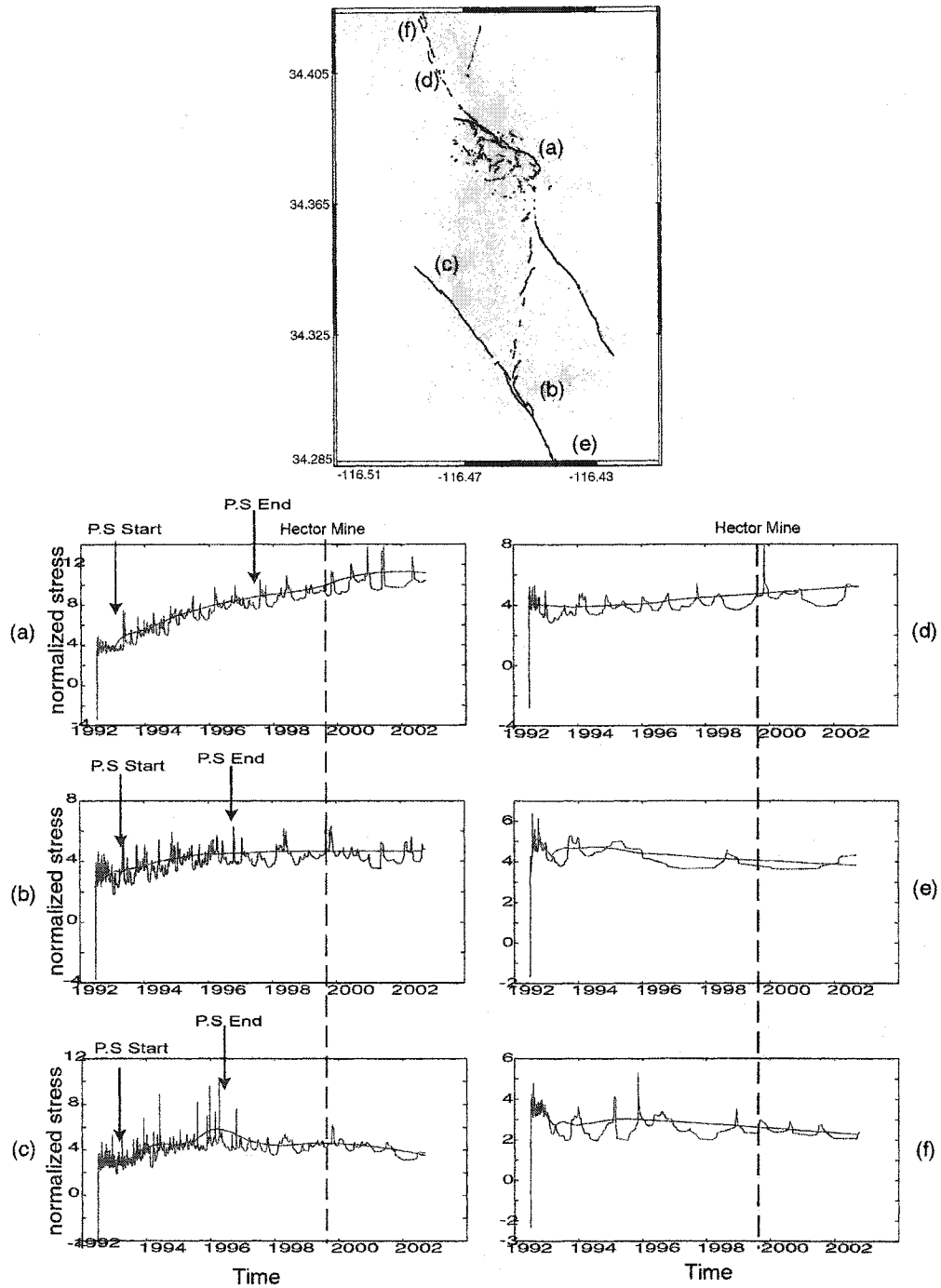


Figure 6.6: Map view of the JV-HV fault jog, as well relocated Landers aftershocks. Letters indicate locations of the nodes where stress histories were recovered. Stress vs. time for various nodes corresponding to fractures within the JV-HV fault jog; (a), (b), (c) are fractures within the jog; (d) (e) (f) are outside the jog. P.S. = Protracted aftershock Sequence. Pore pressure, and therefore stress, should gradually increase within the jog, (nodes a, b, and c).

The stress histories outside the jog (e) and (f) show a clear stress step associated with the Landers mainshock and not much else. Those within the jog, (a-c), show an initial stress step with the mainshock, but continue to accumulate a stress change afterwards. Approximately 0.5 years after the mainshock these sequences show varying degrees of stress increase until sometime in 1997, with a net change ranging from 0.5 ± 0.1 MPa. Nodes (a) and (b) show a fairly linear trend with time, while node (c) shows a brief period where stress remains constant before increasing again in two increments, perhaps related to the fact that this node contains two main seismicity features of different depths and orientation (Chapter 5). Although no discernable time-dependence was seen in the spatial patterns of aftershocks on these features, the stress history points to stress changes at different times on different planes.

We believe that the change in Coulomb stress is the signature of changes in pore pressure over time. To the first order, through equation (6.3), changes in Coulomb stress can be equated to changes in pore pressure. Poroelastic modeling guided by the inferred stress history could, in principle, motivate a more complete analysis of the evolution of pore pressure in the jog. This evolution of pore pressure in time and space would be important for understanding changes not only in seismic displacements but also in hydraulic material properties such as permeability, which are often taken as constant but have been shown to be heterogeneous (*Hickman et al.*, 1995; *Bosl*, 2003).

We also look for stress changes in the fault jog due to the 1999 Hector Mine earthquake. The dashed line in Figure 6.6 shows the onset of the Hector Mine event. Although the Hector Mine mainshock is only 40 km away, for most nodes along the Landers rupture, there is minimal stress change. To the north of the jog, there is a brief spike in stress following the mainshock in node (d). Nodes within the jog appear to show an increase in stress from Hector Mine, of ~ 0.4 MPa initially. We also note that within the jog stress does not continue to increase in the same trend as before 1997. In two of the sequences, nodes (b) and (c), stress shows a general trend of stress decrease for the next two years, while node (a) shows an increasing trend in the same time

period. There is no clear stress step, however, following the Hector Mine earthquake-only periodic bursts of stress increase or decrease, so these changes may be associated with continuing small clusters of earthquakes unrelated to the Hector Mine earthquake.

STRESS HISTORY LEADING UP TO THE HECTOR MINE EARTHQUAKE

The 1999 M 7.1 Hector Mine earthquake occurred over 7 years after the Landers earthquake and approximately 30 km to the Northeast of the Landers' mainshock hypocenter. Given that large earthquake recurrence intervals are measured in millennia it seems inescapable that the Hector Mine event was triggered by the Landers event. The mechanism of triggering is uncertain, however, and ideas range from direct stress triggering by the static stress change of the Landers mainshock (*Parsons and Dreger, 2000*) and delayed dynamic triggering by the Landers mainshock (*Kilb, 2001*) to postseismic viscoelastic relaxation following Landers (*Freed and Lin, 2001; Pollitz and Sacks, 2002*) and a slow cascade of failure starting with the 1992 Pisgah event and continuing through 1996 near the hypocenter of the Hector Mine mainshock (*Felzer et al., 2002; Harris and Simpson, 2002*). We now look at the stressing history determined from the seismicity to understand better the evolution of stress prior to the Hector Mine earthquake.

Figure 6.7 shows the location of the Hector Mine rupture and the Coulomb stress change in the area immediately following the Landers earthquake. Stress changes that might be due to the M 5.4 July 5, 1992 Pisgah event are not distinguishable from those due to the M 7.3 June 28, 1992 Landers earthquake because the events occur within the same time interval. Stress change along the Lavic Lake fault is approximately 0.8 MPa. Much of the future Hector Mine rupture zone shows an apparent decrease in stress, except for the region near, but to the west of the eventual Hector Mine hypocenter. The region near the eventual mainshock hypocenter (marked by the star) experiences less stress from the Landers and Pisgah events - about 0.3-0.4 MPa.

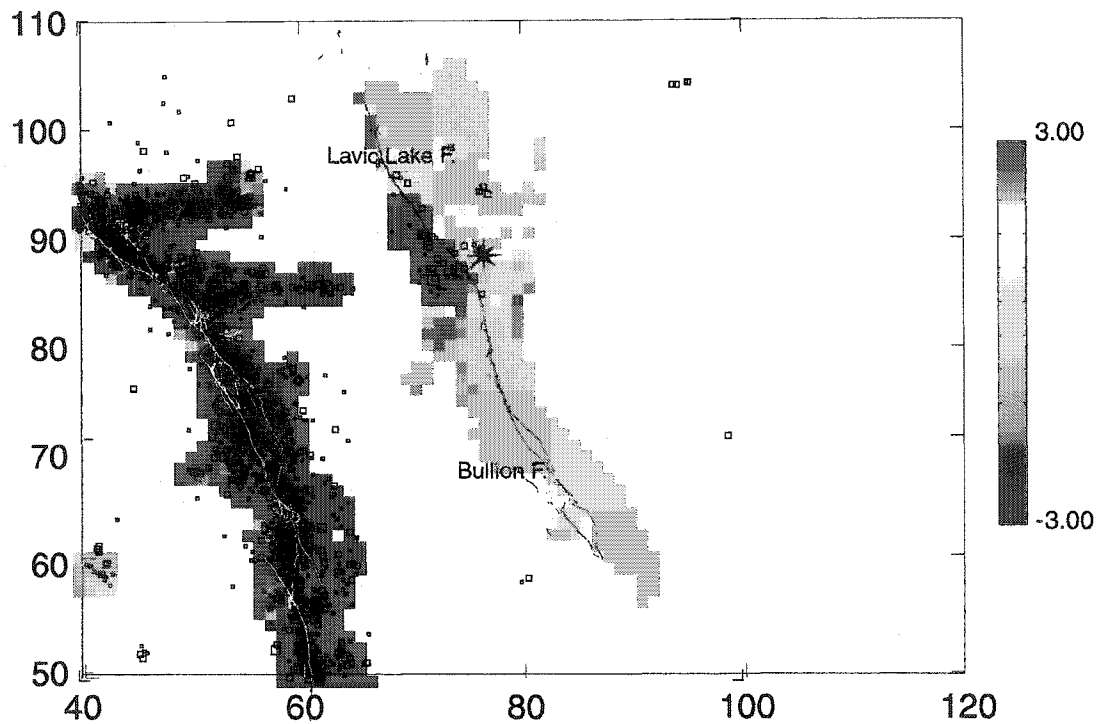


Figure 6.7: Coulomb stress changes in the Hector Mine area post-Landers. White lines indicate Landers rupture, and black lines are Hector Mine surface ruptures. Squares are Landers aftershocks. Red areas indicate stress increase. Axes are in km.

To understand what may have triggered the Hector Mine earthquake, we plot normalized Coulomb stress over time in Figure 6.8 for various nodes including the node that contains the Hector Mine hypocenter (Figure 6.8f). Time is in years after 1992, so the Hector Mine earthquake occurred at year 7.79. Prior to the Hector Mine earthquake the greatest stress increase occurs near the end of 1996 (year 4). We find that this jump corresponds to a cluster of earthquakes that occurred from August through October 1996. The slight decrease after the onset of the stress step may be attributable to either a poorly defined aftershock duration, or some kind of dynamic triggering while the earthquakes are occurring. The stress change related to the 1996 events are clearly seen in nodes 731 and 693, which are situated near the Hector Mine hypocenter, and node 653, on the Lavic Lake Fault. Nodes 446, which falls on the Pisgah Fault, and node 372, which

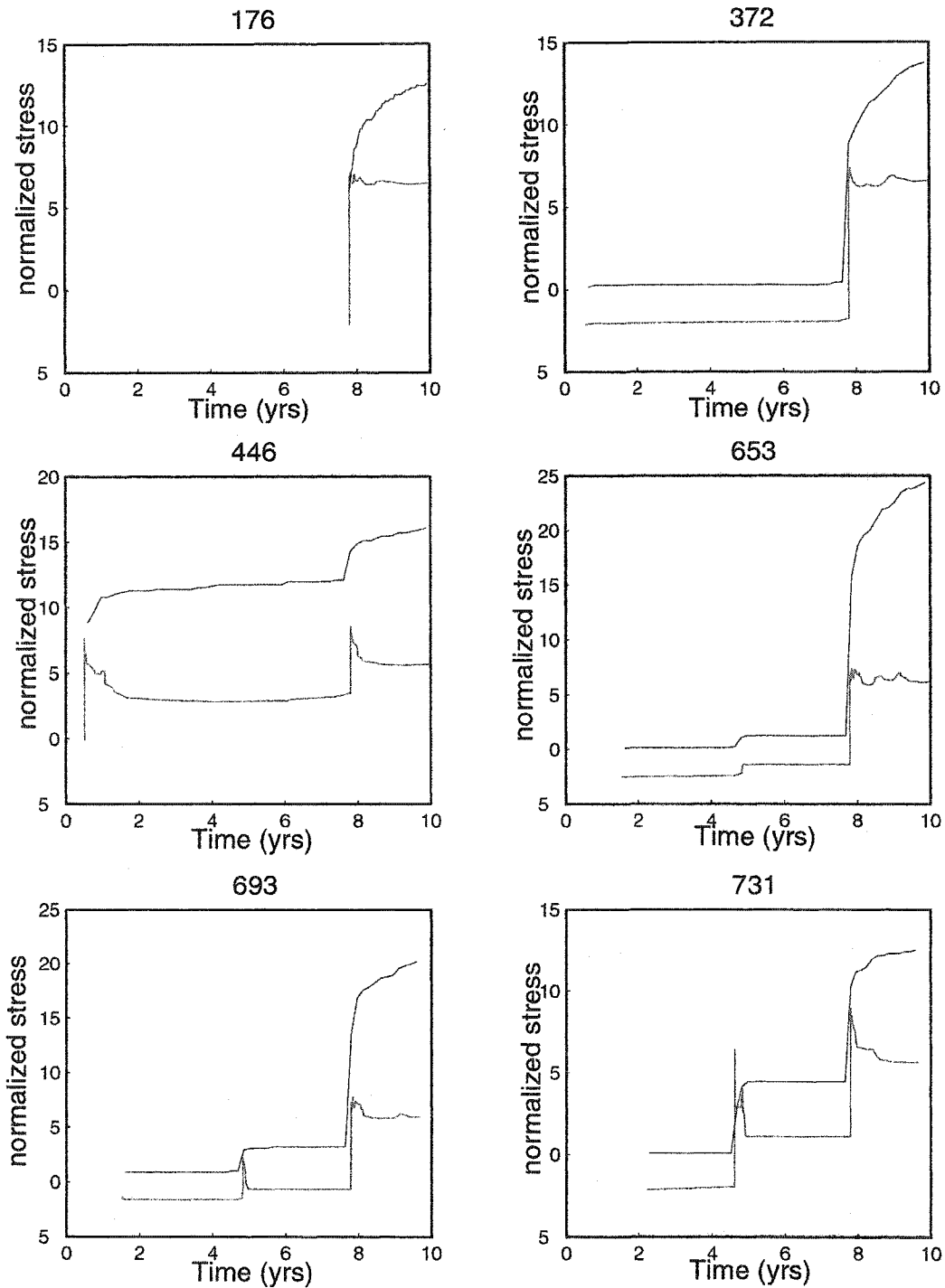


Figure 6.8: Normalized Coulomb stress changes (blue lines) and normalized cumulative # of events (red lines) vs. time for the Hector Mine area. Time 0 starts as 1992; the Hector Mine earthquake occurred at 7.79. Panel 731: Stress vs. time for the Hector Mine epicenter. Node 176: Stress vs. time on the Lavic Lake fault. Nodes 446 and 372: Stress vs. time within the Pisgah event sequence and Hector Mine sequence. Locations of nodes labeled on Figure 6.9.

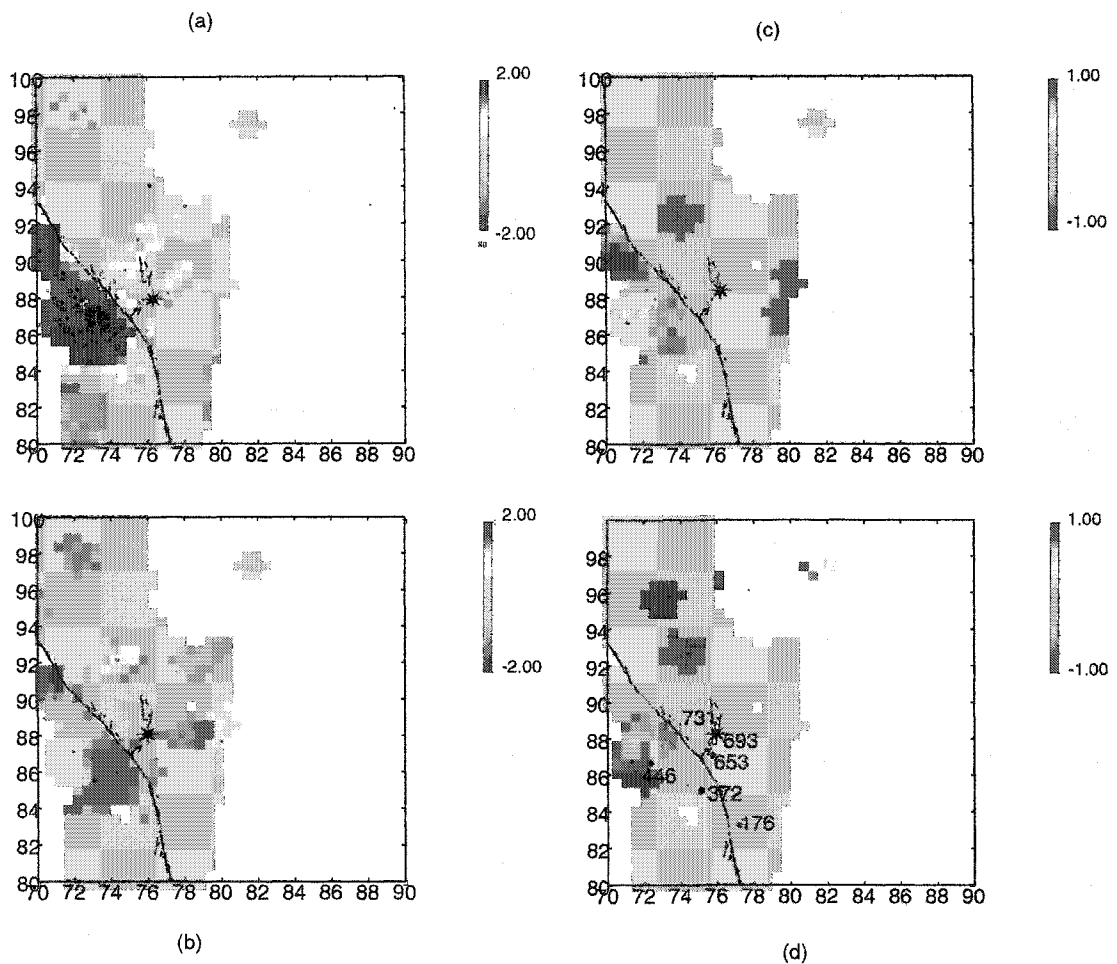


Figure 6.9: Coulomb stress for various intervals following the 1992 Pisgah earthquake. Time intervals are averaged over 2.5 months. Black lines indicate the 1999 Hector Mine surface Rupture and the black star marks the Hector Mine mainshock location. (a) Stress change in the time interval 1992.4 - 1992.6; this time period encompasses the 1992 Pisgah earthquake. (b) Stress change in the time interval 1992.6 - 1992.9. (c) Stress change between 1992.9 - 1993.1. (d) Stress change between 1993.1 - 1993.3. Numbers represent nodes for which stress histories are plotted in Figure 6.8. Axes are in km.

straddles the Lavic Lake and Bullion Faults, both experience stress increases in 1992, following the Landers and Pisgah earthquakes. In Node 446 a decrease of stress after the initial stress increase is apparent. This node shows a similar decrease following a stress increase after the Hector Mine event, as well. Node 176 is on the Bullion Fault and only shows a stress step related to the Hector Mine earthquake.

We track stress change over a year following these earthquakes in Figure 6.9. Although there is a stress increase immediately after the Landers and Pisgah earthquakes, in subsequent time intervals stress appears to decrease. This behavior is inconsistent with the predictions based on the static stress change from the Landers earthquake. It might be the signature of stress triggering due to dynamic stressing during the mainshock since that would be a transient effect. Although dynamic triggering would produce a strain event that would produce the stress change we see, it is not possible to distinguish between dynamically triggered strain events with this signature from other mechanisms such as local pore pressure changes that eventually decay over time.

By 1993 the area near the Lavic Lake fault experiences a stress drop equal to that gained after the Pisgah event. The location of the stress increase is also important. The greatest increase occurs near the location of the Pisgah event, to the west of the Lavic Lake fault. There is also a slight stress increase in stress to the east and north of the future Hector Mine mainshock initiation point, but the initiation point itself does not appear to be stressed.

The next significant activity to occur in the area is the sequence associated with two $M > 4$ events, occurring in August and October 1996. Figure 6.10a shows the initial stress increase associated with the earthquake sequence from the first of these events. The largest stress increase occurs between the Lavic Lake fault and the fault where the mainshock initiated. This region did not show a stress increase in 1992, but it was surrounded on 3 sides by areas that did. In the second timestep, the largest stress increase has moved to the east and towards the eventual hypocenter of the Hector Mine earthquake, shown in Figure 6.11. By the end of 1996, stress has decreased slightly, but the sequence of events has stressed the faults where the Hector Mine foreshocks and ultimately the mainshock initiate.

Using Monte Carlo simulations of the Landers aftershock sequence, *Felzer et al.*, (2002) suggest that stress changes from small events are as likely to trigger large events as changes from other large events. Furthermore they propose that the Pisgah event led to the 1996 earthquake

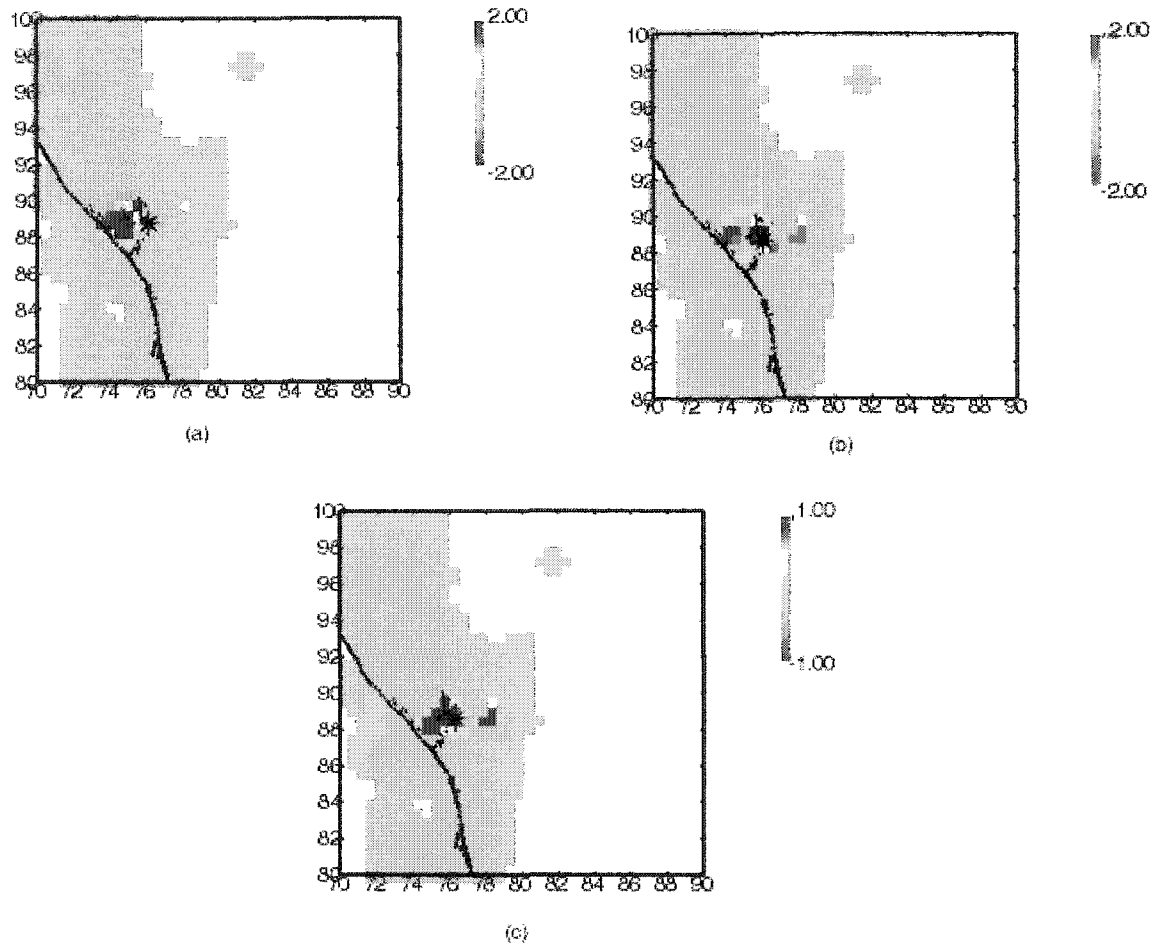


Figure 6.10: Stress evolution following a set of earthquakes in 1996 near the epicenter of the Hector Mine earthquake (black star). Red areas show increase in Coulomb stress. (a) Stress change between 1996.4 to 1996.8. This time interval includes the first of two $M > 4$ events in the sequence. The stress increase occurs to the west of the future location of the Hector Mine mainshock. (b) Stress Change between 1996.6 and 1997.1. This section includes the second $M > 4$ event in the sequence. The stress increase is closer to the Hector Mine mainshock. (c) Stress change in the interval 1996.8-1997.2. There is nearly 0.1MPa of stress decrease in the area of the 1996 earthquake sequence, but the decrease does not equal the previous stress increase. Axes in km.

sequence which in turn triggered the Hector Mine foreshocks. Our results support this interpretation. We may also suggest that the progression we see in the stress change, from west to east towards the Hector Mine hypocenter, may include aseismic creep perhaps following the 1992 Pisgah sequence, on a fault trending in that direction. *Dieterich (2000)* found similar stress patterns for fault creep near the Kilauea Volcano, Hawaii. Other evidence of such a small creep

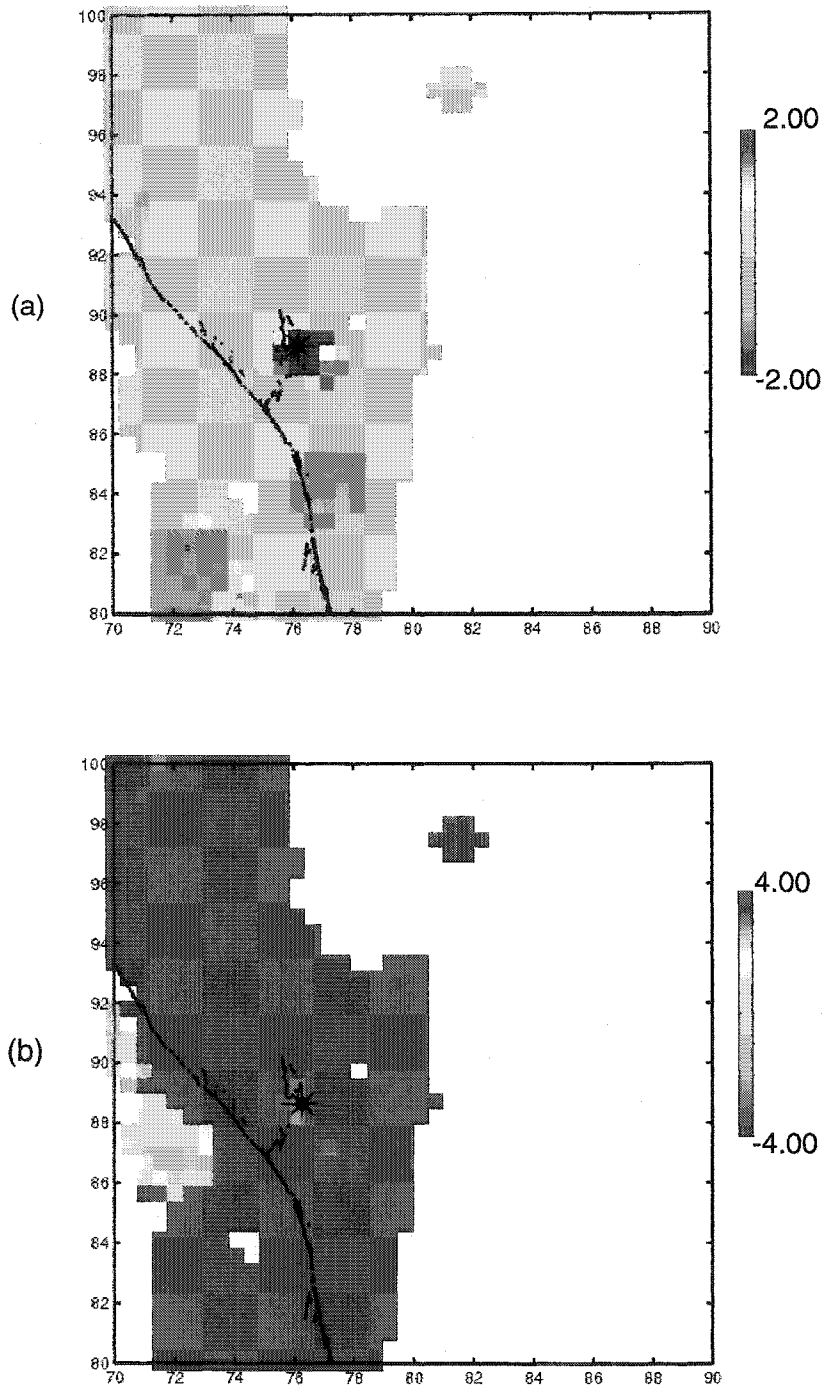


Figure 6.11: Coulomb Stress change near the Hector Mine mainshock hypocenter (black star). (a) Stress changes from the foreshocks of the Hector Mine earthquake. They stress the same area previously stressed by the 1996 earthquake sequence. (b) Stress Change near the Hector Mine mainshock following the Hector Mine earthquake. Axes in km.

event is lacking. *Mellors et al.* (2002) looked for precursory slip prior to the Hector Mine earthquake using InSAR data. Although they examine a track that contains the 1996 sequence, they see no evidence for deformation. They looked, however, for slip in the direction of the Lavic Lake – Bullion Fault and the Hector Mine mainshock, northwest-southeast. The signal of creep from the 1996 sequence would trend in an east-west direction.

Figure 6.11a, shows the evolution of stresses immediately prior to the Hector Mine mainshock. The time step includes the Hector Mine foreshocks but not the mainshock itself. The inferred stress increase is approximately 1.0 MPa near the mainshock hypocenter using $\Delta\sigma=0.2\text{MPa}$. This stress increase is only slightly smaller than the stress change calculated following the Landers earthquake for the Landers hypocenter, 1.2 MPa. Also, to the west of the Bullion fault, there is a stress increase and decrease of about 2 bars, as well as a stress decrease of the same magnitude on that fault south of the foreshocks. *Mellors et al.* (2002) find no significant evidence of aseismic strain along this fault prior to Hector Mine. And closer inspection of these areas suggests that the stress change was produced by only two events occurring two months apart.

REMOTE TRIGGERING AT BIG BEAR?

The 1992 M 6.5 Big Bear earthquake was the largest aftershock of the Landers earthquake. Figure 6.12a shows the relationship of the Big Bear event to the Landers earthquake as well as the stress change in the Big Bear area inferred by changes in the seismicity rate following the Landers and Big Bear mainshocks. Included in the Big Bear area is part of the San Bernardino branch of the San Andreas Fault near which a small region experienced stress increase following the Landers-Big Bear sequence. To the north of the area of increased post-Landers Coulomb stress is the North Frontal Fault Zone, a thrust fault system that defines the northern boundary between the San Bernardino mountains and the Mojave Block. A clear stress step can be related to the Landers – Big Bear earthquakes for most of the Big Bear area.

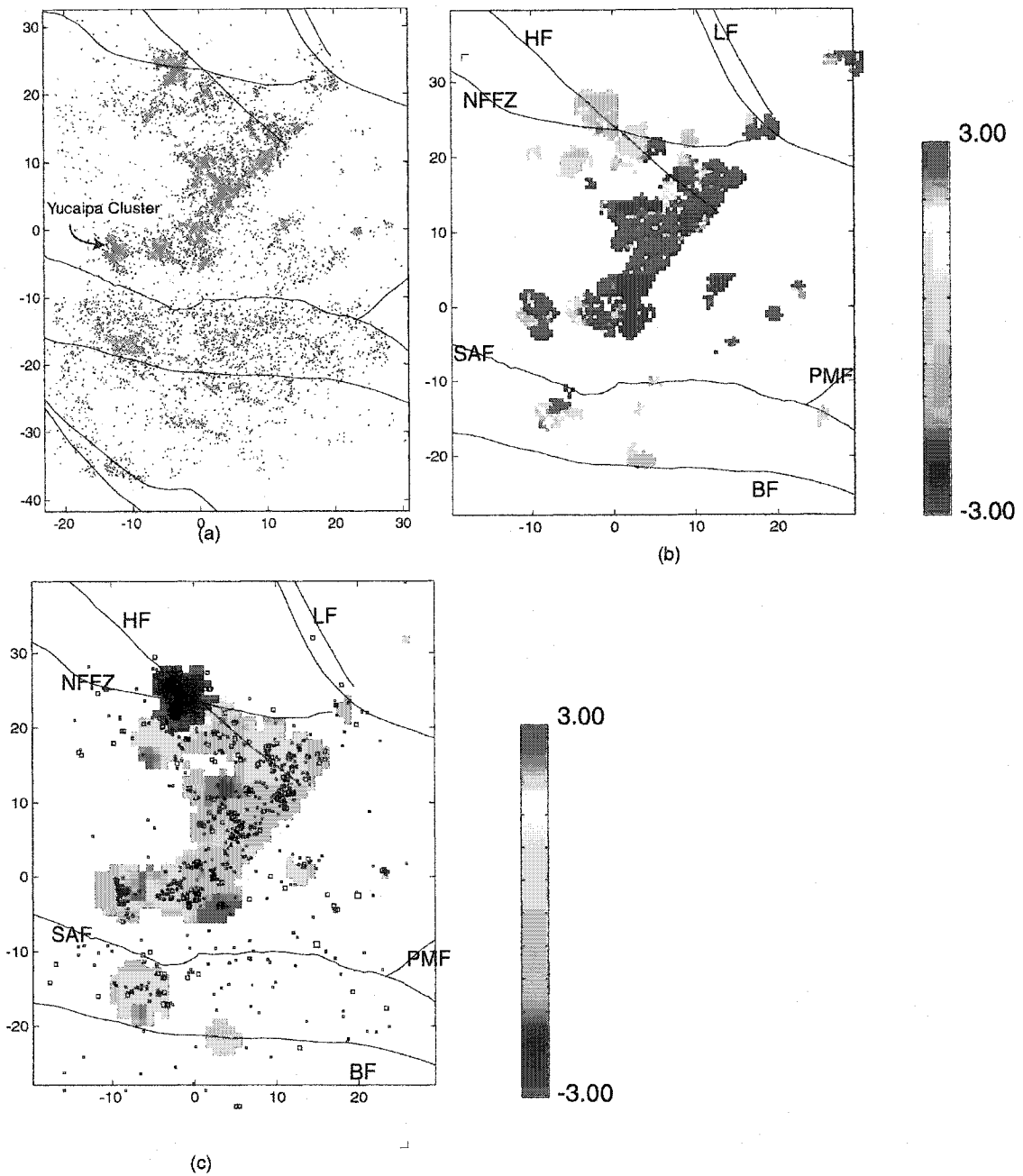


Figure 6.12: (a) Earthquakes between 1992-2002 in the Big Bear region. (b) Stress change at Big Bear due to the 1992 Landers earthquake. (c) Stress change 0.5 years after the 1992 Landers earthquake. The time interval represented is 1992.7 – 1993.3. Axes in km. LF: Lenwood Fault, HF: Helendale Fault, NFFZ: North Frontal Fault Zone, PMF: Pinto Mountain Fault, SAF: San Andreas Fault, BF: Banning Fault.

Six months after the Big Bear mainshock, stress in the area near the NFFZ increases while the rest of the region shows a steep decrease in stress, Figure 6.12b. This increase is associated with two $M > 5$ earthquakes in November and December 1992 and their ensuing aftershock sequences. The stress state near the Big Bear mainshock rupture does not change significantly, though there is a slight decrease in stress. The Yucaipa cluster to the southwest and another cluster of events to the east of that are reactivated in 1998. The next major changes in stress seem to occur after the M 7.1 Hector Mine earthquake nearly 70 km away.

Figure 6.13 shows the change in stress as inferred from seismicity rate in the Big Bear region for a year following the Hector Mine mainshock. Areas at the edges of the Big Bear sequence, such as the region between the North Frontal Fault Zone and the Helendale Fault, as well as the region near the San Andreas fault and the Banning thrust fault, show large changes in Coulomb Stress in this time period. In the northern part of the San Bernardino mountains, seismicity, that initiated in 1998, defines a set of conjugate northwest and northeast trending subfaults (marked 1 in Figure 6.13) that seem to correspond to sections of the NFFZ and the Helendale fault, and that show a stress decrease following Hector Mine. But directly to the east and southwest of this region of stress decrease, stress rises (marked 2 in Figure 6.13). In particular, the fault to the southwest, with a northeast trend delineated by seismicity, experiences stress increases nearing 1.5 MPa. The timing of the stress changes, the decrease immediately following Hector Mine, and the nearby stress increase occurring at the end of 2000, suggest that they are not related. A set of small north-northeast trending faults (marked as 3 in Figure 6.13) near the Helendale Fault also become stressed immediately following the Hector Mine earthquake.

Other features that show changes in stress following Hector Mine include the previously active Yucaipa cluster (marked as 4 in Figure 6.13), which experiences an additional increase in stress following Hector Mine, and the region between the San Andreas fault and the San Gorgonio and Banning faults. The areas that are stressed appear to move to the east over time,

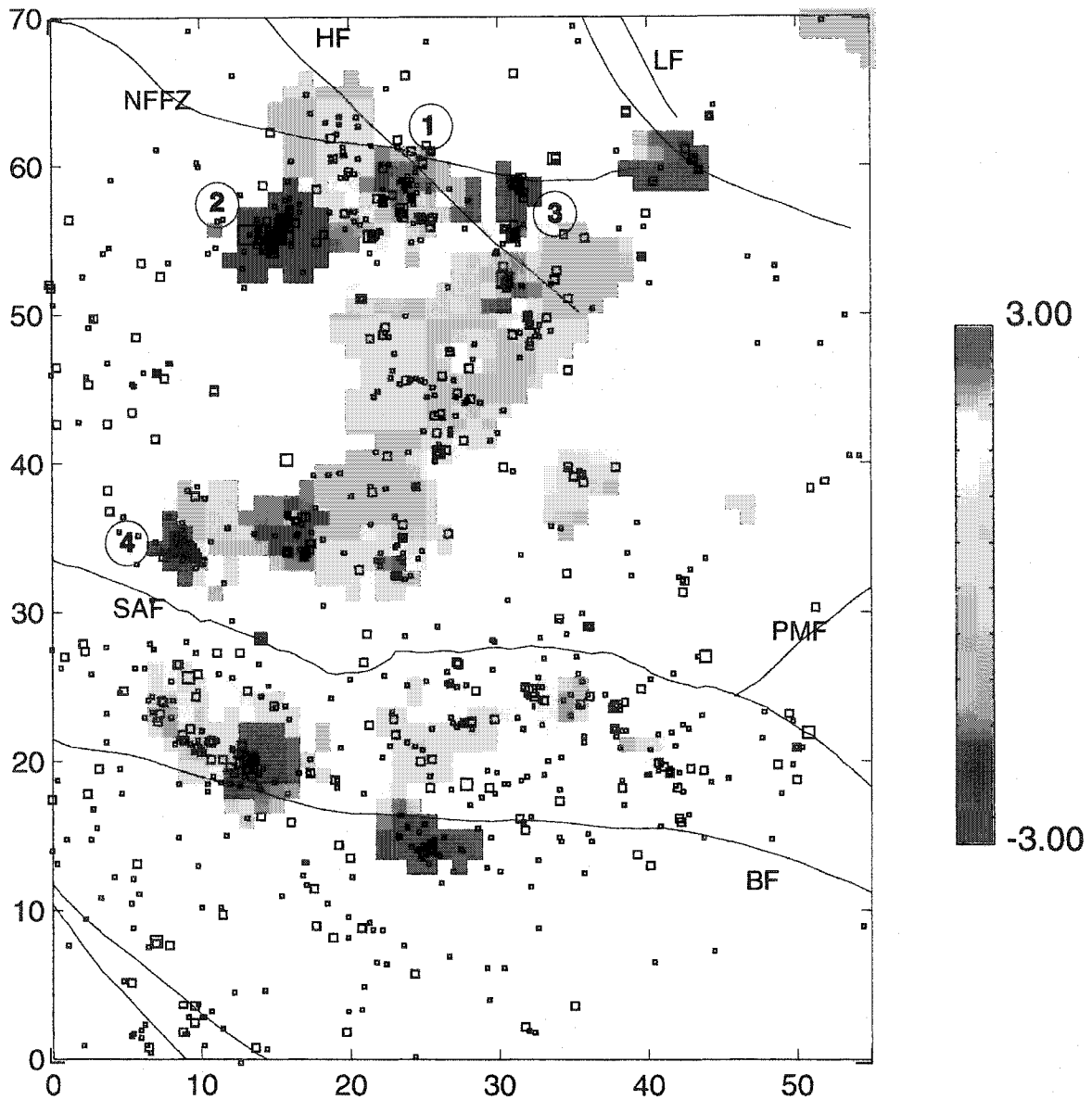


Figure 6.13 Stress change in the Big Bear Region due to the 1999 Hector Mine earthquake. The time interval spans 1998.5 to 2001. Red Areas indicate a stress increase, and blue areas a stress decrease. A NW trending lineament near the Helendale fault gains stress, while the intersection of the Helendale fault and the NFFZ experiences a stress decrease. Numbers mark different clusters of earthquakes; 4=Yucaipa Cluster. LF: Lenwood Fault, HF: Helendale Fault, NFFZ: North Frontal Fault Zone, PMF: Pinto Mountain Fault, SAF:San Andreas Fault, BF: Banning Fault. Axes in km.

starting on the northwestern part of the San Geronio fault and ending on the eastern section of the San Andreas Fault.

Although the timing of the stress changes in these clusters might suggest triggering by the Hector Mine earthquake, the evidence is not clear. For instance, most of these clusters have been active in the past, even before the Big Bear earthquake, though with a much smaller seismicity rate; thus the stress changes in these areas do not denote new features becoming active following Hector Mine. Also, a closer examination of the timing of the stress changes shows that a number of stress increases are initiated many months after the Hector Mine earthquake, again suggesting that there may be other causes for these changes. Only the features marked in area 3 in Figure 6.13 are triggered immediately following Hector Mine and are not active prior to that event.

CONCLUSIONS

Using aftershock rates as a stress meter following *Dieterich (2000)*, we find clear signals of stress changes in the Landers earthquake sequence. We find a postseismic stress increase within the JV-HV fault jog that we attribute to a postseismic increase in pore pressure. The stress change has a similar amplitude to that derived in an independent modeling of poroelastic effects, provided the normalizing parameter, $A\sigma$, is ~ 1.5 -2 bars. This value is consistent with $A = 0.005$, as found in laboratory measurements and by *Gross and Kisslinger (1997)* and super-hydrostatic pore pressure in the fault jog.

The stress analysis suggests that some areas are stressed immediately after the Landers earthquake, but that they appear to become destressed with time. We suggest that dynamic triggering could cause such a pattern. It is, however, not possible to distinguish between that mechanism and other temporary strain events or mechanisms, such as local fluctuations in pore pressure or relaxation of stress by local aseismic creep.

A sequence of earthquakes in 1996 near the eventual initiation point of the Hector Mine earthquake was instrumental in stressing the area where the foreshocks of Hector mine occurred

in 1999. The 1996 events initially indicate increased stress to the west of the mainshock initiation point that slowly migrated to the east and towards the eventual hypocenter of the Hector Mine mainshock. This migration could be the signature of a creep event on an east trending fault, but there is no geodetic signal of such an event (*Mellors et al.*, 2002). While there is some indication of a stress decrease following the 1996 events, a stress history of the node positioned near the Hector Mine mainshock epicenter indicates that this sequence of events did cause a net increase in stress at that location. The actual value of the stress increase is not known because the inversion technique only changes stress enough to account for the apparent seismicity rate change, thus the actual stress decrease could be greater (*Dieterich*, 2002)

Finally, we note that although the features on the periphery of the Big Bear sequence show stress increases from 2000-2001, it is not clear that the 1999 Hector Mine earthquake remotely triggered these features.

BIBLIOGRAPHY

- Abercrombie, R. E., D. C. Agnew, and F. K. Wyatt, Testing a model of earthquake nucleation, *Bull. Seismol. Soc. Am.*, 85, 1873-1878, 1995.
- Abercrombie, R. E., and J. Mori, Occurrence patterns of foreshocks to large earthquakes in the Western United States, *Nature*, 381, 303-307, 1996.
- Angelier, J. Determination of the mean principal directions of stresses for a given fault population. *Tectonophysics*, 56, T17-T26, 1979.
- Barka, A.A. and K. Kadinsky-Cade, Strike-slipfault geometry in Turkey and its influence on earthquake activity, *Tectonics*, 7, 663-684, 1988.
- Beeler, N.M., T.E. Tullis, M.L. Blanpied, and J.F. Weeks. Frictional behavior of large displacement experimental faults, *J. Geophys. Res.*, 101, 8697-8719, 1996.
- Bell, M.L., and A. Nur. Strength changes due to reservoir-induced pore pressure and stress and application to Lake Oroville, *J. Geophys. Res.*, 83, 4469-4483, 1978.
- Beroza, G. C., E. E. Zang, and K. Felzer, A Signature of Pore Fluid Effects in the Landers Aftershock Sequence, *Nature*, (in revision), 2003.
- Beroza, G. C., and M. D. Zoback, Mechanism diversity of the Loma Prieta aftershocks and the mechanics of mainshock-aftershock interaction, *Science*, 259, 210-213, 1993.
- Blanpied, M.L., T.E. Tullis, and J.D. Weeks. Effects of slip, slip rate, and shear heating on the friction of granite, *J. Geophys. Res.*, 103, 489-511, 1998.
- Booker, J. R., Time dependent strain following faulting of porous medium, *J. Geophys. Res.* 79, 2037-2044 (1974).
- Bosl, W. J., and A. Nur, Aftershocks and pore fluid diffusion following the 1992 Landers earthquake, *J. Geophys. Res.*, 107(B12), 2366, doi:10.1029/2001JB000155, 2002.
- Carter, J.N, B.P. Luyendyk, and R.R. Terres, Neogene clockwise rotation of the eastern Transverse Ranges, California, suggested by paleoseismic vectors, *Geol Soc Am Bull*, 98, 199-206, 1987.
- Cleveland, W.S. Robust Locally Weighted Regression and Smoothing Scatterplots, *Journal of the American Statistical Association*, 74, 829-836, 1979.
- Cohee, B.P, and G.C. Beroza. Slip distribution of the 1992 Landers earthquake and its implications for earthquake source mechanics, *Bull. Seismol. Soc. Am.*, 84, 692-712, 1994.
- Coombs, D.S., Dehydration veins in diagenetic and very-low-grade metamorphic rocks; features of the crustal seismogenic zone and their significance to mineral facies, *J. Metamorphic Geology*, 11, 389-399, 1993.

- Das, S., and C. Scholz. Off-fault aftershock clusters caused by shear stress increase? *Bull. Seismol. Soc. Am.*, 71, 1669-1675, 1982.
- Davis, D., J. Suppe, and F.A. Dahlen, The mechanics of fold and thrust belts and accretionary wedges, *J. Geophys. Res.*, 88, 1153-1172, 1983.
- Dieterich, J. A constitutive law for rate of earthquake production and its application to earthquake clustering, *J. Geophys. Res.*, 99, 2601-2618, 1994.
- Dieterich J.H., and B.D. Kilgore. Implications of fault constitutive properties for earthquake prediction: *Proceedings of the National Academy of Sciences*, 93, 3787-3794, 1996.
- Dieterich, J., V. Cayol, P. Okubo. The use of earthquake rate changes as a stress meter at Kiluaea volcano, *Nature*, 408, 457-461, 2000.
- Dieterich, J. H., Earthquake nucleation on faults with rate- and state-dependent strength, *Tectonophysics*, 211, 115-134, 1992.
- Dodge, D. A., G. C. Beroza, and W. L. Ellsworth, Detailed observations of California foreshock Sequences: implications for the earthquake initiation process, *J. Geophys. Res.*, 101, 22,371-22,392,1996.
- Dokka, R.K., The Mojave extensional belt of Southern California, *Tectonics*, 8, 363-390, 1989.
- Dokka, R. K., and C.J. Travis, Late Cenozoic strike-slip faulting in the Mojve Desert, California, *Tectonics*, 9, 311-340, 1990.
- Efron, B., The jackknife, the bootstrap, and other resampling plan, *SIAM*, 92pp, 1982.
- Felzer, K.R. and G.C. Beroza. Deep structure of a fault discontinuity, *Geophys. Res. Let.*, 26, 2121-2124, 1999.
- Felzer, K.R., T. W. Becker, R. E. Abercrombie, G. Ekstrom, and J. R. Rice. Triggering of the 1999 Mw 7.1 Hector Mine earthquake by aftershocks of the 1992 Mw 7.3 Landers earthquake, 107 (B9), 2190, doi:10.1029/2001JB000911, 2002.
- Fertl, W.H., G.V. Chilingarian and H.H. Rieke, *Abnormal Formation Pressures*, Elsevier, New York, 1976.
- Freed, M., and J. Lin. Delayed triggering of the 1999 Hector Mine earthquake by viscoelastic stress transfer, *Nature*, 180-182, 1999.
- Fyfe, W.S., N.J. Price and A.B. Thomson, *Fluids in the Earth's Crust*, Elsevier, New York, 1978.
- Got, J. -L., J. Frechet, and F.W. Klein, Deep fault plane geometry inferred from multiplet relative relocation beneath the south flank of Kiluaea, *J. Geophys Res*, 99, 15,375-15,386, 1994.
- Gross, S. and C. Kisslinger. Estimating tectonic stress rate and state with Landers aftershocks, *J. Geophys. Res.*, 102, 7603-7612, 1997.
- Harris, R. A., Did the 1999 Hector Mine earthquake occur in the stress shadow of the 1992 Landers earthquake?, *Eos Trans. AGU*, 81, Fall Meet., Suppl., F860, 2000.

- Harris, R.A. and S.M.Day. Dynamics of fault interactions: Parallel strike-slip faults, *J. Geophys. Res.*, 98, 4461-4472, 1993.
- Harris, R. A., and R. W. Simpson, The 1999 Mw 7.1 Hector Mine, California earthquake – A test of the stress shadow hypothesis? *Bull Seismol Soc Am*, 4, 1497-1512, 2002.
- Harris, R.A., R.W. Simpson, and P.A. Reasenberg. Influence of static stress changes on earthquake locations in southern California, *Nature*, 375, 221-224, 1995.
- Hart E.W, W.A. Bryant, and J.A. Treiman. Surface faulting associated with the June 1992 Landers earthquake, California, *Calif Geol.*, 46, 10-16, 1993.
- Hauksson, E., State of stress from focal mechanisms before and after the 1992 Landers earthquake sequence, *Bull Seismol Soc Am.*, 84, 917-934, 1994.
- Hauksson, E.L, M Jones, K. Hutton and D. Eberhart-Phillips, The 1992 Landers earthquake sequence: Seismological observations. *J. Geophys. Res.*, 98, 19835-19858, 1993.
- Hauksson, E., L. M. Jones, and K. Hutton, The 1999 Mw7.1 Hector Mine, California Earthquake Sequence: Complex Conjugate Strike-Slip Faulting, *Bull. Seismol. Soc. Am.*, 92, 1154-1170, 2002.
- Healy, J. H. , Rubey, W.W., Griggs, D.T. & Raleigh, C.B., The Denver Earthquakes, *Science*, 161, 1301-1310 (1968).
- Hickman, S, R.H. Sibson, and R. Bruhn. Introduction to special section; Mechanical involvement of fluids in faulting, *J. Geophys. Res.*, 100, 12,831-12840, 1995.
- Hough, S.E., J Mori, E. Sembera, G. Glassmoyer, C. Mueller, and S. Lydeen. Southern surface rupture associated with the 6/28/93 M7.4 Landers Earthquake: Did it all happen during the mainshock? *Geophys Res. Lett*, 1993.
- Hubbert, M. K., and W. W. Rubey, Role of Fluid Pressure in Mechanics of Overthrust Faulting, *Geol. Soc. Am. Bull.*, 70, 1959.
- Hudnut, K. W., Seeber, L. & Pacheco, J., Cross-fault triggering in the November 1987 Superstition Hills earthquake sequence, southern California , *Geophys. Res. Lett.* 16, 199-202 (1989).
- Hudnut, K., L. Seeber, T. Rockwell, J. Gormacher, R. Klinger, S. Lindvall, and R. McElwain. Surface rupture on cross-faults in the 24 November 1987, Superstition Hills, California, earthquake sequence, *Bull Seism. Soc. Am.*, 79, 282-296, 1989.
- Humphreys, E.D. and B.H. Weldon. Deformation across the western U.S.: A local estimate of Pacific-North America transform deformation, *J. Geophys. Res.*, 95, 19,975-20,010, 1994.
- Jennings, C.W. Fault Activity Map of California and Adjacent Areas with Locations and Ages of Recent Volcanic Eruptions, California Geologic Data Map Series, Map no. 6, California Division of Mines and Geology, 1994.

- Jones, L.M., and S. E. Hough, Analysis of Broadband Records from the 28 June 1992 Big Bear Earthquake: Evidence of a Multiple-Event Source, *BSSA*, 85, 688-704, 1995.
- Jones, L.E., S.E. Hough, and D.V. Helmberger. Rupture Processes of the June 28, 1992 Big Bear Earthquake, *GRL*, 20, 1907-1910, 1993.
- Jones, L. M., Foreshocks (1966-1980) in the San Andreas Fault system, California, *Bull. Seismol. Soc. Am.*, 74, 1361-1380, 1984.
- Jones, L. M. and P. Molnar, Some characteristics of foreshocks and their possible relationship to earthquake prediction and premonitory slip on faults, *J. Geophys. Res.*, 84, 3596-3608, 1979.
- Jones, L. M., B. Wang, S. Xu, T. Fitch, The foreshock sequence of the February 4, 1975 Haicheng earthquake ($M=7.3$), *J. Geophys. Res.*, 87, 4575-4584, 1982.
- Kagan, Y.Y., and L. Knopoff. Stochastic synthesis of earthquake catalogs, *J. Geophys. Res.*, 86, 2853-2862, 1981.
- Kanamori, H, H.K. Thio, D. Dreger, E. Hauksson, and T Heaton. Initial investigation of the Landers, California, earthquake of 28 June 1992 using TERRAScope, *Geophys. Res. Letters*, 19, 2267-2270, 1992.
- Kilb, D., The Landers and Hector Mine earthquakes: Correlations between dynamic stress changes and earthquake triggering, *Eos. Trans. AGU*, 81, Fall Meet. Suppl., Abstract S62C-10, 2000.
- Kilgore, B.D., M.L. Blanpied, and J.H. Dieterich, Velocity dependent friction of granite over a wide range of conditions, *Geophys. Res. Lett.*, 20, 903-906, 1993.
- King, G.C., R.S. Stein, and L. Jian. Static stress changes and the triggering of earthquakes, *Bull Seism Soc Am*, 84, 935-953, 1994.
- Lachenbruch, A.H. Simple models for the estimation and measurements of frictional heating by an earthquake. Open-File Report –U.S.G.S., Report: OF 86-0508, 1986.
- Li, V. C., Seale, S. H. & Cao, T., Postseismic stress and pore pressure readjustment and aftershock distributions, *Tectonophysics* 144, 37-54 (1987).
- Linker, M.F. and J.H. Dieterich. Effects of variable normal stress on rock friction: observations and constitutive equations, *J. Geophys. Res.*, 97, 4923-4940, 1992.
- Matti, J.C, D.M., Morton, and B.F. Cox. The San Andreas Fault System in the Vicinity of the Central Transverse Ranges Province, Southern California, in *Earthquake Geology San Andreas Fault System Palm Springs to Palmdale*, 35th Annual Meeting, Oct 2-9, 1992, p 13-62.
- Marone, C.J., C.B. Raleigh, and C.H. Scholz. Frictional behavior and constitutive modeling of simulated fault gouge, *J. Geophys. Res.*, 95, 7007-7025, 1990.
- Marone, C.J., C. H. Scholz, and R. Bilham. On the mechanics of earthquake afterslip, *J. Geophys Res*, 96, 8441-8452, 1991.

- Mellors, R.J., L. Sichoix, and D.T. Sandwell., Lack of Precursory Slip to the 1999 Hector Mine, California, Earthquake as constrained by InSAR, *Bull Seismol Soc Am*, 92, 1443-1449, 2002.
- Massonnet, D., K. Feigl, M. Rossi, and F. Adragna. Radar interferometric mapping of deformation in the year after the Landers earthquake, *Nature*, 369, 227-230, 1994.
- Nazareth, J., and E. Hauksson. Preliminary evaluation of the maximum depth of earthquakes in Southern California (abstract), *Eos, Trans.*, 79, 561, 1998.
- Nur, A. & Booker, J. R., Aftershocks caused by pore fluid flow? *Science* 175, 885-887 (1972).
- Ohnaka, M., Earthquake source nucleation: a physical model for short term precursors. *Tectonophysics*, 211, 149-178, 1992.
- Okada, Y., Surface deformation due to shear and tensile faults in a half-space, *Bull. Seismol. Soc. y Am.*, 75, 1135-1154, 1985.
- Parry, W.T., D. Hedderly-Smith and R.L. Bruhn, Fluid inclusions and hydrothermal alteration on the Dixie Valley fault, Nevada, *J. Geophys. Res.*, 96, 19733-19748, 1991.
- Parsons, T.E., and D.S. Dreger. Static-stress impact of the 1992 Landers earthquake sequence on the nucleation and slip at the site of the 1999 M=7.1 Hector Mine earthquake, Southern California, *Geophys. Res. Lett.*, 27, 1949-1952, 2000.
- Peltzer, G., Rosen, P., Rogez, F. & Hudnut, K, Postseismic rebound in fault step-overs caused by pore fluid flow, *Science* 273, 1202-1204 (1996).
- Peltzer, G., P. Rosen, F. Rogez, & Hudnut, K., Poroelastic rebound along the Landers 1992 earthquake surface rupture, *J. Geophys. Res.*, 103, 30,13130,145, 1998.
- Pollitz, F.F, I.S. Sacks. Stress triggering of the 1999 Hector Mine earthquake by transient deformation following the 1992 Landers earthquake, *Bull. Seismol. Soc. Am.*, 92, 1487-1496, 2002.
- Pujols, J. Comments on the joint dermination of hypocenters and station corrections, *Bull Seism Soc Am*, 78, 1179-1189, 1984.
- Raleigh, C. B., Healy J. H. & Bredehoeft, J. D., An Experiment in Earthquake Control at Rangely, Colorado, *Science*, 191, 1230-1237 (1976).
- Reinen, L.A, J.D. Weeks, and T.E. Tullis. The frictional behavior of serpentinite: Implications for aseismic creep on shallow crustal faults, *Geophys. Res. Lett.*, 18, 1921-1924, 1991.
- Rice, J. R. & Cleary, M. P., Some basic stress diffusion solutions for fluid-saturated elastic porous media with compressible constituents, *Rev. of Geophys. and Space Phys.* 14, 227-241 (1976).
- Ron, H., G. C. Beroza, and A. Nur, Simple model explains complex faulting, *Eos Trans. AGU*, 82, 125-129, 2001.
- Rubin, A.M, D. Gillard, and J.-L. Got. Streaks of microearthquakes along creeping faults, *Nature*, 400, 635-641, 1999.

- Sadler, P.M. The Santa Ana basin of the central San Bernardino Mountains: Evidence of the timing of uplift and strike slip relative to the San Gabriel Mountains, *GSA Memoir*, 178, 307-321, 1993.
- Sauber, J., W. Thatcher, and S.C. Solomon. Geodetic measurements of deformation in the central Mojave Desert, California, *J. Geophys. Res.*, 91, 12,683-12,693, 1986.
- Schaff, D. P., G. H. R. Bokelmann, and G. C. Beroza, F. Waldhauser, W.L. Ellsworth, High Resolution Image of Calaveras Fault Seismicity, *J. Geophys. Res.*, 107, 633, 2002.
- Schaff, D. P., G. H. R. Bokelmann, G. C. Beroza, E. E. Zankerka, and W. L. Ellsworth, Exploring correlation techniques for improved earthquake location, *J. Geophys. Res.* (revised), 2003.
- Segall, P., and D.D. Pollard. Mechanics of discontinuous faults. *J. Geophys. Res.*, 85,4337-4350, 1980.
- Segall, P., and J.R. Rice, Dilatancy, compaction and slip instability of a fluid infiltrated fault, *J. Geophys. Res.*, 100, 22,155-22,171, 1995.
- Sibson, R. H., in *Earthquake Source Mechanics*, (eds., S. Das, J. Boatwright, C. H. Scholz) 157-167, (AGU Press, Maurice Ewing Ser. 5, 593, Washington D. C., 1986).
- Sibson, R.H., Rupture nucleation on unfavorably oriented faults, *Bull Seism Soc Am.*, 80, 1580-1604, 1990.
- Sibson, R.H. Geological evidence for fluid involvement in the rupture processes of crustal earthquakes, *Proceeding of Workshop LXIII; USGS Red-Book conference on the Mechanical involvement of fluids in faulting: Ed. Hickman, SH, R.H. Sibson, and R.L. Bruhn. USGS Open-File report, OF 94-0228, 31-38, 1994.*
- Sieh, K., L. Jones, E. Hauksson, K. Hudnut, D. Eberhart-Phillips, T. Heaton, S. Hough, K. Hutton, H. Kanamori, A. Lilji, S. Lindval, S. McGill, J. Mori, C. Rubin, J. Spotilla, J. Stock, H. K. Thio, J. Treiman, B. Wernicke, and J. Zachariasen. Near field investigations of the Landers earthquake sequence, April to July 1992, *Science*, 260, 171-176, 1993.
- Scholz, C.H. Earthquakes and friction laws, *Nature*, 391, 37-42, 1998.
- Simpson, D.W, W.S. Leith, and C.H. Scholz. Two types of reservoir-induced seismicity, *Bull Seismol. Soc. Am.*, 78, 2025-2040, 1988.
- Simpson, R.W, and P.A. Reasenber. Earthquake induced stress changes on central California faults, in *The Loma Prieta, California earthquake of October 12, 1989: U.S. Geological Survey Professional Paper 1550, 55-89, 1994.*
- Sleep, N.H., and M.L. Blanpied. Creep, compaction and the weak rheology of major faults, *Nature*, 359, 687-692, 1992.
- Sleep, N.H, and M.L. Blanpied. Ductile creep and compaction; a mechanism for transiently increasing fluid pressure in mostly sealed fault zones, *Pure and App. Geophys.*, 143, 9-40, 1994.

- Smith, K.D., K.F. Priestley. The foreshock sequence of the 1986 Chalfant, California earthquake, *Bull Seismol. Soc. Am.*, 78, 172-187, 1988.
- Sowers, J.M., J.R. Unruh, W.R. Lettis, and T.D. Rubin, Relationship of the Kickapoo fault to the Johnson Valley and Homestead Valley faults, San Bernardino County, California, *Bull. Seism. Soc. Am.*, 84, 528-536, 1994.
- Spotila, J. A., and K. Sieh, Geologic investigation of a "slip gap" in the surficial ruptures of the 1992 Landers earthquake, southern California, *J. Geophys. Res.*, 100, 545-559, 1995.
- Stein, R.S., King, G.C.P., and J. Lin, Change in failure stress on the Southern San Andreas Fault System caused by the 1992 M=7.4 Landers earthquake, *Science*, 258, 1328-1332, 1992.
- Stein, R.S., and M. Lisowski. The 1979 Homestead Valley earthquake sequence, California: Control of aftershocks and postseismic deformation, *J. Geophys Res.*, 88, 6477-6490, 1983.
- Stein, R.S. The role of stress transfer in earthquake occurrence. *Nature*, 402, 605-609, 1999.
- Talwani, P., and S. Acree. Pore pressure diffusion and the mechanism of reservoir-induced seismicity. *Pure and App. Geophys.*, 122, 947-965, 1985.
- Tchalenko, J.S., and N.N., Ambraseys. Structural Analysis of the Dasht-e Bayaz (Iran) earthquake fractures, *Geol. Soc. Am. Bull.*, 81, 41-59, 1970.
- Terzaghi, K.V. Die Berechnung der Durchlässigkeitsziffer des Tones aus dem Verlauf der hydrodynamischen Spannungserscheinungen, *Sb. Akad. Wiss Wien*, 132, 105, 1923.
- Townend, J. and M.D. Zoback, Implications of earthquake focal mechanisms for the frictional strength of the San Andreas fault system, *Spec. Pub. Geol. Soc. London*, 2001.
- Wald, D. J., and T. H. Heaton, Spatial and temporal distribution of slip for the 1992 Landers, California, earthquake, *Bull. Seismol. Soc. Am.*, 84, 668-691, 1994.
- Wald, D. J., L. K. Hutton, and D. D. Given, The Southern California Network Bulletin: 1990-1993 summary, *Seismol. Res. Lett.*, 66, 9-19, 1995.
- Waldhauser, F., and W. L. Ellsworth, A double-difference earthquake location algorithm: method and application to the northern Hayward Fault, California, *Bull. Seismol. Soc. Am.*, 90, 1353-1368, 2000.
- Wesnousky, S.G. Earthquakes, quarternary faults, and seismic hazard in California, *J Geophys Res.*, 91, 12587-12631, 1986.
- Wiemer, S. and K. Katsumata, Spatial variability of seismicity parameters in aftershock zones, *J. Geophys. Res.*, 104, 13,135-13,151 (1999).
- Zachariesen, J and K. Sieh. The tranfer of slip between two en-echelon strike-slip faults: a case study from the 1992 Landers ertquake, Southern California, *J. Geophys. Res.*, 100, 15,281-15,301, 1995.
- Zoback, M.D., M.L. Zoback, V.S. Mount, J.Suppe, J.P. Eaton, J.H. Healy, D.H. Oppenheimer, P.A. Reasenberg, L.M. Jones, C.B. Raleigh, I.G. Wong, O. Scotti, and C.M. Wentworth, New

evidence on the state of stress of the San Andreas fault system, *Science*, 238, 1105-1111, 1987.

Zanzerkia, E.E. and G.C. Beroza, Evidence of Pore Fluid Triggering in the 1992 Landers aftershock sequence. *Science*, in preparation, 2003.

Zanzerkia, E.E. and G.C. Beroza, Waveform Analysis of the 1999 Hector Mine Foreshock Sequence, *Geophys Res Lett*, 30(8), doi: 10.1029/2002GL016383, 2003.